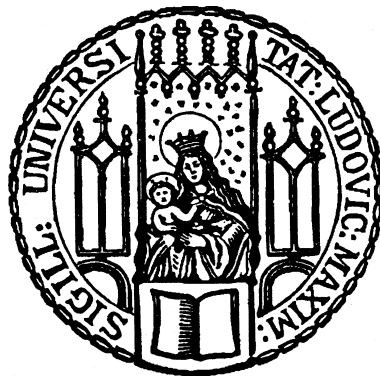

Light-matter interactions in semiconductor moiré heterostructures

Johannes Scherzer



München 2024

Light-matter interactions in semiconductor moiré heterostructures

Johannes Scherzer

Dissertation
an der Fakultät für Physik
der Ludwig-Maximilians-Universität
München

vorgelegt von
Johannes Scherzer
aus Regensburg

München, den 28. Mai 2024

Erstgutachter: Prof. Dr. Alexander Högele

Zweitgutachter: Prof. Dr. Jan von Delft

Tag der mündlichen Prüfung: 02.08.2024

Zusammenfassung

Zweidimensionale Übergangsmetall-Dichalcogenide (TMDs) sind geschichtete Halbleiter mit einer hexagonalen Gitterstruktur, die sich im Grenzfall einer einzigen Monolage durch stark gebundene Exzitonen auszeichnen. Deren hohe Oszillatorstärke in Verbindung mit einem einzigartigen Valley-Freiheitsgrad macht diese Materialgruppe zu einem hervorragenden Kandidaten für die Untersuchung neuartiger Effekte der Licht-Materie-Wechselwirkung. Die vertikale Kombination solcher hexagonaler Gitter mit variierender Gitterkonstante oder kleiner relativer Verdrehung führt im Allgemeinen zu einem neuen, weitreichenden Moiré-Übergitter, das ein periodisches Potenzial für Exzitonen und Ladungsträger bewirkt und eine einzigartige Festkörperplattform für Studien der korrelierten Vielteilchenphysik bietet.

In dieser Arbeit wurden umfassende Untersuchungen von $\text{MoSe}_2/\text{WS}_2$ Van-der-Waals-Heterostrukturen mittels optischer Spektroskopie sowie optischer Resonatoren mit hoher Finesse bei kryogenen Temperaturen durchgeführt. Dabei dienten senkrechte elektrische und magnetische Felder sowie Ladungsdotierung zur Erforschung der zu Grunde liegenden Moiré-Exzitonen-Physik.

In konfokaler Reflektionsspektroskopie wurde die Vielzahl optischer Übergänge von $\text{MoSe}_2/\text{WS}_2$ aufgedeckt. Diese wurden mithilfe eines effektiven Kontinuum-Modells anhand der Exziton-Hybridisierung im elektrischen Feld als Intra- und Interlayer-Moiré-Exzitonen identifiziert. Unter Elektronendotierung zeigten geladene Moiré-Exziton-Komplexe ein stark nichtlineares Verhalten in senkrechten Magnetfeldern, was auf korrelierte magnetische Ordnung der Elektronenspins zurückzuführen ist. Durch die Analyse des Ladungsverhaltens der Bilage mittels eines elektrostatischen Kondensatormodells konnte das Auftreten dieser Coulomb-korrelierten Zustände mit der Elektronendichte innerhalb der einzelnen Monolagen in Verbindung gesetzt werden.

Gekoppelt an faserbasierte, durchstimmbare Fabry-Pérot Mikrokavitäten zeigten $\text{MoSe}_2/\text{WS}_2$ Moiré-Exzitonen Signaturen starker Licht-Materie-Wechselwirkung in Form von neutralen und geladenen Moiré-Exziton-Polaritonen. Deren Verhalten wurde bei variierender Elektronendichte in Abhängigkeit von der Resonanz-Verstimmung zwischen Photonen und Exzitonen sowie als Funktion der optischen Anregungsleistung untersucht und mittels eines gekoppelten Oszillatormodells analysiert. Hierbei zeigte sich eine verstärkte leistungsabhängige Nichtlinearität im Vergleich zu Exziton-Polaritonen in isolierten TMD-Monolagen. Ein weiteres Experiment nutzte einen offenen Mikrokavitätsaufbau mit Zugang zu senkrechten Magnetfeldern um das Verhalten geladener Exziton-Polaritonen in korrelierter magnetischer Ordnung zu untersuchen. Deren Antwort auf korrelierten Magnetismus unterschied sich aufgrund des erhöhten Maßes an Kontrolle durch die Mikrokavität von dem charakteristischen Verhalten ungekoppelter geladener Moiré-Exzitonen.

Die Ergebnisse dieser Arbeit unterstreichen die Vielseitigkeit und Einzigartigkeit von $\text{MoSe}_2/\text{WS}_2$ Heterobilagen für die Untersuchung von Moiré-induzierten Vielteilchenphänomenen, insbesondere im Bereich der starken Licht-Materie-Kopplung.

Abstract

Two-dimensional transition metal dichalcogenides (TMDs) are layered semiconductors with a hexagonal lattice structure hosting tightly bound excitons. Their high oscillator strength, combined with a unique valley degree of freedom, makes this group of materials an outstanding candidate for studying novel effects of light-matter interaction. Vertically stacking hexagonal TMD layers with small lattice mismatch or rotational misalignment generally results in a new, long-range moiré superlattice that introduces a periodic potential for excitons and charge carriers, providing a unique solid-state platform for studies of correlated many-body physics.

This thesis presents a comprehensive optical investigation of MoSe₂/WS₂ van der Waals heterostructures. We explored the moiré exciton physics of this material in dual-gate field-effect devices – subject to perpendicular electric and magnetic fields as well as charge doping – both in optical spectroscopy and cavity-enhanced measurements at cryogenic temperatures.

In confocal reflection spectroscopy, the low-energy optical transitions of MoSe₂/WS₂ could be discerned as intra- and interlayer moiré excitons, elucidated within an effective continuum model by examining exciton hybridization as a function of the electric field. In the presence of electron doping, charged moiré exciton complexes displayed highly nonlinear behavior with varying out-of-plane magnetic fields, attributed to correlated magnetic order of the electron spins. Analyzing the charging response through a capacitor model linked the formation of these Coulomb-correlated states to the density of electrons per moiré unit cell inside the individual monolayers.

To probe moiré excitons in the regime of strong light-matter interaction, we utilized a fiber-based open Fabry-Pérot microcavity in a closed-cycle cryostat. We investigated the formation of neutral and charged moiré exciton-polaritons and their behavior as a function of the electron doping, cavity-exciton detuning and optical excitation power. Our findings from a coupled oscillator model analysis reveal an enhanced power dependent nonlinearity of moiré exciton-polaritons as compared to exciton-polaritons in bare TMD monolayers. In a complementary experiment we leveraged an open microcavity setup with access to out-of-plane magnetic fields to study the response of charged moiré exciton-polaritons in the presence of correlated magnetic order. These polaritons unveiled an intriguing enhancement effect of the correlation-induced optical response compared to uncoupled moiré excitons as a result of the cavity control.

The findings of our study underscore the versatility and uniqueness of MoSe₂/WS₂ heterobilayers as a platform for studying moiré-induced many-body phenomena, particularly in the regime of strong light-matter coupling.

Contents

| | |
|---|-----------|
| 1. Introduction | 1 |
| 2. Fundamentals of monolayer semiconductors and optical resonators | 5 |
| 2.1. Excitons in monolayer semiconductors | 5 |
| 2.1.1. Crystal and band structure | 5 |
| 2.1.2. Tightly bound (charged) excitons | 7 |
| 2.1.3. Excitons exposed to external fields | 9 |
| 2.2. Light-matter interaction in Fabry-Pérot cavities | 11 |
| 2.2.1. Basics of Fabry-Pérot resonators | 12 |
| 2.2.2. Plano-concave optical resonator | 14 |
| 2.2.3. Quantum theory of strong light-matter coupling | 16 |
| 3. Experimental methods | 21 |
| 3.1. Sample fabrication | 21 |
| 3.1.1. Components of the van der Waals heterostructure | 21 |
| 3.1.2. Heterostructure design and assembly | 26 |
| 3.1.3. Sample treatment and contacting | 29 |
| 3.2. Confocal spectroscopy in cryogenic environment | 29 |
| 3.2.1. Spectroscopy techniques | 30 |
| 3.2.2. Dual-gate operation | 34 |
| 3.2.3. AC modulation measurements | 35 |
| 3.3. Open microcavity in a closed-cycle cryostat | 37 |
| 3.3.1. Cavity design and setup | 37 |
| 3.3.2. Damping of vibrational noise for high finesse operation | 39 |
| 3.3.3. Limitations of vibration suppression | 46 |
| 3.3.4. Cavity transmission spectroscopy | 49 |
| 4. Moiré exciton physics in MoSe₂/WS₂ heterostructures | 53 |
| 4.1. Introduction and theoretical concepts | 54 |
| 4.1.1. Modelling of the moiré exciton bandstructure | 54 |
| 4.1.2. Capacitor model | 60 |
| 4.1.3. Coulomb-interaction of moiré excitons and ordered electrons | 64 |
| 4.2. Heterostructure devices and characteristics | 65 |

| | |
|--|------------|
| 4.3. Field-induced hybridization | 67 |
| 4.3.1. Modeling of moiré excitons exposed to out-of-plane electric fields . . . | 68 |
| 4.3.2. AC modulation spectroscopy for hybridization studies | 70 |
| 4.3.3. Real space distribution of moiré exciton states | 72 |
| 4.4. Charge doping in presence of a moiré potential | 74 |
| 4.4.1. Optical signatures in the electron doping regime | 75 |
| 4.4.2. Electrostatic simulations | 76 |
| 4.4.3. Sensing of correlated electron-spin lattices | 82 |
| 5. Moiré exciton-polaritons in MoSe₂/WS₂ heterostructures | 85 |
| 5.1. Introduction | 85 |
| 5.2. Characterization of moiré exciton-polaritons | 86 |
| 5.2.1. Charge tunability | 88 |
| 5.2.2. Moiré-induced nonlinearity | 89 |
| 5.3. Correlated magnetism of moiré exciton-polaritons | 92 |
| 5.3.1. Polarization-contrasting response in high magnetic fields | 94 |
| 5.3.2. Nonlinear polariton response to varying magnetic fields | 98 |
| 5.3.3. Role of the polarization-contrasting Rabi splitting | 100 |
| 5.3.4. Modelling of effective polariton g-factors | 103 |
| 6. Summary and outlook | 107 |
| A. Extended data: Moiré exciton physics in MoSe₂/WS₂ heterostructures | 111 |
| A.1. Laterally varying conduction band alignment | 111 |
| A.2. Signatures of the hole doping transition | 113 |
| B. Polariton engineering at MoSe₂-graphite interfaces | 117 |
| Bibliography | 121 |
| List of publications | 137 |
| List of symbols and abbreviations | 139 |
| Acknowledgments | 141 |

Introduction

Understanding the intricate interactions of atoms or other elementary particles lies at the heart of physics. In the words of Richard Feynman, "atoms are very special: they like certain particular partners, certain particular directions, and so on. It is the job of physics to analyze why each one wants what it wants. At any rate, two oxygen atoms form, saturated and happy, a molecule" [1]. In the first of his famous lectures, Feynman encapsulated the essence of curiosity-driven research by examining the problem of interacting oxygen atoms. Linus Pauling first described this interaction in 1931 as covalent bonding [2], marking an early milestone in our understanding of atomic behavior. Just two decades ago, the idea that covalent bonds in graphite could enable stable, isolated single atomic layers was unexpected. However, Andre Geim and Konstantin Novoselov, driven by their curiosity to explore the unknown, succeeded in achieving exactly this: a single layer of carbon atoms that can be separated from the bulk of van der Waals layers – so-called graphene. In doing so, they opened up the field of two-dimensional (2D) materials for fundamental research exploring the physics of elementary particles confined to two dimensions [3]. In the following years, groundbreaking discoveries were made on graphene-based structures, including the observation of massless Dirac fermions [4], the quantum Hall effect [5, 6], and exceptional electron mobility [7], paving the way for future technologies. Transition metal dichalcogenides (TMDs) emerged as another member of the 2D materials family, exhibiting a hexagonal lattice structure similar to graphene. They are semiconductors with a direct bandgap in the monolayer limit and provide intriguing optical properties for studying new aspects of light-matter interaction [8].

Recently, particular interest captured the phenomenon that arises when two single atomic layers with hexagonal lattices are stacked on top of each other – the formation of a moiré lattice. This effect, originally observed in art and photography, occurs when two overlapping patterns with different periodicity or a finite rotational misalignment interfere with each other and create a new, visually apparent pattern. In such van der Waals moiré struc-

tures, elementary charges experience the effect of a periodic moiré potential in the lateral dimension in addition to the vertical confinement. Exploiting this confinement to study and control the interactions of elementary charges and engineer the electrical and optical material properties on a nanoscale has opened new frontiers in the study of 2D materials [9, 10]. The arrangement of a graphene-based moiré lattice has been implicated in the emergence of superconductivity at specific “magic” twist angles where the charge carrier density diverges due to the modulation of the material bandstructure by the moiré potential [11, 12]. Similarly, in TMD-based moiré structures, the exciton bandstructure is modulated [13–15], leading to the formation of moiré excitons localized at distinct positions within the underlying superlattice [16, 17].

Moiré excitons are unique candidates for studying and controlling fundamental interactions in the hosting moiré materials in different ways. Their sensitivity to external fields and charge doping enabled the observation of correlated many-body phenomena emergent in TMD moiré structures [18, 19]. The formation of Wigner crystals [20, 21] or correlated Mott-insulator states [20, 22–27] at finite doping levels allowed to study aspects of Hubbard model physics and correlation-induced magnetism [28, 29]. Furthermore, the confinement of moiré excitons leads to enhanced exciton-exciton interactions and a modified optical response [30, 31]. This property makes them particularly suitable for studies in the regime of strong light-matter coupling, where exciton-polaritons emerge as superpositions of cavity photons and excitons [32]. These new quasiparticles inherit properties from both components, such as the small effective mass of cavity photons or the optical non-linearity related to exciton-exciton interactions [33, 34]. The implementation of effective photon-photon interactions using such exciton-polariton systems promises applications in quantum information processing [35].

In this thesis, we performed elaborate studies of moiré exciton physics in $\text{MoSe}_2/\text{WS}_2$ heterostructures. This material combination exhibits both key aspects mentioned above: Coulomb correlated phases, which can be sensed by the optical response of moiré excitons [36, 37], as well as moiré-induced nonlinearities, which were demonstrated in cavity-assisted experiments [38]. With our work, we contributed to the understanding of the $\text{MoSe}_2/\text{WS}_2$ bandstructure by analyzing the electric field-induced conduction band hybridization [P2]. We revealed an intricate layer-by-layer charging behavior for electrons in anti-parallel $\text{MoSe}_2/\text{WS}_2$ stacks with near-resonant conduction band alignment, which effectively implements a bilayer Hubbard model [P3]. Furthermore, we demonstrated how coupling to a photonic microcavity promotes the formation of charged moiré exciton-polaritons in parallel $\text{MoSe}_2/\text{WS}_2$ stacks showing signatures of correlation-induced magnetism which go beyond the response of the bare excitons [P4].

This thesis is structured as follows: After the introduction, Chapter 2 provides an overview of the fundamental properties of TMD monolayers and the corresponding exciton physics, followed by an introduction to the fundamentals of light-matter interaction in Fabry-Pérot microcavities.

Chapter 3 presents the experimental techniques and setups that were developed and employed in the course of this thesis. First, we describe how dual-gated van der Waals heterostacks were fabricated and treated. Subsequently, the setup and techniques for cryogenic spectroscopy are introduced, and we present the design of the open microcavity setup that was developed in collaboration with Khaled Karraï at attocube systems AG. We explain the mechanisms and limitations of vibration induced cavity length fluctuations and introduce the procedure of cavity transmission spectroscopy using this setup.

In Chapter 4, we present our understanding of moiré exciton physics developed for $\text{MoSe}_2/\text{WS}_2$ heterostructures in the scope of this work. We initially introduce the theoretical models and subsequently demonstrate their validity on the basis of the experimental data obtained from reflection spectroscopy on various $\text{MoSe}_2/\text{WS}_2$ devices. The first part of the Chapter focuses on modeling the experimentally observed intra- and interlayer moiré exciton dispersions using an effective continuum model. In the second part, we elucidate the optical response of moiré excitons as a function of the applied electric fields and doping potential, employing a discretized capacitor model. Additionally, we unveil the existence of correlation-induced magnetism at specific electron filling factors per moiré unit cell.

Chapter 5 treats $\text{MoSe}_2/\text{WS}_2$ moiré excitons, coupled to confined photons in open microcavities. We demonstrate the observation moiré exciton-polaritons, exhibiting properties that can be controlled by electron doping. Specifically, charged excitons with significant oscillator strength allow the formation of moiré polaron-polaritons at integer electron doping per moiré unit cell, which exhibit moiré induced non-linearity as a function of the polariton density. Furthermore, we studied the magnetic response of moiré exciton- and polaron-polaritons in collaboration with Christian Schneider at the University of Oldenburg. We reveal an enhancement of the correlation-induced magneto-optical signatures compared to uncoupled moiré excitons resulting from strong coupling with cavity photons.

The final Chapter summarizes the results and gives a short outlook on possible issues related to our findings that could be addressed in future experiments. This thesis is the outcome of collaborative efforts, as evidenced by the co-author lists and contributions in the relevant publications and manuscripts [P2–P4, P8, P6]. The specific contributions of each collaborator are detailed in the introductions of the corresponding Chapters.

Fundamentals of monolayer semiconductors and optical resonators

2

This Chapter provides an overview of the physical background and concepts underpinning the work conducted within the scope of this thesis. Firstly, we introduce the basic properties of excitons in two-dimensional materials, including their response to external electric and magnetic fields. In the second part, we present the fundamentals of optical resonators, in particular focusing on plano-concave Fabry-Perot microcavities as a platform for studying light-matter coupling.

2.1. Excitons in monolayer semiconductors

In the following we review the basics of TMD monolayers, focusing on the properties of the momentum-bright excitons in MoSe₂ and their response to external forces, such as charge doping, electric and magnetic fields. The theoretical concepts are underpinned with experimental data acquired on the MoSe₂ ML area of device D1 (see Section 4.2 for details).

2.1.1. Crystal and band structure

TMDs represent a diverse family of materials consisting of transition metal atoms M (W, Mo), sandwiched between two layers of chalcogen atoms X (S, Se, Te) - forming a honeycomb lattice akin to graphene as shown in Figure 2.1a featuring an invariance under threefold rotation. The individual atoms within a single layer are tightly bound to each other by covalent forces, while relatively weak van der Waals forces act in between different layers, enabling to separate single layers from the bulk material and stack van der Waals heterostructures from different monolayers [39]. Unlike graphene, which lacks an intrinsic bandgap, TMDs exhibit semiconducting behavior with a direct bandgap in the monolayer limit [40, 41], making them promising candidates for various electronic and optoelectronic applications [42].

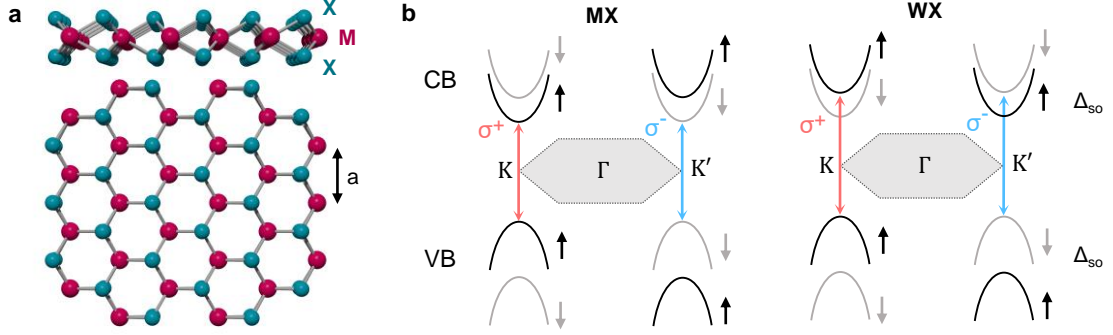


Figure 2.1.: **MoSe₂ crystal and bandstructure.** **a**, Crystal structure of a TMD monolayer (MoSe₂). Metal atoms ($M = W, Mo, \dots$) are sandwiched between two chalcogen atom layers ($X = S, Se, \dots$) forming a hexagonal honeycomb lattice with lattice constant a . The schematics are adapted from Ref. [43]. **b**, Schematic bandstructure for MX (left panel) and WX (right panel) TMD monolayers at the K -points at the corners of the hexagonal Brillouin zone. The polarization-contrasting optical selection rules give rise to valley selective excitation with σ^+/σ^- polarized light as highlighted by red/blue arrows for the energetically lowest spin-bright transitions. The spin orbit splitting Δ_{so} is of the order of 10 meV in case of the conduction band and of the order of 100 meV for the valence band.

According to the hexagonal crystal structure of TMD monolayers, the Brillouin zone also takes on a hexagonal shape, with high symmetry points positioned at the center (Γ) and the corners (K). The direct bandgap is situated at the K points of the Brillouin zone, leading to several remarkable properties inherent to TMD monolayers.

Firstly, a substantial spin-orbit splitting of several hundred meVs occurs in the valence band (VB) at the K points. This effect arises because the electronic states within the VB are dominated by contributions from the in-plane d -orbitals ($d_{x^2-y^2}$ and d_{xy}), as determined from first-principle density functional theory (DFT) [44, 45]. Conversely, the primary electronic states at the conduction band (CB) edge, located at the K points, predominantly comprise out-of-plane d -orbitals of the transition metals. As these orbitals lack angular momentum, they do not contribute to the spin-orbit interaction. However, there is a minor contribution to the total orbital weight stemming from the p orbitals of the chalcogen atoms. Consequently, a finite but substantially weaker spin splitting of the CB at the K points is observed compared to that in the VB.

Secondly, the broken inversion symmetry within the TMD monolayer enables valley-contrasting optical selection rules at the K points [46–48]. The spin-orbit-split states within the CB and VB possess opposite spin quantum numbers corresponding to spin up and down. As the system must preserve time reversal symmetry, and given that the K points are positioned at finite angular momentum, the assignment of spin up and down states must

be reversed at opposite corners of the Brillouin zone. Consequently, these opposite corners are denoted as K and K' valleys. Upon optical excitation with σ^+/σ^- polarized light, lowest energy excitons are exclusively created in the K/K' valley.

The resulting band structure at the K valleys, with assigned spins and allowed optical transitions, is depicted in Fig. 2.1b. Utilizing the material parameters derived from DFT calculations, $k \cdot p$ theory or tight-binding approaches allow to accurately model the band structure for different TMDs at these high symmetry points [49–51]. These models reveal that the spin order within the conduction band is reversed for molybdenum (MoX) and tungsten-based (WX) TMD monolayers, as evidenced by the comparison between the left and right panels of Fig. 2.1b. Consequently, in the case of MoX, the lowest energy transition at the K points is spin-allowed and therefore optically bright, while WX exhibits a spin-forbidden ground state transition that does not manifest in optical measurements employing in-plane polarized excitation [52–54].

2.1.2. Tightly bound (charged) excitons

In semiconductors, optical irradiation below the free particle bandgap can induce the formation of excitons – bound states of an electron in the conduction band and a hole in the valence band. In conventional 3D semiconductors like GaAs or Si, the corresponding binding energy E_b typically ranges in the order of a few meV preventing the observation of excitons at room temperature [55]. However, in TMD monolayers, excitons with binding energies of several hundred meV dominate the optical response even at elevated temperatures due to their two-dimensional confinement. As depicted in Figure 2.2a, the electric field of the electron-hole pair extends far into the surrounding medium, which usually possesses a smaller electric susceptibility compared to the TMD monolayer itself. Consequently, this leads to reduced dielectric screening of the Coulomb interaction in TMD monolayers, reinforcing the exciton binding energy [56, 57].

The two VB subbands offer the possibility to create two different types of excitons, A and B, by optically exciting electrons from the upper or lower VB level, respectively [8]. Figure 2.2b presents a differential reflection (DR) spectrum acquired on a MoSe₂ monolayer (see Section 3.2.1 for experimental details). In MoSe₂ monolayers, the ground state A exciton, also referred to as X exciton, manifests at an energy of ~ 1.63 eV at cryogenic temperature (4 K). Its large binding energy allows for the observation of the hydrogenic Rydberg series of Wannier-Mott excitons. The energy separation of different exciton states (1s, 2s, 3s, ...) can be used to determine the exciton binding energy and free carrier band gap as illustrated on the right side Figure 2.2b [57, 58].

Free charge carriers inside a TMD monolayer significantly influence excitons and their optical response. Early investigations of basic TMD-based field-effect devices revealed that TMD monolayers often exhibit intrinsic n-doping [59, 60]. In optical measurements such as

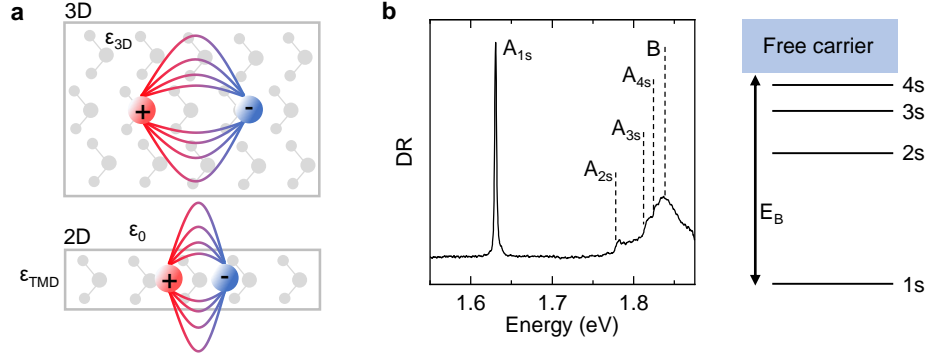


Figure 2.2.: **Excitons in TMD MLs.** **a**, Schematics of exciton formation in bulk TMD (upper panel) and in the limit of a single layer (lower panel). Reduced dielectric screening leads to an increased binding energy E_B for the latter case. The illustration is adapted from Ref. [57]. **b**, A MoSe₂ neutral differential reflection spectrum shows a series of excitonic Rydberg states of the ground state A exciton as schematically shown in the energy diagram on the right. The B exciton shows up ~ 200 meV blue-shifted to the ground state, due to the valence band spin-orbit splitting.

Photoluminescence (PL) and Differential Reflection (DR), the presence of these charge carriers results in the emergence of a new ground state, typically red-shifted by approximately 20-30 meV relative to the X exciton resonance, depending on the specific TMD material [60–62]. The evolution of charged exciton complexes with varying charge density is exemplified in electron-doped MoSe₂ monolayers in Figure 2.3a. In the presence of free electrons ($V_\mu > 0$ V), the new ground state appears with a binding energy E_B of approximately 30 meV relative to the neutral X exciton in both PL and DR. The contrasting behavior of the two resonances with increasing electron density in DR compared to PL has sparked some controversy in the field.

On one hand, the ground state can be interpreted as a trion resonance – a new quasi-particle consisting of two electrons and one hole in the case of n-doping – as illustrated in the left panel of Figure 2.3b. This interpretation has mainly been applied to PL measurements in the regime of low charge carrier density [60, 61, 63, 64]. Alternatively, a different approach describes the charged complexes within the framework of many-body physics as exciton-polarons, originating from a collective interaction of the Fermi sea of electrons with optically excited excitons [65–67]. In this framework, the new ground state in the presence of charge carriers is represented by an attractive polaron resonance (AP), as illustrated in the center panel of Figure 2.3b. The second resonance, shifting to higher energies relative to the neutral X exciton, represents a metastable excitation described by a repulsive polaron (RP), as schematically shown in the right panel of Figure 2.3b. This approach explicitly captures the maintained oscillator strength of the ground state resonance at higher charge carrier densities, as observed in DR, which is not expected from a molecular trion state [66]. At low

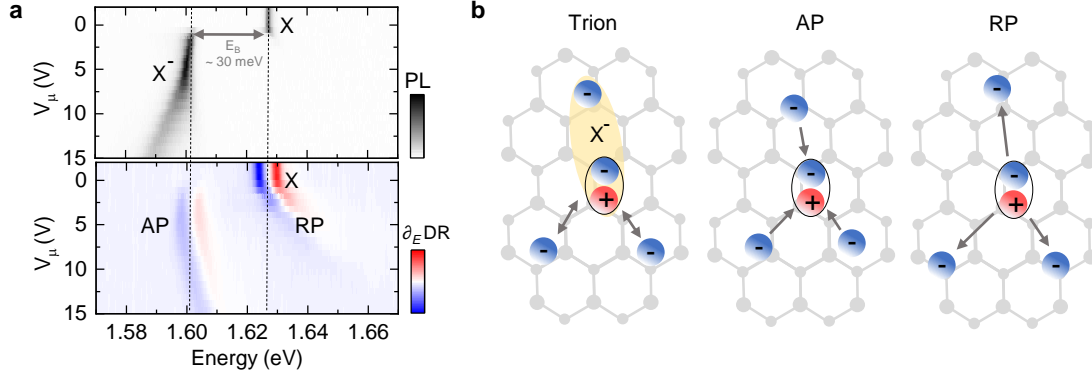


Figure 2.3.: **MoSe₂ X excitons in the presence of charge doping.** **a**, Illustration of exciton interaction with a surrounding sea of electrons. As indicated by the arrows, the interaction can be of an attractive nature, leading to the formation of attractive polarons (AP) or of a repulsive nature to form repulsive polarons (RP). The ground state charged complex of an exciton interacting with a single charge carrier is called trion (X^-) and highlighted in yellow. **b** PL (upper panel and DR (lower panel) response of a MoSe₂ monolayer as a function of the charge density (applied gate voltage V_μ). At low charge carrier density, attractive polaron and trion are equivalent with binding energy $E_B \approx 30$ meV.

to intermediate charge densities where the Fermi energy is significantly smaller than the binding energy of the trion/AP ground state, both approaches provide equivalent descriptions of charged exciton complexes [68]. Since this condition is met for the measurements presented in this study, we use the terms trions and polarons interchangeably in our discussions. Importantly, the presented model applies regardless of the sign of induced charge carriers - electrons and holes.

2.1.3. Excitons exposed to external fields

Investigating the behavior of excitons in TMD monolayers, bilayers or multilayers under external fields offers valuable insights into the underlying physical mechanisms. Applying an out-of-plane magnetic field can induce a Zeeman effect, a phenomenon well established in atomic physics, while finite out-of-plane electric fields can lead to the observation of the linear Stark effect.

Valley Zeeman effect

As discussed in Section 2.1.1, TMD monolayers exhibit valley-contrasting optical selection rules. Excitons in the K (K') valley are coupled to σ^+ (σ^-) polarized light, and without an applied magnetic field, the corresponding resonance energies are identical, rendering the

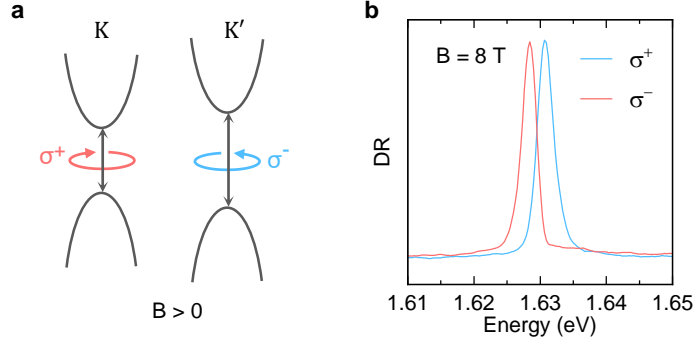


Figure 2.4.: **MoSe₂ X excitons in the presence of a magnetic field.** At finite out-of-plane magnetic fields, the spin degeneracy at the K (K') points is lifted, revealing a valley Zeeman splitting Δ_X between the exciton response in σ^+ and σ^- polarization.

valley-contrasting transitions energetically degenerate. However, this degeneracy can be lifted by applying an out-of-plane magnetic field, inducing a valley Zeeman effect. This effect leads to an energy difference, termed Zeeman splitting ΔE_Z , between the exciton resonance energies corresponding to the K and K' valleys, as illustrated in Figure 2.4a.

In TMD monolayers, this splitting is in the order of a few meVs (see Figure 2.4b) and scales linearly with the magnetic field B [69–74]:

$$\Delta E_Z = E^+ - E^- = g\mu_B B, \quad (2.1)$$

where E^+ (E^-) denote the exciton resonance energies in σ^+ (σ^-) polarization and μ_B represents the Bohr magneton. The exciton g -factor g is dimensionless effective value dependent on the spin and orbital angular momenta $L_C(\mathbf{k})$ and $L_V(\mathbf{k})$ of the contributing conduction and valence bands ($n = C, V$), respectively [75, 76]:

$$g_n = \pm g_0 + 2L_n(\mathbf{k}), \quad (2.2)$$

where $+$ ($-$) corresponds to spin-up (spin-down) projections along the out-of-plane axis and g_0 is the free electron Landé factor, approximately 2. Therefore, the exciton g -factor is calculated as:

$$g(\mathbf{k}_C, \mathbf{k}_V) = g_C(\mathbf{k}_C) - g_V(\mathbf{k}_V). \quad (2.3)$$

With knowledge of the conduction band (CB) and valence band (VB) orbital angular momenta from first-principle calculations, the g -factor becomes a crucial tool for extracting information about the contributing bands of specific excitonic resonances observed in optical experiments. For instance, momentum-direct excitons are expected to possess $g \approx -4$, a value confirmed in numerous experimental studies [69–74].

Additionally, the g -factor can serve as an indicator of local magnetization M , which might contribute to the exciton Zeeman splitting in Eq. (2.1), particularly in the presence of a

polarized spin-charge lattice [28]:

$$\Delta E_Z = E^+ - E^- = g\mu_B(B + \lambda M) = g_{\text{eff}}(M)\mu_B B, \quad (2.4)$$

where λ denotes the coupling constant. This leads to renormalized effective g -factors g_{eff} as we discuss in Section 4.4.3, particularly for n-doped MoSe₂/WS₂ heterostructures.

Stark effect for interlayer excitons

The two-dimensional nature of isolated TMD monolayers results in excitonic dipole moments confined purely within the plane, making them insensitive to out-of-plane electric fields. However, in bilayer or multilayer configurations, where the electron and hole constituents may reside in distinct layers, interlayer excitons emerge. These interlayer excitons possess finite out-of-plane dipole moments, allowing the coupling to out-of-plane electric fields. This coupling effect is quantified by the linear Stark shift of the corresponding exciton resonances:

$$\Delta E_S = eE_z d_z, \quad (2.5)$$

where E_z represents the magnitude of the applied out-of-plane electric field. The interlayer exciton dipole moment d_z depends on its degree of layer delocalization. Analysis of the dispersion of the Stark shift with respect to the applied electric field facilitates conclusions regarding the contributing layers and bands [77–81].

While intralayer excitons, confined within a TMD monolayer, exhibit high oscillator strength and short lifetimes [82, 83], interlayer excitons are characterized by long lifetimes owing to increased electron-hole separation, but have vanishing oscillator strength [84, 85]. Out-of-plane electric fields can be employed in TMD multilayer systems to tune interlayer excitons into resonance with intralayer excitons, thereby achieving hybridization between the two exciton species to combine the best of both worlds - high oscillator strengths with a dipolar character and long lifetimes, successfully realized TMD homobilayer systems [86, 87] and different TMD heterostructures such as MoTe₂/MoSe₂ [88], MoSe₂/hBN/MoSe₂ [22] and also MoSe₂/WS₂ [89], serving as example for our study on electric field-induced hybridization in MoSe₂/WS₂ heterobilayers, presented in Section 4.3.

2.2. Light-matter interaction in Fabry-Pérot cavities

The Fabry-Pérot interferometer, named after its inventors Charles Fabry and Alfred Pérot [90], is an optical resonator originally consisting of two planar mirrors facing each other. Its concept has found wide applications, such as in narrow-band optical filtering and laser resonators [91]. In the field of cavity quantum electrodynamics (QED), Fabry-Pérot resonators serve as important tools for controlling interactions between light and optical emitters

[92–94]. The following section provides a brief introduction to the principle of Fabry-Pérot resonators, following common textbook descriptions [91, 95–97]. Specifically, we focus on the plano-concave Fabry-Pérot resonator geometry, which is utilized in the experiments presented in this work (see Sections 3.3.1 and 5), aiming to establish strong light-matter interactions between excitons and photons.

2.2.1. Basics of Fabry-Pérot resonators

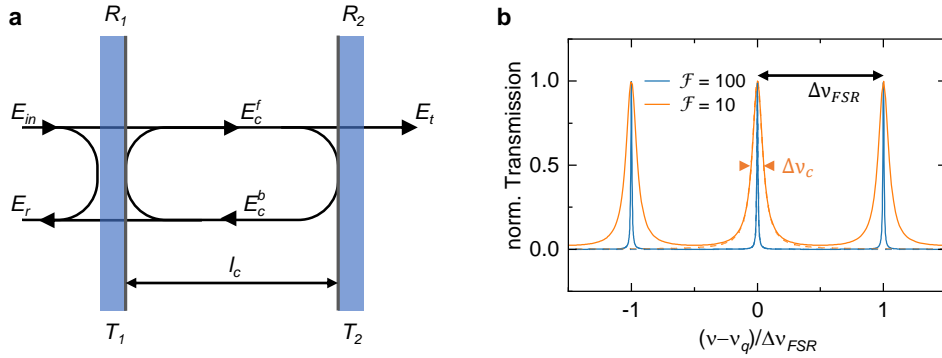


Figure 2.5.: **Concept of a Fabry-Pérot cavity.** **a**, Schematic of a Fabry-Pérot resonator consisting of two mirrors with respective reflectivities R_1 and R_2 , transmissivities T_1 and T_2 and separation distance l_c . The electric field incident to the resonator is E_{in} , the field circulating back and forth in between the two mirrors $E_c^{f/b}$ and the field transmitted through the resonator E_t . E_r consists the part of E_{in} that is directly reflected at the first mirror and the field that launches back through the first mirror out of the cavity. **b**, Airy distribution around the resonant mode q at frequency ν_q obtained from transmission through a Fabry-Pérot resonator with symmetric mirror reflectivities $R_1 = R_2 = R$ and corresponding finesse $\mathcal{F} = 10$ and $\mathcal{F} = 100$ shown in orange and blue lines, respectively. The distribution is shown in units of the free spectral range $\Delta\nu_{FSR}$. For high \mathcal{F} , the intensity profile is well described by the sum of Lorentzian lines (dashed lines in corresponding color) representing individual resonant cavity modes, each with linewidth $\Delta\nu_c$, which is inversely proportional to \mathcal{F} and increases with the total losses L_{tot} of the system.

Figure 2.5 shows a schematic of the working principle of a Fabry-Pérot resonator. Two mirrors with reflectivities R_1 and R_2 form the optical resonator. An incident electric field is partly reflected and transmitted at the first mirror. The presence of the second mirror leads to the formation of a circulating field E_c between the two mirrors. The composition of the field that is reflected at the first mirror before entering the cavity and the field that launches back through the first mirror from the cavity is denoted by E_r . The light that is finally transmitted through the cavity is denoted by E_t .

We are interested in the intensity distribution as a function of the optical wavelength transmitted through the resonator. Using the approach of a circulating electric field between the two mirrors R_1 and R_2 the transmitted intensity profile is described by the generic Airy distribution:

$$A_t = \frac{I_t}{I_{in}} = \frac{|E_t|^2}{|E_{in}|^2} = \frac{(1 - R_1)(1 - R_2)}{(1 - \sqrt{R_1 R_2})^2 + 4\sqrt{R_1 R_2} \sin^2(\Phi)}, \quad (2.6)$$

where the phase shift accumulated by the field E_c with wavelength λ propagating over the distance l_c between the two mirrors (half a round trip) is defined by $\phi = 2\pi l_c / \lambda$. In case of identical reflectivities of the two mirrors, the expression for the Airy distribution simplifies to

$$A_t = \frac{I_t}{I_{in}} = \frac{1}{1 + \frac{4R}{(1 - R)^2} \sin^2(\Phi)} = \frac{1}{1 + \left(\frac{2\mathcal{F}}{\pi}\right)^2 \sin^2(\Phi)}, \quad (2.7)$$

where we introduced the finesse $\mathcal{F} = \pi\sqrt{R}/(1 - R)$ of the resonator. The intensity profile resulting from Equation (2.7) is shown in Figure 2.5b. The separation distance l_c between the two mirrors imposes a resonance condition to the light that is circulating inside the cavity in form of a standing wave and we find the maxima of the periodic transmission intensity profile at the corresponding resonance energies

$$\nu_q = q \frac{c}{2l_c}, \quad (2.8)$$

where q defines the longitudinal mode order and c the speed of light, depending on the dielectric permittivity of the medium inside the resonator. The resonant modes manifest with a spectral separation $\Delta\nu_{FSR}$, which is denoted as the free spectral range and inversely proportional to the cavity length:

$$\Delta\nu_{FSR} = \frac{c}{2l_c}. \quad (2.9)$$

For a Fabry-Pérot resonator with highly reflective mirrors, the Airy distribution is matched by a sum of Lorentzian lines of the resonant cavity modes with corresponding Lorentzian linewidths $\Delta\nu_c$. The finesse is approximately given by

$$\mathcal{F} \approx \frac{\Delta\nu_{FSR}}{\Delta\nu_c} = \frac{2\pi}{-\ln(R_1 R_2)} = \frac{2\pi}{-\ln(1 - T_1) - \ln(1 - T_2)} \approx \frac{2\pi}{T_1 + T_2} = \frac{2\pi}{L_{tot}}, \quad (2.10)$$

where L_{tot} denotes the total losses of the cavity system resulting from transmission $T_{1/2}$ through the cavity mirrors, neglecting additional losses through scattering and absorption. In this sense, the finesse can be understood as a measure of the number of cavity round-trips of a photon before it leaks out of the resonator. Besides transmission through the imperfect mirrors, scattering and absorption in the medium between the two mirrors can contribute to L_{tot} , leading to a reduced finesse \mathcal{F} in (2.10) and a drop in the transmitted intensity A_t in (2.7) at the resonance energies as shown in Figure 2.5b [98].

2.2.2. Plano-concave optical resonator

In real experiments the original geometry of the Fabry-Pérot resonator with two planar mirrors is unpractical due to its high sensitivity to misaligned mirrors leading to high losses. The use of spherical mirrors provides a practical way to confine the light in a more efficient way and form stable low-loss transverse modes.

Stability criterion

Optical rays inside a resonator of such geometry propagate close to the optical axis, which is why the conditions of confinement can be derived by the matrix-optics method (or ABCD-matrix method) in the paraxial approximation [95].

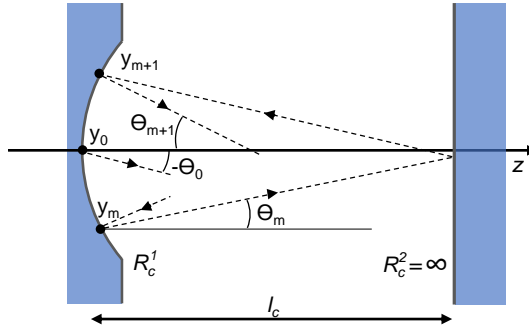


Figure 2.6.: **Ray confinement in plano-concave Fabry-Pérot resonators.** The trajectory of an optical ray between the two mirrors with respective radius of curvature R_c^1 and R_c^2 after $m/m+1$ round trips is described by the position $y_{m/m+1}$ and the angle $\theta_{m/m+1}$ of the beam with respect to the optical axis z . The separation distance between the two mirrors is denoted as l_c

The scenario is depicted in Figure 2.6 for a plano-concave resonator geometry, consisting of a concave spherical mirror with radius of curvature R_c^1 on one side and a planar mirror ($R_c^2 = \infty$) on the other side: An optical ray after m round trips inside the cavity is defined by its position y_m and the inclination θ_m of its trajectory to the optical axis z . The relation between the (y_m, θ_m) and (y_{m+1}, θ_{m+1}) after the next round trip is linear for paraxial rays and can be written in matrix-optics notation:

$$\begin{pmatrix} y_{m+1} \\ \theta_{m+1} \end{pmatrix} = \begin{pmatrix} A & B \\ C & D \end{pmatrix} \begin{pmatrix} y_m \\ \theta_m \end{pmatrix}, \quad (2.11)$$

where the ABCD-matrix for a single round trip is

$$\begin{pmatrix} A & B \\ C & D \end{pmatrix} = \begin{pmatrix} 1 & 0 \\ \frac{2}{R_c^1} & 1 \end{pmatrix} \begin{pmatrix} 1 & l_c \\ 0 & 1 \end{pmatrix} \begin{pmatrix} 1 & 0 \\ \frac{2}{R_c^2} & 1 \end{pmatrix} \begin{pmatrix} 1 & l_c \\ 0 & 1 \end{pmatrix} \stackrel{R_c^2 \rightarrow \infty}{=} \begin{pmatrix} 1 & 2l_c \\ \frac{2}{R_c^1} & \frac{4l_c}{R_c^1} + 1 \end{pmatrix}, \quad (2.12)$$

Starting from (y_0, θ_0) , we arrive at $(y_m, \theta_m / y_{m+1}, \theta_{m+1})$ by repeated propagation of the distance l_c between the two mirrors, reflection at the planar mirror, propagation back to and finally reflection from the curved mirror with radius of curvature R_c^1 . The harmonic solution of Equation (2.11) is generally given by [95]

$$\begin{aligned} y_m &= y_{max} F^m \sin(m\varphi + \varphi_0) \\ \varphi &= \cos^{-1} \left(\frac{b}{F} \right), \end{aligned} \quad (2.13)$$

where y_{max} and φ_0 are constants determined from the initial positions y_0 and y_1 , and

$$\begin{aligned} b &= \frac{A + D}{2} \\ F^2 &= AD - BC. \end{aligned} \quad (2.14)$$

Here, we find $F = 1$ for the ray transfer matrix in Equation (2.12). A bounded solution requires φ being real leading to the stability criterion for a confined ray inside the plano-concave cavity:

$$0 \leq |b| = \frac{|A + D|}{2} = 1 + \frac{2l_c}{R_c^1} \leq 1. \quad (2.15)$$

The latter condition of Eq. (2.15) implies that a stable cavity is formed as soon as the cavity length becomes smaller than the radius of curvature $l_c \leq R_c$.

Gaussian eigenmodes

The eigenmodes of a plano-concave Fabry-Pérot cavity are given by Gaussian beams, provided that the radius of curvature of its wavefronts $R(z)$ at the positions z_1 and z_2 in Figure 2.7 matches the radius of curvature of the mirrors $R(z_1) = R_c^1$ and $R(z_2) = R_c^2 = \infty$. It is given by:

$$R(z) = z + \frac{z_0}{z}, \quad (2.16)$$

where z_0 denotes the Rayleigh range at which the wavefronts of the Gaussian beam have their maximum curvature. Since $R_c^2 = \infty$, the position of the planar mirror is at $z_2 = 0$, where the curvature of the Gaussian beam diverges. Here, the waist radius of the Gaussian beam:

$$w(z) = w_m \sqrt{1 + \left(\frac{z}{z_0} \right)^2}, \quad (2.17)$$

has its minimum value w_m , which is a function of the radius of curvature R_c^1 , the cavity length, and the resonant optical wavelength λ :

$$w_m = \sqrt{\frac{\lambda}{\pi}} (l_c R_c^1)^{1/4}. \quad (2.18)$$

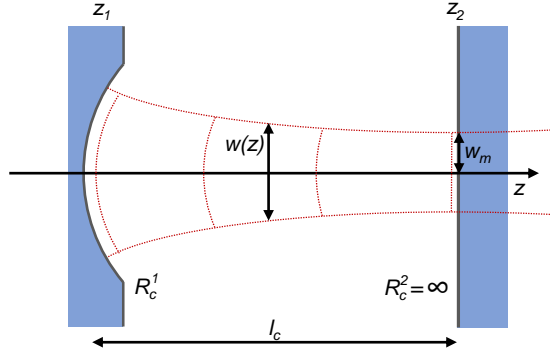


Figure 2.7.: **Gaussian eigenmodes of the plano-concave optical resonator.** The curvature of the Gaussian wavefronts at position z_1 and z_2 have to match the radius of curvature of the mirrors R_c^1 and R_c^2 which are placed at respective positions. w_m is the minimum $1/e$ mode waist of the Gaussian beam, where the curvature of the wavefronts diverges. The mode waist $w(z)$ at any position z follows from Equation (2.17).

The mode waist defines the spatial resolution of a scanning plano-concave Fabry-Pérot microscope [98, 99] and can be used to estimate the cavity mode volume:

$$V_m = \frac{\pi}{4} w_m^2 l_c. \quad (2.19)$$

The fundamental transverse Gaussian modes, also referred to as TEM_{00} modes, are supplemented by a set of higher-order modes, which fulfill the stability condition of the plano-concave optical resonator geometry. Mathematically complete sets of eigenmodes can be described by the Laguerre-Gaussian or Hermite-Gaussian beams. The former presents the solution of the paraxial Helmholtz equation in cylindrical coordinates, while the latter employs Cartesian coordinates [95]. In experiments, a non-symmetric shape of the concave spherical mirror, due to imperfections in the fabrication process, would break the cylindrical symmetry of the system and preferably give rise to the observation of Hermite-Gaussian higher-order modes spectrally blueshifted to the TEM_{00} mode [98, 100, 101].

2.2.3. Quantum theory of strong light-matter coupling

Optical emitters inside a resonant cavity with a high Q -factor and small mode volume show enhanced emission rates, quantified by the so-called Purcell factor [102]. It describes an effect of coherent light-matter interaction between the two oscillators representing the cavity photons and the optical dipole of the emitter in the weak coupling regime. Purcell enhancement and other signatures of weak light-matter coupling have successfully been demonstrated for TMD-based heterostructures integrated in various types of optical resonators [103–107, P5, P1]. The high oscillator strength of TMD monolayer excitons makes

them candidates not only to study effects of weak but also strong light-matter coupling, where the coherent coupling rate exceeds the individual decay rates of the photonic and excitonic resonators. In such systems, excitons and photons are not treated as independent anymore, but as hybrid light-matter states, called exciton-polaritons [108]. The study of such polariton states in TMD heterobilayer structures represents the focus of this work and the following section gives a short introduction to their theoretical description in the framework of two coupled quantum mechanical oscillators, which can be found in detail in Ref. [109] and [110].

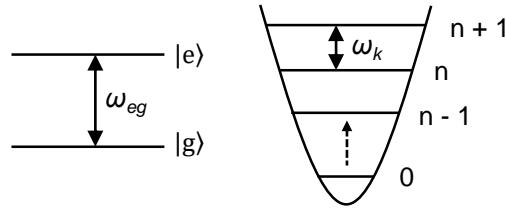


Figure 2.8.: **Quantization of coupled oscillators.** Schematic energy diagrams of a two-level system describing the energetically lowest transition of a strongly bound exciton (left side) and of a quantised harmonic oscillator describing the light field inside a strongly confined optical cavity (right side).

The problem can be treated analogously to the interaction of a single mode of an electromagnetic field with an atom which is described by the Jaynes-Cummings model [111]. In the latter, both components are treated as quantum harmonic oscillators, giving rise to discrete energy levels for a photon of a cavity mode and the atom as sketched on the right side in Figure 2.8. Neglecting higher order excitations, a strongly bound exciton in a TMD monolayer can be approximated by an atom-like two-level system with a ground state $|g\rangle$ and an excited state $|e\rangle$ and we define the creation x^\dagger and annihilation x operators of the quantized system:

$$\begin{aligned}\hat{x}^\dagger &= |e\rangle\langle g| \\ \hat{x} &= |g\rangle\langle e|.\end{aligned}\tag{2.20}$$

The Hamiltonian of the two-level exciton system writes

$$\hat{H}_X = E_X \hat{x}^\dagger \hat{x},\tag{2.21}$$

with the exciton energy $E_X = \hbar\omega_{eg}$. The quantization of the electromagnetic field is introduced by defining the corresponding ladder operators \hat{a}_k^\dagger and \hat{a}_k which act on a state $|n_k\rangle$ ($|n_k + 1\rangle$) of the quantum harmonic oscillator that describes a cavity mode k with a number

of n_k ($n_k + 1$) photons:

$$\begin{aligned}\hat{a}_k^\dagger |n_k\rangle &= \sqrt{n_k} |n_k + 1\rangle \\ \hat{a}_k |n_k + 1\rangle &= \sqrt{n_k + 1} |n_k\rangle.\end{aligned}\quad (2.22)$$

The Hamiltonian of the quantized electric field of a cavity mode with energy $\hbar\omega_k$ and assuming a large number of photons $n \gg 1$ is given by

$$\hat{H}_c = \sum_k \hbar\omega_k \hat{a}_k^\dagger \hat{a}_k, \quad (2.23)$$

where the energy of a cavity mode is given by $E_c = \hbar\omega_k$. The quantized electromagnetic field can be expressed by the ladder operators as sum over all cavity modes k :

$$\hat{E} = \sum_k \mathcal{E}_k \sqrt{\frac{\hbar\omega_k}{2\epsilon_0 V_m}} \left(\hat{a}_k e^{ik \cdot r} + \hat{a}_k^\dagger e^{-ik \cdot r} \right), \quad (2.24)$$

where the amplitude of the electromagnetic field depends on the mode volume of the cavity V_m . To express the interaction between an electric field and the dipole moment of the exciton transition we introduce the dipole operator

$$\hat{d} = \sum_{i,j} |i\rangle \langle i| e \hat{r} |j\rangle \langle j| = e d_{eg} (|e\rangle \langle g| + |g\rangle \langle e|) = e d_{eg} (\hat{x}^\dagger + \hat{x}) \quad (2.25)$$

and the interaction Hamiltonian for a cavity mode k ($\omega_k = \omega_c$ and $E_c = \hbar\omega_c$) interacting with a two-level exciton system can be written using the expressions (2.24) with $r = 0$ for simplicity and (2.25)

$$\begin{aligned}\hat{H}_{int} &= -\hat{d} \hat{E} = \hbar g (\hat{a} + \hat{a}^\dagger) (\hat{x} + \hat{x}^\dagger) \\ &= \hbar g (\hat{a} \hat{x}^\dagger + \hat{a}^\dagger \hat{x})\end{aligned}\quad (2.26)$$

with the coupling constant

$$g = \sqrt{\frac{\omega_c}{2\epsilon\hbar V}} \mathcal{E} d_{eg}. \quad (2.27)$$

In the last expression of Equation (2.26), we neglected the energy non-conserving terms. This is because in the case of a two-level exciton system, there are only two possible states in the eigenspace of the coupled system, and the possible ways of interaction are limited to:

$$\begin{aligned}\hat{H}_{int} |n + 1, g\rangle &= |n, e\rangle \\ \hat{H}_{int} |n, e\rangle &= |n + 1, g\rangle.\end{aligned}\quad (2.28)$$

The first expression describes the absorption of a photon and creation of an exciton in the state $|n, e\rangle$, while the second expression describes the process of photon emission by

an exciton to transition to the state $|n+1, g\rangle$. The complete Hamiltonian of the coupled exciton-photon system writes as

$$\hat{H} = \hat{H}_X + \hat{H}_c + \hat{H}_{int} = \hbar\omega_X \hat{x}^\dagger \hat{x} + \hbar\omega_c \hat{a}^\dagger \hat{a} + \hbar g (\hat{a} \hat{x}^\dagger + \hat{a}^\dagger \hat{x}) \quad (2.29)$$

For better visualization and practical treatment we can write this Hamiltonian in matrix notation in the basis of the eigenstates $|n, e\rangle = \begin{pmatrix} 1 \\ 0 \end{pmatrix}$ and $|n+1, g\rangle = \begin{pmatrix} 0 \\ 1 \end{pmatrix}$ as

$$H = \begin{pmatrix} E_X & \hbar g \\ \hbar g & E_c \end{pmatrix}. \quad (2.30)$$

Diagonalization of H gives the new eigenenergies of the coupled exciton-photon system:

$$E_{U/L} = \frac{E_X + E_c}{2} \pm \frac{1}{2} \sqrt{(E_c - E_X)^2 + 4\hbar^2 g^2}, \quad (2.31)$$

which are denoted as the upper (E_U) and lower polariton branch (E_L). In the terminology of cavity QED in atomic physics the corresponding eigenstates are referred to as *dressed states*. Their spectral separation at a specific energetic detuning between the cavity mode and the exciton resonance is referred to as Rabi splitting $\Omega = 2g$ and scales with the oscillator strength f of the underlying exciton resonance as [112, 113]

$$\Omega = \alpha \sqrt{f}, \quad (2.32)$$

where α is a proportionality coefficient. Exciton-polaritons are bosonic quasi-particles of partly excitonic and partly photonic nature. The fraction of either component depends on the cavity-exciton energy detuning and is quantified by the so-called Hopfield coefficients [32]:

$$\begin{aligned} |\mathcal{X}|^2 &= \frac{E_U E_X - E_L E_c}{(E_c + E_X) \sqrt{(E_c - E_X)^2 + \Omega^2}} \\ |\mathcal{C}|^2 &= \frac{E_U E_c - E_L E_X}{(E_c + E_X) \sqrt{(E_c - E_X)^2 + \Omega^2}}, \end{aligned} \quad (2.33)$$

which satisfy $|\mathcal{X}|^2 + |\mathcal{C}|^2 = 1$. In Eq. (2.33), $|\mathcal{X}|^2$ ($|\mathcal{C}|^2$) defines the excitonic (photonic) part of the upper polariton branch, while the coefficients swap roles in the case of the lower polariton branch.

Experimental methods

This Chapter summarizes the experimental techniques applied in this work, starting from the fabrication procedure of van der Waals heterostructures and followed by an overview of the optical measurements that were carried out in cryogenic environment. The latter divides into two sections, optical experiments in a standard confocal configuration and measurements in an optical microcavity.

THIS CHAPTER IS PARTLY BASED ON THE PUBLICATION [P8]
S. Vadia, J. Scherzer, H. Thierschmann, et al., “Open-Cavity in Closed-Cycle Cryostat as a Quantum Optics Platform,” *PRX Quantum* **2021**, 2, 040318

3.1. Sample fabrication

In the following we discuss the fabrication process of the MoSe₂/WS₂ dual-gated field-effect devices starting from the exfoliation and characterization of the individual flakes, followed by the stacking procedure, postprocessing and contacting of the gates.

3.1.1. Components of the van der Waals heterostructure

The van der Waals heterostacks studied in this work consisted of three different building blocks of the family of 2D materials as schematically shown in Figure 3.1. The TMD layers were encapsulated by two flakes of hexagonal boron nitride (hBN) to ensure a homogenous dielectric environment free of defects. In addition, the hBN flakes served as dielectric spacers between the TMDs and the few layer graphene (FLG) electrostatic gates, completing the heterostack at the top and bottom end.

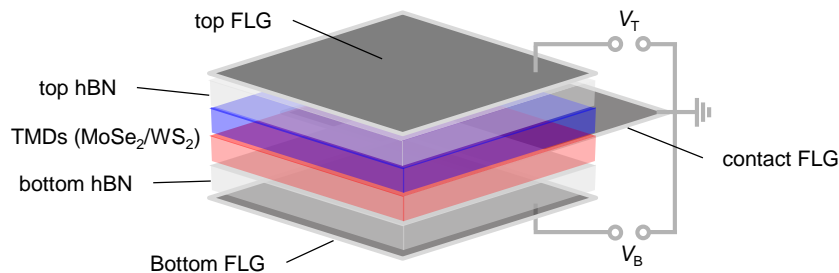


Figure 3.1.: **Schematics of a TMD based field-effect device.** A TMD heterobilayer is encapsulated by dielectric hBN layers from top and bottom side. One FLG layer, in direct contact with the TMD layers, is linked to a ground reservoir. Two FLG flakes cap the heterostack from the top and bottom, allowing to apply gate voltages V_T and V_B to control the doping level and out-of-plane electric field.

TMD monolayers

We obtained TMD monolayers either from mechanical exfoliation from Bulk crystals (*HQ Graphene*) using adhesive tape or in-house chemical vapor deposition (CVD) synthesis [114, 115]. Both methods yield flakes of comparable high optical quality, however, CVD growth brings several advantages as can be seen in Figure 3.2a comparing standard optical microscope images of CVD grown (left panel) and exfoliated (right panel) MoSe₂ flakes on Si/SiO₂ substrates with oxide thickness of 285 nm. A large number of monolayer flakes can be obtained on a single Si/SiO₂ chip during CVD synthesis and their triangular shapes facilitate relative orientation during the heterobilayer (HBL) stacking. While CVD only produces single or fewlayer TMD flakes, additional bulk material on exfoliated substrates complicates the search for monolayers and their subsequent pickup. Furthermore, such regions of bulk material in close proximity to the monolayer of interest can cause uncontrolled stray fields when integrated into the dual-gate field-effect device. CVD synthesis, on the contrary, provides per construction isolated flakes of a very controlled geometry, such that the overall heterostructure is more controllable in electrostatic terms. Finally, the maximum lateral expansion of CVD grown monolayers can be hundreds of micrometers, one order of magnitude larger than typically observed for exfoliated monolayers.

The number of layers of a TMD flake was determined in an optical microscope by its optical contrast compared to the background substrate. Since TMDs exhibit a transition from an indirect to a direct semiconductor in the limit of a single layer, another way to distinguish a monolayer from a fewlayer flake is to image its photoluminescence (PL) response under optical excitation above the material bandgap. Monolayer regions feature pronounced PL signal, while the emission of bi- or fewlayer flakes is quenched as can be seen in Figure 3.2b. Additionally, PL imaging helped to identify flakes of lower quality not identifiable in standard optical microscopy. The MoSe₂ monolayer on the left of the investigated area in Figure 3.2b

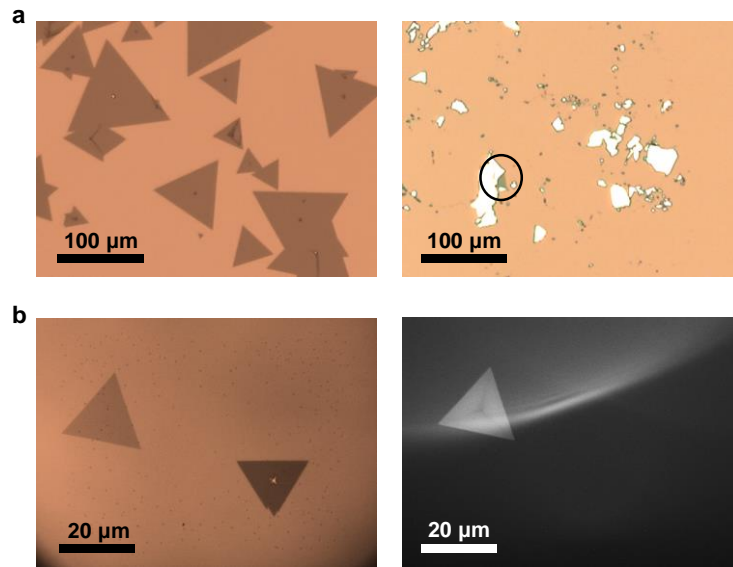


Figure 3.2.: **TMD monolayers from CVD growth and exfoliation.** **a**, Optical microscope images of CVD grown MoSe_2 monolayers (*left*) and MoSe_2 exfoliated (*right*) on Si wafer with 285 nm SiO_2 cover. White areas in the right image are bulk crystal flakes, the black circle marks a characteristic MoSe_2 monolayer. **b**, CVD grown WS_2 mono- and bilayer, distinguishable by the difference in the optical contrast of a bright field microscope image (*left*) and via PL imaging (*right*).

looks clean and homogenous in the optical microscope image, but PL imaging reveals dark stripes in the center of the same flake which can be attributed to cracks or surface contamination. We observed an increase of surface contaminations on CVD grown flakes that were stored over a longer period of time ($> 1-2$ weeks), especially in ambient environment. Such surface contaminations complicate the pick-up of the respective TMD flakes and diminish the optical and electrical properties of the material. Possible sources of degradation are photoinduced oxidation of the monolayers [116] or the formation of atomically thin polymeric contamination layers in the presence of polydimethylsiloxane (PDMS) during storage [117]. To quantitatively analyse the surface composition of TMD layers a scanning electron microscope (SEM) can be employed for secondary electron imaging [118] or energy dispersive X-ray spectroscopy (EDX) [119]. We tried work around the problem of surface contamination by processing CVD grown TMD layers immediately after the synthesis. Once encapsulated by hBN, the monolayers did not show any sign of degradation over time.

hBN for dielectric encapsulation

Photoluminescence spectra of TMD monolayers directly exfoliated on SiO_2 substrates show strong inhomogenous linewidth broadening due to strain and charged impurities at the

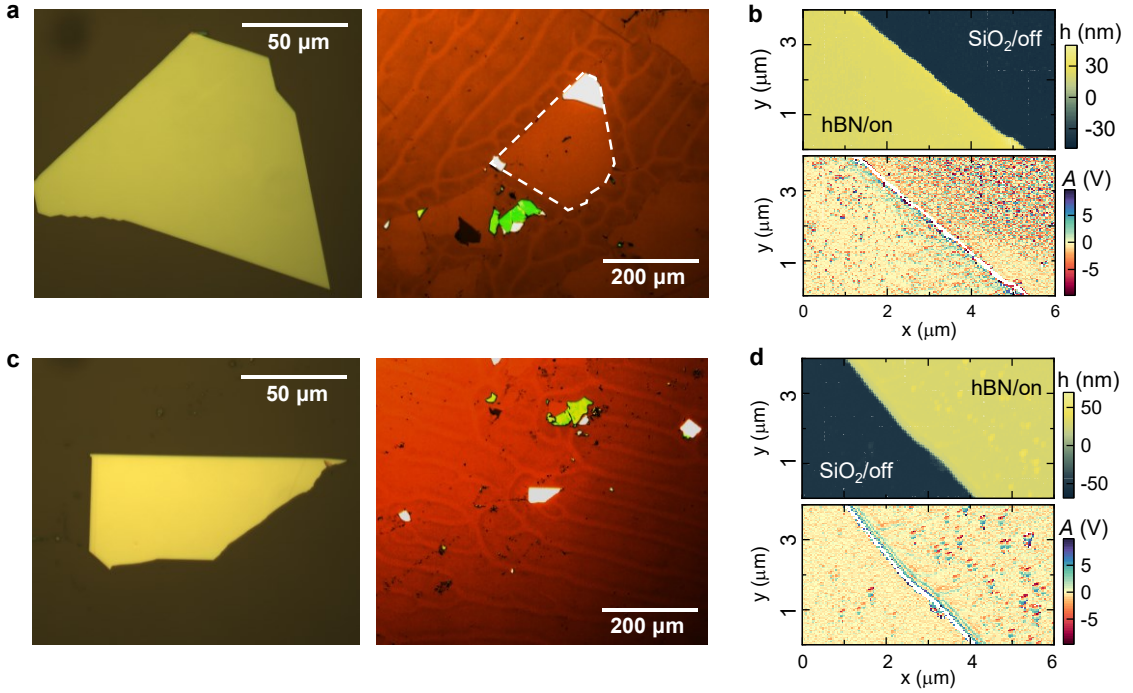


Figure 3.3.: **hBN characterization.** **a**, Optical microscope images of an exfoliated hBN flake on a Si/SiO₂ substrate with 50x (*left*) and 10x (*right*) magnification, respectively. Increasing the optical contrast by applying gamma correction in the *right* image reveals areas of the wafer which are contaminated by glue residues. The white dashed shape marks an area free of glue residues including the hBN flake of interest. **b**, AFM characterization of the hBN flake shown in **a**. *Upper panel*: Height (h) profile measured around the hBN edge to extract the thickness of the flake. *Lower panel*: Amplitude error (A) of the AFM measurement in the same area ($A_{\text{on}}^{\text{rms}} / A_{\text{off}}^{\text{rms}} = 0.48$). **c**, Optical microscope images of another exfoliated hBN flake on a Si/SiO₂ substrate with 50x (*left*) and 10x (*right*) magnification. The gamma corrected image on the *right* reveals glue residues across the whole area around the hBN flake of interest. **d**, Height profile (*upper panel*) and amplitude error (*lower panel*) at the edge of the respective hBN flake ($A_{\text{on}}^{\text{rms}} / A_{\text{off}}^{\text{rms}} = 2.0$).

SiO₂ - TMD interface. Encapsulating monolayer TMDs with atomically flat hBN has proven to be an efficient method to avoid this problem [120]. Furthermore, hBN has a large bandgap in the UV-range, establishing it as an ideal insulator for TMD based field effect devices. In this work, multilayer hBN flakes for TMD encapsulation were exfoliated from synthetically grown high-quality bulk crystals with low defect density, provided by the National Institute for Materials Science (NIMS) in Japan. We selected the flakes for encapsulation according to their thickness, homogeneity and cleanness.

The first can be estimated via the color of the flake under an optical microscope, which varies for different layer numbers due to interference effects, and precisely determined with

atomic force microscopy (AFM) as shown in the upper panel of Figure 3.3b and d. Important prerequisite to the hBN thickness is the intended symmetry of the field-effect device, i.e. top and bottom hBN are supposed to have nearly identical thickness. Furthermore, thin-film interference effects at the different interfaces of a heterostack can be of destructive nature in certain ranges of the optical spectrum, depending on the total hBN layer thickness. To prevent strongly reduced signal in broadband reflection measurements in the relevant spectral range for our optical studies, we performed a transfer matrix (TM) simulation of the reflection response of the heterostack [121, 122]. Figure 3.4a shows the experimentally observed and TM simulated reflection response from a 410 nm thick hBN layer on top of a Si wafer with 285 nm SiO₂ cover. The dip in the spectrum around 590 nm can be attributed to the above explained destructive thin-film interferences. The simulation reveals a multiplicity of interference dips at different wavelengths of the optical spectrum depending on the total thickness of the heterostack as shown in Fig Figure 3.4b. We neglected the contribution of TMD and FLG layers with vanishingly small thickness as compared to the 50-90 nm thick hBN layers used for the encapsulation of the devices built during this work. For a corresponding total hBN thickness of 100-180 nm the TM simulation predicted the appearance of an interference dip between 450-700 nm. Excitonic transitions in MoSe₂/WS₂ HBLs (700-800 nm) could be studied without any consequences.

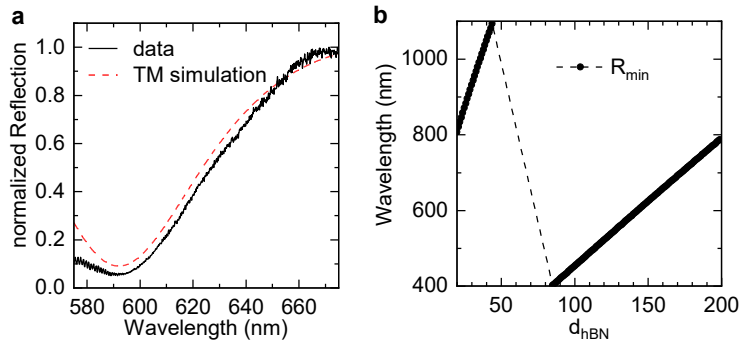


Figure 3.4.: **TM Simulation of the optical reflection response.** **a**, Normalized reflection spectrum of a broadband halogen signal from a Si/SiO₂ substrate with a 410 nm thick hBN flake (black solid line) on top and corresponding TM simulated reflection response (red dashed line). The black arrow marks the optical wavelength of maximum destructive interference in the spectral range shown. **b**, Spectral position of the destructive interference dip in TM simulated reflection spectra from a Si/SiO₂ substrate with an hBN layer on top as a function of the hBN thickness (d_{hBN}).

It is advisable to only use hBN flakes with a homogenous surface for encapsulation. Cracks or areas with an inhomogenous height profile are sources of error during the stacking procedure, since they reduce the fracture strength of a flake.

Finally, the cleanness of the encapsulating hBN layer is crucial for the optical quality of the sample. Surface contaminations due to glue residues of the adhesive tape can cause

inhomogeneous linewidth broadening of the optical transitions due to strain and charged impurities at the hBN-TMD interface undermining the effect of encapsulation. To avoid this problem, we identified hBN flakes within clean areas of the SiO₂ wafer by increasing the optical contrast of a microscope image via gamma correction. In this case, the hBN flake was exfoliated from a larger bulk area that covered the flake during the exfoliation process preventing surface contamination with adhesive tape glue. Figures 3.3a and c compare two exfoliated hBN flakes, within a residue free SiO₂ area and within a film of glue residues, respectively. We extract the cleanliness of an hBN flake from an AFM measurement as shown in Figure 3.3b/d by comparing the rms amplitude error ($A_{\text{on/off}}^{\text{rms}}$) of the AFM tip, which quantifies the surface roughness, on and off the flake. In case of a contaminated surface, the $A_{\text{on}}^{\text{rms}} \geq A_{\text{off}}^{\text{rms}}$ is dominated by the source of contamination. In case of a clean area, the surface roughness on the hBN layer should be reduced due to its atomical flatness, in contrast to the SiO₂ substrate, $A_{\text{on}}^{\text{rms}} < A_{\text{off}}^{\text{rms}}$.

FLG for electrostatic gating

FLG flakes exfoliated from bulk graphite (*HQ Graphene*) served as electrostatic gates for our heterostructures. The exfoliation process and characterization of the layers worked analogously to the procedure explained for hBN. After exfoliation, flakes of interest were identified by their optical contrast against the substrate in a standard optical microscope. The exact thickness was again determined by an AFM measurement and chosen to be as small as possible, especially in case of the top FLG, in order to minimize absorption of the optical signal from the TMD layers. However, FLG flakes with a small number of atomic layers are difficult to pick-up and tend to break under the effect of strain. For the samples in this work we were using FLG flakes with 3-8 atomic layers as the best trade-off between efficient transmission behaviour and high fracture resistance. Via optical and AFM characterization, analogously to the procedure for hBN, we selected graphite flakes free of glue residues to ensure clean heterostructure interfaces.

3.1.2. Heterostructure design and assembly

Having all the components introduced above at hand, we designed the assembly of the heterostructure according to the geometry of the individual flakes. Figure 3.5b illustrates the stacking plan for a set of TMD, hBN and FLG flakes. The dual-gate functionality of the field-effect device is confined to the active area of the plate capacitor, which is defined by the overlap of the top and bottom FLG layers highlighted in yellow. Therefore, it is crucial to position the TMD heterostructure, including the contacting FLG layer, within this active area. It is important to note that the regions of the TMD layers directly in contact with the

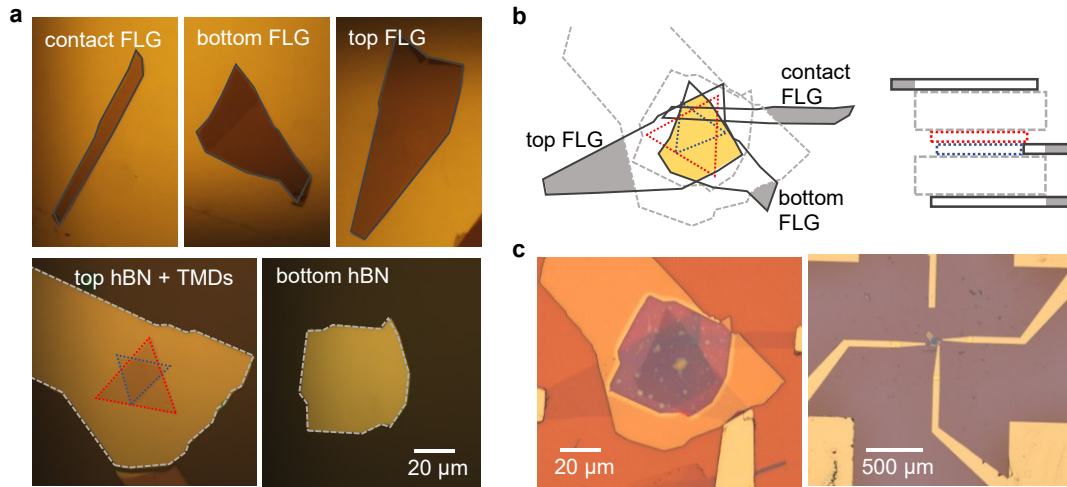


Figure 3.5.: **Assembly of the heterostructure.** **a**, Individual components of a dual-gated field effect device with a TMD HBL. **b**, Plan of the heterostructure assembly for the representative set of flakes. The active area of the dual-gate device, defined by the overlap of top and bottom FLG, is highlighted in yellow. Exposed ends of the FLG flakes for contacting via optical lithography are highlighted in grey. **c**, Completed heterostructure on the final substrate including gold contacts.

FLG layer do not exhibit any charging response to applied gate voltages. This is because of the neutralization of the TMD layer through non-radiative transfer of charged excitons to the graphene layer on a picosecond timescale [123]. A short study of this effect – mixing charged and neutral exciton species in a MoSe_2 monolayer partly covered by a FLG layer with photons in an optical microcavity – is presented in Appendix B.

In summary, the active area should encompass regions of both separate TMD monolayers, an overlapping region of TMD monolayers and an area where both monolayers are covered with the contacting FLG flake. All graphite layers should have exposed surfaces for contacting with gold via optical lithography. It is essential to ensure that there is no direct contact between different FLG gates to prevent electrical short circuits.

The assembly of a heterostack was accomplished using the layer-by-layer dry pick-up and transfer technique introduced by [124, 125]. A detailed, step-by-step explanation of the fabrication procedure employed for this work is given in Ref. [126]. We used polycarbonate (PC) coated PDMS stamps with a curved surface to facilitate position control during the pick-up and release of individual flakes. To obtain the curved PDMS shape we placed a glass slide with a droplet ($\varnothing \approx 1$ cm) of liquid silicone elastomer in a solution with a curing agent upside down on a heating plate at 140°C for 20 minutes and kept it in this position for 12 hours until the PDMS was completely cured, forming a dome of 2-3 mm in height. Thin PC films were formed by putting droplets of PC in a chloroform (CHCl_3) solution (6 % PC) between two clean glass slides under light manual pressure. Pulling the two slides apart

and letting the CHCl_3 evaporate leaves behind an elastic PC film. This film was then placed over the PDMS droplet and fixed on the glass slide around the PDMS using adhesive tape. Controlling the concentration of the PC in the CHCl_3 solution is crucial to obtain a PC film with the desired adhesive properties for a functional stacking process. To control the pick-up and transfer of 2D layers, a wafer with a flake of interest and a prepared stamp were fixed on top of a set of piezo nanositioners under an optical microscope. A heater in direct contact with the wafer allowed us to control the temperature during the stamping process up to 200°C. The entire setup was placed inside a glovebox with an argon atmosphere. Using piezo nanositioners, the sample and stamp were brought into contact close to the flake of interest at a fixed temperature of 70°C. Subsequently, increasing the temperature up to 90-100°C led to an expansion of the PDMS until the PC film fully covers the flake. At this temperature, we let the system thermalize for 10 minutes before pulling up the stamp again by simultaneously stepwise moving the nanositioners and reducing the temperature. Ideally, the flake of interest is lifted from the substrate in a continuous and smooth motion together with the PC film. The ideal pick-up temperature can vary depending on the PC concentration in the CHCl_3 solution when fabricating the film. If the PC film strongly sticks to the surface of the wafer and flips up abruptly when moving the stamp upwards, the temperature or the PC concentration in the CHCl_3 solution might be too high. If low adhesion impedes a pick-up of the flake, the temperature can be further increased up to 110-120°C. After successfully lifting the flake from the substrate, the procedure was repeated to stack the desired heterostructure. Once the assembly was completed, the PC film was brought into contact with the final substrate, and the temperature increased up to 190°C, far above the glass transition temperature of PC (147°C). The area of PC in contact with the substrate exceeded the area of the heterostack on the film by a few hundred micrometers. When the stamp was moved away from the substrate the melted PC film detached from the PDMS stamp in this area and stayed on the substrate, covering the heterostack. Finally, we dissolved the PC residues from the substrate surface in CHCl_3 , followed by rinsing with acetone and isopropanol.

We began the assembly by picking up the top hBN flake, followed by the two TMD layers. The TMD layers, grown through chemical vapor deposition (CVD), exhibited strong adhesive behavior to the surface of the original glass substrate. To avoid tearing these layers, we did not pick them up directly. Instead, we released the top hBN flake onto the first TMD layer, followed by several hours of annealing at 300°C in a vacuum chamber ($p = 1 \times 10^{-8}$ mbar). This annealing process helped to remove interface contaminants and reduced the hBN-TMD interlayer spacing, facilitating a smoother TMD pick-up. The same procedure was repeated for the second TMD layer, followed by the direct pick-up of the contact FLG, bottom hBN, and bottom FLG, following the sample design. This heterostack was then released onto a substrate prepared with gold markers and contact pads. Finally, the top FLG layer was picked

up separately and released on top of the heterostructure. The completed dual-gate device is depicted in Figure 3.5c after contacting the exposed ends of the FLG flakes via optical lithography.

3.1.3. Sample treatment and contacting

With the heterostructure assembled and positioned on the designated substrate, the next steps involved preparing a mount for conducting optical measurements inside a cryostat and contacting the gates of the sample. The mount was custom-made from titanium and designed for the use in a confocal setup as well as in the open microcavity setup, introduced in Section 3.2 and Section 3.3.1, respectively. Two-component UHU Endfest glue has proven to be most resistant under cryogenic conditions for fixing the sample substrate and contact pads next to the substrate, forming the foundation for subsequent wiring. Next, we soldered shielded copper wires to the contact pads, thin single wires bridged the gap from the pads on the sample mount on one side to the gold contact on the sample surface using silver conductive epoxy adhesive. The contacting wires should stand out from the sample surface as low as possible to avoid contact to the microscope objective or the cavity fiber in optical measurements. An exemplary mounted sample substrate with contact pads and wires in place is shown in Figure 3.6. Given the electrostatic sensitivity of the dual-gate device, careful handling is most important. We always wore a wrist strap band with a grounding connection while handling the sample to avoid potential sample destruction resulting from electrostatic discharge. Furthermore, heat application, such as soldering, should be avoided when connections to the gold contact pads on the sample are already established since they are directly linked to the graphite gates of the sample. Instead, we established connections to the gold pads as the final step in the process. This approach ensured the structural integrity of the sample for dual-gate operation in cryogenic optical measurement.

3.2. Confocal spectroscopy in cryogenic environment

We employed confocal spectroscopy to examine the optical properties of the excitonic ground states of the the TMD heterostructures introduced in Section 2.1 in a cryogenic environment. To understand their physical origin, we investigated the optical transition responses under the application and variation of various external forces, such as doping and electric or magnetic fields. The following section provides an overview of the cryogenic systems and experimental techniques utilized during the optical measurements in this work.

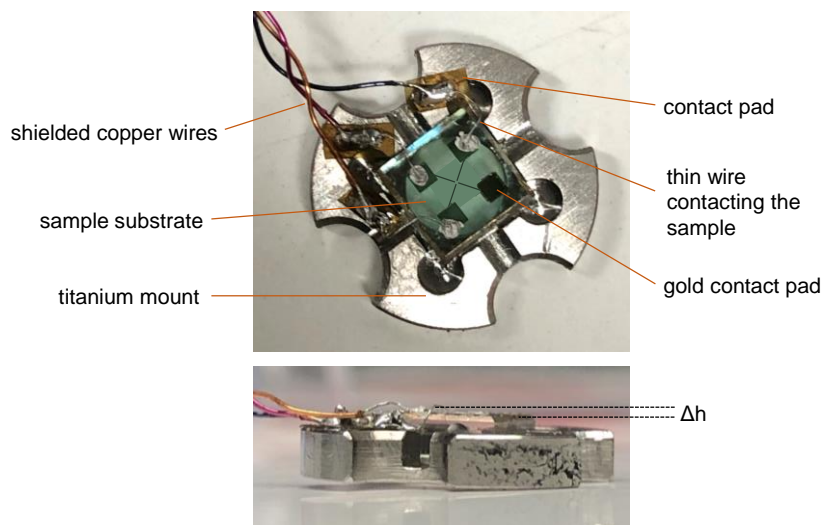


Figure 3.6.: **Mounting of the sample substrate.** A 5x5 mm glass substrate with a distributed Bragg reflector (DBR) coating, hosting a completed dual-gate heterostructure including gold contacts, was fixed on a titanium mount for optical experiments. Contact pads on the titanium mount serves as connecting platform between shielded copper wires and thin wires, which, in turn, are guided to the gold pads on the sample. The height difference (Δh) between the sample surface and connecting wires is minimized for optimal performance.

3.2.1. Spectroscopy techniques

To study exciton physics without being hindered by temperature-induced decoherence effects, the dual-gate samples were loaded either in helium bath cryostats at 4.2 K or in a closed-cycle-cryostat (attocube systems, attoDRY1000) with a base temperature of 3.2 K and equipped with a superconducting magnet providing magnetic fields of up to ± 9 T. We performed the optical measurements using a home-built fiber-based confocal microscope in back-scattering geometry as shown in Figure 3.7a. Two broadband collimators (attocube systems, RT-APO/NIR-IR/0.13) and a apochromatic objective (attocube systems, LT-APO/VISIR/0.82) above the sample inside the cryostat formed the basic confocal configuration, superimposing the diffraction limited projection of the detection and excitation fiber core in the focal plane of the objective in linear polarization basis. For optimal performance, the numerical aperture (NA) of the two collimators matched the one of the single-mode fibers (NA = 0.13), the high NA = 0.82 of the objective maximized the resolution of the focal spot. The choice of the excitation light source, detection device and the set of optical waveplates and filters (marked by dashed lines in Figure 3.7) depended on the type of measurement.

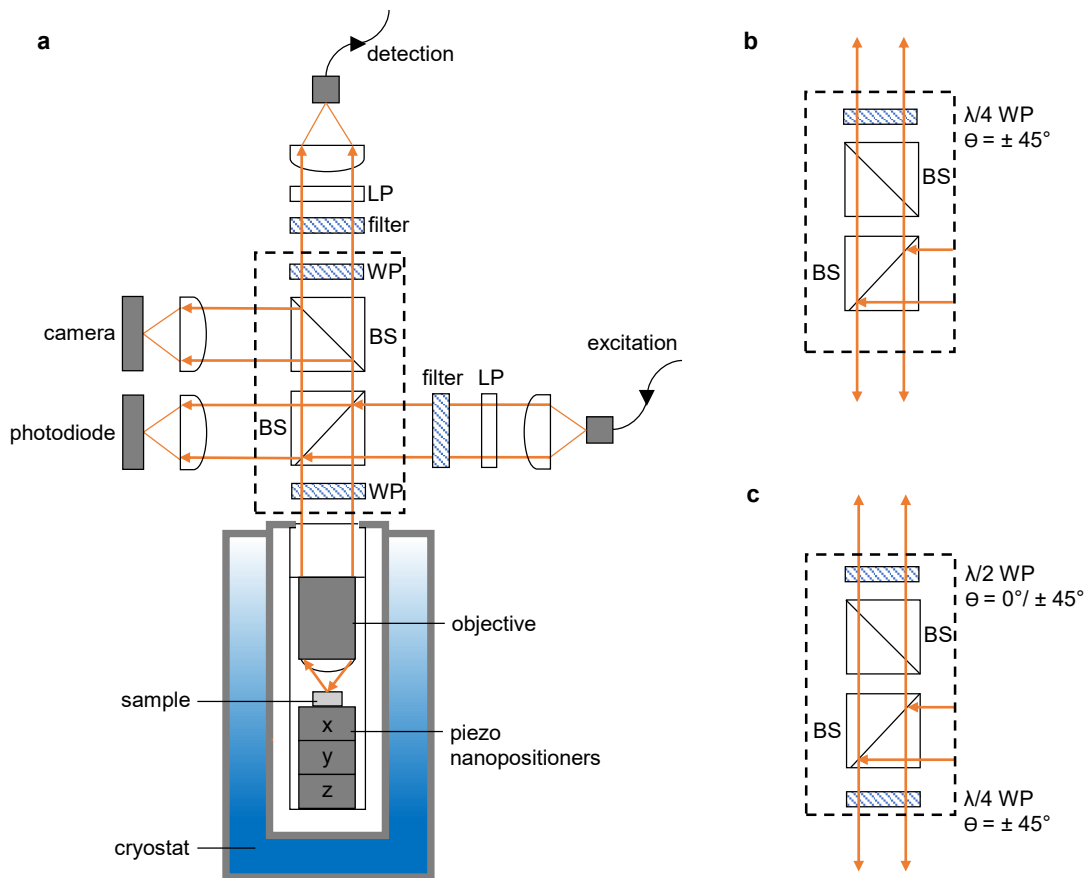


Figure 3.7.: **Setup schematics for cryogenic spectroscopy.** **a**, Laser light from an excitation fiber is collimated and guided through a linear polarizer (LP) and optional optical filters to a beam sampler (BS, Laseroptik), which partially reflects it towards the sample mounted in a cryostat (the transmitted part of the light can be used for excitation power monitoring with a photodiode). A waveplate (WP) can be used to control the polarization of the excitation beam. An apochromatic objective focuses the light onto the sample mounted on a set of piezo-stepping and scanning units (attocube systems, ANPxyz and ANSxy100) for positioning with respect to the focal spot of the objective. Light reflected or emitted from the sample is collected by the objective and guided to the top of the setup passing another BS (a fraction of the light can be used for imaging using a camera), a set of waveplates and filters and a linear polarizer for polarization and wavelength selection and finally coupled into a detection fiber. The latter is used to guide the light to a detection device for analysis. **b**, Waveplate configuration for polarization selective PL or DR measurements. **c**, Waveplate configuration for measuring the degree of circular polarization in PL. Θ is the angle between the given direction of linear polarization, defined by LP, and the slow axis of respective waveplate.

Differential reflection measurements

Differential reflection (DR) spectroscopy was applied to study the absorption characteristics of a heterostructure in a specific spectral range. We used a supercontinuum laser (NKT, Super K Varia and Super K Extreme) or a tungsten halogen lamp (Ocean optics, HL-2000-HP) as broadband light sources and guided the reflected light from the detection fiber through a monochromator (Roper Scientific, Acton SP2500 a 300/1200 grooves/mm grating) for spectral dispersion to a liquid nitrogen cooled charge-coupled device (CCD, Roper Scientific, Spec-10:100BR). The DR spectra were obtained by normalizing the reflected spectra from the region of interest on the TMD heterostructure (R) to that from the sample region without MoSe₂ and WS₂ layers (R_0) as $DR = (R - R_0)/R_0$.

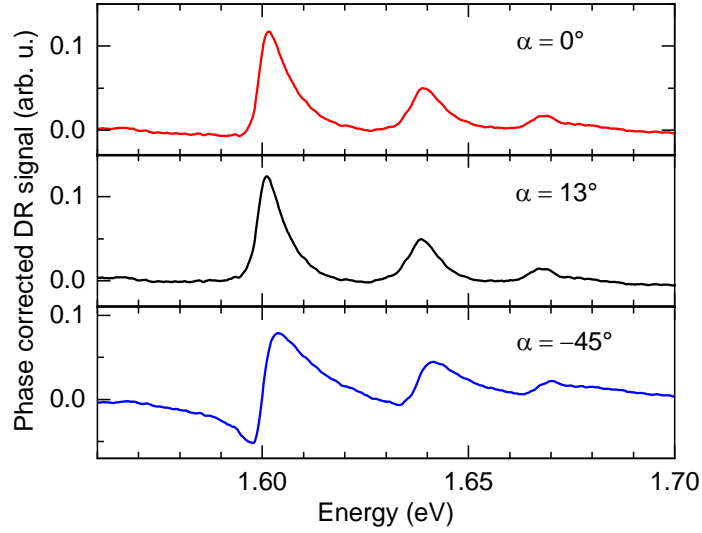


Figure 3.8.: **DR phase correction.** Top panel: Raw DR signal corresponding to the data shown in Fig. 1b of the main text. Center panel: Phase corrected DR with the phase $\alpha = 13^\circ$ which was used in the main text. Bottom panel: Phase corrected DR with $\alpha = -45^\circ$.

For comparison between measurements and theory the DR signal can be translated into the imaginary part of the dielectric susceptibility $\chi = \chi' + i\chi''$ by following Refs. [127, 128]. Without hBN encapsulation the DR signal would simply be proportional to χ'' , however, top and bottom hBN add additional interfaces that influence the lineshape of the reflected signal by interference effects. As shown in [127], these effects can be taken into account by introducing a phenomenological phase factor for the effective susceptibility $\tilde{\chi} = \chi e^{i\alpha}$, where α is an *a priori* wavelength-dependent phase factor and the DR signal is now proportional to the imaginary part of $\tilde{\chi}$, $DR \sim \text{Im}(\tilde{\chi})$. Here, for simplicity, we assume α to be a constant in the relevant spectral range. Then, using the Kramers-Kronig relations for the complex-valued function $\tilde{\chi}(\omega)$, we can compute χ'' from DR as

$$\chi''(\omega) = \text{Im} \left(e^{-i\alpha} \tilde{\chi}(\omega) \right) = \cos(\alpha) \text{DR}(\omega) - \sin(\alpha) \int_{\mathbb{R}} \frac{\text{DR}(\omega')}{\omega - \omega'} d\omega'. \quad (3.1)$$

Figure 3.8 shows a representative raw DR signal ($\alpha = 0^\circ$) alongside the corresponding phase-corrected data ($\alpha = 13^\circ$) and a third example with an arbitrary phase for illustration of the principle ($\alpha = -45^\circ$). The phase which was used in the main text is chosen such that the individual moiré exciton peaks exhibit approximately Lorentzian lineshapes, as expected for the absorption of individual exciton resonances.

Photoluminescence measurements

Photoluminescence (PL) measurements were employed to study the ground state optical transition characteristics of a heterostructure. A complementary set of short- and longpass filters is additionally introduced in the excitation and detection path of the confocal setup, respectively; the first hindering Raman-generated photons from entering the detection device, the latter blocking the excitation laser. For standard PL measurements we used a continuous wave (CW) laser source at 635 nm (Helium Neon Laser) or 532 nm for optical excitation above the excitonic bandgap. Light was guided to a spectrometer and detected by a CCD in analogous fashion to DR measurements.

Polarization resolved measurements

The unique valley degree of freedom of monolayer TMDs features polarization-contrasting dipolar selection rules [48, 129–132] which become non-degenerate once time reversal symmetry is broken by an out-of-plane magnetic field. As a result, a Zeeman splitting or degree of polarization of the polarization contrasting exciton transitions can be studied in optical experiments [70–72, 74]. In this work, we studied the polarization resolved optical response of our TMD heterostructures in DR with an applied out-of-plane magnetic field by introducing a $\lambda/4$ -waveplate in the detection path before the linear polarizer (LP) as shown in Figure 3.7b. The combination of waveplate and linear polarizer selects light from either of the two directions of circular polarization depending on the angle of the slow axis of the waveplate with respect to the direction of linear polarization defined by the polarizers.

The degree of spin-polarization ρ was then determined as

$$\rho = \frac{f_+ - f_-}{f_0} = \frac{\Delta f}{f_0}, \quad (3.2)$$

the difference of the exciton oscillator strength f_{\pm} in σ^+ and σ^- polarization normalized by the polarization independent exciton oscillator strength f_0 at $B = 0$ T. A measure for f is the amplitude of a Lorentzian profile which is fitted to the spectral lineshape of the polarization resolved DR peaks [88].

The Zeeman splitting is the difference of the respective peak energies:

$$\Delta E_X = E_+ - E_- \quad (3.3)$$

Finally, we define the polarization contrasting optical response, referred to as magnetic circular dichroism, as

$$MCD(\lambda) = DR_+(\lambda) - DR_-(\lambda) \quad (3.4)$$

where $DR_{+/-}(\lambda)$ is the DR spectrum measured in $\sigma_{+/-}$ polarization as function of the wavelength λ . Both finite degree of polarization ρ and Zeeman splitting ΔE_X lead to a non zero MCD response as a function of λ , i.e. excitons in a specific spectral range are polarized and preferably occupy either of the two K -valleys.

3.2.2. Dual-gate operation

At room temperature no voltage should be applied between the electrostatic gates to prevent thermally activated discharge through defect states in the hBN layers. After loading the device into a cryostat all gates were grounded during the cool-down procedure, since, given its electrostatic sensitivity, charging effects induced by temperature gradients could potentially disrupt the sample. Before starting to explore the exciton physics in different charge configurations, we conducted tests to assess the functionality and limits of the device gates. Using a voltage source (Keithley, 2400 SourceMeter) capable of measuring resistive circuit currents with pA precision simultaneously, we carefully tested the applicable voltage range between the gates. The limit of applicable voltage is reached once the resistive current starts following the behaviour of an ohmic contact indicating electrical shorting between the FLG electrodes through the hBN spacer layer as a result of increased defect density [133]. Keeping the applied gate voltage below this critical value allowed to reliably operate the dual-gate device over an extended period of time and several cryogenic cycles. Monitoring the optical response in the active area of the heterostructure in reflection or PL during the testing of the gates provides direct feedback on the functionality of the gates via the observation of expected charged exciton features at finite gate voltages.

The dual-gate layout of the field-effect device with symmetric hBN layer thickness around the TMD HBL allows to precisely control and manipulate the charge carrier distribution inside the HBL through a perpendicular electric field F or to vary the doping level V_μ . The former regime can be reached by an imbalanced tuning of the top and bottom gate voltages V_T and V_B as $\Delta V_{TB} = (V_B - V_T) = F d_{\text{hBN}}$ with respect to the grounded reservoir in contact with both TMD monolayers (d_{hBN} denotes the total hBN thickness of the heterostack between the two graphite electrodes) and probes the static out-of-plane exciton dipole moment via the Stark effect. The latter is achieved by balancing both gates and tuning them simultaneously against the ground as $V_\mu = (V_T + V_B)/2$.

3.2.3. AC modulation measurements

In our experiments we studied the optical response of the TMD heterostructure at different dual-gate configurations in PL and DR spectroscopy. However, certain features of the moiré modulated bandstructure and spatial arrangement of specific exciton and charge complexes cannot be observed by standard spectroscopy techniques if their physical origin is decoupled from bright optical transitions or weak optical signals are buried in noise due to slow drifts in the experimental setup.

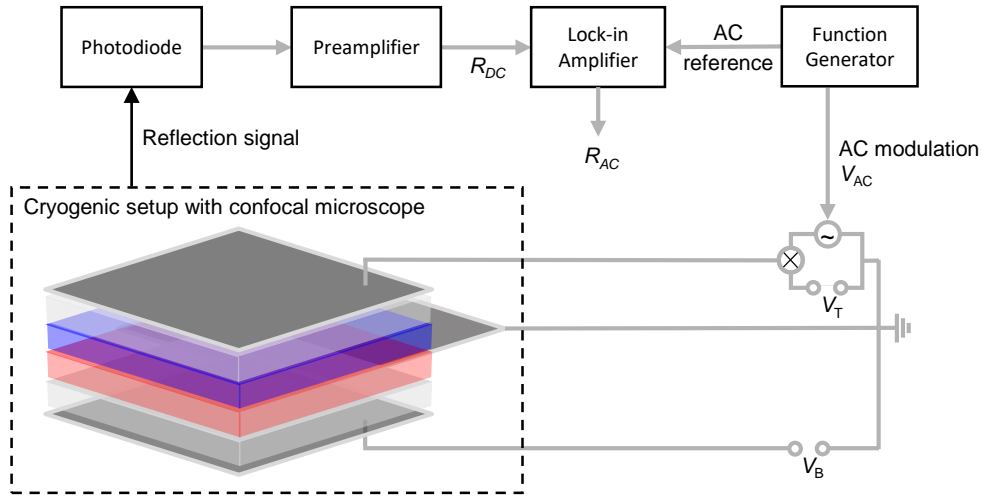


Figure 3.9.: **Setup schematics for AC modulation spectroscopy.** A narrow-band tunable laser is used for excitation in the standard configuration of the confocal setup, the corresponding reflection signal from the sample coupled to the detection fiber and guided to a photodiode. The resulting photocurrent signal is amplified (R_{DC}) and subsequently demodulated by a lock-in amplifier at the same frequency at which the top gate voltage V_T is modulated (V_{AC}).

AC modulation measurements using a lock-in amplifier can help to extract such hidden information from a system. In this technique, an experimental variable is modulated with an alternating current or voltage signal. The impact of this modulation on a physical observable is then detected and analyzed with a lock-in amplifier, which operates at the specific modulation frequency.

For example, interlayer excitons in TMD heterostructures typically exhibit a vanishingly small oscillator strength under in-plane polarized optical excitation due to their out-of-plane transition dipole moment. However, the application of an out-of-plane electric field induces a notable shift in the resonance energy due to the Stark effect (see Section 2.1.3). Bringing interlayer and intralayer excitons into resonance through electric field tuning can result in field-induced hybridization [14, 15, 134] depending on the coupling strength of the two resonances. To render this effect observable, we employed a modulation-spectroscopy

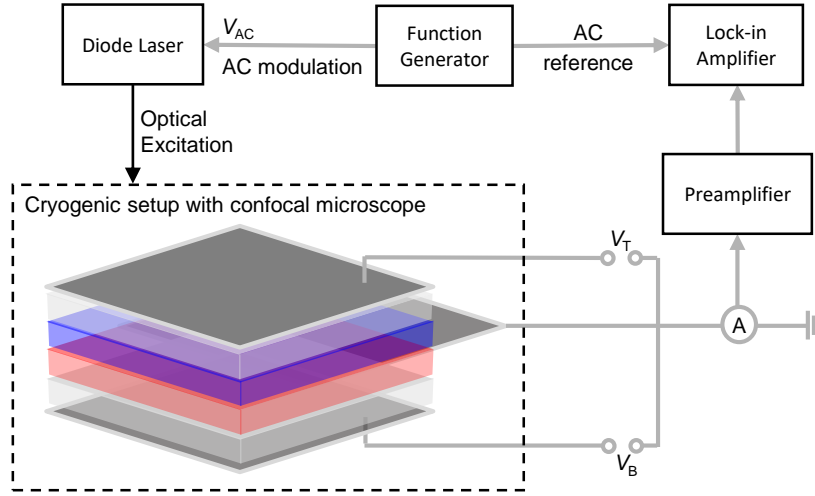


Figure 3.10.: **Setup schematics for photocurrent measurements.** The excitation laser power is modulated at a specific frequency before it is coupled into the confocal microscope in standard configuration. A preamplifier measures the current between ground reservoir and the TMD bilayer, while DC voltages are applied to top (V_T) and bottom gate (V_B). The signal from the preamplifier is demodulated with a lock-in amplifier at the same frequency as for the laser power modulation to extract the resulting photocurrent.

technique utilizing a narrow-band wavelength-tunable laser to measure the differential absorbance or reflectance at a specified laser energy [P2, 135–137]. The results of this measurement on a $\text{MoSe}_2/\text{WS}_2$ heterostructure are presented in Section 4.3. The schematic of the setup is depicted in Figure 3.9: We excited the sample with a Ti:sapphire laser (M squared) featuring a $50 \mu\text{eV}$ linewidth, while modulating one of the device gates with a small AC-voltage (V_{AC}). Subsequently, the reflected optical signal was detected by a silicon photodiode, with the output preamplified using an Ithaco 1211 preamplifier. The amplified DC part of the photosignal (R_{DC}) was measured, and the AC part was further demodulated and amplified by a lock-in amplifier (EG & G 7260), synchronized with the reference frequency of the modulation voltage to yield R_{AC} . Finally, the narrow-band differential reflectance ($\Delta R'$) was computed as the ratio of the demodulated AC part to the DC photosignal, i.e., R_{AC}/R_{DC} . Each data point acquisition involved an integration time constant of 1 s. In certain straightforward modulation conditions, the signal may be directly proportional to the derivative of ΔR [135], while in more complex cases, a microscopic analysis, including optical pumping of charge carrier reservoirs, is necessary.

Another AC modulation technique applied in this work is photocurrent spectroscopy, measuring the photo-excited current in a semiconductor device under laser irradiation at a specific wavelength [138]. The schematics of the measurement setup are shown in

Figure 3.10. Here, we used a diode laser for excitation, the output power of which can be modulated by an AC input signal V_{AC} . Another possibility is the use of an optical chopper in the beam path of the excitation laser before coupling it into the excitation fiber. In this experiment, the physical observable of interest was the current of charge carriers from the ground reservoir into the TMD heterostructure via the FLG contact gate. The current was measured and converted to a voltage signal by an Ithaco preamplifier (model 1211) and subsequently demodulated and further amplified by a lock-in amplifier (EG & G 7260). The frequency of the laser power modulation was given as a reference input to the lock-in amplifier to obtain the part of the photoinduced current between ground reservoir and TMD heterobilayer. Monitoring the photocurrent while tuning the Fermi level inside the TMD heterostructure by applying DC voltages at top and bottom gate could provide information about incompressible charge configurations at specific densities of electron or hole filling (see Section A).

3.3. Open microcavity in a closed-cycle cryostat

The introduction of an optical resonator can enable efficient and precise interaction between a photon and a solid-state emitter. It presents a powerful platform to study strong light-matter interaction and polaritonic physics. A pivotal aspect in the progress of light-matter interaction with solid-state systems is the challenge of combining the requirements of cryogenic temperature and high mechanical stability against vibrations while maintaining sufficient degrees of freedom for in situ tunability. In the scope of this thesis, we implemented a fiber-based open Fabry-Pérot cavity in a closed-cycle cryostat, developed by Samarth Vadia [139], Holger Thierschmann, Clemens Schäfermeier and Claudio Dal Savio at attocube systems. Lukas Husel contributed to the setup of the measurement protocols. The system exhibits ultrahigh mechanical stability while providing wide-range tunability in all three spatial directions. The following section presents the functionality and characterization of the open cavity platform, followed by an overview of the cavity-based spectroscopy techniques applied for the study of moiré excitons in $\text{MoSe}_2/\text{WS}_2$ heterostructures in the strong light-matter coupling regime, which are presented in Section 5.2. The Sections 3.3.1 and 3.3.2 were partly published verbatim in [P8] and are subject to the copyright of the American Physical Society.

3.3.1. Cavity design and setup

The design of our open Fabry-Pérot cavity is based on the plano-concave geometry as introduced in Section 2.2. A micromirror is formed by a fiber end facet with a dimple that has been produced using the CO_2 laser ablation technique and can be approximated by a

3. EXPERIMENTAL METHODS

sphere [99]. Its macroscopic counterpart is a planar mirror and supports a solid-state system of interest, as illustrated in Figure 3.11a. For the experiments, both mirrors were coated with either a thin film of silver or a distributed Bragg reflector (DBR) coating.

The fiber and the macroscopic mirror were mounted in a configuration as shown in Figure 3.11b. To ensure large tunability of the cavity not only along its optical axis (z), but also along lateral dimensions (x, y), we placed the two cavity mirrors on two separate mounts. The macroscopic mirror was fixed on top of a commercial xyz-nanopositioner (attocube, two ANPx311 and ANPz102) for precise and independent position control in the x and y direction over a range of 6 mm each and cavity length control along z over a range of 4.8 mm. The fiber mirror is mounted on another stack, consisting of rigid titanium blocks and a piezo, which only provides a tunability in the z direction through the piezo element for cavity fine tuning and active feedback control. The fiber position in the xy -plane is fixed. This ensures alignment of the optical axis of the cavity with an aspheric lens (Thorlabs, AL1210, NA = 0.55) mounted on a nanopositioner (attocube, ANPx311HL) with z displacement providing a free-space optical access to the cavity.

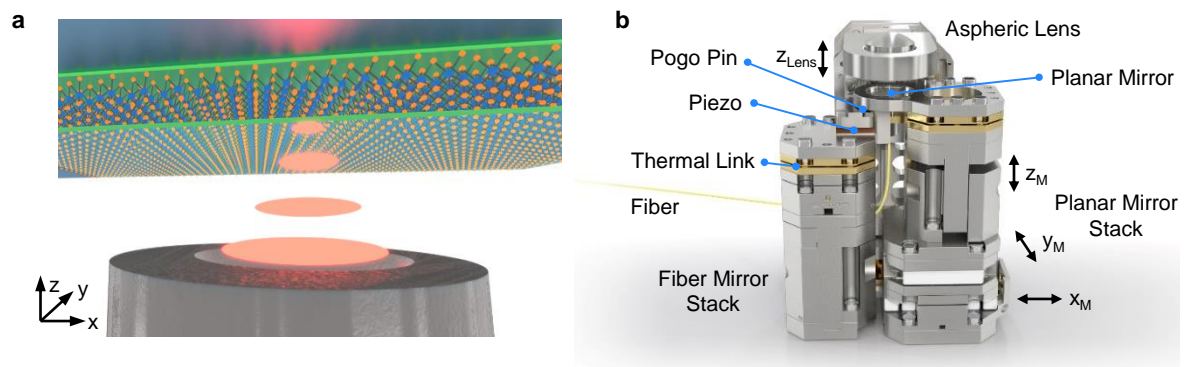


Figure 3.11.: **Concept and setup of a fiber-based open-cavity.** **a**, An illustration of the cavity composed of a concave-profiled fiber mirror and a macroscopic mirror with a TMD monolayer. **b** Sketch of the tunable cavity assembly that mounts on top of a vibration isolation stage. The stack on the right holds the planar mirror and consists of xyz-nanopositioner with a thermal link connecting the mirror to the cold plate to thermalize it to cryogenic temperature. The other stack on the left holds the fiber mirror and consists of a piezo element, thermal link and metal blocks to reach the same height as the right stack. A spring-loaded pogo pin introduces a connection between the two stacks to reduce differential motion. The aspheric lens is mounted via another metal piece at the back with an additional nanopositioner to adjust the focal spot in z direction.

3.3.2. Damping of vibrational noise for high finesse operation

The key challenge when using the above setup in a closed-cycle cryostat lies in the mechanical vibrations induced by the cooling cycle of the cryostat and other external sources of motion in the low-frequency range. With the cryostat in operation, the mechanical vibration amplitude at the cold plate is in the range of 10 – 20 μm , mostly due to the impact of high pressure helium flow during the cooling cycle [140]. The displacement amplitude is brought down to the level of a few nanometers at the cold plate of the cryostat (attocube systems, attoDRY800) that is aligned with the surface of the optical table [141].

Identification of vibrational noise

We verified the low level of vibrations with a fiber-based optical interferometer (attocube systems, FPS3010) that measures the displacement of the cold plate with respect to the optical table. The resulting time trace at the measurement bandwidth of 100 kHz is presented in the left panel of Figure 3.15. The data reveal a 1 Hz periodic pattern of mechanical pulses characteristic of closed-cycle coolers. These pulses excite a set of high frequency vibrations resulting in a peak-to-peak (p-p) amplitude below 10 nm at the given full bandwidth. This amplitude quickly rings down leading to a rather inhomogeneous distribution of vibrations in time with rms displacement fluctuations of 2.2 nm. Although this is not entirely surprising, it is worthwhile to point out that the displacement fluctuations (often referred to as *vibrational noise*) arise from a set of mechanical oscillators being excited by an impulse force during the cryo-cooler cycle and do not follow a well-defined statistical distribution, such as the Brownian noise.

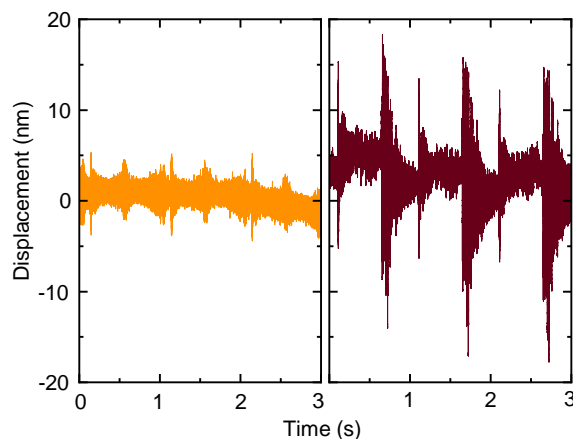


Figure 3.12.: **Mechanical vibration characteristics at room-temperature.** Displacement of the cold plate of the cryostat (*left panel*) and of a xyz-nanopositioner stack on the cold plate (*right panel*), acquired with an integration bandwidth of 100 kHz.

The mechanical vibrations become naturally exacerbated when mechanical degrees of freedom are added to the system. In our case, the addition of nanopositioners was necessary to provide in-situ control. As a demonstration, we measured the displacement amplitude along the z-axis of a xyz-nanopositioner set (attocube systems, two ANPx101 and ANPz102) directly mounted on the cold plate. The time trace in the right panel of Figure 3.12 shows that the p-p displacement increases significantly by more than a factor of three, reaching up to a maximum of around 35 nm at each pulse of the cryo-cooler. We note that in contrast to the p-p amplitude at the mechanical pulses, the displacement amplitude between two pulses remains fairly similar, with an increase in rms fluctuations by less than factor of two to a value of 3.4 nm.

These results make clear that additional measures were needed for the cavity setup shown in Figure 3.11b to be operational in the cryostat. Without any modifications, the rigid fiber mirror stack would closely follow the motion of the cold plate and thus feature fluctuations as in the left panel of Figure 3.12, whereas the planar mirror stack would vibrate similar to the nanopositioner stack with characteristics in the right panel of Figure 3.12. The differential motion between the two cavity mirrors is expected to be of the order of tens of nm, rendering experiments even with a low finesse cavity impossible.

Passive vibration isolation

To improve the mechanical stability, we implemented a set of vibration isolation springs to decouple the cavity setup from vibrations of the cold plate. A detailed description of the development of the vibration isolation system can be found in Ref. [139]. A sketch including the cavity setup and the spring stage is depicted in Figure 3.13a. The cavity setup, which is shown in Figure 3.13b, is represented here by two springs, corresponding to the fiber mirror stack and the planar mirror stack with their respective spring constants k_F and k_M (where rigid fiber mirror stack implies $k_F \gg k_M$). This full cavity setup is mounted on a titanium plate, labeled as a spring table in Figure 3.13a. The spring table rests on a set of four springs (represented by a single spring in the sketch), each of which has a nominal spring constant of $k_S = 1.52$ N/mm (Smalley, CM08-L7) at ambient conditions. With total mass $m = 0.686$ kg compressing the springs, the nominal resonance frequency f_R of the vibration isolation stage calculates as

$$f_R = \frac{1}{2\pi} \sqrt{\frac{k_S}{m/4}} = 15 \text{ Hz.} \quad (3.5)$$

We chose the payload and spring constant such that the resulting resonance frequency lay sufficiently far above the resonance frequency of the optical table (5 Hz) to suppress their coupling.

Additionally, a link of high stiffness between the two mirror stacks helps to minimize their differential motion. Of course, introducing direct contact between the two mirrors

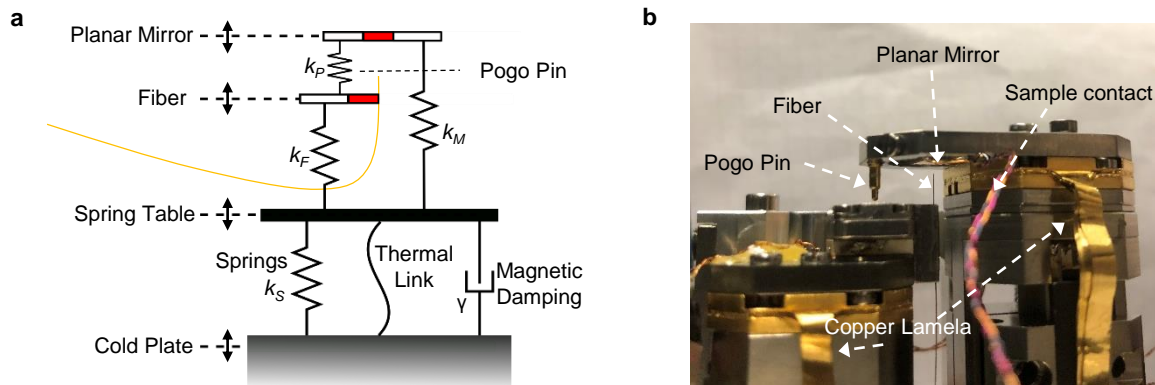


Figure 3.13.: **Mechanism for damping vibrational noise.** **a**, Schematic of the cavity assembly and vibration isolation stage built on top of the cold plate of the closed-cycle cryostat. Vibration isolation stage consists of the spring table placed on top of four springs (k_S) along with magnetic damping (damping constant γ), which are all placed on the cold plate. The thermal link enables cavity operation at cryogenic temperature. The cavity setup is represented as two springs on the spring table - planar mirror stack (with spring constant k_M) and fiber mirror stack (with spring constant k_F) - which are connected by a rigid spring (with spring constant k_P) representing the pogo pin for damping of differential motion between the two. **b**, Optical image of planar mirror and fiber stack including the pogo pin. Thin copper lamella are used for thermalization of the cavity stacks with the cold plate of the cryostat.

completely eliminates any vibrational limitations of the cavity measurement. However, we aimed to maintain the tunability of the open-cavity configuration. To achieve this, we introduced a spring-loaded pin (N&H, SVPC-F-N005M2), commonly referred to as a pogo pin, similar to those used in the electronic testing industry. This approach provided a rigid connection between the two mirrors while still allowing us to tune the mirror position with the piezo stack [139].

An important challenge was to ensure reliable thermalization of the cavity with the cryostat cold plate without reducing the vibration isolation by the spring stage. This is crucial because an efficient thermal link inevitably constitutes an additional mechanical connection that can potentially allow vibrations to bypass the vibration isolation stage. We addressed this challenge by attaching to the spring table a bundle of thin copper lamella with high thermal conductivity that are sufficiently soft and flexible to suppress transfer of mechanical vibrations.

To suppress high oscillation amplitudes at the spring stage resonance, we included a soft magnetic eddy current damper, denoted with damping constant γ . The spring system as a whole acts as a mechanical low pass filter, that suppresses vibrations by a factor 100 per decade above resonance frequency with a transition to suppression by a factor 10 per decade

3. EXPERIMENTAL METHODS

towards higher frequencies due to the eddy current damping. This means that contributions to the mechanical vibrations become suppressed from tens of nm down to the order of 0.1 nm for the frequencies above 180 Hz.

Vibration characterization

To characterize the performance of the complete assembly, we measured the relative displacement between the fiber and macroscopic mirrors using the cavity itself as an interferometer. A schematic overview of the experiment on the optical table is presented in Figure 3.14a. The optical excitation is provided through the fiber side of the cavity. The transmitted light through the planar mirror of the cavity is guided to a photodiode (Siemens, BPW34 with DL Instruments, 1211 Current Preamplifier). A part of the transmission signal can optionally be guided to another photodiode via a beamsplitter which can then be used to perform active feedback stabilization of the cavity length using the piezo actuator below the fiber mirror.

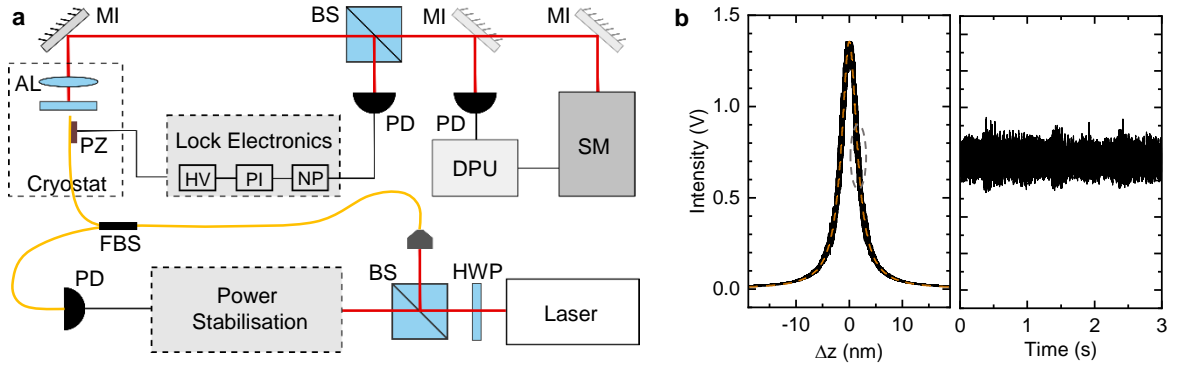


Figure 3.14.: **Cavity length fluctuation measurement.** **a**, Sketch of the experimental setup used for the stability characterization and strong-coupling operation. Assignment of abbreviations: $\lambda/2$ -waveplate (HWP), beamsplitter (BS), fiber beamsplitter (FBS), photodiode (PD), aspheric lens (AL), piezo element (PZ), mirror (MI), data processing unit (DPU); lock electronics: high voltage amplifier (HV), proportional-integral (PI) control electronics, notch pass (NP), (SM) spectrometer. **b**, *Left panel*: Transmission signal as a function of cavity length. The solid black line is the data around a cavity resonance obtained by applying a voltage to the piezo actuator. The orange dashed line shows the corresponding fit to the Fabry-Pérot transmission function of Eq. (2.7) with $\mathcal{F} = 110$. *Right panel*: Transmission signal measured with active stabilization at the maximum slope of the cavity resonance shown on the left at a temperature of 6.5 K. The measurement bandwidth was 100 kHz.

For the stability characterization measurements, we used a fiber with a dielectric coating (LaserOptik, $T = 0.0032$), while the macroscopic mirror had a silver coating ($T \approx 0.008$) which leads to higher photon leakage towards the free-space side. The laser light at 780 nm

(MSquared, SolsTiS) is coupled to the cavity through the fiber. To determine the cavity displacement induced by mechanical vibrations, the transmission signal through the planar mirror was recorded at the slope of a cavity resonance where the sensitivity to changes in transmission as a function of the cavity length is highest. Changes in transmission were subsequently converted to changes in the cavity length.

To this end, the transmission signal across a cavity resonance was recorded while sweeping the voltage applied to the piezo below the fiber that acts as an actuator (see Figure 3.14b, right panel). The finesse of the cavity resonance can be determined from the transmission signal as a function of the cavity length using Eq. (2.7). Close to a cavity resonance, any change in the transmission as a function of time is converted to a change in the cavity length. We used the derivative of the transmission function in Eq. (2.7):

$$\frac{dA_t}{dl_c} = -\frac{4G^2\pi}{\lambda} \frac{\sin(\phi)\cos(\phi)}{\left[1 + (G\sin\phi)^2\right]^2}, \quad (3.6)$$

with $G = 2\mathcal{F}/\pi$ and $\phi = 2\pi l_c/\lambda$ to derive small fluctuations around the half-maximum position of a cavity mode from transmission intensity fluctuation in a linear approximation as indicated by the grey circle in the left panel of Figure 3.14b.

In our experiments, the transmission signal was measured with a time resolution of $10\ \mu\text{s}$. The rms displacement fluctuations were calculated from the cavity length fluctuations as a function of time as:

$$d_{rms} = \sqrt{\frac{1}{n} \sum_{i=1}^n d_i^2}, \quad (3.7)$$

where n is the total number of data points acquired over 10 s and d_i is the cavity displacement at each point.

The effect of the passive vibration isolation system on the cavity stability at room temperature can be seen in Figure 3.15a. The cavity length fluctuations as a function of time are drastically reduced as compared to the displacement of a single set of positioners, shown in the right panel of Figure 3.12 on the same scale. The inset in Figure 3.15a shows the time trace with a 20-fold magnification. Here, it becomes visible that the vibration kicks at intervals of 1 s are strongly suppressed down to a p-p amplitude of 0.3 nm. The rms cavity length fluctuations are $31.6 \pm 0.5\ \text{pm}$ at an integration bandwidth of 100 kHz. This large measurement bandwidth encompasses all significant mechanical resonances of the system. We identify the source of additional vibrations by analyzing the Fourier transform (FT) in Figure 3.15b for the cavity length fluctuations shown in Figure 3.15a. The peaks around 20 Hz can be assigned to resonances of the vibration isolation stage. The stage excites both mirror stacks and a small but visible relative displacement of the two mirrors is observed. Starting from 250 Hz, more peaks are visible in the FT, eluding a detailed analysis. Some can presumably be attributed to the various components in the setup, but also the thermal links

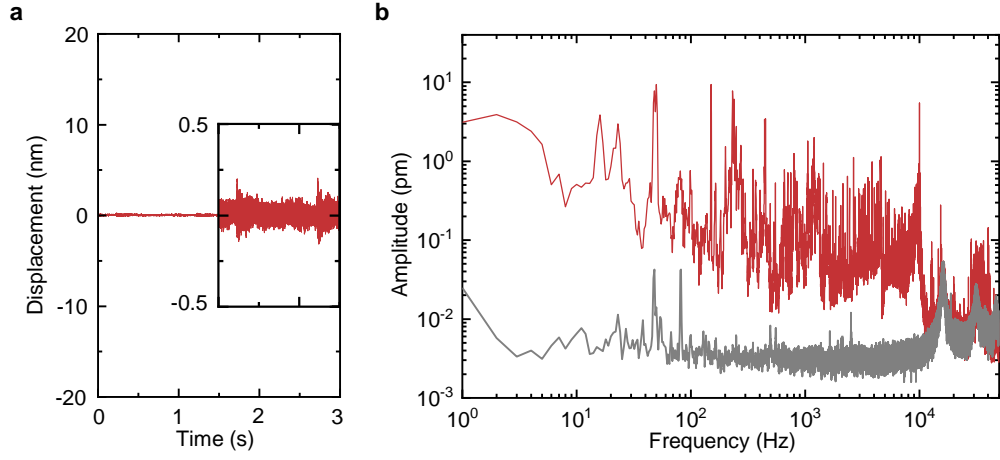


Figure 3.15.: **Cavity length fluctuations at room-temperature.** **a**, Cavity length fluctuations of the open-cavity on the vibration isolation stage inside of the cryostat, acquired with an integration bandwidth of 100 kHz. **b**, Fourier transform of cavity length fluctuations (red) and noise floor (grey) with a frequency resolution of 1 Hz.

possibly provide a path for vibrations to be transmitted from the cold plate to the cavity that may not get fully filtered by the vibration isolation stage. Finally, there are also several sharp resonance peaks which are ascribed to the higher harmonics of 50 Hz. All preceding room temperature vibration measurements were done by turning on the cryo-cooler for several minutes to evaluate the vibrations without performing a full cool-down to the base temperature. This is a useful tool for a quick characterization, especially during the development stage.

At cryogenic conditions the mechanical properties of various components can differ with change in temperature and pressure, and result in different mechanical fluctuation characteristics. The cryogenic vibration characteristics of the cavity at 6.5 K in vacuum (the nominal base temperature of about 4 K was not reached in this specific experiment due to a temporary modification of the radiation shield for a wire feed-through) are shown in Figure 3.16 for an integration bandwidth of 100 kHz. Figure 3.16a shows the cavity length fluctuations of the passively stabilized system with p-p amplitude and rms fluctuation values of 0.7 nm and 117 ± 7 pm, respectively. It is important to note that the cavity length fluctuations should be measured with an appropriate dynamic range defined by the finesse of the cavity. For example, the measurements shown in this work were performed with $\mathcal{F} = 110$ leading to the spatial-equivalent cavity linewidth of $\Delta L \simeq 3.5$ nm. Thus, the maximum displacement of the cavity length for a vibration kick of 0.7 nm is still well within the interferometric measurement range of the cavity as illustrated in the right panel of Figure 3.14b.

Subsequently, we evaluated the effect of additional active feedback stabilization of the cavity length as schematically shown in Figure 3.14a. Here, a part of the transmission signal

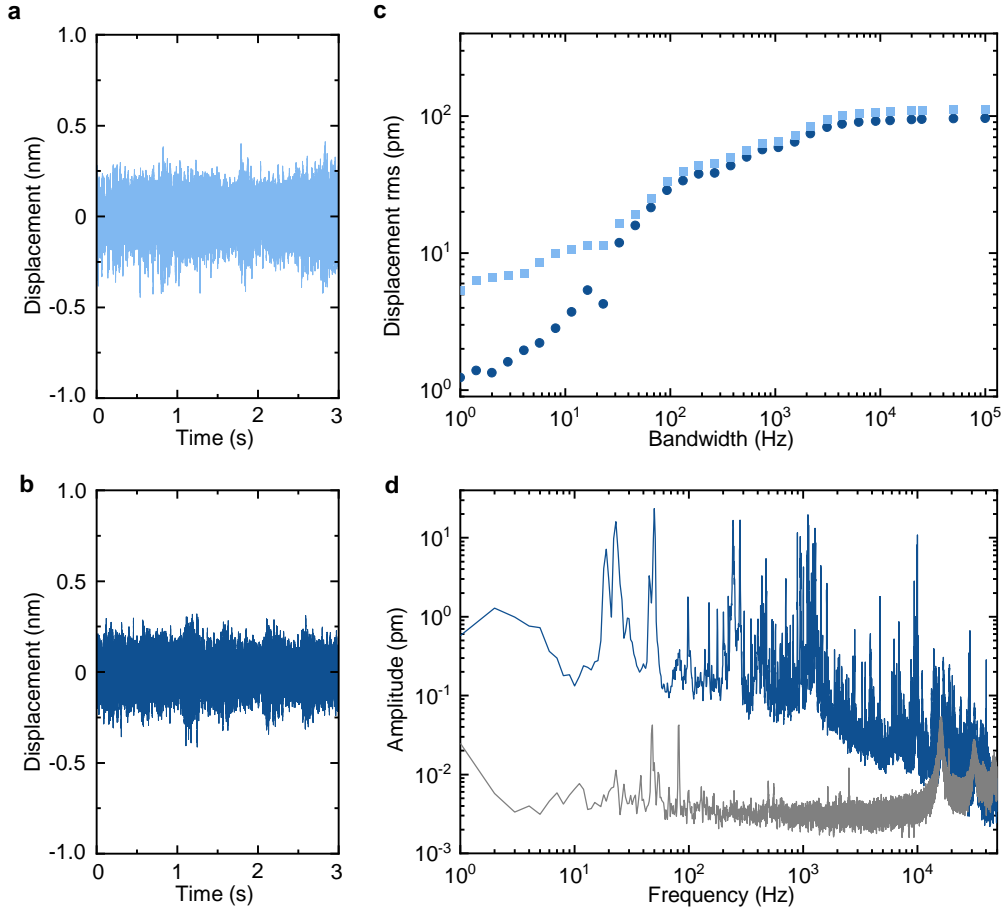


Figure 3.16.: **Cavity length fluctuations at cryogenic temperature.** **a**, Vibration displacement of the tunable cavity at 6.5 K without lock and **b** with lock at a bandwidth of 100 kHz. **c**, Displacement rms of cavity fluctuations as a function of integration bandwidth without lock (square) and with lock (circle). **d**, Fourier transform of cavity fluctuations with lock (blue) and noise floor (grey) with a frequency resolution of 1 Hz.

from the cavity was directed to a photodiode and into a servo, built at attocube systems (atto servo rev. 1). The output of the servo, which is fed with an error signal, is connected to the piezo actuator to adjust for cavity length fluctuations against a defined resonance condition. The resulting change in transmission is again detected by the photodiode and fed back to the servo. The result of the cavity locking through active feedback can be seen in Figure 3.16b. While the p-p amplitude remained at 0.7 nm, the rms fluctuations reduced to 89 ± 5 pm, or by 25% compared to the solely passively damped cavity. The comparison of the rms fluctuations as a function of bandwidth is shown in Figure 3.16c. The active feedback stabilization works efficiently up to ~ 50 Hz, indicating an upper limit for the bandwidth of the feedback at that frequency. However, the analysis of rms fluctuations as a

function of bandwidth shows that the mechanical stability of around 1 pm can be reached with small measurement integration bandwidth. The FT of the cavity fluctuations with an active feedback is shown in Figure 3.16d. Here, we observe similar features as in the room-temperature data of Figure 3.15b, namely a relatively strong increase in rms fluctuations at low frequencies (10-100 Hz), where the resonance of the vibration isolation stage at around 15-20 Hz and a sharp peak around 50 Hz dominate. For frequencies above 200 Hz, two sets of resonances dominate the vibrations, one of which lies in the range ~ 200 -500 Hz and the other between ~ 1 -2 kHz. In Figure 3.16c, a step-wise increase in the displacement rms can be clearly observed at these frequency ranges. As discussed above, those contributions presumably arise from the mechanical resonance of individual components of the cavity setup and, potentially, from vibrations of the cryostat that get transferred via the thermal links. At 10 kHz, the sharp peak originates from the carrier frequency of the pulse width modulator built in the inverter driving the 1 Hz rotating valve of the three phase motor of the cryostat.

3.3.3. Limitations of vibration suppression

The previously explained reduction of cavity length fluctuations to rms stability of 89 pm enables cavity measurements with resolvable finesse in the order of 10^4 , qualifying the platform for state-of-the-art cavity QED experiments with Q-factors in the range of $10^5 - 10^6$ and in-situ tunability for a wide variety of solid-state emitters. However, reaching this benchmark demands a high control of various setup components and optimal environmental conditions. The following gives a short overview over the limiting factors.

After completing the measurements detailed in the previous section, the cavity setup was relocated to a different attoDRY800 cryostat, which featured a smaller optical table. Following the disassembly and reassembly of the setup, the cavity stability was significantly diminished compared to the results presented earlier, as depicted in Figure 3.17a. The rms fluctuations at room temperature increased from approximately 20 pm on the old table to nearly 100 pm on the new one for the passively damped cavity setup with the cryostat compressor switched off. The corresponding Fourier transforms in Figure 3.17b offer insights into the underlying causes of this reduced stability. The main contribution to the increase in cavity displacement lies, on one hand, in the low-frequency range between 10–30 Hz and, on the other hand, in a broader spectral range between 100 – 1000 Hz. The former corresponds to the resonance frequency of the vibration isolation stage (~ 15 Hz), suggesting a potential heightened excitation of the cavity stage resulting from vibrations originating from the cold plate of the cryostat, the optical table or environmental vibration noise. The latter suggests an increased vibration level of the cavity setup possibly caused by loose or broken parts.

To address the first issue, we examined the vibration behavior of both optical tables through accelerometry measurements in three orthogonal directions utilizing a vibration

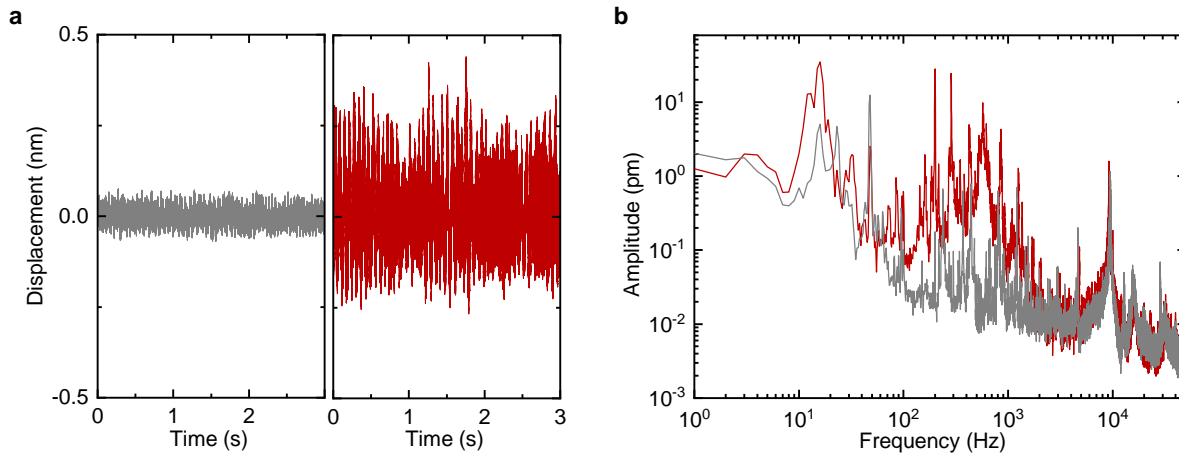


Figure 3.17.: **Limited cavity stability.** **a**, Vibration displacement of the tunable cavity at room temperature at a bandwidth of 100 kHz with compressor turned off before (left panel) and after (right panel) moving the setup to a different optical table. **b**, Fourier transform of respective cavity fluctuation data with a frequency resolution of 1 Hz, plotted in corresponding colors.

analyzer (Table Stable, VA-2C). Achieving optimal vibration damping performance for a floating optical table necessitates operating the table's vibration isolators (Newport, S-2000) within the recommended pressure range tailored to the weight of the optical table and its specific load. The left panel of Figure 3.18 illustrates the Fourier transform of vertical accelerometry measurements conducted on both, the old and new optical table. Notably, the resonance frequency of the new table is shifted to higher frequencies by approximately 2 Hz owing to its reduced weight. Moreover, the measured acceleration of the new table exhibits an increase in the low-frequency range up to 100 Hz. In particular, the acceleration around the resonance frequency of the cavity vibration isolation stage (~ 15 Hz) is increased by almost one order of magnitude compared to the old table from less than $10 \mu\text{m}/\text{s}^2$ to over $100 \mu\text{m}/\text{s}^2$. This accounts for the diminished cavity stability, as the motion of the new table introduces a resonant drive to the vibration isolation stage. One potential solution could involve swapping the springs of the cavity stage to shift the stage resonance frequency away from the vibration maximum, although this was not pursued within the scope of this thesis. Furthermore, accelerometry measurements were directly performed on the cold plate of the new attoDRY800 cryostat, to which the cavity setup was mounted. The resulting Fourier transform, compared to measurements on the corresponding optical table, is depicted in the right panel of Figure 3.18. At low frequencies, the spectral evolution of cold plate acceleration follows the one of the optical table. However, an enhancement can be observed at higher frequencies between 400-1000 Hz. These mechanical vibrations, transmitted through the thermal links of the cavity setup, may cause the observed increased

3. EXPERIMENTAL METHODS

cavity length fluctuations within the same frequency range, as can be seen in Figure 3.17b. In addition to the diminished vibration damping performance of the new optical table and cryostat cold plate, the second phase of cavity measurements coincided with construction works in the building, resulting in increased environmental vibrational noise, not possible to eliminate. To rule out loose or damaged components within the cavity setup as sources of vibrational noise, we disassembled the setup, reglued the springs of the vibration isolation stage (UHU Plus Endfest) and the cavity fiber (UHU Plus Schnellfest), replaced the pogo pin (Mouser Electronics, 575-0964015208514110) and inspected the piezo stack to which the planar mirror was affixed for any broken parts.

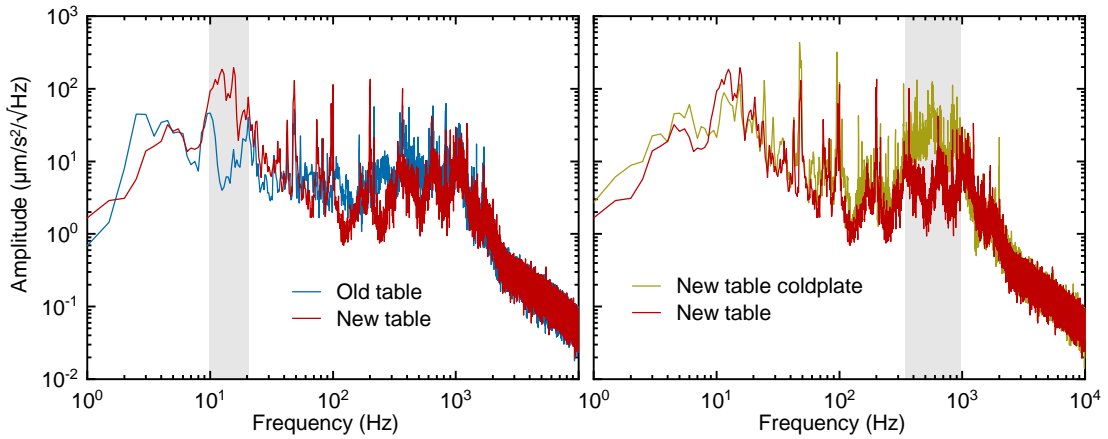


Figure 3.18.: **Vibration characterization of optical table and cold plate.** Comparison of the fourier transform (FT) of vertical accelometry measurements on the old and new optical table hosting the cavity setup (*left panel*) and the new optical table and the corresponding attoDRY800 cryostat cold plate (*right panel*). Spectral bands of highest relative amplitude increase between the shown data are highlighted in grey. The FT was determined with a frequency resolution of 0.5 Hz.

Given the limitations of the cryostat setup, the resolvable finesse is reduced to a few hundred. Nonetheless, TMD mono- and bilayers, which were investigated in the strong light-matter coupling regime in this thesis, exhibit excitons with optical transitions in the visible and near-infrared spectral range, featuring homogeneous linewidths exceeding 1 meV at cryogenic temperatures due to their substantial exciton oscillator strength. Even with increased vibrational noise, the vibration-limited resolution of the optical cavity remains comparable or smaller than the exciton linewidth at low mode orders, still qualifying our cavity platform for the intended measurements.

3.3.4. Cavity transmission spectroscopy

The following section gives an overview of the procedure of transmission spectroscopy measurements done with the above described cavity setup. The heterostructures were placed on a DBR optimized to reflect the spectral range of exciton transitions of interest. The DBR design features a field-node at the surface of the mirror, such that the encapsulating hBN acts as a spacer layer to place the TMD layers in a field maximum. The transmissions of both DBR coatings as a function of wavelength are shown in Figure 3.19a and theoretically expected finesse follows directly using the formula (2.10).

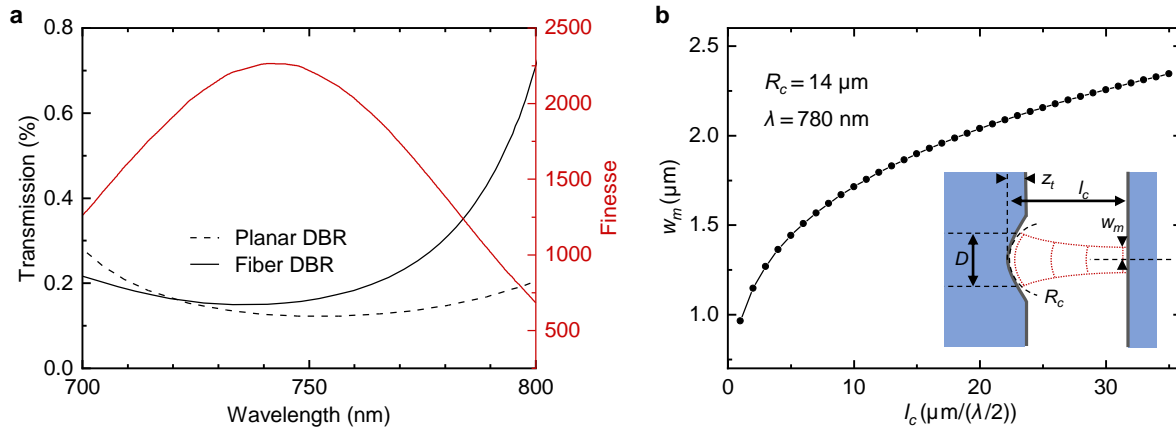


Figure 3.19.: **Cavity characteristics.** **a**, The expected transmission (T) of the fiber and macroscopic planar DBR in the spectral range of interest shown in solid and dashed lines, respectively. The expected finesse of the assembled cavity calculated from the corresponding reflectivities (R) is plotted in red. We assume $R = 1 - T$ neglecting further losses in the given spectral range. **b**, Expected mode waist as function of the cavity length for a given radius of curvature $R_c = 14 \mu\text{m}$ and wavelength $\lambda = 780 \text{ nm}$. *Inset*: Illustration of the plano-concave fiber cavity geometry with laser-machined fiber tip. The full-width of the Gaussian profile at $1/e^2$ is denoted as D , the depth of the indentation as z_t .

After assembling the cavity setup, we employed broad band white light for optical excitation from the fiber side (NKT, Super K Varia and Super K Extreme) and detected the spectrally dispersed (Roper Scientific, Acton SP2500) transmission signal in the range of the highly reflective bands of the DBRs with a liquid nitrogen cooled CCD (Roper Scientific, Spec-10:100BR). The free spectral range (FSR) $\Delta\lambda$ between adjacent TEM_{00} modes in the spectrum with respective resonance wavelength λ_1 and λ_2 allowed to monitor the cavity length $l_c = \lambda_1\lambda_2/2|\lambda_1 - \lambda_2|$. We gradually reduced the cavity length, as we wanted to operate the cavity in the range where the plano-concave resonator geometry supports the formation of stable Gaussian modes and minimum effective mode volume V_m , when coupled to an exciton emitter (see Section 2.2 for details). Figure 3.19b shows the expected Gaussian mode waist as a function of the cavity length l_c , determined from Equation (2.18) at a wavelength

3. EXPERIMENTAL METHODS

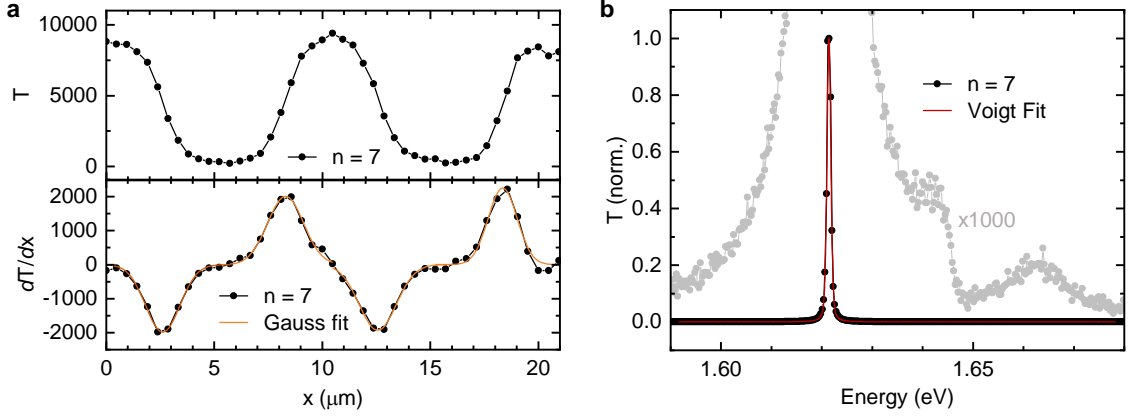


Figure 3.20.: **Cavity transmission characteristics at low mode order ($n = 7$).** *a, upper panel:* Transmission profile of a lateral cavity scan across a silver chessboard pattern with $5 \mu\text{m}$ lattice constant. Gaussian fits (orange lines) to the derivative of the transmission profile at the edges of the silver structure in the *lower panel* allow to extract the resolution of the cavity scan, i.e. the mode waist of the cavity. *b,* Transmission spectrum using broadband white light for excitation through the cavity fiber. The cavity setup is placed inside the cryostat and cooled to cryogenic temperatures. The fundamental cavity mode at 1.621 eV ($\lambda = 765 \text{ nm}$) can be fitted with a Voigt profile, yielding the Lorentzian contribution with homogenous linewidth $\kappa = 0.13 \text{ meV}$ and the Gaussian contribution with linewidth $\gamma = 0.38 \text{ meV}$.

$\lambda = 780 \text{ nm}$. The stability criterion for the plano-concave cavity geometry (see Equation (2.13)) allows the formation of stable Gaussian modes for cavity length $l_c \leq R_c$, with the radius of curvature of the fiber tip indentation R_c . It is worth noting, that the CO_2 laser ablation technique leads to a Gaussian profile of the fiber tip indentation as illustrated in the inset of Figure 3.19b [99]. However, in a paraxial approximation, the center of the imprinted dimple with depth z_t and diameter D can be treated as a sphere with radius of curvature

$$R_c \approx \frac{D^2}{8z_t}. \quad (3.8)$$

For our specific cavity geometry, the minimum possible mode order was $n = 3$ before introducing contact between the planar mirror and the fiber tip, corresponding to a cavity length of $1.5 \mu\text{m}$.

To estimate V_m at a specific cavity length in our measurements we determined the cavity mode waist experimentally by laterally scanning the cavity mode across a defined nanostructure, employing the open cavity geometry. Here, a 70 nm thick silver (Ag) chessboard pattern, fabricated via optical lithography on a planar DBR substrate, was utilized. The upper panel of Figure 3.20a shows the transmission intensity of the cavity at a fixed cavity length, corresponding to mode order $n = 7$ at a wavelength of $\lambda = 780 \text{ nm}$. The planar mirror with

the Ag nanostructure was incrementally moved with respect to the cavity fiber, with Ag areas identified by low transmission intensity, enabling the calibration of cavity steps in units of micrometers (μm) based on the periodicity of the chessboard pattern. The derivative of the transmission profile, dT/dx , in the lower panel of 3.20a provides a measure of the resolution of the cavity mode at the edges of the Ag nanostructure. This resolution corresponds to the averaged half-width at $1/e^2$ of a series of Gaussian functions fitted to dT/dx , yielding a value of $1.86\mu\text{m}$, which is close to the theoretically expected value for the cavity mode waist ($w_m = 1.24\mu\text{m}$). Small deviations may arise artificially due to a finite twist angle between the axis of the chessboard pattern and the scanning direction or diffraction losses due to transverse mode mixing [100].

To avoid such contribution of higher order modes or signal from the uncoupled emitters, disturbing the spectral signatures, we intended to optimize the mode matching ($> 30\%$) of the fundamental Hermite-Gaussian mode with the detection fiber, which guides the light into the spectrometer. Figure 3.20b shows an exemplary transmission signal at mode order $n = 7$ of the empty cavity inside the cooled cryostat with optimized mode matching, where contributions of higher order modes are strongly suppressed compared to the TEM_{00} mode. Its spectral lineshape is inhomogeneously broadened due to the cavity length fluctuation as explained in the previous section 3.3.3 and is best fitted with a Voigt profile, the convolution of a Lorentzian and a Gaussian function $L(E)$ and $G(E)$, respectively:

$$V(E) = \int G(E')L(E - E')dE', \quad (3.9)$$

$$L(E) = \frac{A}{\pi} \frac{\gamma/2}{E^2 + (\gamma/2)^2}, \quad (3.10)$$

$$G(E) = \frac{1}{\sqrt{2\pi}\sigma} e^{-E^2/(2\sigma^2)}. \quad (3.11)$$

The Lorentzian full-width at half-maximum linewidth γ reflects the ideally stable cavity with Finesse defined by the reflectivity of the two mirrors, A is a normalization coefficient. In Figure 3.20b, we extract a Finesse $\mathcal{F} = 1250$ at wavelength $\lambda = 765\text{ nm}$, slightly smaller than the theoretically expected value shown in Figure 3.19a, which could be explained by potential losses of the cavity due to surface contamination. The Gaussian broadening parameter σ of the Voigt profile describes the inhomogeneous broadening due to imperfect cavity stability as introduced in the previous section 3.3.3.

In the next step we, introduced the TMD heterostructure on the planar mirror into the cavity. To find the position of interest on the sample, we laterally moved the planar mirror at high mirror spacing ($l_c > 100\mu\text{m}$) and used a camera to monitor the cavity transmission signal of a 532 nm laser coupled into the cavity through the fiber side. The DBR coatings exhibit high transmission in this spectral range, while structural changes on the mirror surface at the edges of the heterostructure or gold contacts introduce losses due to scattering

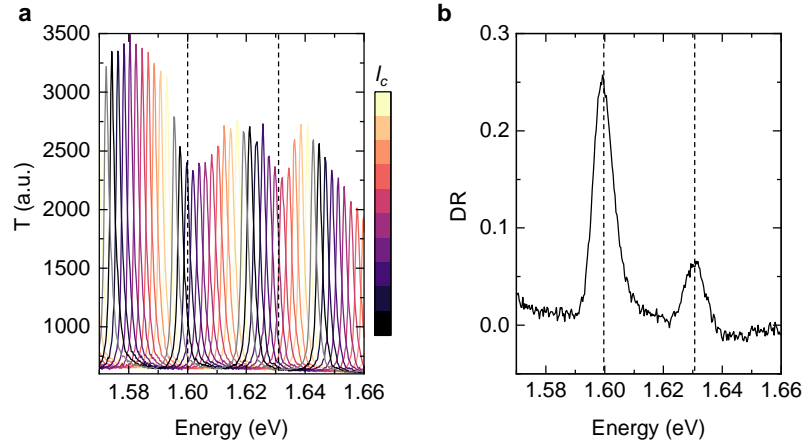


Figure 3.21.: **Cavity transmission spectroscopy at high mode order.** **a**, Transmission spectra of the cavity including the MoSe₂/WS₂ heterostructure at various cavity lengths around $l_c \approx 25 \mu\text{m}$. The transmission dips around 1.6 eV and 1.63 eV arise due to absorption at moiré exciton resonances (vertical dashed lines) in agreement with a DR spectrum measured without the cavity at the same position on the heterostructure, shown in **b**.

processes, which could be identified during the position scan. The area illuminated by the cavity fiber on the sample is large compared to the cavity mode waist at small cavity lengths and covers large parts of the heterostructure facilitating a rough orientation.

With the TMD heterostructure inside the cavity, we switched back the detection device from the camera to the spectrometer and found an absorption induced drop of cavity transmission in the spectral range around the respective exciton resonance, as shown in Figure 3.21a. Using the exciton resonance energy and the strength of absorption, determined from confocal spectroscopy in Figure 3.21b, as a reference, we optimized the position of the TMD heterostructure inside the cavity. In this manner, we studied the light-matter interaction at specific positions of interest as a function of the cavity length, excitation laser power and wavelength as well as the charge configuration inside the TMD field-effect device. The results are presented in Section 5.2.

Moiré exciton physics in MoSe₂/WS₂ heterostructures

4

Bilayer moiré materials provide a unique platform for studies of correlated many-body effects, including Hubbard model physics or Mott insulating states of generalized Wigner crystals. In this context, we studied the moiré exciton physics of MoSe₂/WS₂ heterostructures experimentally and theoretically in a highly collaborative project, the findings of which are presented in this Chapter. Utilizing the dual-gate design of the heterostacks, we subjected the moiré excitons to out-of-plane electric fields and charge doping. This allowed us to investigate the underlying bandstructure and interactions with single- and bilayer spin-charge lattices in the presence of out-of-plane magnetic fields.

THIS CHAPTER IS PARTLY BASED ON THE PUBLICATIONS [P2], [P3] AND [P6]
[P2] B. Polovnikov*, J. Scherzer*, S. Misra*, et al., “Field-Induced Hybridization of Moiré Excitons in MoSe₂/WS₂ Heterobilayers,” *Phys. Rev. Lett.* **2024**, *132*, 076902
[P3] B. Polovnikov*, J. Scherzer*, S. Misra*, et al., “Implementation of the bilayer Hubbard model in a moiré heterostructure,” *arxiv* **2024**, 2404.05494
[P6] B. Polovnikov*, J. Scherzer*, S. Misra*, et al., “Coulomb-correlated states of moiré excitons and charges in a semiconductor moiré lattice,” *arXiv* **2022**, 2208.04056

* equal contribution

4.1. Introduction and theoretical concepts

In the scope of this work, we fabricated and studied various samples of $\text{MoSe}_2/\text{WS}_2$ heterobilayers with both, parallel (R-type, $\sim 0^\circ$ relative twist angle) and antiparallel (H-type, $\sim 180^\circ$ relative twist angle) layer orientation. An overview of the different samples and their basic optical signatures at cryogenic temperatures (see Chapter 3.2) is provided in Section 4.2 of this Chapter. The near-resonant conduction band alignment in $\text{MoSe}_2/\text{WS}_2$ heterobilayers unveils an intricate interplay of both intra- and interlayer moiré excitons, which was studied by applying out-of-plane electric fields in the dual-gate configuration of the heterostacks as presented in Section 4.3. Finally, we investigated the magnetic response of the moiré excitons in the presence of fractional electron doping, implementing a two dimensional bilayer Hubbard model with triangular geometry, discussed in Section 4.4. The Sections 4.1.1 and 4.3 were partly published verbatim in [P2] and are subject to the copyright of the American Physical Society.

The work presented in this Chapter was carried-out in close collaboration with Borislav Polovnikov and Subhradeep Misra. Ismail Bilgin, Jonas Göser and Zhijie Li synthesized TMD layers by CVD growth and Xin Huang, Christian Mohl and Julian Trapp helped fabricating the heterostacks. Anvar Baimuratov developed the effective continuum model to describe the complexity of intra- and interlayer excitons in Ref. [P2] and Henning Schlömer, Fabian Grusdt and Annabelle Bohrdt contributed numerical calculations for theoretical insight in the magnetic properties of correlated many-body systems in Ref. [P3].

4.1.1. Modelling of the moiré exciton bandstructure

Vertically stacking two atomically thin layers with hexagonal lattice geometry and small lattice mismatch or rotational misalignment generally results in a new, long-range moiré superlattice that introduces a periodic potential for charge-carriers and provides a scaffold for ordered electronic states [10, 11, 142]. The periodicity $a_{\text{moiré}}$ of the moiré lattice can be approximated as [143]

$$a_{\text{moiré}} = \frac{(\delta + 1)a_2}{\sqrt{\delta^2 + (\delta + 1)\theta^2}} \quad (4.1)$$

for small relative twist angles θ between the two layers and lattice mismatch $\delta = a_1/a_2 - 1$, where a_1 and a_2 denote the lattice constants of the individual layers.

The upper panel of Fig. 4.1a shows $a_{\text{moiré}}$ as a function of the twist angle and lattice mismatch, diverging around $\theta \approx 0^\circ$ and $\delta = 0$. In real samples, small twist angles between near-commensurate sublattices do not rigidly produce infinitely large $a_{\text{moiré}}$ but lead to the formation of mesoscopically reconstructed domains [144]. In our study, however, we investigated heterostructures comprising MoSe_2 and WS_2 monolayers with substantially different lattice constants $a_M = 3.289 \text{ \AA}$ and $a_W = 3.154 \text{ \AA}$ [145], forming superlattices that

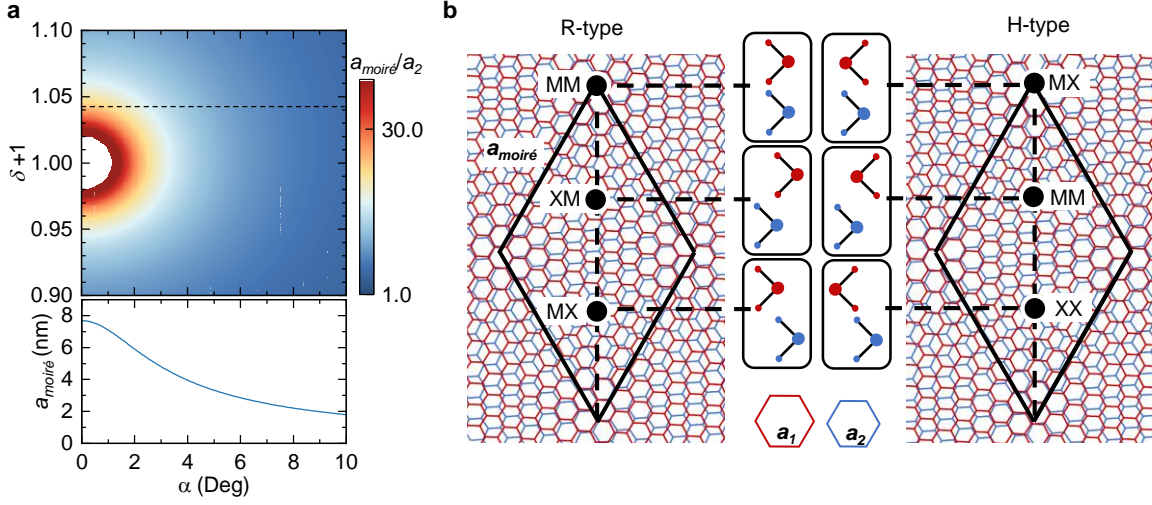


Figure 4.1.: **Moiré superlattice of a TMD heterostructure.** **a**, Upper panel: $a_{\text{moiré}}$ in units of the sublattice constant a_2 as a function of θ and the ratio of two sublattice constants (a_1/a_2). Lower panel: $a_{\text{moiré}}$ as a function of θ with fixed $a_1 = 3.288 \text{ \AA}$ and $a_2 = 3.154 \text{ \AA}$ ($a_1/a_2 = 1.042$, cp. dashed horizontal line in the upper panel) for the specific case of respective MoSe_2 and WS_2 layers. **b**, Schematic illustration of the moiré superlattice with lattice constant $a_{\text{moiré}}$ resulting from the overlay of two hexagonal sublattices with relative twist angle θ and respective lattice constants a_1 and a_2 . Left and right panel highlight the location of specific high symmetry points within the moiré unit cell for R-type and H-type stacking, respectively.

give rise to distinct moiré excitons. The lattice constant of the moiré unit cell for this material combination, shown in the lower panel of Fig. 4.1a as a function of the twist angle θ , reaches a maximum value of $a_{\text{moiré}} = 7.7 \text{ nm}$ at $\theta = 0^\circ$. This twist angle is commonly referred to as parallel or AA-stacking and denoted as R-type configuration in the scope of this thesis. The three-fold rotation symmetry (\hat{C}_3) of the hexagonal sublattices leads to the existence of a tantamount configuration at $\theta = 180^\circ$, referred to as anti-parallel or AB-stacking and denoted as H-type, here. Figure 4.1b illustrates the moiré unit cell for the H-type and R-type configuration, highlighting the respective alignment of transition metal M (Mo, W) and chalcogen atoms X (Se, S) in the two layers at the high-symmetry points of the moiré unit cell. At these high-symmetry points, the bilayer moiré lattice has a \hat{C}_3 symmetry strongly constraining the optical selection rules for exciton formation of holes in the valence band electrons in the conduction band at the respective locations in the heterobilayer and resulting in the formation of a periodically modulated in-plane moiré potential for electrons, holes and excitons [13, 146, 147].

Figure 4.2a illustrates the ordering of the lowest conduction (CB) and highest valence bands (VB) in a $\text{MoSe}_2/\text{WS}_2$ heterobilayer for R-type and H-type alignment. In reciprocal

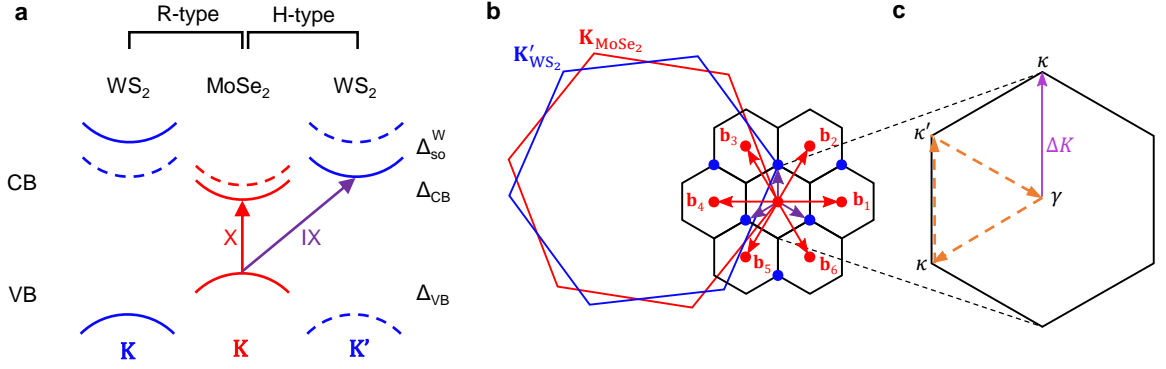


Figure 4.2.: **Bandstructure schematics of the moiré heterostructure** **a**, Parallel (R-type) and antiparallel (H-type) stackings give rise to $\mathbf{K}_{\text{MoSe}_2}/\mathbf{K}'_{\text{WS}_2}$ and $\mathbf{K}_{\text{MoSe}_2}/\mathbf{K}_{\text{WS}_2}$ alignment of MoSe_2 and WS_2 valleys. Note the reversed ordering for H- and R-stacks of the spin-up (solid lines) and spin-down (dashed lines) polarized conduction sub-bands of WS_2 with spin-orbit splitting Δ_{so}^W . Both stackings are in type-I band alignment with conduction and valence band offsets Δ_{CB} and Δ_{VB} , respectively. **b**, Formation of the mini-Brillouin zones (mBZs) resulting from the valley mismatch $\Delta\mathbf{K}$ between the two hexagonal sublattices, with moiré reciprocal vectors \mathbf{b}_j (red arrows) and interlayer coupling (violet arrows) for the case of H-type alignment. The red and blue points represent intra- and interlayer states considered in the model. **c**, Magnification of the zero order mini-Brillouin zone from **b** with center γ ($\mathbf{K}_{\text{MoSe}_2}$) and corner κ ($\mathbf{K}'_{\text{WS}_2}$) defined by $\Delta\mathbf{K}$. The dashed orange arrows highlight the k values for the CB dispersions shown in Figure 4.3.

space, these two configurations respectively correspond to $\mathbf{K}_{\text{MoSe}_2}/\mathbf{K}_{\text{WS}_2}$ and $\mathbf{K}_{\text{MoSe}_2}/\mathbf{K}'_{\text{WS}_2}$ alignments of the MoSe_2 and WS_2 valleys, leading to a reversed ordering of spin-polarized conduction sub-bands of WS_2 with spin-orbit splitting Δ_{so}^W . The large VB offset between MoSe_2 and WS_2 [148] simplifies the analysis of the lowest-energy spin-allowed transitions: It is sufficient to consider only intralayer excitons (X) of MoSe_2 and interlayer excitons (IX) consisting of a hole in MoSe_2 and an electron in WS_2 as illustrated by the respective arrows in Figure 4.2a. The long-range periodicity of the moiré lattice is reflected by the formation of a mini Brillouin zone (mBZ) in reciprocal space [143] with the moiré reciprocal lattice vectors $\mathbf{g}(n, m) = n\mathbf{b}_1 + m\mathbf{b}_2$ as illustrated in Figure 4.2b for the H-type case. Here, n and m are integers, $\mathbf{b}_j = (C_6^{j-3} - C_6^{j+1})\Delta\mathbf{K}$ are the first-shell reciprocal lattice vectors, $j = 1, 2, \dots, 6$, C_6^μ represents rotation by $2\pi\mu/6$ and $\Delta\mathbf{K} = \mathbf{K}'_{\text{WS}_2} - \mathbf{K}_{\text{MoSe}_2}$ the valley mismatch related to the finite lattice mismatch and twist angle of the two layers. We define the angle-dependent mBZ as shown in Figure 4.2b with the center γ matching the K -valley of MoSe_2 ($\mathbf{K}_{\text{MoSe}_2}$), and the point κ at the \mathbf{K}' -valley of WS_2 ($\mathbf{K}'_{\text{WS}_2}$).

In previous works, the experimental signatures of excitons in such moiré modulated heterostructures have been theoretically studied from two different perspectives. The first

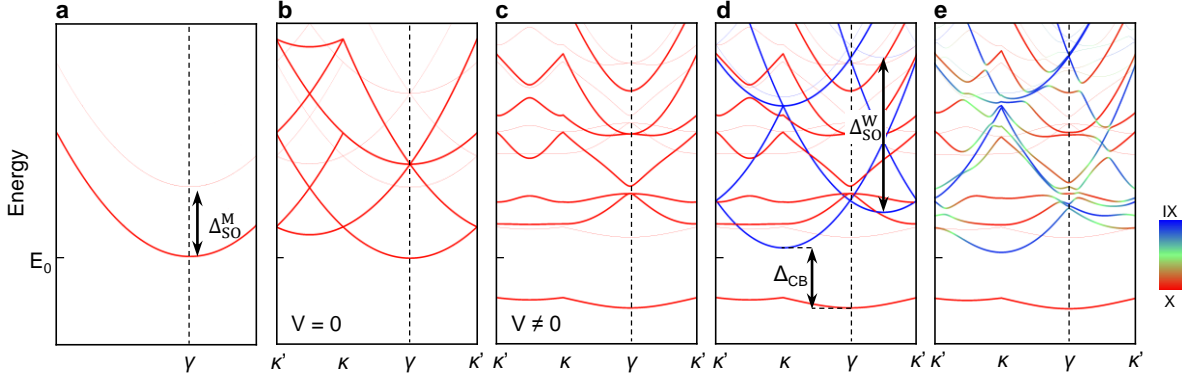


Figure 4.3.: **Moiré bandstructure modelling.** **a**, Parabolic MoSe₂ X exciton dispersion. In MoSe₂, the lowest X transition is spin-bright (bold line) and separated by the spin-orbit splitting Δ_{SO}^M from the first spin-dark transition (thin line). **b** and **c**, MoSe₂ X exciton dispersion taking into account all first order moiré bands without and with presence of a moiré potential V , respectively. **d**, Included first order IX bands (blue lines) in the presence of a near-resonant WS₂ conduction band. Here, an H-type heterostructure alignment gives rise to a spin-bright lowest energy IX transition at κ with energy offset Δ_{CB} compared to the X band minimum at γ . In this work, we assume a vanishing IX moiré potential $W = 0$. **e**, Finite interlayer hopping t leads to the formation of bandgaps at crossing points of X and IX bands. The hybrid X-IX nature at these points is visualized in green color. The vertical dashed lines mark the γ point where momentum direct transitions can be observed in optical absorption measurements.

treats the wavefunction modulation of non-resonant intra- and interlayer excitons due to the presence of respective moiré potentials V and W in the framework of a continuum model [13, 146, 147]. The second deals with the effect of interlayer hybridization in case of energetically aligned conduction or valence bands by introducing a hopping parameter t [14, 15, 17]. To model our experimental results presented in Section 4.3 and compute the band dispersion within the full mBZ we developed an effective continuum model as a combination of both approaches in [P2]. In the following, we introduce, step by step, the constituents of this phenomenological model based on the example of an H-type MoSe₂/WS₂ heterostructure.

Starting with the bare MoSe₂ X exciton state, we restrict ourselves to the low-energy physics of the system and assume a parabolic exciton dispersion, $E(\mathbf{k}) = E_0 + \hbar^2 |\mathbf{k}|^2 / (2M_X)$, inside the zero order mBZ. Here, \mathbf{k} denotes the center-of-mass wave vector of the X excitons measured from γ , M_X their effective mass, and E_0 the exciton bandgap without any other constraints. The resulting energy dispersion of the conduction band in the zero order mBZ is plotted in Figure 4.3a along the k -space trajectory indicated by dashed arrows in Figure 4.2c ($\kappa - \kappa' - \gamma - \kappa'$). Next, we additionally consider the six first order X exciton bands, which are represented by the red dots in Figure 4.2b and the corresponding folded mBZ is shown in Figure 4.3b. To define the general moiré Hamiltonian, we introduce the moiré potential [13,

146, 147] for X excitons:

$$V(\mathbf{r}) = \sum_{j=1}^6 V_j \exp(i\mathbf{b}_j \mathbf{r}) \quad (4.2)$$

These are the lowest-order harmonic expansions of the moiré potential which, due to the 120° rotational symmetry, present the usual symmetry relations $V_1 = V_3 = V_5 \equiv V$ and $V_2 = V_4 = V_6 \equiv V^*$. The parabolic dispersion, $E(\mathbf{k}) = E_X + \hbar^2 |\mathbf{k}|^2 / (2M_X)$, has a renormalized bandgap E_X obtained by averaging over the moiré supercell. The first order moiré modulated X exciton bands follow from

$$\langle \mathbf{k} + \mathbf{g}' | H_X | \mathbf{k} + \mathbf{g} \rangle_X = \delta_{\mathbf{g}, \mathbf{g}'} E(\mathbf{k} + \mathbf{g}) + \sum_{j=1}^6 V_j \delta_{\mathbf{g}-\mathbf{g}', \mathbf{b}_j}, \quad (4.3)$$

as plotted in Figure 4.3c. Until now, we have neglected the presence of WS₂ conduction bands and the corresponding IX exciton transitions. In analogy to Eq. (4.2) we introduce the moiré potential [13, 146, 147] for IX excitons:

$$W(\mathbf{r}) = \sum_{j=1}^6 W_j \exp(i\mathbf{b}_j \mathbf{r}) \quad (4.4)$$

The corresponding parabolic dispersion $\mathcal{E}(\mathbf{k}') = E_{IX} + \hbar^2 |\mathbf{k}'|^2 / (2M_{IX})$, with the center-of-mass wave vector \mathbf{k}' of IX excitons measured from κ , their effective masses M_{IX} and the bandgap E_{IX} averaged over the moiré supercell, results in:

$$\langle \mathbf{k}' + \mathbf{g}' | H_{IX} | \mathbf{k}' + \mathbf{g} \rangle_{IX} = \delta_{\mathbf{g}, \mathbf{g}'} \mathcal{E}(\mathbf{k}' + \mathbf{g}) + \sum_{j=1}^6 W_j \delta_{\mathbf{g}-\mathbf{g}', \mathbf{b}_j}. \quad (4.5)$$

Here, we take into account the first 6 IX exciton transitions specified by the blue dots in Figure 4.2b. We obtain satisfactory fits for the observed data by assuming a vanishing non-resonant part of the interlayer potential, $W_{1...6} = 0$ resulting in the mBZ in Figure 4.3d including the first 7 X exciton bands (red lines) and 6 IX exciton bands (blue lines). The minima of X and IX bands are separated by the effective conduction band offset Δ_{CB} .

Notably, V and W do not include resonant interaction terms between X and IX excitons yet, which we introduce explicitly [15] by defining the Hamiltonian as:

$$H = \begin{pmatrix} H_X & T \\ T^* & H_{IX} \end{pmatrix} \quad (4.6)$$

where the tunneling is described by interlayer hopping elements

$$\langle IX, \mathbf{k}' + \mathbf{g}' | T | X, \mathbf{k} + \mathbf{g} \rangle = \sum_{\eta=0}^2 t \delta_{\mathbf{k}+\mathbf{g}-\mathbf{k}'-\mathbf{g}', C_3^\eta \Delta \mathbf{K}} \quad (4.7)$$

with the hopping parameter t . We follow the approximation introduced in Refs. [14, 15] and assume the same term t in all mBZs, mediating the hybridization of MoSe₂ excitons X with the closest three IX states in the reciprocal space denoted by the violet arrows in Figure 4.2b. Again restricting the number of bands to the first seven X-bands and six IX-bands we describe the system with the 13-band Hamiltonian:

$$H(\mathbf{k}) = \begin{pmatrix} E_0 & V & V^* & V & V^* & V & V^* & t & t & t & 0 & 0 & 0 \\ V^* & E_1 & V & 0 & 0 & 0 & V & 0 & 0 & t & 0 & t & 0 \\ V & V^* & E_2 & V^* & 0 & 0 & 0 & t & 0 & 0 & 0 & t & 0 \\ V^* & 0 & V & E_3 & V & 0 & 0 & t & 0 & 0 & 0 & 0 & t \\ V & 0 & 0 & V^* & E_4 & V^* & 0 & 0 & t & 0 & 0 & 0 & t \\ V^* & 0 & 0 & 0 & V & E_5 & V & 0 & t & 0 & t & 0 & 0 \\ V & V^* & 0 & 0 & 0 & V^* & E_6 & 0 & 0 & t & t & 0 & 0 \\ t^* & 0 & t^* & t^* & 0 & 0 & 0 & \mathcal{E}_0 & 0 & 0 & 0 & 0 & 0 \\ t^* & 0 & 0 & 0 & t^* & t^* & 0 & 0 & \mathcal{E}_1 & 0 & 0 & 0 & 0 \\ t^* & t^* & 0 & 0 & 0 & 0 & t^* & 0 & 0 & \mathcal{E}_2 & 0 & 0 & 0 \\ 0 & 0 & 0 & 0 & 0 & t^* & t^* & 0 & 0 & 0 & \mathcal{E}_3 & 0 & 0 \\ 0 & t^* & t^* & 0 & 0 & 0 & 0 & 0 & 0 & 0 & 0 & \mathcal{E}_4 & 0 \\ 0 & 0 & 0 & t^* & t^* & 0 & 0 & 0 & 0 & 0 & 0 & 0 & \mathcal{E}_5 \end{pmatrix}. \quad (4.8)$$

The first seven diagonal terms correspond to the X bands marked by the red dots in Figure 4.2b, with

$$E_0(\mathbf{k}) = E(\mathbf{k}), \quad E_j(\mathbf{k}) = E(\mathbf{k} - \mathbf{b}_j) \quad (4.9)$$

for $j = 1, 2, \dots, 6$; the last six diagonal terms relate to IXs marked by the blue dots in Figure 4.2b:

$$\mathcal{E}_\eta(\mathbf{k}) = \mathcal{E}(\mathbf{k} - C_3^\eta \Delta \mathbf{K}), \quad \mathcal{E}_\zeta(\mathbf{k}) = \mathcal{E}(\mathbf{k} + 2C_3^{\zeta-3} \Delta \mathbf{K}), \quad (4.10)$$

where $\eta = 0, 1, 2$ and $\zeta = 3, 4, 5$. The finite interlayer hopping t results in avoided crossing of X- and IX-bands in Figure 4.3e, where the hybrid X-IX nature of the moiré excitons is shown in green color.

After diagonalizing the Hamiltonian in Eq. (4.8), we obtain χ'' by projecting the eigenstates onto the fundamental A-exciton state at the γ point as:

$$\chi''(\omega) \approx \chi_0'' \sum_{m=1}^{13} |\langle m|A\rangle|^2 \frac{\gamma_0^2}{\hbar^2(\omega - \omega_m)^2 + \gamma_0^2}, \quad (4.11)$$

where $|A\rangle$ is the MoSe₂ intralayer exciton state corresponding to the first row and column in Eq. (4.8), χ_0'' is its dielectric susceptibility [13], $|m\rangle$ and $\hbar\omega_m$ are the eigenstates and eigenvalues of the m -th exciton band obtained from the diagonalized Hamiltonian in Eq. (4.8), and γ_0 is a peak broadening parameter. Notably, this implies that the oscillator strength of the $|A\rangle$ exciton is redistributed among the set of the moiré excitons $|m\rangle$.

In Section 4.3 we demonstrate the validity of this phenomenological model by reproducing the multiplicity and relative oscillator strengths of the experimentally observed moiré excitons for fixed material parameters $a_{\text{MoSe}_2} = 0.3288$ nm, $a_{\text{WS}_2} = 0.3154$ nm, $M_X = 1.44m_0$, and $M_{\text{IX}} = 0.86m_0$ [145, 149] with electron mass m_0 , and using the following free fitting parameters: E_X and E_{IX} capture the band offset of the heterostructure. The twist angle θ , the X exciton moiré potential with $|V|$ and $\arg(V)$ and the hopping parameter t fit the layer character of moiré excitons as well as their energy separations and oscillator strengths. Finally γ_0 determines the moiré exciton linewidth.

4.1.2. Capacitor model

An important quantity closely tied to the moiré lattice constant $a_{\text{moiré}}$ is the superlattice density n_0 , which is defined as $n_0 = 1/A_{\text{moiré}}$, where $A_{\text{moiré}} = \sqrt{3}a_{\text{moiré}}^2/4$ represents the area of the moiré unit cell. The existence of a long-range moiré potential significantly influences the optical behavior of moiré excitons at specific electron and hole filling fractions per moiré unit cell. To determine the quantity of elementary charges per moiré site within our heterostructures under specific gate voltage conditions, we conducted electrostatic simulations of the dual-gate devices. For this purpose, we employed a capacitor model as introduced in the subsequent discussion, following the methodology outlined in Refs. [150–153]. Section 4.4 presents the applicability of the model to our experimental findings in dual-gate $\text{MoSe}_2/\text{WS}_2$ heterostructures [P3].

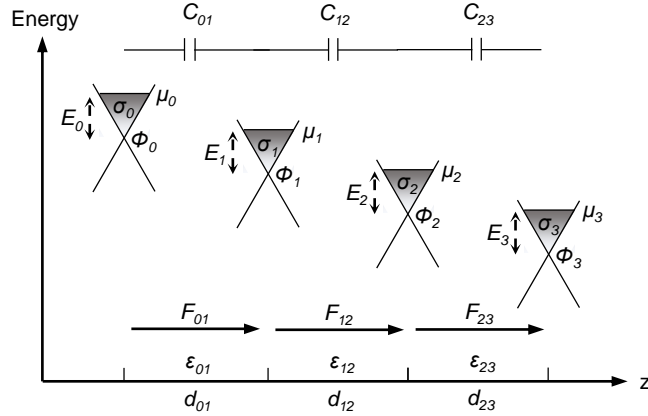


Figure 4.4.: **Capacitor model schematics and notation.** Energy diagram of a generalized heterostructure consisting of four layers with respective electrochemical and electrostatic potentials μ_i and Φ_i , the chemical potential $E_i = \mu_i - \Phi_i$ ($i = 0, 1, 2, 3$) and corresponding electric fields $F_{ij} = -(\Phi_j - \Phi_i)/ed_{ij}$. Charge densities of the layers are denoted as σ_i . Dielectrics with ϵ_{ii+1} separate the capacitor layers with distance d_{ii+1} leading to the geometric capacitances C_{ii+1} .

Figure 4.4 introduces the relevant physical parameters for the capacitor model simulation

of an arbitrary four-layer heterostructure. We examine the electrochemical potentials μ_i and electrostatic potentials Φ_i present in the capacitance circuit that describes the heterostack. The chemical potential, which we refer to as Fermi energy in the following, within a layer follows as

$$E_i = \mu_i - \Phi_i \quad (4.12)$$

and describes the energy cost to introduce a charge carrier inside the respective layer. Assuming we want to derive σ_1 , the charge density in layer 1, as a function of the Fermi energy and the voltages V_i applied to the layers of the capacitor, we compare the electrochemical and electrostatic potentials of adjacent capacitor plates. The electrochemical potential results from applying a gate Voltage between the two layers:

$$\mu_1 = -eV_{01}, \quad (4.13)$$

where we set reference potential $\mu_0 = 0$. A difference of the electrostatic potential is equivalent to an electric field F_{ij} pointing from one layer to the other:

$$\Phi_1 - \Phi_0 = -ed_{01}F_{01} = -e\frac{\epsilon_0\epsilon_{01}}{C_{01}}F_{01} \quad (4.14)$$

Here, we used the definition of the geometric capacitance $C_i = \epsilon_0\epsilon_i/d_i$ with vacuum permittivity ϵ_0 and permittivity of the respective dielectric spacer layer ϵ_i . Employing (4.14) the electron density inside layer 1 in Figure 4.4 derives from the Gauss law of Maxwell's equations as

$$\begin{aligned} \sigma_1 &= \epsilon_0\epsilon_{01}F_{01} - \epsilon_0\epsilon_{12}F_{12} = \\ &= C_{01}\frac{\Phi_0 - \Phi_1}{e} - C_{12}\frac{\Phi_1 - \Phi_2}{e} = \\ &= C_{01}\frac{\Phi_0}{e} - (C_{01} + C_{12})\frac{\Phi_1}{e} + C_{12}\frac{\Phi_2}{e} = \\ &= -C_{01}\left(V_0 + \frac{E_0}{e}\right) + (C_{01} + C_{12})\left(V_1 + \frac{E_1}{e}\right) - C_{12}\left(V_2 + \frac{E_2}{e}\right). \end{aligned} \quad (4.15)$$

Here, the last step involves expressing the electrostatic potential Φ_i in terms of the applied voltage V_i and the Fermi energy E_i , utilizing equations (4.12) and (4.13). All charge densities σ_i ($i = 0, 1, 2, 3$) of the system can be derived analogously to σ_1 and written in matrix form as

$$\begin{pmatrix} \sigma_0 \\ \sigma_1 \\ \sigma_2 \\ \sigma_3 \end{pmatrix} = \begin{pmatrix} C_{01} & -C_{01} & 0 & 0 \\ -C_{01} & C_{01} + C_{12} & -C_{12} & 0 \\ 0 & -C_{12} & C_{12} + C_{23} & -C_{22} \\ 0 & 0 & -C_{23} & C_{23} \end{pmatrix} \begin{pmatrix} V_0 + E_0/e \\ V_1 + E_1/e \\ V_2 + E_2/e \\ V_3 + E_3/e \end{pmatrix}. \quad (4.16)$$

In our specific case, the top and bottom layers of the MoSe₂/WS₂ heterostructures consist of graphite layers, which can be assumed to have metallic character. Therefore, the density of

states (DOS) in these layers can be considered infinitely large, allowing us to set the Fermi energies as $E_0 = E_3 = 0$. The hBN separation between the top and bottom gates of the TMD bilayer defines the respective geometric capacitances, C_{01} and C_{23} , which are represented as $C_{01} = C_T = \epsilon_0 \epsilon_{\text{hBN}} / d_T$ and $C_{23} = C_B = \epsilon_0 \epsilon_{\text{hBN}} / d_B$, respectively. Here, ϵ_0 denotes the vacuum permittivity, ϵ_{hBN} the dielectric constant of hBN, and $d_{T(B)}$ the top (bottom) hBN thickness, determined individually via atomic force microscopy before the assembly of the heterostacks. By adjusting the gate voltages $V_0 = V_{TG}$ and $V_3 = V_{BG}$, we control the charge density inside the top and bottom TMD layers, denoted as $\sigma_1 = \sigma_T$ and $\sigma_2 = \sigma_B$, which are functions of the respective Fermi energies E_T and E_B . As we are primarily interested in the respective electron densities $n_{T/B} = -\sigma_{T/B}/e$, we can express the relevant electrostatic equations as

$$e \begin{pmatrix} n_T \\ n_B \end{pmatrix} = \begin{pmatrix} C_T & -C_T - C_S & C_S & 0 \\ 0 & C_S & -C_B - C_S & C_B \end{pmatrix} \begin{pmatrix} V_{TG} \\ E_T/e \\ E_B/e \\ V_{BG} \end{pmatrix}, \quad (4.17)$$

where $C_S = C_{12}$ denotes the geometric capacitance formed by the two TMD layers, which are set to ground ($V_1 = V_2 = 0$). In this work, we used $\epsilon_{\text{hBN}} = 4$, $\epsilon_{\text{TMD}} = 8$ and interlayer distance $d_S = 0.6$ nm.

The electron density in a monolayer is given by $n_i(E) = \int_0^E \text{DOS}_i(E') dE'$, where $\text{DOS}_i(E')$ represents the density of states of layer i and E is the Fermi energy of that layer. We note, that the electron density can take a non-linear form as long as it is monotonically non-decreasing. For a given DOS_i , we numerically solve Eqs. (4.17) to determine the Fermi energies (E_T, E_B), and subsequently evaluate $n_{T(B)}$ at the computed energies. Figure 4.5 illustrates the results of the electrostatic simulations for a heterostructure under two different sets of simulation parameters. The geometric capacitances are identical for both cases, assuming symmetric hBN thickness $d_T = d_B = 55$ nm (cp. geometry of device D2 in Figure 4.6).

In the first case (Figure 4.5a and b), we highlight the effect of a finite conduction band offset, $\Delta_{CB} = \Phi_T - \Phi_B = 30$ meV, on the simulated charge distribution which is significant because it influences the spatial distribution of electrons at the interface between the top and bottom layer. We account for Δ_{CB} by introducing a finite onset in the electron density of states (DOS) of the bottom layer, represented as $n_B(\Delta_{CB}) = \int_0^{\Delta_{CB}} \text{DOS}_B(E') dE' = 0$. Apart from this adjustment, we assume a constant DOS in both layers, as expected for a 2D electron gas and depicted in Figure 4.5a, resulting in a linear evolution of electron densities with respect to the Fermi energy. The left and right panels of Figure 4.5b illustrate the respective electron densities n_T and n_B for simulated Fermi energies E_T and E_B , corresponding to a given set of gate voltages (V_{TG}, V_{BG}), plotted in the characteristic basis (V_μ, F). Here, $V_\mu = (V_{TG} + V_{BG})/2$ represents the doping potential, and $F = (V_{BG} - V_{TG})/l$ the electric field, with $l = 110$ nm being the total thickness of the hBN layers between the top and bottom

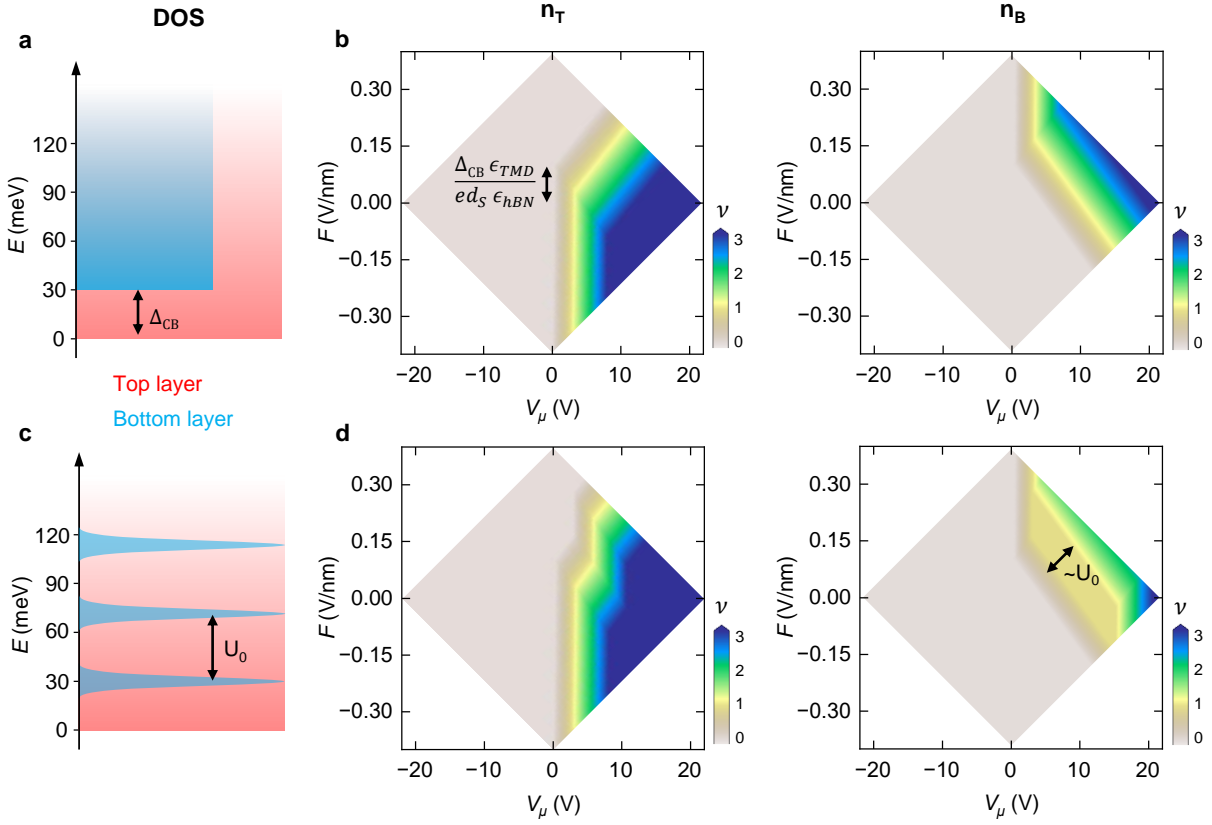


Figure 4.5.: **Capacitor model simulation for differing DOS.** **a**, Schematics of constant DOS in top and bottom layer of an exemplary bilayer heterostructure with conduction band offset Δ_{CB} and graphite top and bottom gates. **b**, Electron densities in top and bottom layer by numerically solving Eqs. (4.17) for the DOS shown in **a** for a given set of (V_{TG}, V_{BG}) . **c**, Schematics of a constant DOS in the top layer and discretised DOS in the bottom layer resulting in the simulated electron densities shown in **d**. The gaps U_0 in the bottom layer DOS lead to extended areas of constant n_B in the right panel.

graphite layers. Note, that the electron densities are shown as $\nu = n_{T/B}/n_0$ in units of $n_0 = 2.0 \times 10^{12} \text{ cm}^{-2}$. Comparing both charging diagrams for small values of V_μ at $F = 0$, we observe a linear increase in electron density n_T in the top layer, while the bottom layer remains at $n_T = 0$. However, compensating for the difference in electrostatic potential between the two layers by applying an electric field $F > (\Delta_{CB}\epsilon_{TMD})/(ed_S\epsilon_{hBN})$ leads to the reversed situation, where electrons enter the bottom layer first for small values of V_μ , while the top layer remains charge free.

In the second case (Figure 4.5c and d), we demonstrate the effect of a non-constant density of states (DOS) in one of the layers, as depicted in Figure 4.5c. The DOS in the top layer remains the same as in Figure 4.5a, with a conduction band offset $\Delta_{CB} = 30 \text{ meV}$. However, in the bottom layer, carrier doping occurs in discrete steps of n_0 , each step corresponding to

a peak in the DOS. The gaps U_0 between these peaks represent the energetic cost to induce another electron into the bottom layer, which is already filled with a multiple of n_0 electrons. In a TMD heterobilayer, these steps in electron density can be attributed to on-site Coulomb repulsion arising from the strong confinement of electrons in moiré potential pockets. We discuss this phenomenon further based on our experimental results in Section 4.4. Figure 4.5d presents the electron densities n_T and n_B for simulated Fermi energies E_T and E_B as functions of V_μ and F . The discretized density of states (DOS) for the bottom layer results in a stepwise evolution of the charging onset in the top layer, as illustrated in the left panel of Figure 4.5d. This effect is particularly evident along the line $\nu = n_T/n_0 = 1$, which is highlighted in yellow. In the bottom layer, n_B exhibits extended areas of constant charge in the (V_μ, F) diagram, as a result of the gap U_0 .

4.1.3. Coulomb-interaction of moiré excitons and ordered electrons

Using our phenomenological model, introduced in Section 4.1.1, it is possible to obtain information about the spatial distribution of the different moiré exciton wavefunctions. As we describe in Section 4.3, higher order moiré excitons in $\text{MoSe}_2/\text{WS}_2$ preferably localize at different sites of the moiré unit cell as compared to electrons or holes under charge doping. To calculate the interaction energy (binding energy) of moiré excitons with electrons ordered on the moiré lattice, we assume that the exciton is confined in one moiré cell and interacts with the surrounding ordered electrons as illustrated in Figure 4.15b. We further assume that the main contribution to the binding energy stems from charge-induced modification of the electron-hole relative motion $\boldsymbol{\rho} \equiv (\rho, \theta) = \mathbf{r}_e - \mathbf{r}_h$, where $\mathbf{r}_{e(h)}$ are the coordinates of the electron and hole forming the exciton. The corresponding Schrödinger equation takes the form:

$$-\frac{\hbar^2}{2\mu}\Delta\varphi(\boldsymbol{\rho}) + [V_{\text{RK}}(\rho) + V(\boldsymbol{\rho})]\varphi(\boldsymbol{\rho}) = E\varphi(\boldsymbol{\rho}),$$

where E is the exciton energy, $\mu = m_e m_h / (m_e + m_h)$ is the reduced exciton mass, m_e and m_h are the electron and hole effective masses, and the Rytova–Keldysh potential [56, 154] of the electron-hole attraction is given by:

$$V_{\text{RK}}(\rho) = -\frac{\pi e^2}{2\varepsilon\rho_0} \left[H_0\left(\frac{\rho}{\rho_0}\right) - Y_0\left(\frac{\rho}{\rho_0}\right) \right].$$

Here, e is the electron charge, ρ_0 is the screening length, ε is the effective dielectric constant, and $H_0(x)$ and $Y_0(x)$ are the Struve and Neumann functions.

The interaction of the exciton with the charge lattice is described by the Coulomb sum:

$$V(\boldsymbol{\rho}) = \pm \frac{e^2}{\varepsilon} \sum_{\mathbf{n}} \left[\frac{1}{|\beta_e \boldsymbol{\rho} + \mathbf{n}|} - \frac{1}{|\beta_h \boldsymbol{\rho} - \mathbf{n}|} \right],$$

where the plus and minus signs correspond to positive and negative elementary charges, $\beta_e = m_e/(m_e + m_h)$, $\beta_h = m_h/(m_e + m_h)$, and \mathbf{n} are the coordinates of electrons/holes on the lattice. The two terms in the brackets determine the interaction of the charge lattice with the hole and the electron that constitute the exciton.

To determine the binding energy of the state, we calculate the free exciton energy E_X to obtain:

$$E_b = E_X - E.$$

To calculate E_X , we set $V(\boldsymbol{\rho}) = 0$, and use in the calculations of both E_X and E the set of 2D hydrogen-like wave functions with the Bohr radius as variational parameter [57, 64, 155] and the basis of six functions [156] with quantum numbers $(n, l) = (1, 0), (2, 0), (2, \pm 1), (4, \pm 3)$ to take into account polarization effects on the exciton relative motion. Due to the lower rotational symmetry of the potential $V(\boldsymbol{\rho})$, we also include hydrogen-like wave functions with angular momenta $l = \pm 1, \pm 3$. The explicit expression for the trial function is:

$$\varphi(\rho, \theta) = e^{-\alpha\rho} + \zeta\rho e^{-\beta\rho} + \eta\rho e^{-\gamma\rho} \cos\theta + \xi\rho^3 e^{-\delta\rho} \cos 3\theta.$$

We solve the minimization problem numerically for seven parameters $(\alpha, \beta, \gamma, \delta, \zeta, \eta, \xi)$ using MATLAB R2017B and experimental material parameters of MoSe₂ monolayers [157]: $m_e = 0.84m_0$, $m_h = 0.6m_0$, $\varepsilon = 4.4$, $\rho_0 = 0.89$ nm. In Section 4.4.2, we apply this model to fit the evolution of the moiré exciton binding energy as a function of electron doping. The only fitting parameter for comparison between the experimental data and the theoretical model is the moiré superlattice constant, which in Figure 4.15a is taken to be 7.7 nm.

4.2. Heterostructure devices and characteristics

In the scope of this work we fabricated and investigated several dual-gated MoSe₂/WS₂ heterostacks as introduced in Chapter 3.3. The observed optical signatures showed up to be robust among the multiplicity of samples. Here, we focus on two selected heterostacks fabricated from CVD grown TMD monolayers with R-type (D1) and H-type (D2) alignment, respectively, to demonstrate and compare the relevant experimental signatures and present our understanding of the underlying moiré induced physical phenomena.

Figure 4.6 shows optical microscope images of D1 and D2 and their respective stacking order. The relevant elements of the heterostructures are framed with colored lines for better orientation. The triangular shape of the monolayer flakes facilitates to determine the relative twist angle θ from optical inspection with accuracy of $\pm 1^\circ$, yielding $\theta \approx 2^\circ (179^\circ)$ for D1 (D2). In both devices, the TMD layers were encapsulated in hBN with (near-)identical thickness as shown in the middle panel of Figure 4.6 and sandwiched between top and bottom few-layer graphene electrodes. The data discussed in this work were acquired in regions where the

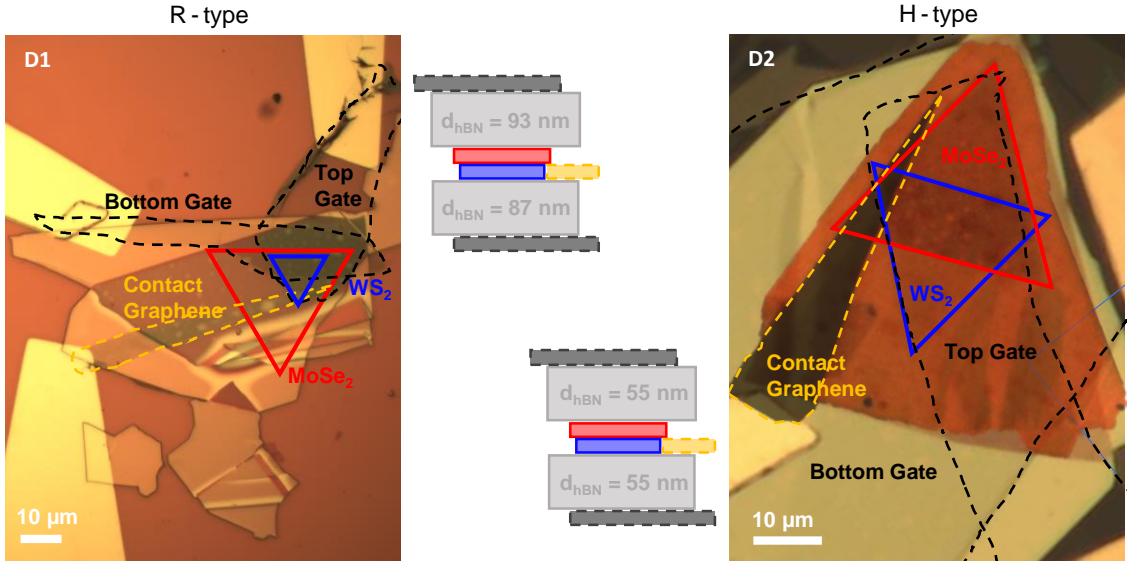


Figure 4.6.: **Device microscope optical images** of D1 (R-type) on the left and D2 (H-type) on the right. The spatial dimensions of the individual layers are highlighted by respectively colored lines. The middle panel illustrates the vertical stacking order, which is equivalent for both devices.

TMD bilayer is overlapping with both bottom and top gate to ensure symmetric doping and linear electric fields.

We first examine the cryogenic optical response of excitons in the charge-neutral regime of the two devices, where no voltages are applied to the top and bottom gates ($V_{TG} = V_{BG} = 0$), at a temperature of $T = 4$ K. The differential reflection spectra in the upper panels of Figure 4.7a and b, acquired in the MoSe₂ monolayer region of D1 and D2, respectively, feature the characteristic X exciton resonance around 1.63 eV. A Lorentzian linewidth of approximately 2 meV confirms the high optical quality of the two devices. The center panels of Figure 4.7a and b reflect the expected multiplicity of moiré excitons in twisted MoSe₂/WS₂ HBLs, which acquire the distributed oscillator strength of the MoSe₂ X exciton [17, 36, 89]. The lowest energy resonance with highest oscillator strength, denoted as M_1 , appears around 1.6 eV for both stacking configurations and is the renormalized X exciton ground state. In photoluminescence measurements (lower panels of Figure 4.7a and b), this resonance appears as a single bright peak with a Lorentzian linewidth of 5-10 meV, identifying the transition as the energetic ground state of the system with pure MoSe₂ intralayer character and efficient population relaxation from higher-energy moiré states. This observation suggests a type-I band alignment for both stacking configurations which is confirmed by studying the dual-gate response of D1 and D2 in following sections. The general band alignment in MoSe₂/WS₂ heterostacks has been a matter of continuing debate, with reported CB offset values between

-60 meV (type-II) and +100 meV (type-I) [17, 36, 89, 158–161]. As demonstrated by another H-type MoSe₂/WS₂ device in the appendix of this thesis (see Section A.1), inhomogeneity can lead to shifts in the CB offset on the order of tens of meV even within a single device. This phenomenon provides an explanation for the contradictory observations of type-I and type-II CB alignment reported in the literature. The second DR peak in Figure 4.7a and b, denoted as M₂, represents the first Umklapp peak due to the moiré potential, and the energy separation between M₁ and M₂ is determined by the relative twist angle between the two monolayers. In a polarization-resolved measurement with an applied out-of-plane magnetic field (see Section 3.2 for details), the exciton Zeeman shift of these two lowest energy resonances yields exciton Landé factors around -4 in Figure 4.7c and d, matching the well-known monolayer MoSe₂ X exciton *g*-factor [73, 162]. This observation manifests the MoSe₂ intralayer origin of M₁ and M₂.

Upon close examination of the DR spectra in the center panels of Figure 4.7a and b, we discern a higher-order moiré resonance M₃, which appears approximately 70 meV (30 meV) blue-shifted compared to M₂ in the R-type (H-type) sample. For the first case in Figure 4.7a, this peak exhibits nearly negligible oscillator strength, while its strength is significant in the latter case in Figure 4.7b. As detailed in the following section (Section 4.3), the H-type M₃ peak displays characteristics of interlayer hybridization attributed to the resonantly aligned conduction band edge of WS₂. Due to the reversed ordering of the spin-polarized MoSe₂ and WS₂ conduction bands, the energetically lowest spin-bright interlayer transition in the R-type configuration blue shifts compared to the H-type configuration by the spin orbit splitting Δ_{SO}^W in the conduction band of WS₂. Furthermore, the conduction band offset for R-type device D1 turns out to be significantly larger than that for H-type D2 (see Section 4.4.1), elucidating the absence of interlayer hybridization in the corresponding M₃ resonance.

4.3. Field-induced hybridization

In early studies on MoSe₂/WS₂ devices [15, 17, 161], the multiplicity of low energy moiré peaks has been interpreted as a result of hybridization of intra- and interlayer excitons and successfully modeled via interlayer tunneling [14, 15]. However, recent experiments on the exciton dispersion in perpendicular electric fields observed vanishing out-of-plane dipoles for these resonances, suggesting that they are of pure intralayer character [36, 89]. In the following, we apply our phenomenological model, presented in Section 4.1.1, to unravel the roles of intra- and interlayer excitons and their interactions in the observed reflection spectra.

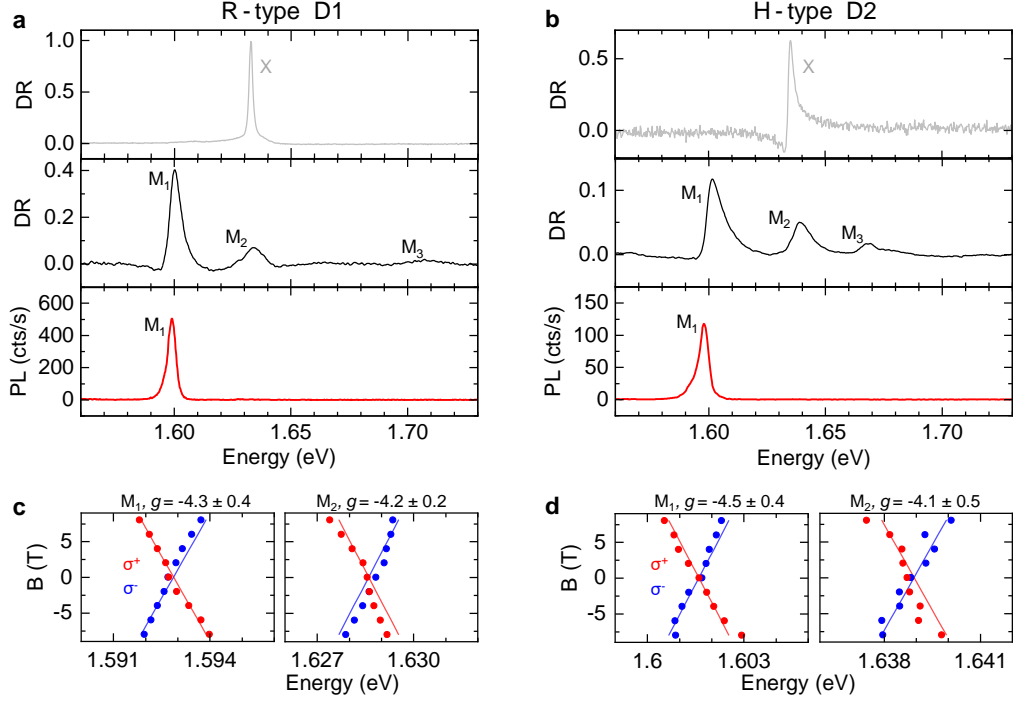


Figure 4.7.: **Intralayer character of neutral moiré excitons.** **a** and **b**, Upper and center panels show DR spectra of the bare MoSe_2 monolayer and $\text{MoSe}_2/\text{WS}_2$ heterobilayer, the lower panels show PL spectra in the charge neutral regime acquired on D1 and D2, respectively. X denotes the monolayer X exciton. M_1 , M_2 and M_3 denote the moiré exciton peaks in energetically ascending order. **c** and **d** Zeeman-shifted moiré exciton energies in σ^+ (red dots) and σ^- polarization (blue dots) for different magnetic fields for M_1 (M_2) in the left (right) panels. The corresponding exciton Landé factors g_1 (g_2) are determined from simultaneous linear fits to the peak energy dispersion as function of the magnetic field in both polarizations, represented by solid lines of corresponding color.

4.3.1. Modeling of moiré excitons exposed to out-of-plane electric fields

Figure 4.8a and b show the evolution of the DR spectra while tuning the out-of-plane electric field via $\Delta V_{\text{TB}} = V_{\text{BG}} - V_{\text{TG}}$ for R- and H-type heterostacks, respectively. As expected from their intralayer character (derived in the previous Section 4.2) M_1 and M_2 exhibit vanishingly small linear slopes of the first-order Stark effect, for both R- and H-type devices. This implies that these peaks can be captured in terms of the non-resonant moiré potential V , whereas interlayer tunneling plays a negligible role. The same holds for the peak M_3 and M_4 in the R-type device. For the H-type configuration, on the contrary, M_3 exhibits two branches with finite dispersion indicative of an anticrossing of X and IX states with weak coupling.

In the following, we use our model introduced in Section 4.1.1 to describe and understand

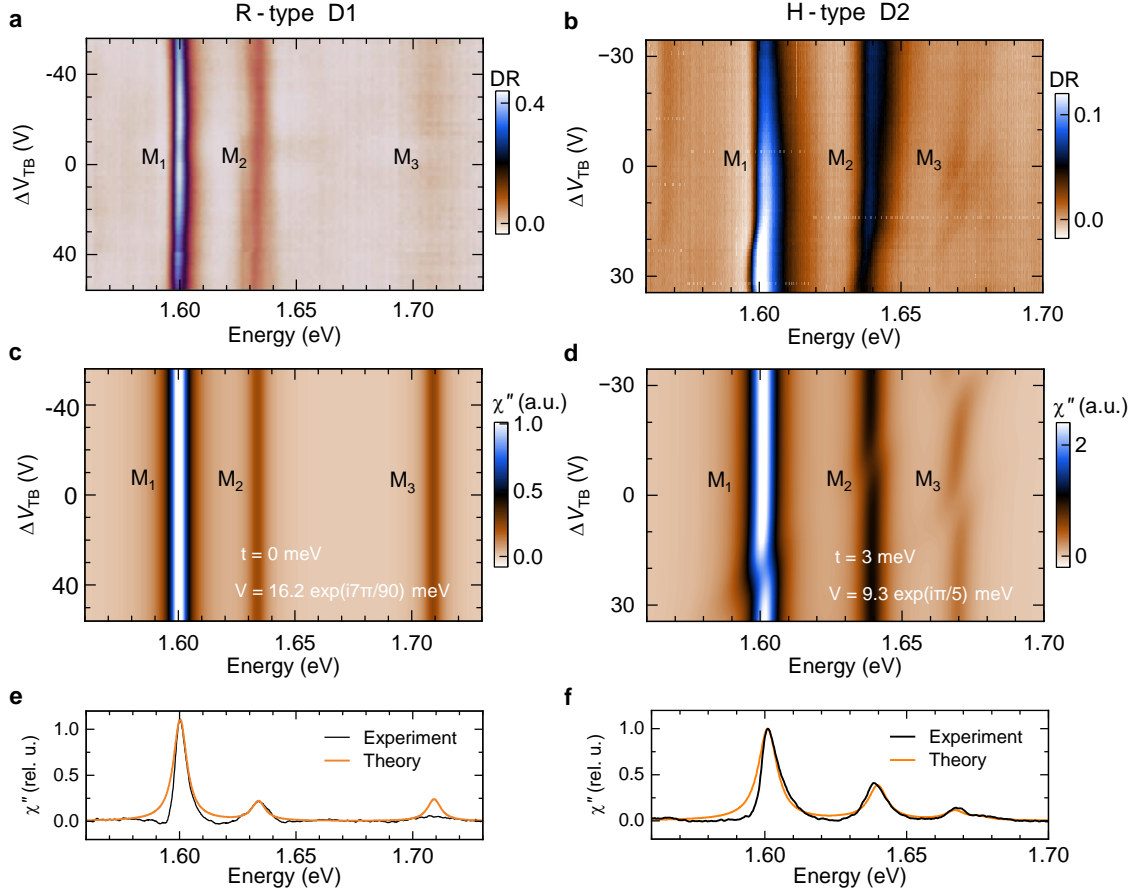


Figure 4.8.: **Moiré excitons exposed to out-of-plane electric fields in experiment and theory.** **a** and **b**, Evolution of HBL DR spectra with an applied electric field ΔV_{TB} in the charge neutral regime for R-type and H-type device, respectively. While there is no field dispersion of the moiré excitons in the R-type case, M_3 shows anti-crossing behavior in the H-type case as a sign of hybridization between intra- and interlayer excitons. **c** and **d**, Corresponding simulation of $\chi''(\omega)$ capturing the strong intralayer character of the three lowest-energy moiré exciton peaks as well as their relative oscillator strengths. Inhomogeneous broadening was included by smoothing $\chi''(\omega)$ over a 5 meV broad Gaussian kernel in the fit parameter E_{IX} for the H-type case. **e** and **f**, Comparison of experimental data and theory at $\Delta V_{\text{TB}} = 0$

the nature and interaction of moiré intra- and interlayer excitons. Here, we use the amplitude $|V|$ and phase $\arg(V)$ of the intralayer moiré potential, the hopping parameter t and the intra-/interlayer exciton bandgap $E_{\text{X}}/E_{\text{IX}}$ as fitting parameters, while assuming a vanishing interlayer moiré potential $|W| = 0$.

In the case of D1 with R-type configuration, we describe the absence of interlayer exciton response with a vanishingly small hopping parameter $t = 0$. For a twist angle of $\theta = 2^\circ$

the energy separation of intralayer moiré excitons and their relative oscillator strength is best reproduced with a moiré potential $V = 16.2\exp(i7\pi/90)$ meV with $|V| = 16.2$ and $\arg(V) = 7\pi/90$ and $E_X = 1622$ meV as shown in Figure 4.8c. The anti-crossing of the M_3 field dispersion in the H-type case with twist angle $\theta = 179^\circ$ in Figure 4.8c necessitates a non-vanishing hopping parameter t in the model. Also, on closer inspection, M_1 and M_2 show minor narrowing with a small red shift at high $\Delta V_{\text{TB}} \geq 18\text{V}$. This behavior indicates the crossing of IX resonances which appear dark due to vanishing spatial overlap with M_1 and M_2 but induce a crossover from type-I to type-II band alignment. We computed the evolution of $\chi''(\omega)$ as a function of ΔV_{TB} using Eq. (4.11) by shifting the IX resonance energies in Eq. (4.10) as

$$\mathcal{E}(\Delta V_{\text{TB}}) = \mathcal{E} - \frac{ed\Delta V_{\text{TB}}}{\epsilon l}, \quad (4.18)$$

where e is the electron charge, $d = 0.6$ nm the distance between the two TMD layers, $l = 110$ nm the distance between the gates, and $\epsilon \approx 4$ [153]. The modeled susceptibility is plotted in Figure 4.8d for $t = 3$ meV, $V = 9.3\exp(i\pi/5)$ meV, $E_X = 1617$ meV, $E_{\text{IX}} = 1614$ meV and $\gamma_0 = 4$ meV. It captures the main features of the experimental data such as the relative strengths of the peaks, the strong intralayer character of M_1 and M_2 , the anticrossing of the M_3 doublet and the IX perturbation of M_1 at high positive fields. At the same time, it predicts a weak coupling of M_2 with an IX state at $\Delta V_{\text{TB}} \approx -10$ V which can not be observed in white-light DR. We emphasize that although $E_{\text{IX}} < E_X$, the fitting implies a type I heterostructure due to the relation $E_{\text{IX}} > \min[E_X + V(\mathbf{r})] \approx 1566$ meV, with a CB offset in the order of 50 meV.

To optimize the comparison and fitting of the moiré exciton peaks with $\chi''(\omega)$ in Eq. (4.11) we applied a phase correction to the corresponding DR spectra as introduced in Section 3.2.1. Figure 4.8e and f show the phase-corrected experimental data and results of the theoretical model using the respective fitting parameters from above at the zero-field line ($\Delta V_{\text{TB}} = 0$) for the R-type and H-type case, respectively.

4.3.2. AC modulation spectroscopy for hybridization studies

In the following, we studied in more detail the effect of interlayer hybridization focusing on the H-type device. To improve the sensitivity to interlayer states we repeated the field-dependent measurement with the modulation-spectroscopy technique using a narrow-band tunable laser to measure differential reflectance DR' as introduced in Chapter 3.2.3. The measurement is performed by modulating one of the gates of the device by a small AC-voltage (V_{AC}) and using a lock-in amplifier to detect the reflected signal at the same frequency, R_{ac} , simultaneously with the DC part of the photosignal, R_{DC} . In Fig. 4.9a we show $\text{DR}' = R_{\text{ac}}/R_{\text{DC}}$ with signatures of both intra- and interlayer states: The interlayer character of the M_3 doublet becomes much more prominent compared to the white-light DR data, the red shifts of M_1 and M_2 at high ΔV_{TB} confirm the admixing of IX excitons, and

the contrast change of M_2 at $\Delta V_{\text{TB}} \approx -20$ V suggests the coupling to a dark IX state visualized with this technique. Section 4.3.3 explains the difference of dark and bright IX states by the respective overlap of the different intra- and interlayer moiré exciton wave functions.

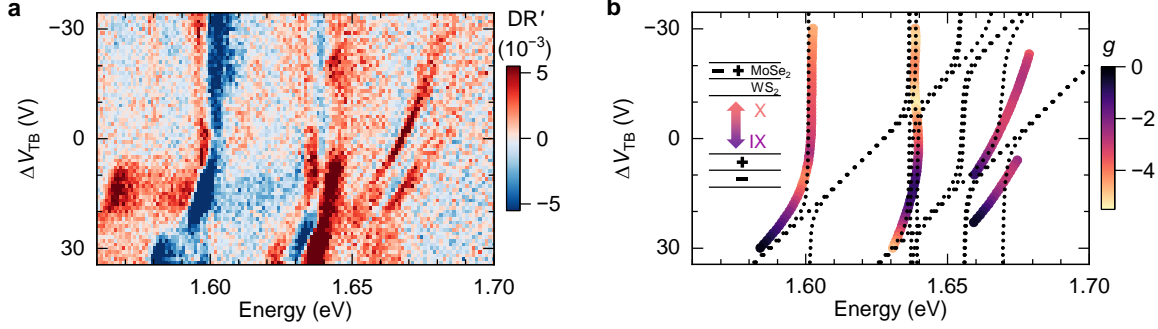


Figure 4.9.: **Field-induced hybridization of moiré excitons in H-type MoSe₂/WS₂.** **a**, Narrow-band modulation spectroscopy signal of MoSe₂/WS₂ as a function of the applied out-of-plane electric field. **b**, Dispersion of the eigenvalues of the Hamiltonian in Eq. (4.8) as a function of the electric field and experimental exciton g -factors of the respective resonances color-coded from -5.5 (yellow) to 0 (black) .

In Fig. 4.9b we show the dispersion of the peaks extracted from Fig. 4.9a alongside the evolution of the eigenvalues of the Hamiltonian in (4.8) as a function of ΔV_{TB} . In contrast to Fig. 4.8d, where the oscillator strengths of the three bright excitons are visible, here the dotted lines indicate the eigenvalues corresponding to all 13 moiré exciton bands irrespective of their oscillator strength. The experimental dispersion of both M_1 and M_2 in Fig. 4.9a is well reproduced, and the strong anticrossing of the M_3 doublet is qualitatively captured within our theoretical model. We note that although the magnitude of the X-IX coupling changes between the M_2 and M_3 resonances, they are both controlled by the same parameter t , and introducing different hopping parameters for different mBZs [89] would allow to improve on the quantitative agreement with the data. Finally, we find that in the neutral regime the first IX state – which is momentum-dark and can not be observed in Fig. 4.8b – lies 30 meV above the ground state M_1 , indicating type I character for the studied MoSe₂/WS₂ heterostack.

In addition to the electric-field dependence we studied the Zeeman effect of moiré excitons by repeating the modulation-spectroscopy measurements for out-of-plane magnetic fields in the range of $B = \pm 6$ T. As described in Chapter 3.2.1 the measurements were performed under linearly polarized excitation with detection in both σ^+ and σ^- polarization, from which we determined the valley Zeeman energy splittings and the corresponding g -factors. The colors of the data in Fig. 4.9b show the g -factors of the respective peaks for different electric fields, ranging from $g = -5.5$ (yellow) through -2 (purple) to 0 (black). We observe that for electric fields where M_1 and M_2 follow vertical lines of zero Stark effect due to nearly-pure MoSe₂ character, the corresponding g -factors are close to the fundamen-

tal MoSe_2 A-exciton with $g_A \approx -4$. Near the IX-X anticrossings, on the contrary, all three states exhibit sizable changes in the g -factors reaching values up to 0. The effect is most pronounced for the dispersive branch of M_1 at high positive electric fields as well as the M_3 doublet, which we attribute to field-induced hybridization with interlayer states. The values of the exciton g -factors depend on both the degree of layer hybridization and the exciton momentum [163, 164], making a full quantitative description of this behavior out of scope for this work. The overall trend, however, is consistent with the intralayer character of the peaks M_1 and M_2 at negative electric fields, and with interlayer admixing near anticrossings captured by our theoretical model.

4.3.3. Real space distribution of moiré exciton states

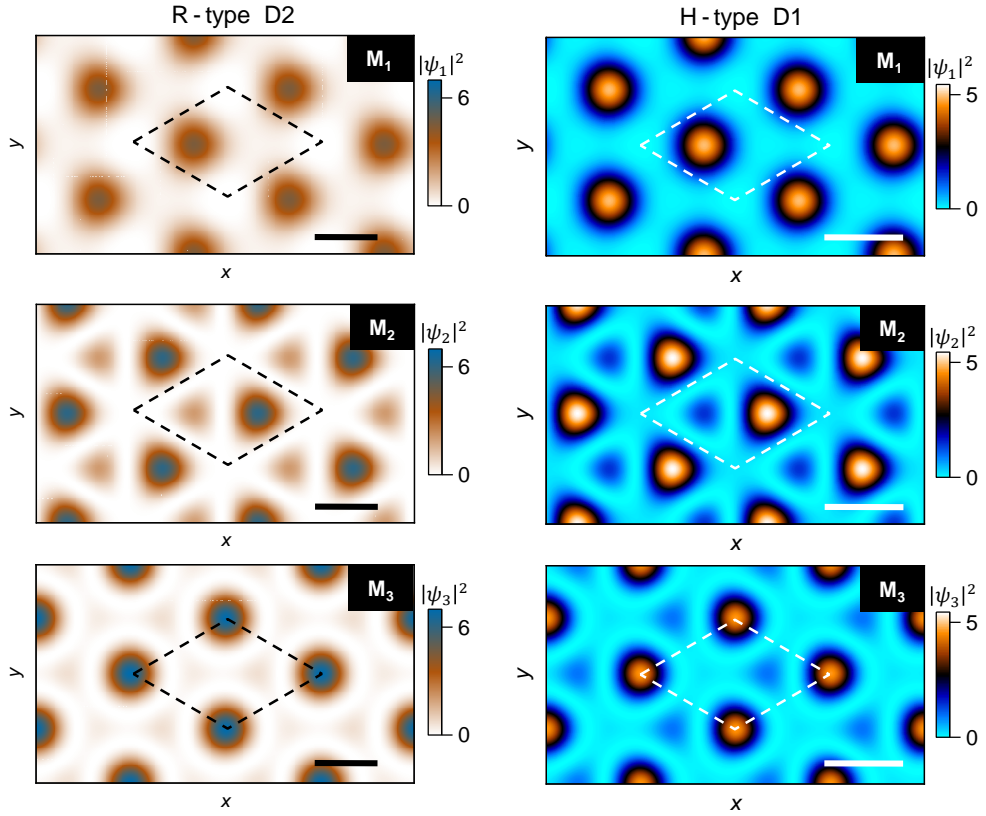


Figure 4.10.: **Spatial distribution of the exciton wavefunction** for the three lowest-energy bright states M_1 , M_2 and M_3 in case of R-type (left) and H-type (right) stacking. All scale-bars are 5 nm. All three states are located in different positions of the moiré supercell delimited by the dashed lines with moiré lattice constant $a_{\text{moiré}} \approx 6$ nm (7 nm) for the R-type (H-type) case with respective twist angle $\theta = 2^\circ$ (179°).

In order to deepen the understanding of moiré excitons and their behavior, it is instructive

to visualize their spatial distribution within the moiré unit cell. First, we denote the original basis of the Hamiltonian (4.8) by $|j\rangle$ with $j = 0, \dots, 12$, s.t. it holds e.g. $\langle j|H|j\rangle = E_j$ for $j = 0, \dots, 6$ (cp. (4.9)) and $\langle j|H|j\rangle = \mathcal{E}_{j-7}$ for $j = 7, \dots, 12$ (cp. (4.10)). Similarly, the Hamiltonian's eigenbasis corresponding to the moiré excitons is denoted by $|m\rangle$.

We define $\mathbf{b}_0 = \mathbf{0}$ such that the intralayer states $|j\rangle$, $j = 0, \dots, 6$ correspond to the plane waves $\exp(i\mathbf{b}_j\mathbf{r})$. Then, the intralayer distribution of the moiré excitons $|m\rangle$ is simply computed by the plane-wave projections of these first seven states:

$$\psi_m(\mathbf{r}) = \sum_{j=0}^6 \langle j|m\rangle e^{i\mathbf{b}_j\mathbf{r}} \quad (4.19)$$

Using this formula for the bright moiré excitons M_1 , M_2 and M_3 results in the plots in Fig. 4.10. For both, R-type and H-type devices, all three states are located at different points of the moiré supercell and exhibit different spatial distributions: The ground state exciton M_1 is tightly localized, whereas both M_2 and M_3 have non-negligible spatial extents.

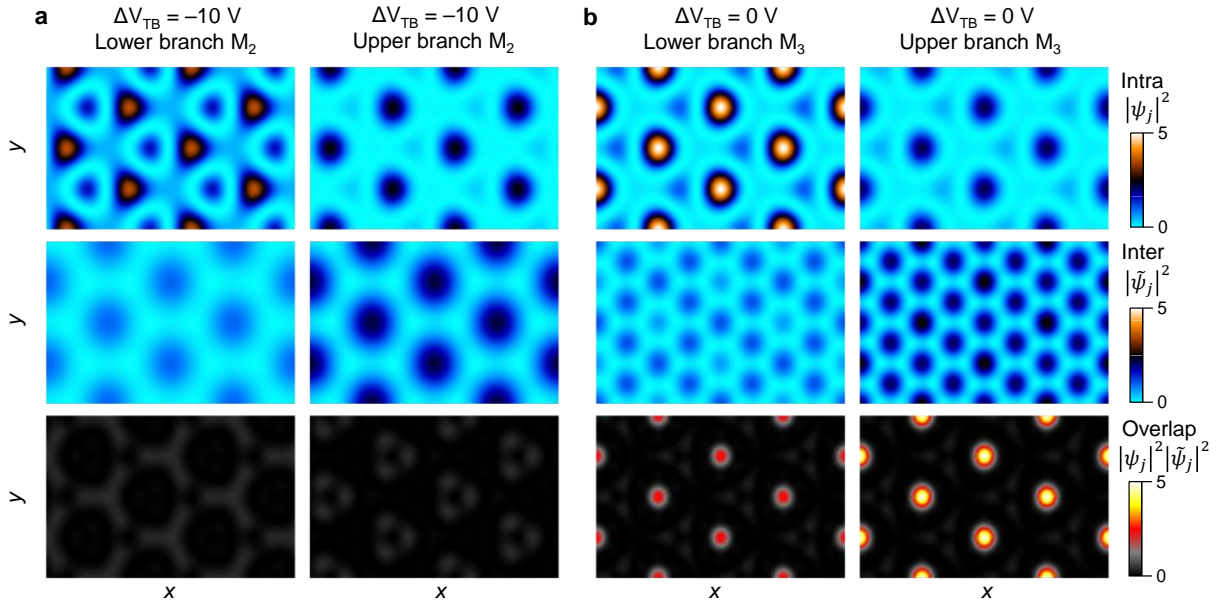


Figure 4.11.: X-IX wavefunction overlap in H-type D2. In Figure 4.9 the theoretical model predicts an interlayer hybridization of M_2 at $\Delta_{TB} = -10$ V and M_3 at $\Delta_{TB} = 0$ V, resulting in pronounced anti-crossing with upper and lower energetic branches. The left and right panels of **a** and **b** correspond to the upper and lower branches of these hybrid states, respectively. Upper and middle panels show spatial distributions of intra- and interlayer exciton wave functions, the bottom panels show their wave function overlap, which is much stronger for the M_3 doublet in **b** as compared to the M_2 hybrid branches in **a**.

In H-type D2 interlayer hybridization plays a significant role as derived in the previous Sections 4.3.2 and 4.3.1. The distributions of the corresponding interlayer excitons are obtained from projections onto the six interlayer states;

$$\tilde{\psi}_m(\mathbf{r}) = \sum_{j=7}^{12} \langle j|m \rangle e^{i\mathbf{b}_j \cdot \mathbf{r}}, \quad (4.20)$$

where \mathbf{b}_j are the vectors pointing to the blue states defined in Figure 4.2b. Comparing the intra- and interlayer exciton distributions provides intuition on the coupling strengths between these excitons. In Figure 4.9, we observed clear anti-crossing behavior of the M_3 peak around $\Delta_{TB} = 0$ V due to interlayer hybridization in the H-type D2. Furthermore, the model in Figure 4.9b predicts an interlayer crossing with a smaller coupling strength of M_2 around $\Delta_{TB} = -10$ V, which was not observed in the experiment. Visualizing the overlap of the respective intra- and interlayer resonances extracted from the model reinforces this observation. The lower panel of Figure 4.11 shows the overlap of the respective intra- and interlayer exciton wave functions for each branch. It is evident that the overlap for the M_3 doublet is much larger than for the M_2 peak, resulting in pronounced anti-crossing behavior. Interlayer resonances, which exhibit vanishing overlap with respective intralayer states at their crossing point in the electric field dispersion, are referred to as dark IX excitons.

We note that a detailed modeling of such behavior requires explicit knowledge of both the electron and hole potentials [165], whereas in our model, the spatial characteristics of moiré excitons are captured entirely through the exciton potential V .

4.4. Charge doping in presence of a moiré potential

Having established the understanding of moiré excitons and the corresponding bandstructure in $\text{MoSe}_2/\text{WS}_2$ R-type and H-type devices, we focused our studies on the investigation of the effects of charge-carrier doping in these systems. The Fermi level inside the HBL is tuned by varying the doping potential $V_\mu = (V_{TG} + V_{BG})/2$ of top and bottom gate voltages. With increasing gate voltages V_μ , the charging characteristics of the DR response in 4.12a and b exhibit transitions from positive (p) through charge-neutral intrinsic (i) to negative (n) doping regimes for both R-type and H-type stackings. The initial response of the moiré excitons to p-doping is observed only at large negative voltages, indicating a substantial Schottky barrier at the interface between the TMD monolayer and the contact graphite. Consequently, the p-doping transition occurs abruptly, and the evolution of the respective DR features is nonlinear with respect to the applied gate voltage rendering quantitative analysis of the spectral features very challenging. Engineering ohmic contacts between metals and 2D semiconductors remains a challenge in the field of nano-fabrication, despite progress that has been made [166–169]. As this topic was beyond the scope of this thesis, we mainly

focused our studies on the analysis of the n-doping regime, which exhibits a linear response as a function of the doping potential V_μ . Both electrons and holes experience the moiré potential resulting in a periodic localization of these elementary charges just as for moiré excitons. The latter change their optical response due to interactions with these periodic charge lattices reminiscent of the formation of trions/polarons in bare TMD monolayers (see Section 2.1.2). Specific charge configurations at fractional fillings per moiré unit cell support the formation of generalized Wigner crystal or Mott insulator states that are imprinted onto the optical response of moiré excitons [26, 28]. In the following, we use this effect to connect the spectral evolution of charged moiré excitons as a function of V_μ with the electron density per moiré unit cell.

4.4.1. Optical signatures in the electron doping regime

The lowest energy excitons, M_1 , at approximately 1.60 eV, display a series of step-like red shifts (for both R-type/H-type) and blue-shifts (H-type only) on the p-doped side before losing their oscillator strength and giving rise to a faint positive trion, M_1^+ , with a 25 meV red shift. Meanwhile, the higher-energy peaks M_2 and M_3 disappear as soon as charge doping into the valence band sets in. This behavior is reversed on the n-doped side: In a first charging step, M_1 converts abruptly into a negative trion M_1^- with a binding energy of 35 and 33 meV in R- and H-stacks, respectively, whereas M_2 evolves gradually into a slightly red shifted peak \tilde{M}_2^- before jumping abruptly to M_2^- in a second charging step. In case of H-type stacking, this second transition coincides with the emergence of a resonance between M_2 and M_3 which we identify as the charged exciton M_3^- , and with a similarly abrupt quench of the ground state trion M_1^- . In case of R-type stacking the M_3 peak is blue shifted by ~ 65 meV compared to the H-type case which explains the absence of M_3^- in the investigated spectral range. Finally, in a third charging step, both M_2^- and M_3^- red shift and lose their oscillator strength.

Consistent with previous studies [16, P2, 165], the contrasting responses of M_1 and M_2 to positive and negative charge doping can be attributed to distinct spatial positions of the two excitons within the moiré unit cell due to the moiré potential V as we derived in Section 4.3. Figure 4.12c shows the moiré potential for R- and H-type alignment in the left and right panel, respectively. M_1 excitons have the highest probability of residence on MM (XX) sites of the R-type (H-type) moiré unit cell and the charged trion M_1^- indicates that doping-induced electrons are co-localized with M_1 , irrespective of parallel or anti parallel stacking, as illustrated in Figure 4.12d [37, P2, 170]. In this sense, M_1^- can be interpreted as attractive polaron in analogy to the doping behavior of MoSe₂ ML excitons [66, 67, 171]. The second exciton M_2 , on the contrary, is located at the MX (MM) sites in case of R-type (H-type) stacking, which in the limiting case of perfect rotational alignment corresponds to a lateral displacement of ~ 4 nm. Therefore, prior to the second doping transition, the

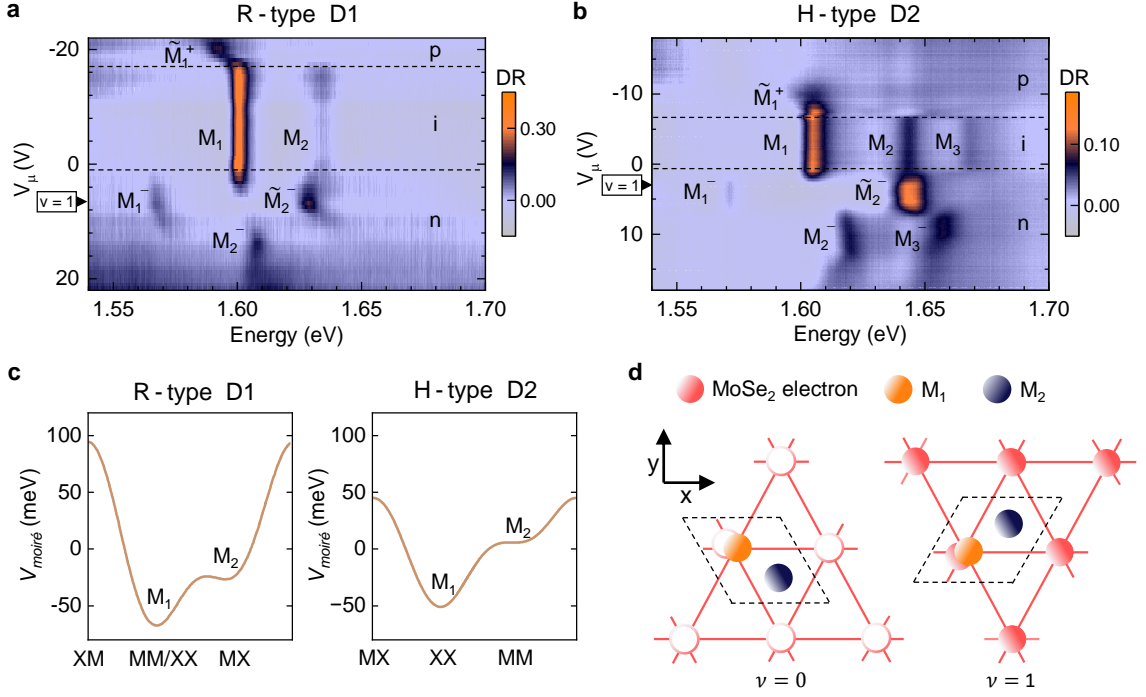


Figure 4.12.: **DR charging characteristics of R-type and H-type stacking.** **a** and **b**, Evolution of the DR spectra as a function of symmetrically applied gate voltages for both hole (p) and electron (n) doping. Neutral moiré excitons M_1 , M_2 , and M_3 show different responses to doping. This is a result of their different spatial localization in the moiré cell due to the moiré potential shown in **c** for both stackings (V was determined in Section 4.3). **d** Localization schematics of M_1 and M_2 moiré excitons with respect to the electron lattice which forms in the MoSe₂ layer up to the filling of $\nu = 1$ electron per moiré cell. Black dashed lines highlight the area of the moiré unit cell as introduced in Figure 4.1.

exciton \tilde{M}_2^- acts as a remote sensor [26], with binding energy and oscillator strength acting as probes of the surrounding electron lattice.

4.4.2. Electrostatic simulations

All sites of the moiré unit cell are occupied by exactly one electron ($\nu = 1$) when M_1 has completely transferred its oscillator strength to the moiré polarons M_1^- and \tilde{M}_2^- , as marked for the respective gate voltages of $V_\mu = 7.9$ V and $V_\mu = 2.8$ V in Figure 4.12a and b. Interestingly, while the second charging step occurs immediately for further increasing gate voltages ($V_\mu > 7.9$ V) in the case of R-type alignment in Figure 4.12a, M_1^- and \tilde{M}_2^- maintain their oscillator strength up to $V_\mu = 6.5$ V in Figure 4.12b in the case of H-type alignment. To understand this contrasting response for parallel and antiparallel stackings at electron

filling $\nu > 1$ per moiré unit cell, we employed hyper-spectral imaging of the DR response as a function of the doping potential and the electric field $F = (V_{BG} - V_{TG})/l$, with l being the respective total thickness of hBN layers of the two heterostacks. In both devices, D1 and D2, the MoSe₂ and the WS₂ layer represent the top and the bottom layer of the heterostacks, respectively, as shown in Figure 4.6.

R-type capacitor model simulation

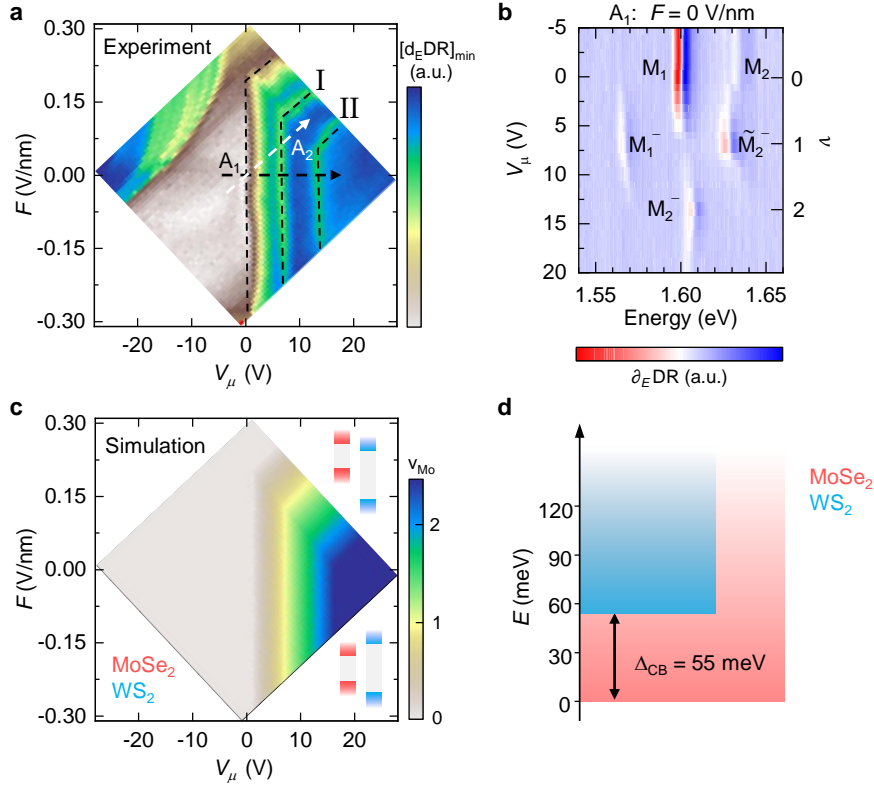


Figure 4.13.: **Capacitor model simulation of R-type D1.** **a**, Hyper-spectral map of the DR signal, where the color of each pixel represents the negative maximum of the derivative $\partial_E \text{DR}(E)$ in the interval between 1.600 and 1.650 eV to highlight the different charging states which have their maximum oscillator strength at integer fillings (black dashed lines). **b**, Line-cut of the data in **a** along the arrow A_1 . A_2 visualizes the (V_μ, F) trajectory of tuning the bottom gate voltage V_B only. **c**, Simulation of the electron density in the MoSe₂ layer as a function of V_μ and F , reproducing the most pronounced features of electron doping. The inset shows the CB alignment changing from type I to type II between large negative and positive fields. **d**, Schematics of the constant DOS in both layers obtained from the simulation with CB offset of 55 meV.

First, we look at the dual-gate DR response of the R-type D1 in Figure 4.13a, where we show for each point $(V_\mu, F)^T$ the negative maximum of the derivative $d(\text{DR})/dE$ between

1.600 and 1.65 eV. The left side of the map represents the p-doped regime, the central vertical stripe the intrinsic, and the right side the n-doped regime. Following the linecut A_1 of the hyper-spectral map at $F = 0$ V/nm with increasing V_μ (see Figure 4.13b), we find, in a linear evolution, the three charging steps discussed above (denoted as I, II, III). The emergence of the charged excitons M_1^-/\tilde{M}_2^- and M_2^- appears as extended straight lines in the hyper-spectral map. This evolution remains unchanged for finite electric fields, except for large positive fields $F > 0.18$ V/nm. In this regime, the conduction band edge of WS₂ has been tuned below that of MoSe₂ through a crossover from type I to type II band alignment, forcing electrons into the WS₂ layer first. Here, at finite V_μ the excitons M_1 and M_2 in the MoSe₂ layer [36, P2, 89] are unable to form intralayer charge-bound states until electrons start filling the MoSe₂ sublattice at higher V_μ , and the emergence of M_1^- and \tilde{M}_2^- is shifted to higher voltages accordingly. The field $F = 0.18$ V/nm corresponds to a conduction band offset $\Delta_{CB} = 55$ meV. At smaller electric fields, electrons continue occupying the MoSe₂ layer even for electron fillings $\nu > 1$, as the charged moiré excitons M_1^- and \tilde{M}_2^- immediately start losing their oscillator strength in transition to M_2^- . We interpret the latter as the counterpart of M_1^- , resulting from electrons co-localizing with the respective excitons inside the moiré unit cell. Following this interpretation, we assume the second electron per moiré unit cell to occupy the MX sites inside the MoSe₂ layer in the R-type alignment.

These suppositions are confirmed by a capacitor model simulation, utilizing respective top and bottom hBN thicknesses of $d_T = 93$ nm and $d_B = 87$ nm to determine the geometric capacitances of the device and the twist angle $\theta = 2^\circ$ to fix the moiré density $n_0 \approx 2.7 \times 10^{12}$ cm⁻². By numerically solving Equation (4.17) for a constant DOS in both monolayers as illustrated in Figure 4.13d, we obtained the electron density ν_{Mo} in the MoSe₂ layer as a function of V_μ and F , shown in Figure 4.13c, perfectly aligning with the experimental data in 4.13a.

The simulation is in accordance with our assumption from above: Line I in Figure 4.13a represents a regime with one electron per moiré cell in MoSe₂ and line II, with the presence of the peak M_2^- , corresponds to two electrons inside MoSe₂. The CB offset between the first DOS peaks in MoSe₂ and WS₂ was fixed to 55 meV by the field F_0 in the simulation, with an uncertainty of about 10% stemming from uncertainties in the thickness and the dielectric susceptibility of the HBL.

H-type capacitor model simulation

Next, we look at the dual-gate DR response of the H-type D2 in Figure 4.14a. Here, in contrast to the R-type response, we find extended regions of constant color, indicating constant optical response in the n-doped regime. Straight lines and kinks between these regions represent transitions mediated by charging. In particular, the three consecutive electron-doping steps in the MoSe₂ layer, denoted by I, II and III, appear as extended regions. The

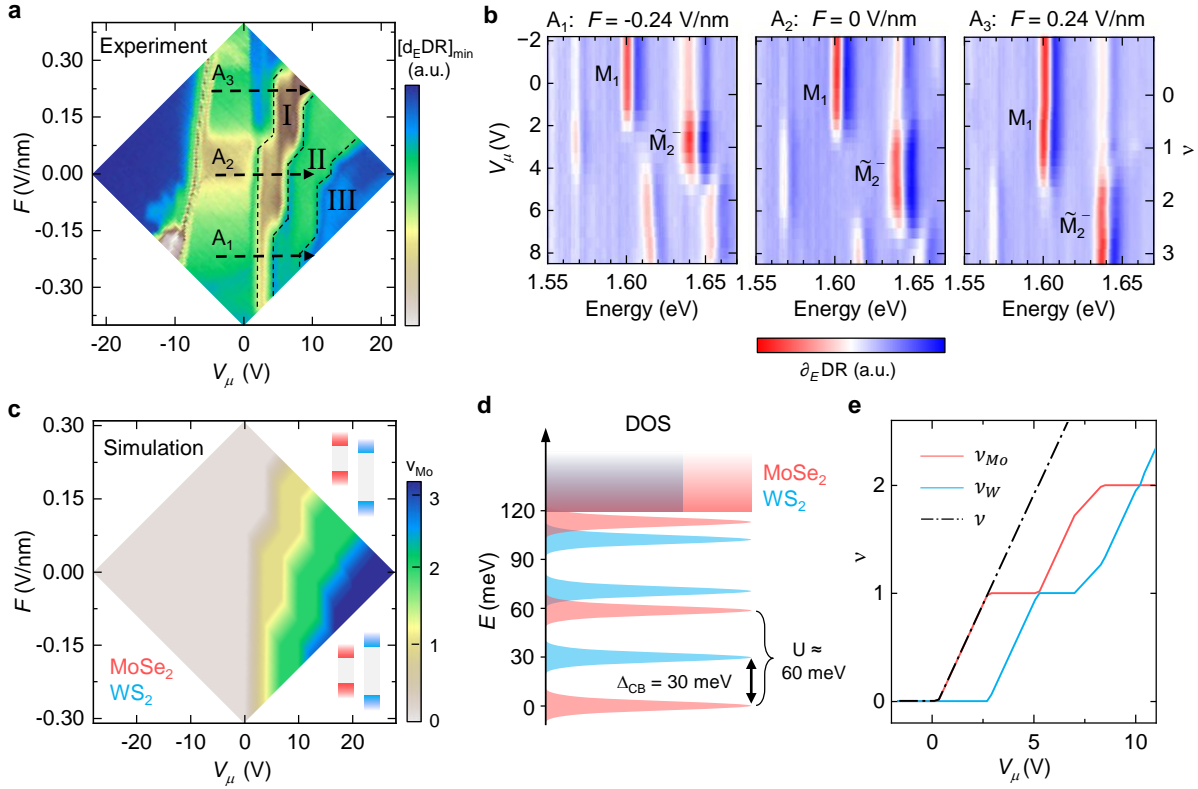


Figure 4.14.: Capacitor model simulation of H-type D2. **a**, Hyper-spectral map of the DR signal, where the color of each pixel represents the negative maximum of the derivative $\partial_E \text{DR}(E)$ in the interval between 1.603 and 1.800 eV to highlight the different charging states. Boundaries of the three distinct regions (I, II and III) signify subsequent charging steps in the MoSe₂ layer. **b**, Line-cuts of the data in **a** for three representative electric fields. **c**, Simulation of the electron density in the MoSe₂ layer as a function of V_μ and F . The inset shows the CB alignment changing from type I to type II between large negative and positive fields. **d**, Schematics of the DOS in both layers obtained from the simulation. Doping of the layers proceeds in steps of n_0 , and the step-like extent of the region I implies Coulomb repulsion of 60 meV between the first and the second electron charging event in the MoSe₂ layer. Together with the CB offset of 30 meV this leads to peculiar charging behavior shown in **e**, with charging of the MoSe₂ layer up to one electron per moiré cell and subsequent charge stability upon consecutive filling of the WS₂ layer up to the same filling factor.

extent of these three charge-stability regions varies strongly with the applied electric field. In Figure 4.14b, we show the evolution of M_1 and M_2 with V_μ for three distinct electric fields indicated by the three lines in Figure 4.14a. For $F = 0.24$ V/nm (right panel), the region I is shifted to higher voltages, with neutral excitons vanishing at ~ 4 V which is half-way through the first charging step at zero-field (central panel). The onset of this shift at a field

of $F_0 = 0.1 \text{ V/nm}$ again marks the crossover from type I to type II band alignment, which is equivalent to a CB offset of 30 meV between MoSe_2 and WS_2 . The red shift of M_1 , observed at $\sim 1.0 \text{ V}$ in the right panel of Figure 4.14b, confirms the presence of electrons, and hence a change of the dielectric environment in the WS_2 layer.

For the negative field $F = -0.24 \text{ V/nm}$ (left panel), on the contrary, the onset of electron doping coincides with the zero-field case, but the width of the charging region I with stability of both M_1^- and \tilde{M}_2^- is reduced by half, similar to the R-type behavior (cp. Figure 4.13a). This behavior is more intriguing, since it indicates that for electric fields pointing from the MoSe_2 to the WS_2 layer, the second charging transition occurs earlier than at zero electric field. From a different perspective, it implies that the number of electrons added to the MoSe_2 layer along the zero-field line is reduced, resulting in an extended charge stability range of region I. As observed in Figure 4.13a, the first charging step into the MoSe_2 layer does not change between negative and small positive electric fields in the R-type D1, signifying that all electrons charge the MoSe_2 layer. We attribute this difference between H-type and R-type alignment to a deeper moiré potential in the R-type device which can accommodate more electrons within one layer. For this reason we were able to assume a constant DOS for the MoSe_2 layer up to a electron filling $\nu = 3$ for the capacitor model simulation of the R-type device above. From Figure 4.12c we estimate the peak-to-peak potential amplitude of 100 meV in the H-type and 170 meV in the R-type heterostack.

To explain the intricate charging behavior in the H-type D2, we performed electrostatic simulations with a discretized DOS inside the two layers [150, 151] as introduced in Section 4.1.2. The geometric capacitance is fixed by the symmetric top and bottom hBN thickness of $d_{T/B} = 55 \text{ nm}$ and the moiré density $n_0 \approx 2.0 \times 10^{12} \text{ cm}^{-2}$ by the twist angle $\theta = 179^\circ$. We assumed that carrier doping happens in steps of n_0 for both layers, with each step corresponding to a peak in the DOS as shown in Figure 4.14d. The gaps between these peaks represent energetic cost associated with on-site Coulomb repulsion U due to strong confinement in moiré potential pockets. To model the charging behavior of the HBL, we adjusted U between the different charging steps to recover the same extents for the regions I, II and III as in Figure 4.14a. Figure 4.14c shows the simulation result for the electron filling inside the MoSe_2 layer with very good agreement with the experimental data.

The simulation implies that region I represents a regime with just one electron per moiré cell in MoSe_2 , with excess electrons populating the WS_2 layer instead. Region II, with the presence of the peaks M_2^- and M_3^- , corresponds to two electrons inside MoSe_2 , and the region III is characterized by reduced oscillator strength of the slightly red shifted M_2^- and M_3^- with three and more electrons per moiré cell inside the MoSe_2 layer. Importantly, to explain the non-uniform width of region I, the Coulomb gap U between the first and second electron charging events in MoSe_2 must be larger than the CB offset. This is at the origin of the difference between R-type and H-type stacking. For the first, we determined $\Delta_{CB} = 55 \text{ meV}$ which has to be larger than U since electrons keep occupying the MoSe_2 layer for $\nu > 1$,

according to our experimental observations. For the latter, our calculation predicts $U \approx 60$ meV which leads to the charging behavior for $\nu > 1$ illustrated on the right of Figure 4.15b. At zero field, after all electrons have filled the moiré potential minima inside MoSe₂ up to a filling factor of $\nu = 1$ (Figure 4.12d), in a second step, successive electrons occupy the WS₂ layer while the charge density on the MoSe₂ sublattice remains constant. The charge carrier doping into the primary MoSe₂ lattice continues only after both layers have accommodated one electron per moiré site. For $F \ll 0$ V/nm, on the contrary, the effective CB offset becomes larger than U , such that the second electron populates the MoSe₂ layer, leading to the continuous transition from region I to region II in the left panel of Figure 4.14b in analogy to the R-type charging behavior in Figure 4.13b.

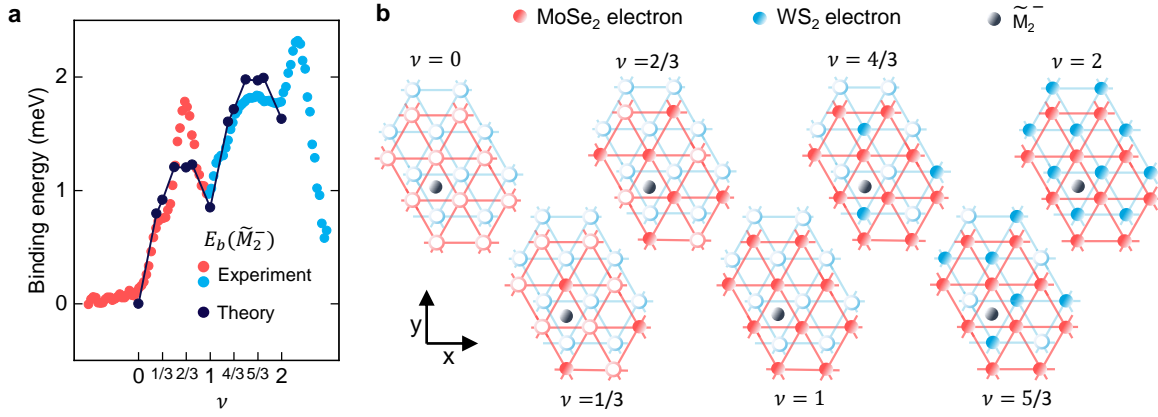


Figure 4.15.: \tilde{M}_2^- exciton binding energy as sensor for electron order in H-type MoSe₂/WS₂. **a**, \tilde{M}_2^- exciton binding energy as function of the electron filling factor ν . Data points corresponding to the filling of the MoSe₂ (WS₂) layer are shown in red (blue). We use the model in Section 4.1.3, assuming a moiré lattice constant of 7.7 nm, to fit the exciton binding energy (purple line) for various electron lattice configurations at selected filling factors, illustrated in **b**.

We emphasize that as the electrons fill the WS₂ lattice, the optical response of both M_1^- and \tilde{M}_2^- is only marginally affected. This indicates that the moiré potential minima in WS₂ are located away from both the XX and the MM sites, and implies that the two excitons act as remote sensors of the emerging secondary lattice. To confirm this scenario, we consider \tilde{M}_2^- pinned on the MM site of the moiré unit cell as depicted in Figure 4.12c and d and subjected to Coulomb interactions with electron lattices of varying geometry for different fractional fillings. Following the approach described in Section 4.1.3, we calculated the change in the exciton binding energy in the presence of the two laterally and vertically displaced charge lattices in MoSe₂ and WS₂ in the process of filling. The quantitative agreement between experiment and theory in Figure 4.15a is compelling: As the filling factor is increased from zero to two electrons per moiré cell, the binding energy varies from zero up to a maximum of 2 meV, providing an estimate for the energy scale of interactions between excitons and

electrons ordered on the surrounding vertically offset and laterally staggered moiré lattices at different filling factors as illustrated in Figure 4.15b.

4.4.3. Sensing of correlated electron-spin lattices

Previously, isolated bands in TMD moiré structures have been theoretically predicted [147] and experimentally observed [28, 29] to mimic the triangular-lattice Hubbard model. When these isolated bands are exactly half filled a Mott insulator ground state can be formed, i.e. strong on-site Coulomb repulsion prevents electrons from doubly occupying single moiré sites in the limit of $\nu = 1 + \epsilon$. In this regime, and assuming next-neighbor coupling only, the Hubbard model maps onto the spin Heisenberg model with antiferromagnetic order. Experimentally, such states of spin-order have been realized in TMD moiré heterostructures and investigated by spin-spin interactions with moiré excitons. These interactions manifest in a diverging magnetic susceptibility which, depending on the optical selection rules, can be probed either by the degree of exciton spin-polarization [37] or renormalized exciton g -factors [28, 29]. In the following, we present our investigations of the emerging electron spin-lattice in our $\text{MoSe}_2/\text{WS}_2$ heterostructures, with moiré excitons M_1 and M_2 as local probes of magnetization. The procedure of the polarization resolved DR measurements, employed to obtain the data that are presented in the following, is explained in Section 3.2.1.

Figure 4.16a and d show the MCD spectra of R-type and H-type heterostacks as a function of the doping potential ($F = 0$ V/nm) with an applied out-of-plane magnetic field of $B = -8$ T, respectively. At $\nu = 0$, the MCD response of M_1 and M_2 takes an asymmetric lineshape with a sign change at the exciton resonance at zero magnetic field, resulting from polarization resolved exciton resonances with identical oscillator strength but different resonance energies. This means, the MCD response is dominated by the exciton Zeeman splittings $\Delta E_X \approx 2$ meV (see Figure 4.7) under the absence of spin-polarization.

Based on the electrostatic simulations in Section 4.4.2, we conclude the existence of bright moiré excitons in the presence of stabilized electron order in MoSe_2 at $\nu_{Mo} = 1$. Focusing on this doping regime, we find a symmetric MCD response at the M_1^- resonances in Figure 4.16a and d at $B = -8$ T, reflecting an almost completely valley polarized exciton resonance. \tilde{M}_2^- , on the other hand, exhibits an asymmetric MCD response, i.e. the exciton maintains a finite oscillator strength in both Zeeman branches but experiences a large Zeeman splitting $\Delta E_X \approx 10$ meV. Both observations are explained by the presence of correlated magnetic order/correlated magnetism of electron-spins at $\nu = 1$ which is sensed by the moiré excitons. The different location of M_1 and M_2 moiré excitons with respect to the electron lattice at this specific doping level (see Section 4.4.1) leads to their different MCD response, as explained in the following:

M_1 excitons are co-localized with the electrons up to an electron filling of $\nu = 1$, and therefore inherit the optical selection rules of monolayer MoSe_2 [66, 67]. This makes the M_1^-

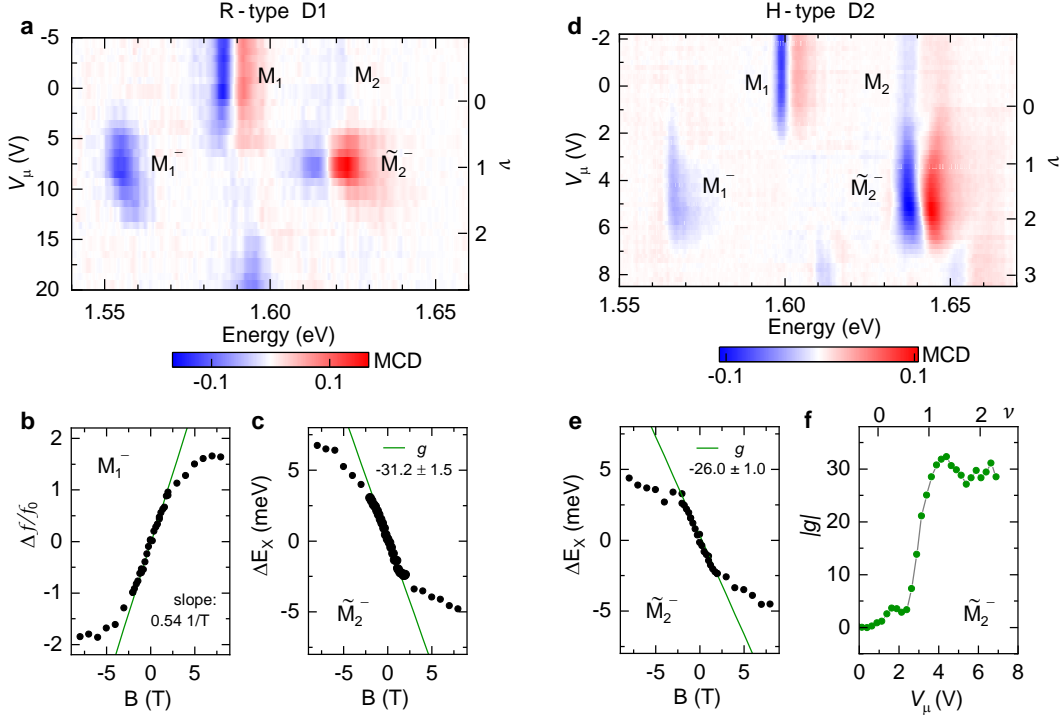


Figure 4.16.: **Correlated magnetism in presence of an electron-spin lattice.** **a** and **d**, MCD evolution at $B = -8$ T as function of the doping potential in R-type and H-type stacking, respectively. M_1^- polarizes completely while \tilde{M}_2^- exhibits large Zeeman splitting. **b**, Nonlinear evolution of the degree of spin polarization ρ_A of M_1^- in R-type D1 as a function of the magnetic field. **b** and **e**, Nonlinear evolution of the Zeeman energy splitting ΔE_X of \tilde{M}_2^- in R-type D1 and H-type D2 as a function of the magnetic field, respectively. **f**, Evolution of the effective g -factor of \tilde{M}_2^- as a function of the electron filling in H-type D2. Linear fits are carried out at small magnetic fields ($B \leq 1$ T).

peak a candidate for probing the influence of the electron-spin lattice through the evolution of the exciton degree of spin-polarization $\rho = (f_+ - f_-)/f_0$ with the magnetic field [37], which is shown in Figure 4.16b for the R-type device (see Section 3.2.1 experimental details). For small positive (negative) magnetic fields the oscillator strength of the σ^+ (σ^-) polarized moiré excitons is quickly transferred to the opposite polarization leading to a negative (positive) increase of the degree of spin-polarization. The evolution of $\Delta f/f_0$ saturates at larger magnetic fields ($B > 2$ T), where one polarization of the M_1^- exciton DR response is almost completely quenched. This non-linear evolution of the degree of spin-polarization results from the change in magnetic susceptibility due to the polarization of the electron-spin lattice that is co-localized to and thus sensed by the M_1^- excitons [37].

Even though \tilde{M}_2^- excitons exhibit a finite degree of spin-polarization with the magnetic field, which is thematized in Section 5.3, both polarizations maintain finite oscillator strength up to large magnetic fields because of the delocalization of M_2 excitons with respect to the

electron-spin lattice (see Section 4.4.1). In this case, the effect of correlated magnetism of the electron spins on the moiré excitons is most pronounced in the evolution of the exciton Zeeman splitting ΔE_X as shown in Figure 4.16c and e for R-type and H-type stacking, respectively. ΔE_X of the \tilde{M}_2^- exciton exhibits a highly nonlinear evolution as function of the magnetic field analogous to hole-mediated magnetism in WS_2/WSe_2 [28] or $\text{MoSe}_2/\text{WSe}_2$ [29]. In the limit of small negative (positive) magnetic fields ($B \leq 1$ T) ΔE_X rapidly increases to positive (negative) values. Here, the slopes of ΔE_X can be approximated as linear functions of B and we obtain respective renormalized moiré exciton g -factors $g = -31 \pm 1.5$ and $g = -26 \pm 1$ for R-type and H-type stacking. These values are strongly enhanced compared to $g \approx -4$ of the neutral M_2 resonance (cp. Figure 4.7) as a result of the paramagnetic response of the excitons to the polarization of the electron-spin lattice in close proximity. At higher magnetic fields, when the electron-spin lattice is fully polarized, the reduced g -factor reflects the conventional paramagnetic exciton response [73, 162].

In contrast to the R-type D1 and other heterostructures [28, 29], g remains at high values in the H-type stacking as long as the peak \tilde{M}_2^- is present between $1 < \nu < 2$, as shown in Figure 4.16f. This is consistent with the understanding developed above: The MoSe_2 electron sublattice is locked in a Mott-insulating state during successive charging of the WS_2 layer. Throughout the plateau, the g -factor values exhibit variations on the order of 10 – 15% due to the emergent filling of the secondary lattice. References [P3] and [172] provide a detailed analysis of this electrostatically tunable bilayer spin-charge lattice in H-type $\text{MoSe}_2/\text{WS}_2$, which was beyond the main-scope of this thesis: Measuring the renormalized exciton g -factor as a function of temperature in a dilution refrigerator down to 0.1 K enabled to confirm the paramagnetic response of the underlying spin lattice. An extracted negative Curie-Weiss temperature suggests antiferromagnetic interactions of the electron spins, as expected for the ground state of a triangular spin lattice with only nearest neighbor interactions [147]. Furthermore, the above mentioned variations of the g -factor in the plateau at electron filling $1 < \nu < 2$ are explained in the framework of Ruderman-Kittel-Kasuya-Yosida (RKKY) magnetism [173, 174], confirming the implementation of a bilayer Hubbard model.

Moiré exciton-polaritons in MoSe₂/WS₂ heterostructures

Embedding materials with excitons of significant oscillator strength in optical micro-cavities allows to study light-matter hybridization on a fundamental quantum level. This Chapter presents the results of studying moiré heterostructures dressed with photons in open micro-cavity setups at cryogenic temperatures. The characterization of moiré exciton- and polaron-polaritons was performed using the home-built open fiber cavity setup, as detailed in Chapter 3.3.1. Expanding upon this research, we investigated the impact of correlated magnetism on these polariton species in collaboration with the Quantum Materials Group at the University of Oldenburg.

THIS CHAPTER IS PARTLY BASED ON THE PUBLICATION [P4]
J. Scherzer*, L. Lackner*, B. Han, et al., “Correlated magnetism of moiré exciton-polaritons on a triangular electron-spin lattice,” *arXiv* **2024**, 2405.12698

* equal contribution

5.1. Introduction

Exciton-polaritons are bosonic quasi-particles arising in the regime of strong coupling between photons and excitons. They become particularly distinct in optical micro-cavities coupled to materials with excitons of significant oscillator strength [112, 113]. Being composite bosons, they possess a variety of unique properties resulting from light-matter hybridization on a fundamental quantum level, including giant optical nonlinearities that give rise to effective photon-photon interactions [175, 176], the formation of quantum condensates at elevated densities from cryogenic to room temperatures [33, 177, 178], as well as friction-

less on-chip propagation [179]. Featuring excitons with high oscillator strength, TMDs and their heterostructures provide novel opportunities for engineering quantum phases in the regime of strong light-matter coupling [108]. Reduced screening enhances nonlinear polariton interactions [180], while controlled electron doping enables the formation of Fermi polaron-polaritons by dressing exciton-polaritons with excitations in the Fermi sea [66, 171]. The paramagnetic behavior of the underlying exciton polarons is inherited to such charged light-matter quasiparticles, rendering polaron-polaritons sensitive to external magnetic fields [181].

As we present in detail in Chapter 4 of this work for $\text{MoSe}_2/\text{WS}_2$ structures, the emergent moiré potential in TMD heterobilayer systems leads to the formation of electron or hole lattices at specific fractional fillings of elementary charges in units of the moiré density, imprinting effects of correlated magnetism on the optical response of moiré excitons. Dressing such charged moiré excitons with cavity photons allowed us to explore and control the nonlinear manifestations of correlated magnetism on polaron-polaritons as an extension to nonlinear optical phenomena observed for charge-neutral moiré exciton-polaritons [38].

The $\text{MoSe}_2/\text{WS}_2$ heterostructure D1 with near-parallel alignment introduced in Section 4.2 was fabricated on a distributed Bragg reflector (DBR) substrate to embed the sample in a high finesse optical micro-cavity. This allows to study the properties of emergent moiré exciton-polaritons and their response to correlated charge order under electron or hole doping. For a first characterization of the charge tunable moiré exciton-polaritons, presented in the first part of this Chapter, we implemented the dual-gate device in the tunable optical micro-cavity in a closed-cycle cryostat (attocube systems, attpDRY800), introduced in Section 3.3.1. To explore how correlated magnetism of electrons maps onto the magnetic response of charged moiré exciton-polaritons we performed a second set of measurements in a tunable optical micro-cavity in a closed-cycle cryostat equipped with a superconducting magnet. These experiments were realized in a collaboration with the Quantum Materials group of Christian Schneider at the University of Oldenburg, and in particular with the help of Lukas Lackner, who guided the measurements at the Institute of physics in Oldenburg. The corresponding results are presented in the second part of this Chapter.

5.2. Characterization of moiré exciton-polaritons

Having assembled the R-type heterostack D1 (see Figure 4.2 for details of the device) in our fiber-based micro-cavity inside the closed-cycle cryostat (see Section 3.3.1), we started the measurements by introducing the MoSe_2 monolayer area inside the mode of the microcavity. Scanning the cavity length with the piezo actuator attached to the cavity fiber, we reduced the cavity length to the small mode orders, where the plano-concave cavity geometry allows the formation of stable Hermite-Gaussian modes (see Section 2.2).

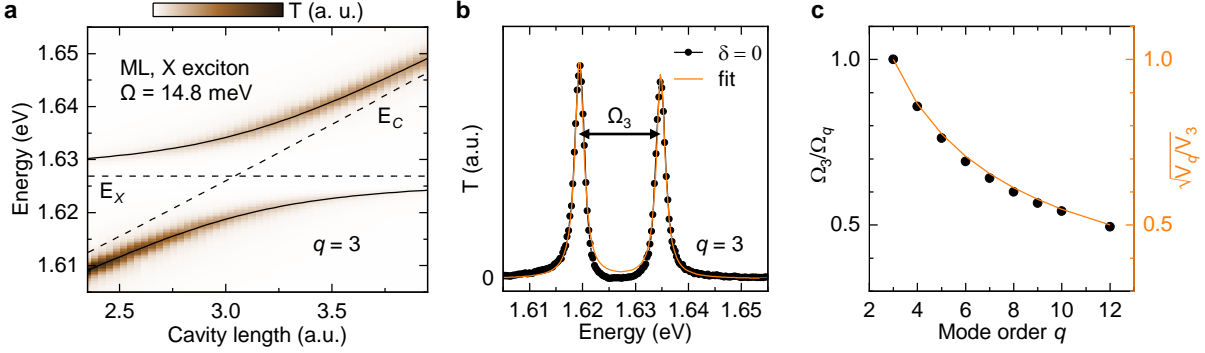


Figure 5.1.: **MoSe₂ exciton-polaritons in a fiber-based open microcavity.** **a**, Characteristic avoided crossing behavior of a strongly coupled exciton-photon system of the MoSe₂ monolayer inside the fiber cavity, observed in transmission (T) behind the fiber microcavity as a function of the cavity length. A Rabi splitting $\Omega = 14.8$ meV is observed for the fundamental mode order $q = 3$. Solid black lines show the result of a two-coupled oscillator model fit to the data, dashed lines the corresponding exciton energy E_X and cavity energy dispersion E_C . **b**, Corresponding transmission spectrum at zero detuning $\delta = E_C - E_X = 0$. **c**, Evolution of the Rabi splitting Ω as a function of q is inversely proportional to the square root of the cavity mode volume V_m .

Figure 5.1a displays the spectrally dispersed transmission response of a broadband white light source through the cavity. Here, the lowest accessible TEM₀₀ mode $q = 3$, before introducing contact between the two mirrors, is tuned through the MoSe₂ exciton resonance. We observe a pronounced anti-crossing, a hallmark of the strong coupling regime, leading to the formation of hybridized exciton-polariton states. The two polariton branches are accurately described by the eigenstates of the coupled oscillator model in Eq. (2.31), represented as black solid lines in Figure 5.1a. The Rabi splitting Ω denotes the spectral separation of the upper and lower polariton branches at zero detuning, $\delta = E_C - E_X = 0$, where E_C is the energy of the cavity mode and E_X is the exciton resonance energy, as shown in Figure 5.1b. At $q = 3$, we observe a Rabi splitting Ω_3 of 14.8 meV, comparable with previous studies [66, 182]. The open geometry of our cavity system enables the study of exciton-photon coupling across a wide range of fundamental mode orders in Figure 5.1c. The evolution of Ω as a function of q follows the expected decrease with increasing mode volume, $\Omega \sim 1/\sqrt{V_m}$ (see Eq. (2.27)).

The hybridization of TMD monolayer excitons with photons in the strong coupling regime has been extensively investigated in various configurations, including monolithic [183, 184] and open micro-cavities [P8, 182, 185], as well as plasmonic [186–189] and other photonic nano-cavities [190]. In the following, we present the results of our investigation into moiré exciton-polaritons in device D1. In the charge-neutral regime, MoSe₂/WS₂ exciton-polaritons exhibited polariton density-dependent nonlinearities, possibly attributed to the spatial confinement of moiré excitons [38]. Here, we compare our experimental findings

with those in the literature and employ the gate control in our field-effect device to explore optical nonlinearities as a function of the electron density.

5.2.1. Charge tunability

Figure 5.2b shows the confocal DR response of D1 with increasing electron doping potential V_μ , following the arrow A₁ in Figure 4.13 in logarithmic scale to visualize the transfer of oscillator strength from the neutral moiré excitons M_1 and M_2 to their charged polaron counterparts M_1^- and M_2^- . The latter emerge in the regime of $0 < \nu < 1$ electron filling per moiré cell and reach maximum oscillator strength at doping density of one electron per moiré unit cell ($\nu = 1$). The decrease in the oscillator strength at electron densities of $\nu = 1 \pm \epsilon$ indicates the formation of an isolated Hubbard band at the incompressible state for $\nu = 1$ [37] (see Section 4.4 for details).

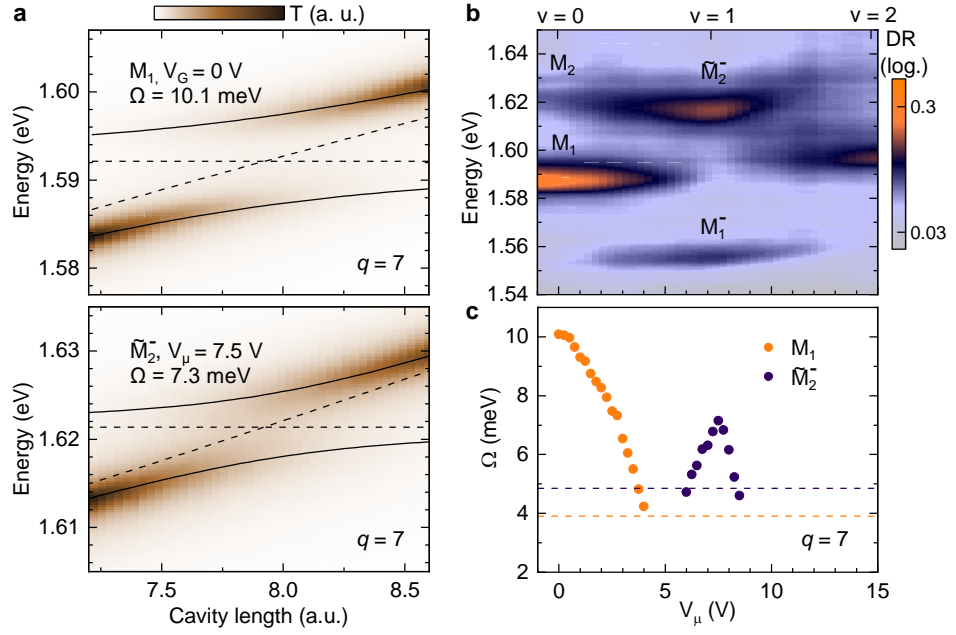


Figure 5.2.: **Charge tunable moiré exciton-polaritons.** **a**, Characteristic anticrossing of M_1 exciton-polariton (upper panel) and M_2^- polaron-polariton (lower panel) branches as a function of cavity-resonance detuning at fundamental mode order $q = 7$ (the model fits are shown by solid lines, and the bare exciton and cavity dispersions by dashed lines). **b**, Electron charging in reflection contrast spectroscopy of moiré excitons M_1 and M_2 and the respective moiré polarons M_1^- and M_2^- as a function of the doping potential V_μ (cp. arrow A₁ in Figure 4.13a). **c**, Rabi splitting Ω of M_1 and M_2^- polaritons obtained from the coupled oscillator model as a function of V_μ . Horizontal dashed lines delimit the strong coupling condition $\Omega > (\gamma + \kappa)/2$.

The transfer of the oscillator strength from the charge-neutral moiré exciton M_1 to the \tilde{M}_2^- exciton-polaron state is most obvious in the regime of coherent light-matter coupling inside the fiber-based microcavity. As for the bare MoSe₂ monolayer, we observe clear anticrossings by sweeping the TEM₀₀ mode (here, $q = 7$) through the resonances of M_1 and \tilde{M}_2^- (see Figure 5.2a upper and lower panel). The respective polariton branches are captured by the coupled oscillator formalism, with Rabi splittings of $\Omega = 10.1$ meV for M_1 at $V_\mu = 0$ V and $\Omega = 7.3$ meV for \tilde{M}_2^- at $V_\mu = 7.5$ V. The evolution of the Rabi splittings as a function of the electron doping is shown in Figure 5.2c for gate voltages where the strong coupling condition $\Omega > (\gamma + \kappa)/2$ is satisfied for both M_1 and \tilde{M}_2^- , with respective linewidths of $\gamma = 7.6$ and 9.5 meV. The homogeneous linewidth $\kappa = 0.13$ meV of the cavity mode was determined from the Lorentzian part of a Voigt profile fit of the cavity lineshape in Section 3.3.4. Inhomogeneous contributions due to cavity vibrations are negligible on the time scale of coherent light-matter coupling (see Section 3.3.2). With increasing electron density, the Rabi splitting of M_1 decreases linearly and collapses around $\nu > 0.5$, while at the same time the anticrossing of the \tilde{M}_2^- polariton reaches its maximum value at electron filling $\nu = 1$ before decreasing again at higher gate voltages.

5.2.2. Moiré-induced nonlinearity

In the following, we focus on MoSe₂ ML X and HBL M_1 exciton-polaritons at electron filling $\nu = 0$ and \tilde{M}_2^- polaron-polaritons at $\nu = 1$, studying their optical response as a function of the excitation power, which determines the polariton density. We present the excitation power-dependent polariton properties and compare the experimental findings with other studies in the literature to categorize the observed data and provide an overview of possible physical explanations. A quantitative analysis of these results, which would require an accurate deduction of the polariton density as a function of the excitation power, was beyond the scope of this work, but the intriguing findings could motivate further studies on this subject.

To this end, we repeated the broad band transmission measurement as shown in Figure 5.2 for M_1 and \tilde{M}_2^- polaritons at various excitation power. We utilized an NKT supercontinuum laser, operating in pulsed mode with a repetition rate of 2.7 MHz and a 100 nm bandwidth centered around the wavelength of 765 nm. Prior to fiber coupling, a combination of neutral-density filters ensured a consistent and uniform intensity distribution of the laser profile. We then analyzed the transmission response of the different polariton species in the framework of the coupled oscillator model to obtain the relevant parameters – the underlying exciton energy, Rabi splitting, energies of the polariton branches and their Lorentzian linewidth at zero detuning $\delta = E_c - E_X = 0$ – as a function of the excitation power. The results are shown in Figure 5.3.

In Figure 5.3a, we first examine the shift of the exciton energy ΔE extracted from MoSe₂ X (black data points) and M_1 (blue) exciton-polaritons as well as \tilde{M}_2^- polaron-polaritons

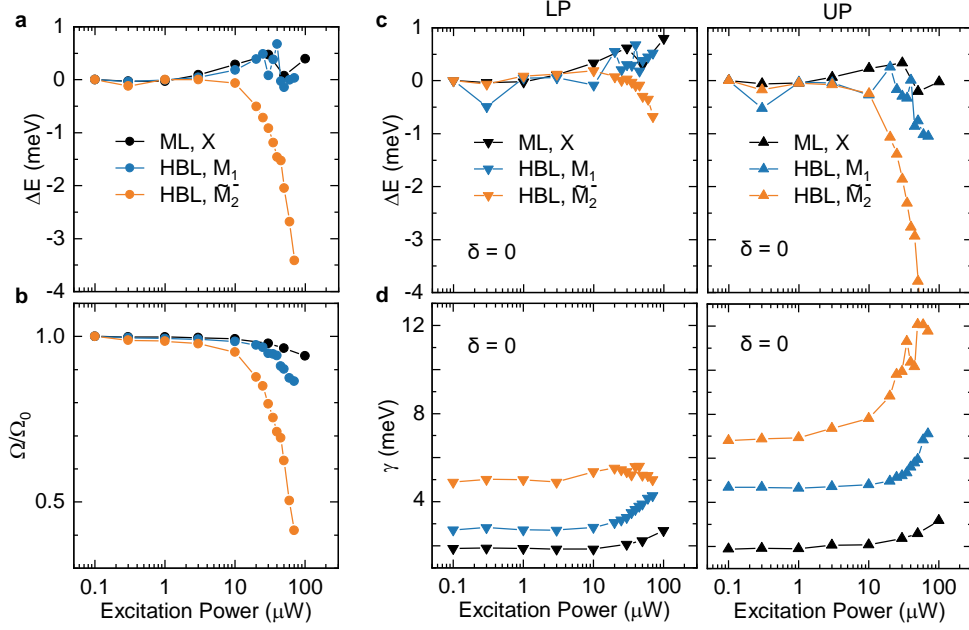


Figure 5.3.: **Moiré exciton-polaritons as function of the excitation power.** **a**, Change of MoSe₂ ML X exciton and the M_1 and \tilde{M}_2^- moiré exciton energy $\Delta E = E - E_0$ as function of the excitation power. E denotes the power dependent exciton energy and E_0 the exciton energy at minimum excitation power ($P = 100\text{ nW}$), obtained from coupled oscillator model fits. **b**, Power dependent evolution of the Rabi splitting Ω of the moiré ML X exciton and the M_1 and \tilde{M}_2^- moiré excitons compared to the Rabi splitting Ω_0 at 100 nW excitation power. **c**, Evolution of the corresponding lower (LP, left panel) and upper (UP, right panel) polariton energies as function of the excitation power. **d**, LP (left panel) and UP (right panel) Lorentzian linewidths γ at $\delta = E_c - E_X = 0$ as function of the excitation power.

(orange) as function of the excitation power. The X and M_1 resonances exhibit minor blue shifts ($\Delta E < 1\text{ meV}$) with increasing excitation power over a range spanning more than three orders of magnitude. Such blue shifts have been observed in TMD monolayers and heterobilayers, commonly attributed to heightened exciton dipole-dipole interaction and phase space filling at elevated exciton/polariton densities [191, 192]. Various studies have reported increased dipole-dipole interactions for excitons confined in 0D systems, like the pockets of a moiré lattice, compared to bare TMD monolayers with a 2D density of states [30, 31, 38, 193, 194]. However, we do not observe this effect here, as moiré-localized M_1 excitons exhibit energy renormalization comparable to MoSe₂ monolayer X excitons in Figure 5.3a. In contrast, the \tilde{M}_2^- exciton energy demonstrates a highly nonlinear red shift as function of the excitation power. Within one order of magnitude of increasing excitation power, the exciton energy shifts by more than 3 meV towards lower energies. Various types of exciton-exciton interactions compete, contributing to the renormalization of the exciton energy at specific

exciton densities [192]. While dipole-dipole interactions, phase space filling, or bosonic exchange interactions result in increased exciton energies, fermionic exchange interactions and screened bosonic exchange interactions would lead to decreased exciton energies. From this, we can conclude that the presence of the triangular electron lattice at $\nu = 1$, combined with the different location of \tilde{M}_2^- excitons within the moiré unit cell, favors one of the latter two effects, leading to the pronounced red shift of the \tilde{M}_2^- exciton energy.

We proceed by investigating the Rabi splitting Ω of the three polariton species as a function of excitation power, as shown in Figure 5.3b. Here, Ω at a specific excitation power is normalized by the Rabi splitting Ω_0 obtained at the lowest excitation power of the measurement series (100 nW). The Rabi splitting of the X exciton-polariton remains remarkably robust, maintaining values of $\Omega/\Omega_0 > 0.95$ even at the highest excitation powers. Conversely, M_1 exciton-polaritons demonstrate a pronounced nonlinear decrease with increasing excitation power. This observation aligns with the documented exciton-blockade phenomenon in neutral moiré polaritons within $\text{MoSe}_2/\text{WS}_2$ heterobilayers, where exciton-photon coupling saturates once the exciton density exceeds one exciton per moiré unit cell [38]. Interestingly, this effect appears to be significantly amplified in the case of \tilde{M}_2^- polaron-polaritons. While the onset of saturation power is comparable to that of M_1 exciton-polaritons, it diminishes to $\Omega/\Omega_0 \approx 0.4$ at 70 μW , contrasting with the $\Omega/\Omega_0 \approx 0.85$ exhibited by M_1 exciton-polaritons. A highly nonlinear reduction in the Rabi splitting of trion-polaritons, comparable to that observed in single quantum dots embedded in microcavities, has been documented in MoSe_2 monolayers [191]. The interplay between electron interaction and moiré confinement in the case of \tilde{M}_2^- polaron-polaritons offers a plausible explanation for the pronounced nonlinear quenching of the Rabi splitting with increasing exciton/polariton density. Nevertheless, the precise mechanism driving this intriguing response remains speculative, necessitating further analysis to attain a comprehensive understanding. An alternative approach to probing and confirming interaction-induced nonlinearities could involve measuring the second-order correlation function in resonant transmission experiments to unveil photon correlations as potential signatures of polariton blockade effects [176].

Figure 5.3c presents the energy shift of the lower (left panel) and upper (right panel) polariton branch at zero detuning $\delta = 0$ as function of the excitation power. The reduced Rabi splitting for high excitation power as well as the marginal shift of the corresponding exciton energy lead to a blue shift (red shift) in the lower (upper) polariton branch in case of M_1 with increasing excitation power. Conversely, the collapse of Rabi splitting, accompanied by the pronounced red shift of the corresponding exciton resonance, leads to red shifts in either of the two polariton branches in the case of \tilde{M}_2^- as the excitation power increases.

Finally, we monitor the evolution of the lower (left panel) and upper (right panel) polariton linewidths at zero detuning in Figure 5.3d as the excitation power increases. For the MoSe_2 X exciton-polariton, both branches exhibit approximately the same Lorentzian linewidth of $\gamma \approx 2$ meV, which only increases at high excitation power due to increased dephasing rates

induced by increased exciton-exciton interactions [195]. In comparison, the moiré exciton linewidth of M_1 and \tilde{M}_2^- expands to $\gamma_x \approx 7.5$ meV and $\gamma_x \approx 10$ meV, respectively (see Figure 4.7), resulting in a proportional increase in the corresponding polariton linewidths. Despite the anticipated higher linewidths of moiré exciton- and polaron-polaritons, they also manifest an asymmetry between the upper and lower branches. This asymmetry suggests an increased in-plane disorder in the heterobilayer region, primarily affecting the upper polariton branch, while the lower polariton branch exhibits signs of motional narrowing [196–198].

5.3. Correlated magnetism of moiré exciton-polaritons

As an extension to nonlinear optical phenomena as function of the polariton density, we explored the nonlinear manifestations of correlated magnetism (see Section 4.4) on polaron-polaritons by dressing \tilde{M}_2^- moiré exciton polarons with cavity photons in the presence of an out-of-plane magnetic field.

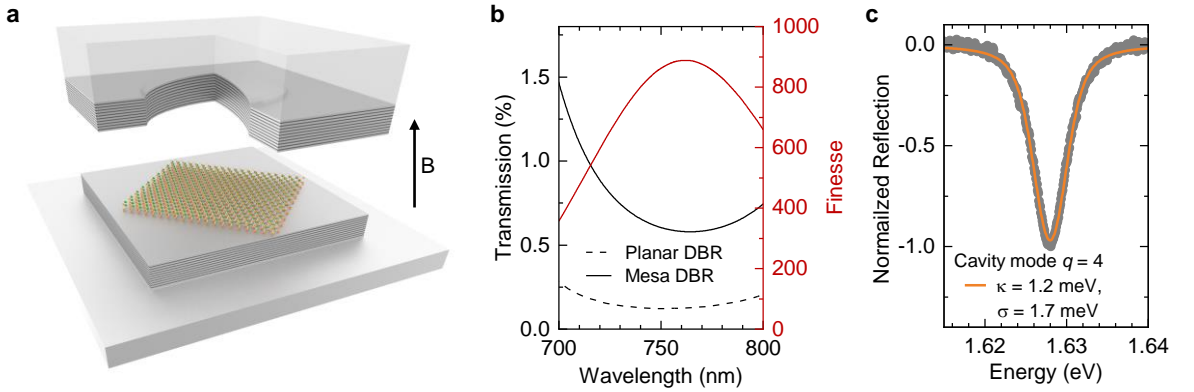


Figure 5.4.: **Mesa-based microcavity design with magnetic field access.** **a**, Schematic of the micro-cavity geometry: The TMD heterostructure is placed on a planar mirror with DBR coating. The mesa counterpart with spherical indentation is DBR coated as well. The setup is placed inside a closed-cycle cryostat with an out-of-plane magnetic field B . **b**, Transmission characteristics of the two DBR coatings and corresponding expected finesse as function of the excitation wavelength. **c**, Reflection spectrum of the empty cavity at fundamental mode order $q = 4$, fitted with a Voigt profile (orange line) with Lorentzian linewidth $\kappa = 1.2$ meV and Gaussian $1/e^2$ broadening $\sigma = 1.7$ meV.

For this study, we implemented D1 in a different open cavity system, mounted inside a low vibration closed-cycle cryostat (attocube systems, attoDRY1000) with a solenoid providing access to out-of-plane magnetic fields [199]. The open cavity design is illustrated in Figure 5.4a. Here, the top part of the cavity was built from a glass mesa containing concave

spherical cap indentations with 300 nm depth and a diameter of 6 μm formed by gallium focused ion beam milling and coated with 5 pairs of $\text{TiO}_2/\text{SiO}_2$ layers with SiO_2 terminating layer. The photonic trapping potential resulting from the spherical indentation supports stable Laguerre-Gaussian modes at small cavity lengths. The macroscopic geometry of the mesa necessitated the removal of the solder joint, which contacted the top FLG gate of the heterostructure, to ensure reaching the lowest mode orders without making contact with the sample. Consequently, the doping-dependent data presented in the following sections were acquired by applying voltage at the bottom gate only. The transmission characteristics of the mesa DBR are shown in Figure 5.4b, together with the ones of the bottom DBR substrate, which was introduced above in Section 5.2 and Section 3.3.4. The corresponding expected finesse calculated from the mirror reflectivities using Equation (2.10) is shown as red line. For the measurements presented in the following, a broadband quartz tungsten-halogen lamp was focused through the top mirror into the cavity by a lens (Thorlabs, 354105-B) to form a Gaussian spot size with a full-width at half-maximum diameter of $< 5.0 \mu\text{m}$. The physical distance between the microcavity mirrors was controlled via nano-positioners with nm accuracy. All cavity measurements were performed using the fundamental longitudinal cavity mode of order $q = 4$, the lowest possible mode order without introducing physical contact between top and bottom DBR mirrors, and employing a spectrometer (Andor Shamrock 500i) equipped with a CCD (Andor iKon-M 934). The normalized reflection spectrum of the bare cavity (far detuned from the exciton resonances) at $q = 4$ is shown in Figure 5.4c. Fitting the lineshape of the cavity mode with a Voigt profile yields a homogeneous cavity linewidth $\kappa = 1.2 \text{ meV}$ equivalent to a finesse $\mathcal{F} \approx 450$. The deviation of the experimentally observed finesse and the expected value in Figure 5.4b can be explained by additional losses due to scattering at sample or mirror imperfections.

In an initial step we repeated the characterization of the doping dependent evolution of exciton- and polaron-polaritons around the M_1 and M_2 moiré exciton resonances (see Section 5.2). The upper and lower panel of Figure 5.5a show the avoided crossing behavior observed for sweeping the cavity resonance across the M_1 and \tilde{M}_2^- resonance at applied bottom gate voltage $V_G = 0 \text{ V}$ and $V_G = 11.5 \text{ V}$, respectively. The strong coupling condition $\Omega > (\gamma + \kappa)/2$ is satisfied for both M_1 and \tilde{M}_2^- , with respective linewidths of $\gamma = 7.6$ and 9.5 meV . The evolution of Rabi splitting Ω in Figure 5.5c as a function of V_G follows the evolution of oscillator strength known from DR measurements with absence of the top DBR mirror which is shown in Figure 5.5b (cp. arrow A_2 in the dual-gate map in Figure 4.13a). With increasing electron density, the Rabi splitting of M_1 decreases linearly and collapses around $\nu \approx 0.5$, while at the same time the anticrossing of the \tilde{M}_2^- polariton reaches its maximum value at electron filling $\nu = 1$ before decreasing again at higher gate voltages.

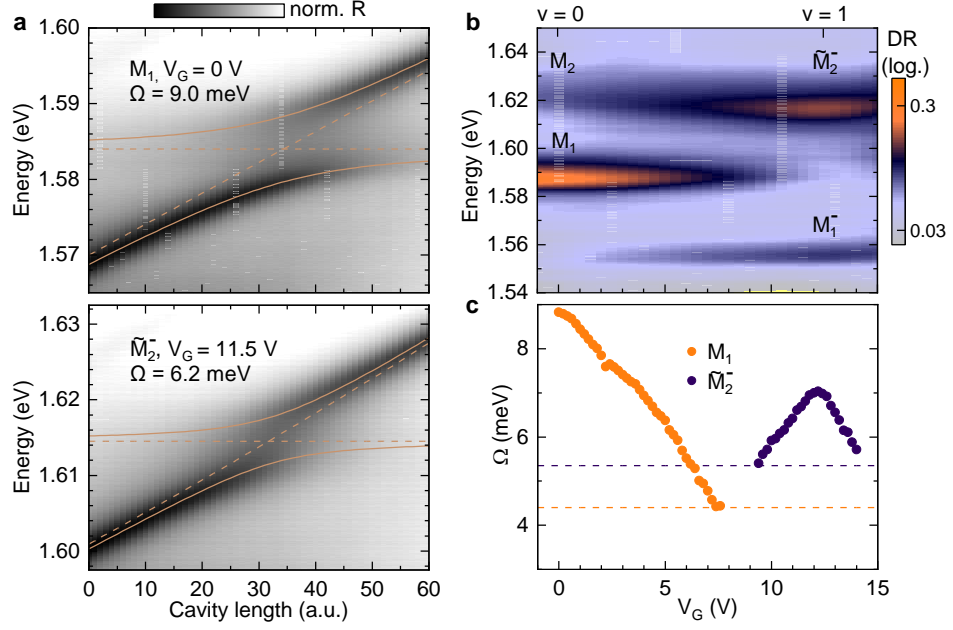


Figure 5.5.: **Charge tunable moiré exciton-polaritons inside the magneto cavity setup.** **a**, Characteristic anticrossing of M_1 exciton-polariton (upper panel) and \tilde{M}_2^- polaron-polariton (lower panel) branches as a function of cavity-resonance detuning (the model fits are shown by solid lines, and the bare exciton and cavity dispersions by dashed lines). **b**, Electron charging in reflection contrast spectroscopy of moiré excitons M_1 and M_2 and the respective moiré polarons M_1^- and \tilde{M}_2^- as a function of the bottom gate voltage V_G (cp. arrow A_2 in Figure 4.13a). **c**, Rabi splitting Ω of M_1 and \tilde{M}_2^- polaritons obtained from the coupled oscillator model as a function of V_G . Horizontal dashed lines delimit the strong coupling condition $\Omega > (\gamma + \kappa)/2$.

5.3.1. Polarization-contrasting response in high magnetic fields

The most remarkable behavior of the strongly coupled exciton-polariton system in the presence of electron doping is induced by an external magnetic field. In polarization-contrasting reflection $R(\sigma^{+/-})$ of M_1 and \tilde{M}_2^- polaritons at 8 T, shown in Figure 5.6a and b, we observe polarized polariton branches as a function of the cavity length which is represented in units of zero-field resonance detuning $\delta_0 = E_c - E_X$ between the cavity and exciton energies E_c and E_X at $B = 0$ T. Upon cavity detuning, the σ^+ and σ^- circularly polarized branches of the \tilde{M}_2^- polaron-polariton in the left and right panels of Figure 5.6b exhibit avoided crossings with respective polarization-specific on-resonance Rabi splittings of 5.2 and 7.5 meV and an exciton Zeeman splitting (i. e. the energy difference between the red and blue dashed horizontal lines in Figure 5.6b) of ~ 7 meV. The latter contrasts the modest exciton Zeeman splitting extracted from the M_1 polariton in Figure 5.6a with a value of 2 meV, comparable to the neutral exciton Zeeman splitting in MoSe₂ monolayers [73, 162].

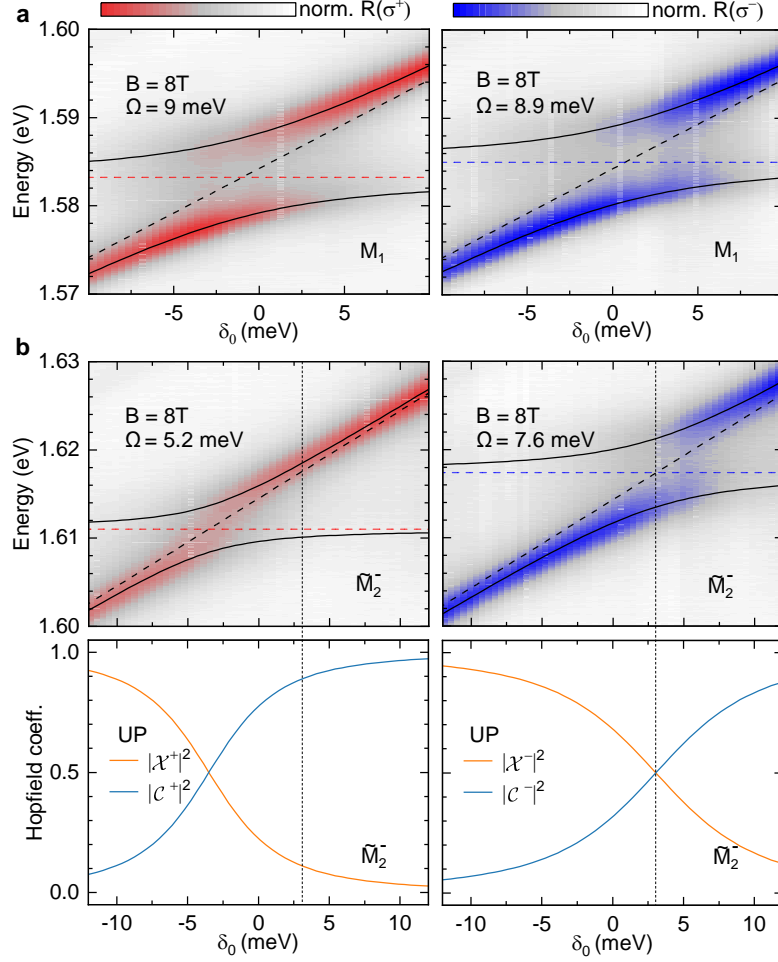


Figure 5.6.: **Magneto-optics of neutral and charged moiré polaritons at large magnetic field.** **a** and **b** (upper panel), Polarization-resolved reflection of M_1 exciton-polaritons and \tilde{M}_2^- polaron-polaritons at $V_G = 0$ and 11 V, respectively, in a magnetic field of $B = 8$ T as a function of the cavity length δ_0 . Black solid lines show the fits of the coupled oscillator model for σ^+ and σ^- circular polarization. The energies of the corresponding bare excitons are shown by red and blue dashed lines, while the field-independent cavity dispersion is shown by black dashed lines. The lower panel of **b** shows the corresponding exciton and photon Hopfield coefficients of the \tilde{M}_2^- upper polariton branch with σ^+ and σ^- polarization. The dashed vertical lines mark the cavity length for zero resonance detuning in σ^- polarization, where the exciton Hopfield coefficients differ significantly for the two circular polarizations ($|\mathcal{X}^+|^2 = 0.15$ for σ^+ and $|\mathcal{X}^-|^2 = 0.50$ for σ^- polarization).

For the following analysis, we introduce the effective Zeeman splitting between the peak energies of the upper/lower polariton branch with σ^+ and σ^- polarization as $\Delta E_{UP/LP} = E_{UP/LP}^+ - E_{UP/LP}^-$. To extract the respective polariton peak energies from the reflection spectra

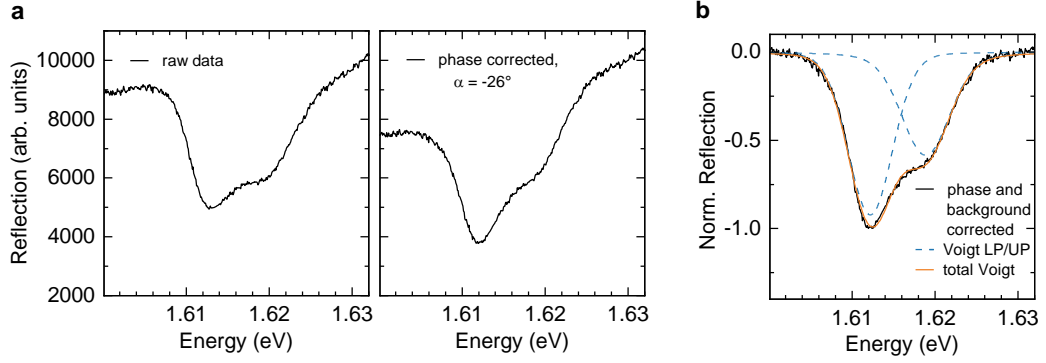


Figure 5.7.: **Deconvolution of polariton reflection spectra.** **a**, Left panel: Raw reflection spectrum of the Zeeman-split M_2^- polariton for a fixed cavity detuning and magnetic field. Right panel: Corresponding phase-corrected spectrum. **b**, Polynomial background correction and normalization of the phase-corrected spectrum allow to fit the lineshape with two Voigt profiles (orange solid line) of the corresponding upper (UP) and lower (LP) polariton resonances shown by blue dashed lines.

of the exciton-polaritons we applied a phase (Eq. (3.1) with $\alpha = -26^\circ$) and subsequent background correction to the raw spectra, as shown in Figure 5.7a. The polariton peak energies were determined by fitting the corrected lineshape using the Voigt function in Eq. (3.9) for each polariton branch:

$$V(E) = [G(L_1 + L_2)](E) = \int G(E')L_1(E - E') + G(E')L_2(E - E')dE', \quad (5.1)$$

as shown in Figure 5.7b. Here, the contributions of two Lorentzians L_1 and L_2 account for the upper and lower polariton resonance, the Gaussian function G for vibration-induced broadening as well as for spatial inhomogeneity of the underlying exciton resonance within the waist of the cavity mode.

With the cavity length set to $\delta_0 = 1.4$ (3.9) meV around the on-resonance condition for the σ^- branch of the M_1 (\tilde{M}_2^-) polariton at $B = 8$ T, we determine the effective Zeeman splitting between the two circularly polarized upper polariton branches, shown explicitly in Figure 5.8a for the upper polariton branch of \tilde{M}_2^- at $V_G = 11$ V. Remarkably, in this large-field limit, the evolution of ΔE_{UP} with the gate voltage in Figure 5.8b shows very distinct behaviors for M_1 and \tilde{M}_2^- polaritons. As the voltage-induced electron filling per moiré cell is increased from 0 to 1, the upper polariton splitting ΔE_{UP} remains constant at -1 meV in the voltage range of M_1 between 0 and 4 V, then undergoes a jump to -1.5 meV with the onset of \tilde{M}_2^- at 8 V, and evolves gradually to its lowest value close to -3 meV at 11 V.

To understand this behavior, we first note that by setting the cavity resonance to zero spectral detuning for the bare exciton Zeeman branch with σ^- polarization (crossing points of blue and black dashed lines in the right panels of Figure 5.6a and b), the cavity mode

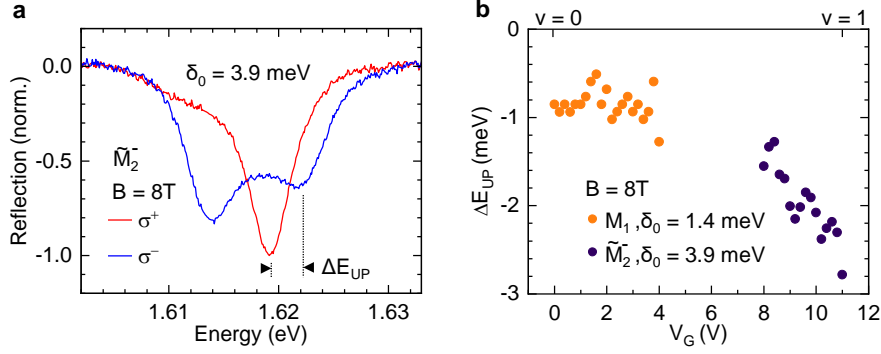


Figure 5.8.: **Magneto-optics of neutral and charged moiré polaritons at large magnetic field.** **a**, Polarization-resolved spectra of \tilde{M}_2^- polaron-polariton with the Zeeman splitting of the upper polariton branch ΔE_{UP} , shown for a cavity length corresponding to the on-resonance condition for σ^- polarization as indicated by dotted vertical lines in Figure 5.6b. **b** ΔE_{UP} of M_1 and \tilde{M}_2^- as a function of V_G in gate voltage regimes of strong coupling.

is blue detuned by the exciton Zeeman splitting with respect to the σ^+ polarized exciton Zeeman branch. Since the presence of the \tilde{M}_2^- exciton resonance is accompanied by an increase in the oscillator strength and thus in the Rabi splitting Ω up to electron filling of $\nu = 1$ (Figure 5.5c), the respective on-resonance σ^- polariton branch is affected by the gate voltage, whereas the σ^+ branch remains almost unchanged due to its primarily photonic nature. The corresponding photon and exciton Hopfield coefficients of polarization-resolved \tilde{M}_2^- upper polaritons at 8 T are shown in the lower panels of Figure 5.6b. Thus, the energy splitting ΔE_{UP} between the two circularly polarized upper polariton branches is the combined result of the exciton Zeeman splitting and the polarization-dependent Rabi splitting for a given cavity-exciton resonance detuning. Consequently, the constant and monotonously evolving Zeeman splittings ΔE_{UP} of the M_1 and \tilde{M}_2^- upper polaritons in Figure 5.8b reflect the respective absence and presence of doping-induced magnetism, which peaks at an electron doping of $\nu = 1$ ($V_G = 11$ V) and thus yields the maximum Zeeman splitting for the \tilde{M}_2^- upper polariton with a value roughly three times that of M_1 .

We point out that both σ^+ and σ^- branches are clearly pronounced for both M_1 and \tilde{M}_2^- polaritons even in the large-field limit (Figure 5.6a and b). Consequently, the enhancement in the polariton Zeeman splitting is distinct from the apparently giant paramagnetic response of MoSe₂ monolayer polaron [67] and its polaron-polariton counterpart [181]. There, at high magnetic fields, the respective σ^+ polarized lower-energy Zeeman exciton and polariton branches exhibit nearly complete quenching of the oscillator strength due to Pauli blocking, which leads to an effectively enhanced splitting [67, 181]. Here, field-dependent Rabi splitting is completely absent for charge-neutral M_1 exciton-polaritons, just like for the

neutral exciton in monolayer MoSe_2 [157, 200]. Electron doping conditions a change in the oscillator strength for the polarized branches of the \tilde{M}_2^- polaron-polariton with magnetic field, yielding different Rabi splittings for polariton branches with σ^+ and σ^- polarization at 8 T (Figure 5.6b). This moderate reduction of the oscillator strength as opposed to the complete quenching of one polarization in the case of the attractive polaron in MoSe_2 monolayers is the result of the spatial separation between the \tilde{M}_2^- exciton wavefunction and the moiré lattice sites of ordered and spin-polarized electrons (see Section 4.4).

5.3.2. Nonlinear polariton response to varying magnetic fields

In the following, we focus on electron-dressed moiré polaritons at low magnetic fields ($|B| \leq 1$ T), where correlated magnetism of charge-spin lattices is most pronounced as shown in Section 4.4.3. For a fixed cavity detuning $\delta_0 = 5.2$ meV, the \tilde{M}_2^- polaron-polariton branches develop pronounced Zeeman shifts already at small magnetic fields, as obvious from Figure 5.9a. Moreover, the Zeeman splittings of the upper and lower polariton branches ΔE_{UP} and ΔE_{LP} , shown in Figure 5.9b for different cavity detunings δ_0 , follow a highly nonlinear evolution with enhanced effective Landé factors in the low-field limit. This behavior is analogous to the nonlinear evolution of the \tilde{M}_2^- moiré polaron g -factors presented in Section 4.4.3. The Zeeman splitting of the neutral M_1 exciton-polariton, in contrast, is linear throughout the whole range of magnetic fields in Figure 5.9c, and the corresponding effective polariton g -factor stems from the conventional paramagnetic response of the M_1 exciton.

Consistently, the effective Landé factors of the M_1 upper and lower polariton branches are determined by the light and matter constituent according to the Hopfield coefficients, which in turn are controlled by the cavity resonance detuning. In the absence of doping, the effective polariton Landé factors derive from the linear Zeeman shift of the neutral moiré exciton as shown in Figure 5.9e. The symmetric evolution of $g_{\text{UP/LP}}$ around $\delta_0 = 0$ is asymptotically bounded at large cavity detunings by the photon and exciton g -factor of 0 and -4 , respectively. Remarkably, this symmetry is absent for \tilde{M}_2^- polaron-polaritons in Figure 5.9d: While g_{UP} exhibits a large negative value at a positive detuning $\delta_0 = 7.9$ meV ($g_{\text{UP}} = -8.0$ in the right panel of Figure 5.9b), its g_{LP} counterpart is much smaller at the corresponding negative detuning $\delta_0 = -6.6$ meV ($g_{\text{LP}} = 1.4$ in the left panel of Figure 5.9b) and, strikingly, even turns positive.

This feature is inexplicable on the basis of the underlying bare exciton g -factor alone. In fact, it is a prime consequence of correlated magnetism on the electron-spin lattice, which conditions polarization-sensitive Rabi splitting of the \tilde{M}_2^- polaron-polariton at finite magnetic fields as we explain in the following.

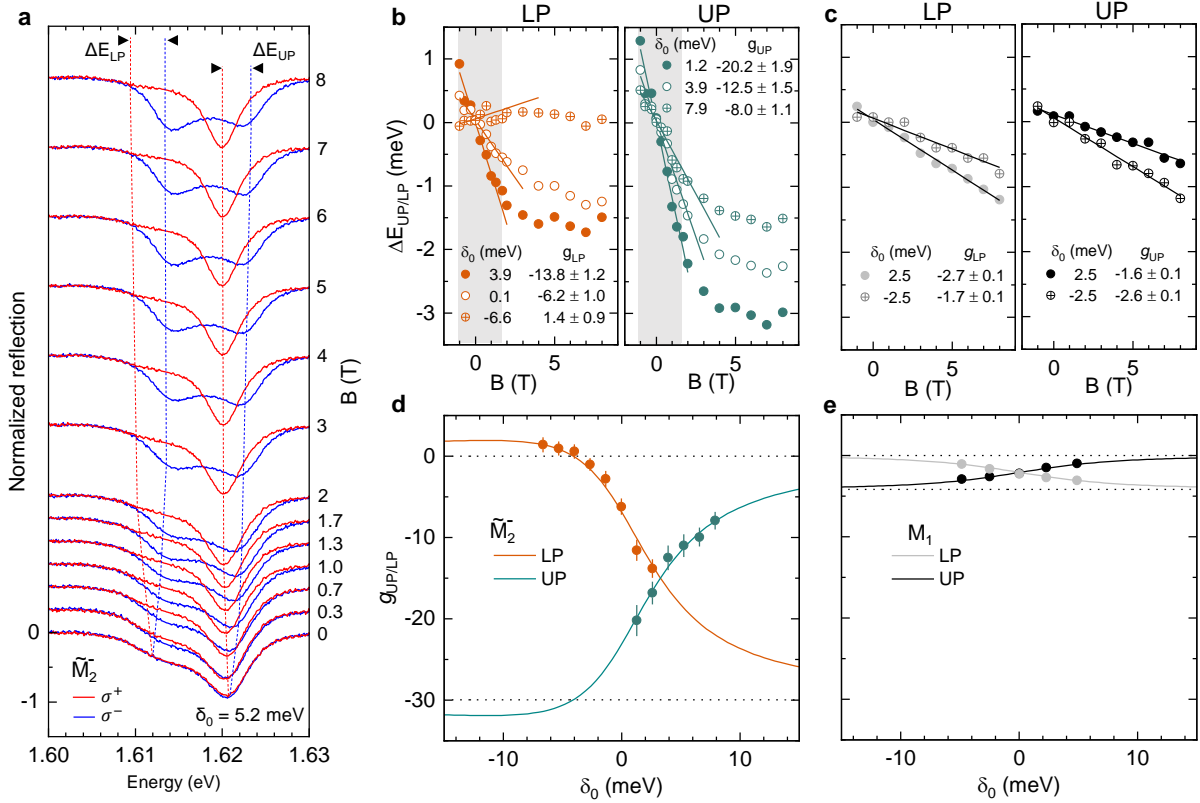


Figure 5.9.: **Magneto-optics of neutral and charged moiré polaritons at small magnetic fields.** **a** Polarization-contrasting reflection spectra of \tilde{M}_2^- polaron-polariton with increasing magnetic field for a fixed resonance detuning $\delta_0 = 5.2$ meV at $B = 0$ T. The dotted red and blue lines are guides to the eye. **b**, Nonlinear effective Zeeman splitting $\Delta E_{LP/UP}$ of \tilde{M}_2^- lower (upper) polariton branch in the left (right) panel as a function of the magnetic field for selected detunings δ_0 . Solid lines show linear fits to the data at small fields ($|B| \leq 1$ T highlighted in grey), yielding the effective upper/lower polariton g -factors $g_{UP/LP}$. **c**, Zeeman splittings $\Delta E_{LP/UP}$ of M_1 lower (upper) polariton branch in the left (right) panel exhibit linear dispersion over the whole range of magnetic fields for $\delta_0 = \pm 2.5$ meV. **d**, Effective Landé factors $g_{UP/LP}$ for \tilde{M}_2^- lower (orange) and upper (turquoise) polariton branch calculated from the coupled oscillator model for small magnetic fields $|B| \leq 1$ T; the data (circles in corresponding colors) are shown for various detunings δ_0 with error bars from linear fits as in **b**. **e**, Calculated $g_{UP/LP}$ of the M_1 upper (black) and lower (grey) polariton branch with a symmetric dependence on δ_0 and effective polariton g -factors (circles) obtained from linear fits as in **c**. The lower horizontal dashed lines in **d** and **e** indicate the g -factors of bare \tilde{M}_2^- and M_1 states, respectively.

5.3.3. Role of the polarization-contrasting Rabi splitting

In a first step, we examine the evolutions of the energy and oscillator strength of the respective bare M_1 moiré exciton and \tilde{M}_2^- moiré polaron states with magnetic field in the absence of the top DBR mirror. With Section 4.4 in mind, we recall that due to different localization sites of moiré excitons M_1 and M_2 , electron doping at integer filling ($\nu = 1$) gives rise to moiré polarons M_1^- with co-localized electrons and wavefunctions of the moiré exciton M_1 , whereas the bulk part of the M_2 moiré exciton wavefunction resides on a moiré site that is distant from the electron localization site, conditioning a distinct charge-doping behavior of the \tilde{M}_2^- polaron (see Section 4.4.1) [P2].

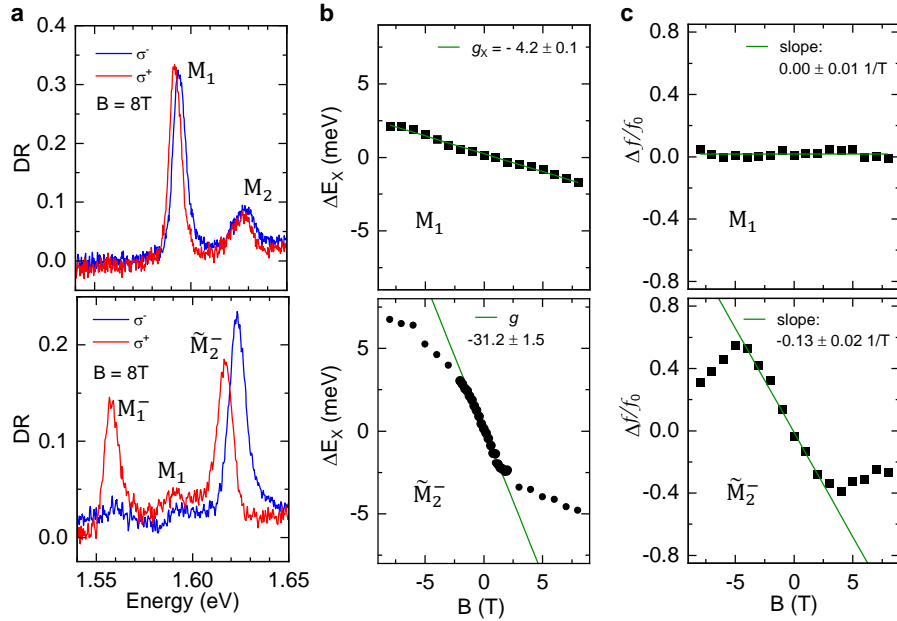


Figure 5.10.: **Polarization-contrasting valley Zeeman splittings and oscillator strengths of moiré excitons and polarons.** **a**, Polarization-contrasting DR spectra of neutral moiré excitons M_1 and M_2 (upper panel) and electron-dressed moiré polarons M_1^- and \tilde{M}_2^- ($\nu = 1$, lower panel) at 8 T in confocal spectroscopy without top DBR mirror (cp. Figure 4.16a). In the neutral regime, M_1 and M_2 moiré peaks exhibit equal oscillator strength for both polarizations. In contrast, at electron filling $\nu = 1$, the attractive polaron M_1^- around 1.56 eV is nearly completely polarized, whereas the \tilde{M}_2^- polaron around 1.62 eV is only partially polarized. The Zeeman-split resonances around 1.59 eV belong to the repulsive polaron of M_1 . **b**, Zeeman splitting of M_1 moiré excitons (upper panel) and \tilde{M}_2^- moiré polarons (lower panel) as a function of the magnetic field, with respective g -factors determined from linear slopes in red solid lines (cp. Figure 4.7d and Figure 4.16c). **c**, Evolution of the degree of polarization of M_1 moiré excitons (upper panel) and \tilde{M}_2^- moiré polarons with magnetic field, shown as the field-induced change of the oscillator strength Δf normalized by the oscillator strength at zero field f_0 .

Consistently, the response of the M_1^- and \tilde{M}_2^- moiré polarons to magnetic field is distinct from the neutral moiré exciton states M_1 and M_2 , and from each other. As shown in the DR spectra of Figure 5.10a, recorded in a magnetic field of 8 T without the top DBR mirror, the bare M_1 and M_2 moiré exciton states exhibit the characteristic valley Zeeman splitting with equal oscillator strengths of σ^+ and σ^- polarized branches (top panel of Figure 5.10a). For the moiré exciton M_1 , the corresponding g -factor is determined by the linear slope of the Zeeman splitting between the peak energies of the two polarized branches as $g_X = -4.2 \pm 0.1$ (top panel of Figure 5.10b), and the change in the oscillator strength between the two Zeeman-split branches Δf (normalized by the zero-field value f_0) is zero (top panel of Figure 5.10c). The bare M_1^- and \tilde{M}_2^- polarons, on the other hand, exhibit drastically different characteristics in the presence of magnetic field. First, we note that the σ^- polarized M_1^- branch is nearly completely quenched at 8 T, whereas both \tilde{M}_2^- peaks retain finite oscillator strength in both σ^- and σ^+ polarization (bottom panel of Figure 5.10a). This stark difference is consistent with the strong Pauli blocking of the σ^- polarized Zeeman branch of the attractive polaron M_1^- forming by co-localization of the M_1 moiré exciton wavefunction with lattice electrons at $\nu = 1$ [37]. The \tilde{M}_2^- polaron with marginal electron co-localization, in contrast, shows much reduced quenching. For this reason, the evolution of both Zeeman branches of the \tilde{M}_2^- polaron can be traced up to highest positive and negative magnetic fields of ± 8 T, as shown for the Zeeman splitting and the change in the oscillator strength in the bottom panels of Figure 5.10b and c, respectively: The respective g -factor exhibits the nonlinear behavior characteristic of correlation-induced magnetism with $g_X = -31.2 \pm 1.5$ at low magnetic fields, and the difference in the oscillator strength of σ^+ and σ^- polarized Zeeman branches changes by moderate 40% between zero and 3 T.

In the framework of M_1 and \tilde{M}_2^- polaritons, any change in the oscillator strength with magnetic field should result in polarization-contrasting Rabi splittings

$$\Delta\Omega(B) = \Omega^+(B) - \Omega^-(B). \quad (5.2)$$

From the analysis in Figure 5.10c, we expect a field-independent Rabi splitting between the two polarized M_1 polariton branches, whereas the field-induced change in the oscillator strength of the bare \tilde{M}_2^- polaron will result in a field-dependent Rabi splitting for the σ^+ and σ^- polarized upper and lower \tilde{M}_2^- polaron-polariton branches. At sufficiently small magnetic fields, the polarization of the electron-spin lattice can be approximated by a linear function [55], and the resulting linearized polarization-contrasting Rabi splitting $\Delta\Omega(B)$ is approximately described by the dimensionless parameter g_Ω introduced in analogy to the exciton g -factor:

$$g_\Omega = \frac{\Delta\Omega}{\mu_B B} = \frac{\Omega^+(B) - \Omega^-(B)}{\mu_B B}, \quad (5.3)$$

and Ω^n is given by

$$\Omega^{\eta}(B) = \Omega_0 + \eta \frac{g_{\Omega} \mu_B B}{2}, \quad (5.4)$$

with the zero-field Rabi splitting Ω_0 .

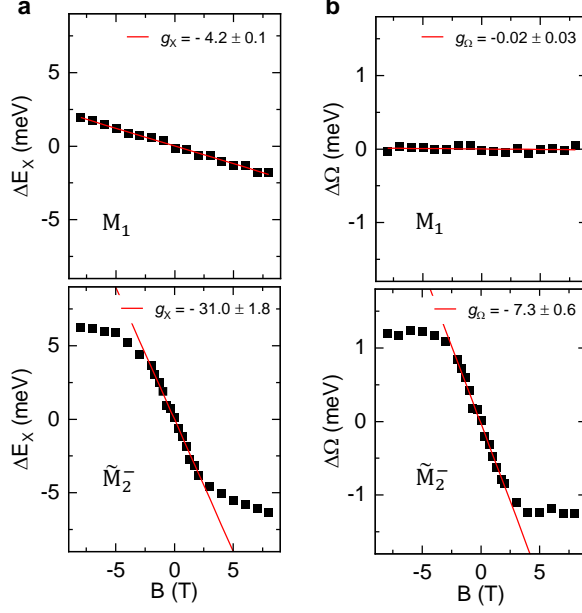


Figure 5.11.: **Polarization-contrasting valley Zeeman and Rabi splittings of neutral and charged moiré polaritons.** **a**, Zeeman splitting of M_1 moiré exciton-polariton (upper panel) and \tilde{M}_2^- moiré polaron-polariton (lower panel) as a function of the magnetic field. **b**, Change in the Rabi splitting with magnetic field for σ^+ and σ^- polarized branches of the M_1 exciton-polariton (upper panel) and \tilde{M}_2^- polaron-polariton. The exciton energies and Rabi splittings in **a** and **b** were obtained from fitting Eq. (5.13) to the respective data.

The consequences of the field-independent and field-dependent oscillator strengths of the M_1 moiré exciton and the \tilde{M}_2^- polaron for the respective polariton Rabi splittings are shown in 5.11b. From the analysis of the polarization-resolved reflection contrast of M_1 exciton-polaritons and \tilde{M}_2^- polaron-polaritons at different magnetic fields and cavity-exciton detunings, we obtained the respective exciton Zeeman and Rabi splittings shown in the top and bottom panels of 5.11a and b, respectively. The evolution of the M_1 polariton Zeeman splitting is linear in the magnetic field and the extracted exciton g -factor $g_x = -4.2 \pm 0.1$ (top panel of 5.11a) matches the one observed for the bare moiré exciton (top panel of 5.10b). Its Rabi splitting is consistently independent of the magnetic field (top panel of 5.11b) and makes no additional contribution to the effective g -factor with $g_{\Omega} = -0.02 \pm 0.03$. For the \tilde{M}_2^- polariton, in contrast, both the exciton Zeeman and the Rabi splitting are nonlinear in magnetic field (bottom panels of 5.11a and b), with $g_x = -31.0 \pm 1.8$ and $g_{\Omega} = -7.3 \pm 0.8$ in the small-field limit of $|B| \leq 1$ T. These two effective g -factors g_x and g_{Ω} quantify the

contribution the behavior of the \tilde{M}_2^- polaron-polariton branches at small magnetic fields as we show in the following Section 5.3.4.

For consistency we check the connection between the polarization-contrasting Rabi splitting with $g_\Omega = -7.3$ at small magnetic fields (bottom panel of Figure 5.11b) and the polarization-contrasting oscillator strength observed for \tilde{M}_2^- which we denote with $g_f = -0.13 \text{ T}^{-1}$ (lower panel of Figure 5.10c). Analogously to Eq. (5.4), we can introduce the B -field dependence for the relative oscillator strength of the σ^+ and σ^- polarized exciton ($\eta = +/-$):

$$f^\eta(B) = 1 + \eta \frac{g_f B}{2}. \quad (5.5)$$

Using the relation between the Rabi splitting and oscillator strength from Eq. (2.32) we find:

$$\Omega^\eta(B) = \alpha \sqrt{f_0 f^\eta(B)}, \quad (5.6)$$

where α is the proportionality coefficient and f_0 is the oscillator strength for $B = 0 \text{ T}$.

Using above equations we can calculate the Rabi splitting

$$\Omega^\eta(B) = \alpha \sqrt{f_0 (1 + \eta g_f B/2)}, \quad (5.7)$$

and find a simplified expression after a Taylor expansion:

$$\Omega^\eta(B) \approx \alpha \sqrt{f_0 (1 + \eta g_f B/4)} = \Omega_0 + \eta \frac{g_f \Omega_0 B}{4}. \quad (5.8)$$

Comparing Eq. (5.4) with Eq. (5.8) we obtain

$$g_\Omega = \frac{g_f \Omega_0}{2\mu_B}. \quad (5.9)$$

With $\Omega_0 = 6.2 \text{ meV}$ (see lower panel of Figure 5.5) in Eq. (5.9), we find consistency in the connection between $g_f = -0.13 \text{ T}^{-1}$ and g_Ω :

$$\text{From fitting in Fig. 5.11} \quad g_\Omega = -7.3 \pm 0.6 \quad (5.10)$$

$$\text{and using Eq. (5.9)} \quad g_\Omega = -\frac{0.13 \cdot 6.2}{2 \cdot 0.058} = -6.9. \quad (5.11)$$

5.3.4. Modelling of effective polariton g-factors

To model the evolution of the upper and lower polariton states with the magnetic field, we used a coupled oscillator model (as derived in Section 2.2) with a 4×4 Hamiltonian, with columns and rows related to the exciton transition with energy E_X^+ (E_X^-) and σ^+ (σ^-) polarization coupled to the cavity field with energy E_c and σ^+ (σ^-) polarization at Rabi

splitting Ω^+ (Ω^-):

$$H = \begin{pmatrix} E_X^+ & \Omega^+/2 & 0 & 0 \\ \Omega^+/2 & E_C & 0 & 0 \\ 0 & 0 & E_X^- & \Omega^-/2 \\ 0 & 0 & \Omega^-/2 & E_C \end{pmatrix}. \quad (5.12)$$

The cavity dispersion E_C is assumed to be a linear function of the cavity length and independent of the external magnetic field. The eigenenergies of the Hamiltonian in Eq. (5.12) corresponding to the upper and lower polariton branch UP and LP, respectively, with σ^+ and σ^- polarization ($\eta = +/-$) are given by

$$E_{\text{UP/LP}}^\eta = \frac{E_C + E_X^\eta}{2} \pm \frac{1}{2} \sqrt{(E_C - E_X^\eta)^2 + (\Omega^\eta)^2}. \quad (5.13)$$

The contribution of the bare exciton valley Zeeman splitting $\Delta E_X(B)$ is given by:

$$\Delta E_X(B) = E_X^+(B) - E_X^-(B), \quad (5.14)$$

with the magneto-dispersion of the circularly-polarized exciton Zeeman branches determined by the exciton Landé factor g_X as:

$$E_X^\eta(B) = E_0 + \eta \frac{g_X \mu_B B}{2}, \quad (5.15)$$

where E_0 is the exciton energy at zero magnetic field and μ_B is the Bohr magneton.

With both contributions, namely the exciton Zeeman splitting and the polarization-contrasting Rabi splitting, we calculate the effective g -factor of the upper and lower polariton $g_{\text{UP/LP}}$ by inserting $E_X^\eta(B)$ and $\Omega^\eta(B)$ from Eqs. (5.15) and (5.4) into Eq. (5.13). In the general case this yields:

$$g_{\text{UP/LP}} = \frac{\Delta E_{\text{UP/LP}}}{\mu_B B} = \frac{E_{\text{UP/LP}}^+ - E_{\text{UP/LP}}^-}{\mu_B B}, \quad (5.16)$$

and in the linearized low-field limit of Eqs. (5.3) and (5.4) we derive:

$$g_{\text{UP/LP}} = \frac{g_X}{2} \pm \frac{g_X \delta_0 + g_\Omega \Omega_0}{2\sqrt{\delta_0^2 + \Omega_0^2}} + \mathcal{O}(B^2), \quad (5.17)$$

with the zero-field cavity-exciton detuning $\delta_0 = E_C - E_0$.

For large detunings δ_0 , the effective polariton g -factors approach the limiting values of 0 and g_X , when the polariton becomes predominantly photonic and excitonic, respectively. At zero detuning $\delta_0 = 0$, the difference between the effective g -factors of the upper and lower polariton branch is determined by g_Ω as $(g_{\text{UP}} - g_{\text{LP}})|_{\delta_0=0} = g_\Omega$. Consequently, field-dependent polarization-contrasting Rabi splitting yields finite g_Ω , and this conditions an

asymmetric evolution of $g_{\text{UP/LP}}$ as function of the cavity detuning δ_0 , as observed for the \tilde{M}_2^- polaron-polariton in Figure 5.9d, in contrast to the symmetric evolution of the M_1 exciton-polariton g -factor in the respective Figure 5.9e. Both cases are well captured by our model, applying Eq. (5.17) with g_Ω and g_X within the error interval of the experimentally determined values in Figure 5.11 ($g_\Omega = -7.8$ and $g_X = -30$ in case of \tilde{M}_2^- , $g_\Omega = 0$ and $g_X = -4.2$ in case of M_1).

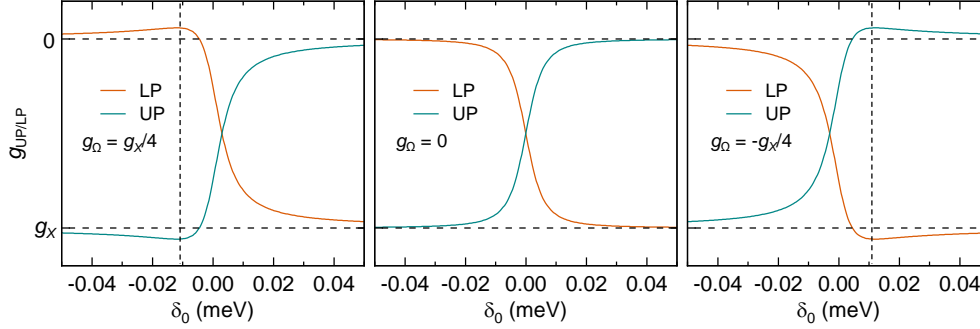


Figure 5.12.: **Effective polariton Landé factors as a function of the cavity detuning.** Upper and lower polariton g -factors $g_{\text{UP/LP}}$, calculated using Eq. (5.17) for a negative exciton g -factor g_X and $g_\Omega = g_X/4$ (left panel), 0 (central panel), and $-g_X/4$ (right panel), respectively. The vertical dashed lines indicate cavity resonance detunings where the upper and lower polariton g -factors exhibit extrema for non-vanishing g_Ω .

Finally, it is instructive to discuss the asymmetry in the evolution of the effective polariton g -factor $g_{\text{UP/LP}}$ with the cavity detuning δ_0 on the basis of the model results shown in Fig. 5.12. Obviously, in magnetic fields within the linear-response condition, finite g_Ω renders the dependence of the polariton g -factors asymmetric for negative and positive detunings, with asymmetry depending on whether the signs of g_Ω and the exciton g -factor g_X are equal or opposite. In the former case of $\text{sgn}(g_\Omega) = \text{sgn}(g_X) = -1$, the upper polariton g -factor g_{UP} is enhanced at intermediate detunings as compared to the bare exciton g -factor g_X , before approaching g_X asymptotically at large detunings. Analogously, g_{LP} changes its sign at intermediate detunings before approaching 0 at large δ_0 . By solving the equation $\partial g_{\text{UP/LP}} / \partial \delta_0 = 0$, we obtain the detuning at which the effective polariton g -factors have their extrema $\tilde{g}_{\text{UP/LP}}$. For $\text{sgn}(g_\Omega) = \text{sgn}(g_X) = -1$, and assuming $g_X \gg g_\Omega$, the respective extremal values are approximately given by

$$\tilde{g}_{\text{UP}} \approx g_X + \frac{g_\Omega^2}{g_X}, \quad (5.18)$$

$$\tilde{g}_{\text{LP}} \approx -\frac{g_\Omega^2}{g_X}. \quad (5.19)$$

This result underscores the pivotal role of cavity control within our system. The $\text{MoSe}_2/\text{WS}_2$ heterostructure alone serves as an intriguing platform for investigating electron-spin correlated many-body phenomena through the magneto-optical response of moiré excitons. Incorporating the heterostructure into the optical microcavity not only endows the excitonic properties to the emergent polariton states and their photonic constituents. In fact, by mixing both contributions – the exciton Zeeman splitting and spin-polarization – the cavity introduces a novel degree of control. This enables the tuning of the magneto-optical response of moiré polariton states beyond the intrinsic exciton behavior which becomes particularly clear from Eq. (5.18).

Summary and outlook

This thesis was dedicated to the investigation of TMD heterobilayers and the light-matter coupling of their excitons with photons in high finesse open microcavities. The TMD heterostructure of our choice was $\text{MoSe}_2/\text{WS}_2$, which at the time of the beginning of this work had not been investigated in detail, as earlier studies mainly focused on $\text{MoSe}_2/\text{WSe}_2$ [16, 17] or WSe_2/WS_2 heterostructures [20, 26, 28], both with well established type-II conduction band alignment. For $\text{MoSe}_2/\text{WS}_2$ on the other hand, theoretical studies predicted closely aligned conduction bands [15], while different experimental studies reported a wide range of conduction band offsets [36, 161].

Employing dual-gated van der Waals heterostacks, we developed the experimental and theoretical tools to shed light on the $\text{MoSe}_2/\text{WS}_2$ low energy bandstructure. In confocal spectroscopy, we identified intra- and interlayer moiré excitons in the charge neutral regime for both R- and H-type stackings of the $\text{MoSe}_2/\text{WS}_2$ heterobilayer. In the latter configuration, the conduction bands are closely aligned enabling resonance-tuning by out-of-plane electric fields, leading to interlayer hybridization, experimentally visualized by AC modulation spectroscopy. An effective continuum model captured the experimental signatures and provided a quantitative understanding of the intra- and interlayer moiré exciton bandstructure [P2]. The model is generally applicable to other systems [88] paving the way for future studies in related two-dimensional moiré structures.

We further investigated the electron doping characteristics of $\text{MoSe}_2/\text{WS}_2$ heterostructures. Both R- and H-type configurations featured the formation of charged moiré excitons with significant oscillator strength, dependent on the spatial overlap of moiré-modulated exciton and electron wavefunctions [165]. Pronounced Coulomb-correlated behavior of these states at an electron filling of $\nu = 1$ inside the MoSe_2 layer results in a renormalized exciton g -factor at small magnetic fields, consistent with observations in comparable systems [28, 29]. The H-type stacking stands out with a distinctive layer-by-layer electron charging response, as determined from capacitor model simulations: With increasing electron

density, the first and second electron per moiré unit cell occupy the MoSe₂ and WS₂ layer, respectively, enabling the study of magnetic correlations of a vertically offset bilayer spin lattice at electron filling $1 < \nu < 2$. This study, conducted beyond the main-scope of this thesis, involved a low-temperature measurement series of the doping-dependent exciton g -factor in a dilution refrigerator. Robust g -factor fluctuations between $1 < \nu < 2$ suggested the presence of Ruderman-Kittel-Kasuya-Yosida (RKKY) magnetism [173, 174], arising from coupling between mobile electrons in the WS₂ layer and the localized spin lattice inside the MoSe₂ layer [P3, 172]. Interestingly, the extracted negative Curie temperature implied an antiferromagnetic order of the MoSe₂ spin-lattice at $\nu = 1$. This contrasts with the recently reported ferromagnetic order in R-type MoSe₂/WS₂ [37], prompting further debate and investigations.

Alongside our investigation of MoSe₂/WS₂ heterostructures, we implemented and characterized a fiber-based open microcavity setup developed in collaboration with Khaled Karraï at attocube systems AG [P8, 139]. Operating the cavity setup within a closed-cycle cryostat necessitates sophisticated damping mechanisms to minimize vibration-induced cavity length fluctuations. Combining passive and active vibration isolation techniques, we achieved high cavity stability, with cavity length fluctuations of less than 100 pm rms under ideal environmental conditions [P8]. This performance qualifies the platform for cavity QED experiments, with a resolvable finesse of up to 10^4 at cryogenic temperatures. In subsequent experiments, despite challenging conditions and increased environmental vibrational noise, the cavity was operated at a finesse of up to 10^3 , corresponding to a resolution well above the linewidth of TMD intralayer excitons.

A well-established understanding of the MoSe₂/WS₂ low-energy physics, along with the operational high-finesse open microcavity platform at cryogenic temperatures, enabled us to investigate the light-matter interaction between cavity photons and TMD moiré excitons. Using a R-type MoSe₂/WS₂ heterostructure inside the microcavity, we observed the emergence of moiré exciton-polariton branches at small mode orders as a hallmark of the strong light-matter coupling regime. Confirming earlier findings [38], we identified nonlinearity in the power dependent response of moiré exciton-polaritons as compared to bare monolayer MoSe₂ exciton-polaritons. The efficient transfer of oscillator strength from neutral to charged moiré excitons under gate controlled electron doping enabled the study of moiré polaron-polaritons, exhibiting even higher power-dependent nonlinearities. Our demonstration of moiré exciton-polaritons at an electron filling of $\nu = 1$ prompted an exploration of correlated magnetism-induced polariton behavior. We utilized a different open microcavity setup with access to out-of-plane magnetic fields, in a collaboration with Christian Schneider's group at the University of Oldenburg. Here, we discovered a highly nonlinear magneto-optical response of moiré polaron-polaritons arising from the presence of a correlated electron-spin lattice. The extracted effective polariton g -factors were controlled via the cavity-exciton detuning and appeared to be enhanced as compared to the uncoupled moiré

exciton counterpart at specific exciton Hopfield coefficients. This behavior is explained by an intricate cavity-induced interplay of correlation-induced exciton Zeeman splitting and correlation-induced polarization contrasting exciton oscillator strength [P4].

In summary, we studied the moiré exciton physics of MoSe₂/WS₂ heterostructures and investigated the emergence of correlation-induced magnetism resulting from the interaction between moiré excitons and ordered phases of elementary charges. Additionally, by establishing a coupling condition with photons confined in optical microcavities, previously independent correlation-induced properties of uncoupled moiré excitons became intertwined, paving the way for new avenues of controlling the observed states.

Our phenomenological theoretical model provided a comprehensive understanding of the observed optical features in MoSe₂/WS₂ heterostructures. However, our system, with its high degree of complexity and control, offers opportunities for obtaining deeper insights into the microscopic nature of moiré-induced many-body phenomena through further experimental and theoretical techniques. Electrical transport measurements could be leveraged to identify generalized Wigner crystal states as a function of the doping level [20]. Particularly in H-type samples, identifying correlated electronic phases within the regime of $1 \leq \nu \leq 2$ would aid in explaining the observed magnetic behavior. Furthermore, advancing Ohmic contact engineering in future devices will pave the way for complementary studies in the hole doping regime, which exhibits related signatures of correlation-induced magnetism. Various scanning transmission electron microscopy (STEM) techniques have served as advanced tools for visualizing effects of atomic reconstruction [115, 201] and exciton localization [202, 203] in moiré systems at a sub-nanometer scale, potentially complementing our optical studies on the nature of different moiré excitons. Advanced sample geometries incorporating an additional TMD monolayer in close proximity to the MoSe₂/WS₂ heterobilayer could be utilized to detect the emergence of electronic correlations via monolayer Rydberg exciton states, akin to studies on the fractional quantum Hall effect in graphene [204]. From a theoretical standpoint, conducting first-principle calculations would further solidify our understanding of the microscopic nature of the moiré exciton potential landscape [165].

Our observations of moiré exciton-polaritons mark a significant advancement towards leveraging moiré lattices and strong light-matter coupling to control condensed matter quantum many-body systems. The incorporation of an H-type MoSe₂/WS₂ device in our microcavity setup would complement the R-type studies outlined in this thesis. In this context, exploring interlayer hybridization within the realm of strong light-matter coupling holds particular promise. The achievement of long-lived dipolar polaritons has been a longstanding goal in the field of polariton physics, given their potential to implement strong photon-photon interactions, as evidenced in TMD homobilayer systems [205, 206]. Layer-hybrid moiré exciton-polaritons offer not just one but two possible mechanisms for exciton-exciton interaction-induced nonlinearities – moiré confinement and dipolar character – rendering

6. SUMMARY AND OUTLOOK

this configuration a compelling prospect for fundamental investigations in the field of quantum information processing [35].

In the spirit of Richard Feynman and his understanding of "the job of physics", our system provided us with an experimental playground that aroused our curiosity and keeps driving our research to gain deeper understanding of the intricate interactions of the involved elementary particles and to "analyze why each one wants what it wants" [1].

Extended data: Moiré exciton physics in MoSe₂/WS₂ heterostructures



We supplement the discussion on MoSe₂/WS₂ heterostructures in the Chapters 4 and 5 by providing additional information and presenting extended data. Section A.1 offers insights into the variation of conduction band alignments in MoSe₂/WS₂ heterostructures, while Section A.2 addresses the MoSe₂/WS₂ p-doping transition.

A.1. Laterally varying conduction band alignment

Within the scope of this study, we fabricated an additional heterostructure, denoted as D3, alongside D1 and D2 as detailed in Section 4.2. In Figure A.1a, an optical microscope image of the H-type device D3 is depicted, accompanied by a schematic illustrating its dual-gate layout. The optical response observed in DR mirrors the characteristics observed in D1 and D2, featuring low-energy moiré excitons M₁ and M₂ with pronounced oscillator strength in the charge-neutral regime. The optical quality of D3 is underscored by the narrow linewidths of the DR response in Figure A.1c ($\gamma_X \approx 2$ meV and $\gamma_{M_{1/2}} \approx 5 - 7$ meV).

However, the sample exhibits spatial inhomogeneities, as evidenced by mapping the moiré exciton energy in the heterobilayer region. Figure A.2a shows the variation of the M₁ peak energy across a DR map of a section of the HBL area, outlined by the black dashed frame in Figure A.1b. Over a few micrometers, the exciton energy shifts by more than 10 meV, while the spectral separation between M₁ and M₂ remains constant at 30 meV, as shown in Figure A.2b for two selected points **A** and **B**. This transition between regions **A** and **B**, characterized by significantly different exciton energies, occurs abruptly within a length scale below the resolution of the diffraction-limited optical spot.

Interestingly, the DR signal in domains **A** and **B** exhibits different responses to electron doping, as depicted in Figure A.2c and d. With an applied doping potential of $V_\mu = 7$ V

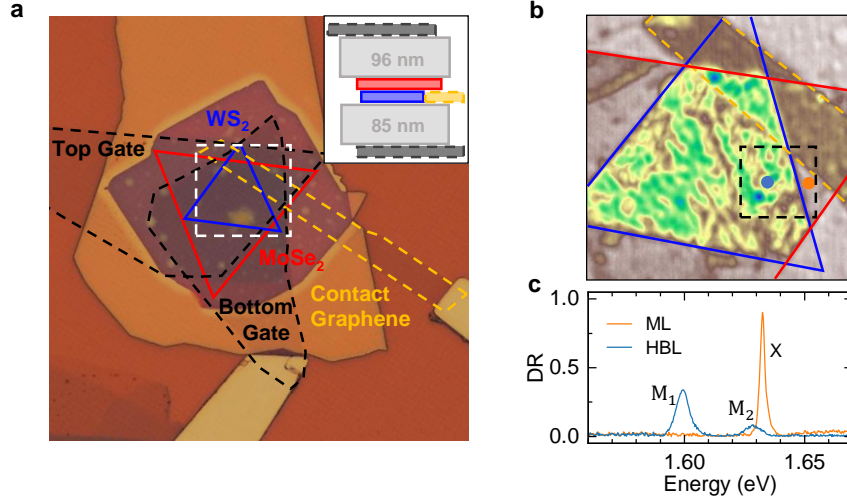


Figure A.1.: **Additional H-type device D3.** **a**, Optical microscope image of D3 with constituents of the heterostack highlighted by colored frames, the inset shows the stacking order of the device. **b**, Mapping the maximum of $d(\text{DR})/dE$ around the M_1 exciton resonance, highlights the $\text{MoSe}_2/\text{WS}_2$ HBL region. **c**, Charge neutral DR spectra of the bare MoSe_2 monolayer with pronounced X exciton resonance and $\text{MoSe}_2/\text{WS}_2$ HBL with moiré excitons M_1 and M_2 .

domain **B** displays signatures of electron doping, as discussed in Section 4.4.1, with the emergence of charged excitons M_1^- and \tilde{M}_2^- . Conversely, in domain **A**, neutral moiré excitons M_1 and M_2 continue to dominate the optical response.

A clearer understanding of this scenario emerges upon examining the complete DR dual-gate response of the HBL, shown in the upper panels of Figure A.3a and b for domains **A** and **B**, respectively. In the n-doping regime, both domains exhibit constant optical signatures over extended regions of $(V_\mu, F)^T$, indicating the formation of a stable incompressible correlated electron state in the MoSe_2 layer at electron filling $\nu_{\text{Mo}} = 1$, while electrons continue to occupy the WS_2 layer at the same time, as discussed for device D2 in Section 4.4.2.

We utilize the quantum capacitor model introduced in Section 4.1.2 to derive the electron filling in both layers as a function of $(V_\mu, F)^T$, illustrated in the lower panels of Figure A.3. Intriguingly, the effective conduction band offset varies spatially between domain **A** and **B** by more than 40 meV, explaining the contrasting responses observed in Figure A.2b. Domain **A** features a conduction band offset $\Delta_{CB} = 8$ meV. When a doping potential V_μ is applied without an electric field F , electrons populate the MoSe_2 layer first leading to the emergence of charged excitons M_1^- and \tilde{M}_2^- . In contrast, domain **B** exhibits a deep type-II band alignment with $\Delta_{CB} = -40$ meV, where electrons occupy the WS_2 layer first at small V_μ . We employed an onset Coulomb potential $U = 40$ meV for both layers in the two domains, defining the layer-by-layer charging condition (see Section 4.4.2 for details).

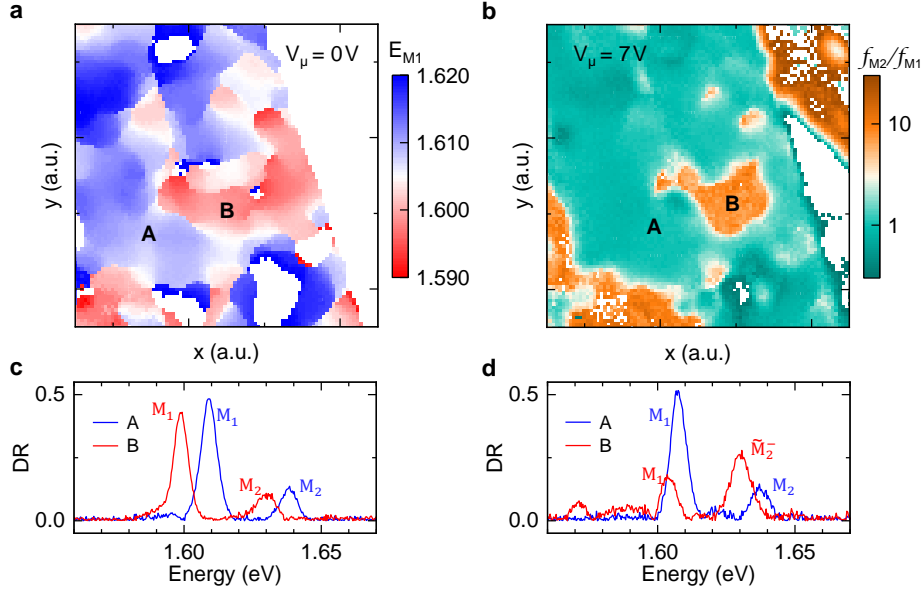


Figure A.2.: **Domain formation on MoSe₂/WS₂ HBL.** **a**, Spatial variation of DR M₁ exciton energy. The extent of the DR scan is highlighted by the dashed black frame in Figure A.1b. **b**, The visualization of the CB offset as a function of position, represented by the ratio of \tilde{M}_2^- exciton oscillator strength f_{M_2} to M₁ oscillator strength f_{M_1} at a doping potential $V_\mu = 7$ V. **c** and **d** show DR spectra acquired at positions A and B in **a** and **b**, respectively.

Notably, the only parameter of the capacitor model simulations for **A** and **B** that was altered besides the conduction band offset was the dielectric constant of the hBN encapsulating layers ($\epsilon = 5$ for **A** and $\epsilon = 4$ for **B**). This fact can provide insight into the origin of the spatially differing responses: Defect-induced local structural changes on the surface of CVD-grown TMDs, reported in various studies [207–210], can lead to changes in the direct dielectric environment due to oxidation at defects [211], explaining the change in refractive index, and correlation to work function [212] explains the change in conduction band offset.

We emphasize that the physical properties of the moiré excitons with narrow linewidths and exhibiting correlation-induced nonlinearities in the presence of charge doping remain robust despite the apparent presence of defects in CVD-grown monolayers. The range of observed conduction band offset of more than $\Delta_{CB} = \pm 40$ meV reflects the multiplicity of values reported in the literature [17, 36, 89, 158–161].

A.2. Signatures of the hole doping transition

All devices examined in this work exhibit a nearly ohmic contact response in the electron doping regime, with the evolution of charged exciton complexes progressing linearly with the

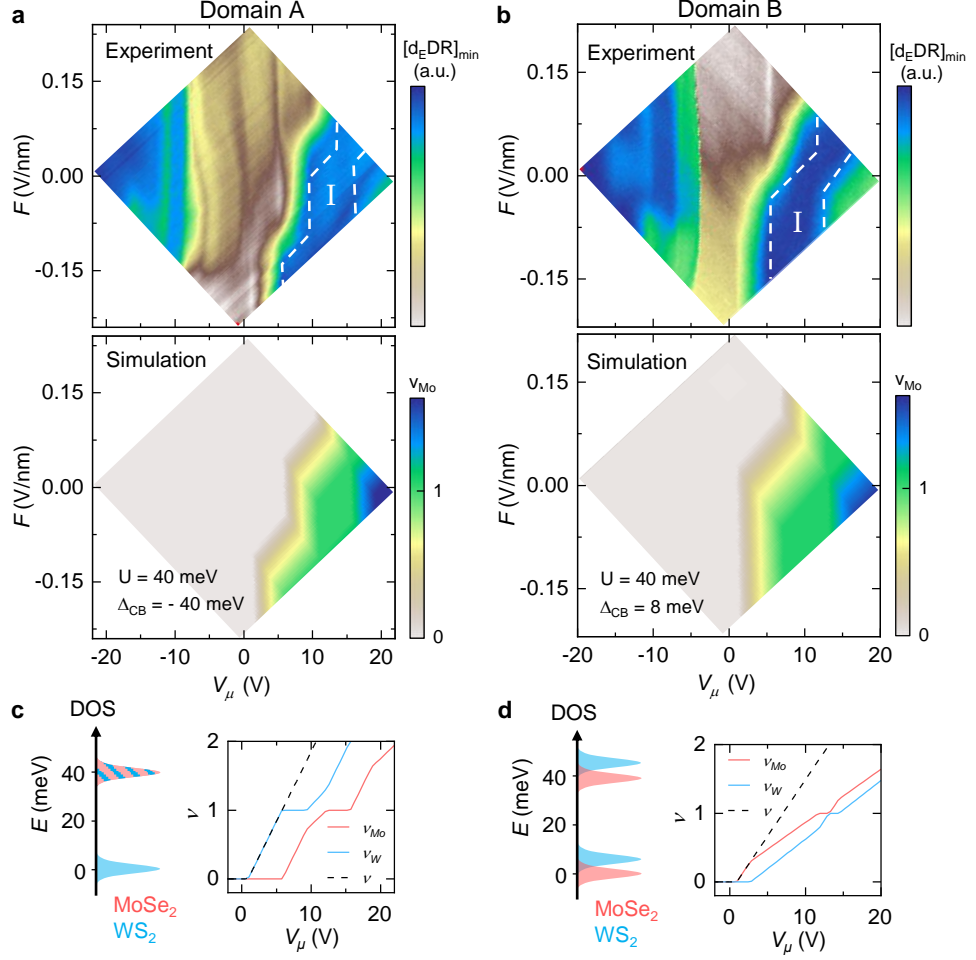


Figure A.3.: **Capacitor model analysis of domain A and B.** **a** and **b**, *Upper panels*: Maximum of the derivative $d(\text{DR})/dE$ between 1.600 and 1.65 eV for each point $(V_\mu, F)^T$ for domain **A** and **B**, respectively. The white dashed lines frame region I of unchanged response of charged excitons M_1^- and \tilde{M}_2^- . *Lower panels*: Electron filling per moiré unit cell obtained from the corresponding capacitor model simulations (see Section 4.1.2 for details). **c** and **d**, Simulated discretized density of states as function of the Fermi energy and electron density in the MoSe₂ layer ν_{Mo} , the WS₂ layer ν_{W} and the total electron density ν as function of V_μ .

doping potential V_μ . However, the transition to the p-doping regime displays nonlinearity concerning the applied gate voltages, as exemplified by device D1 in Figure A.4. In the absence of an applied electric field ($F = 0$ V/nm), the neutral moiré excitons M_1 and M_2 persist up to $V_\mu = -18$ V. Notably, this transition potential varies with different applied electric fields ($F \neq 0$ V/nm), as indicated by the red dashed line in Figure A.4a, suggesting an asymmetric response of the device to applied top gate (V_T) or bottom gate voltages (V_B).

This observation can be explained by considering a Schottky barrier at the interface between the TMD layer and the contact graphite layer, in combination with the geometry of the heterostack. Schottky barriers at TMD-graphite interfaces have been reported since the early studies of TMD-based field-effect devices [60, 213], arising from a mismatch in the semiconductor and metal work functions [214]. Considering the geometry of the D1 heterostack (left panel of Figure 4.6), we note that the top gate graphite layer overlaps with the area where the contact gate covers the TMD layer, unlike the bottom gate graphite layer. Consequently, the plate capacitor formed by the top gate and the contact gate exhibits higher capacitance than that formed with the bottom gate. To overcome the Schottky barrier at the p-doping transition using the top (bottom) gate individually, a relatively lower (higher) V_T (V_B) is necessary, explaining the observed asymmetry.

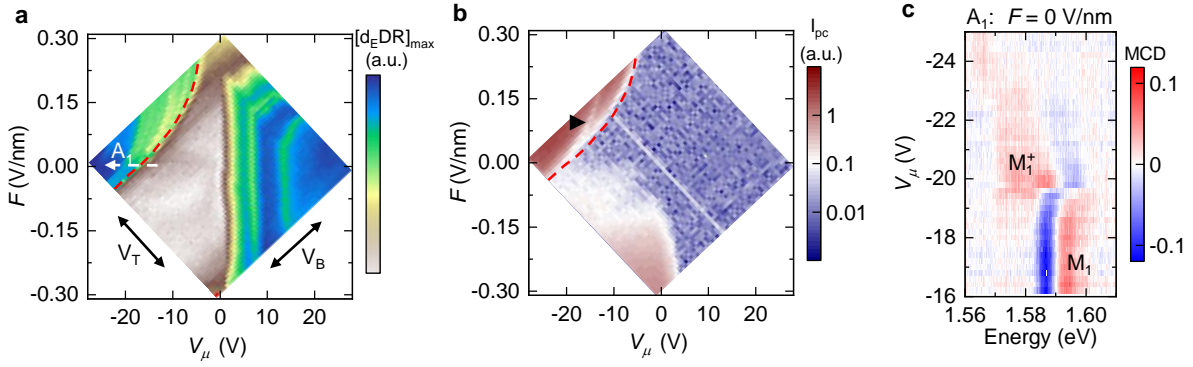


Figure A.4.: **Transition to the p-doped regime in R-type D1.** **a**, Maximum of the derivative $d(\text{DR})/dE$ between 1.600 and 1.65 eV for each point $(V_\mu, F)^T$. The black arrows indicate the basis of top (V_T) and bottom gate voltage (V_B) applied in the experiment, the red dashed line highlights the p-doping transition. **b**, Photocurrent I_{pc} for each point $(V_\mu, F)^T$. The transition to the p-doped regime is highlighted by the red dashed line, the black arrow points at a stripe of the $(V_\mu, F)^T$ exhibiting reduced I_{pc} . **c**, MCD response at $B = 8$ T at the p-doping transition along the white arrow A_1 in **a**.

The breakdown of the Schottky barrier leads to a highly nonlinear hole charging behavior concerning the applied doping potential V_μ . This is evident from the stepwise transition of the hole-charged moiré exciton M_1^+ evolution (see Figure 4.12a), posing challenges in quantifying the precise hole filling per moiré unit cell at a specific $(V_\mu, F)^T$. Nonetheless, we tried to explore the hole doping regime for signs of correlated hole behaviour as result of the moiré potential:

We carried out a photocurrent measurement utilizing a diode laser at 635 nm for excitation, power modulated between 0 – 5 μW at a frequency of 377 Hz. The photocurrent was measured with a lock-in amplifier at the contact gate as a function of the applied top and bottom gate voltages, as described in Section 3.2.3. Figure A.4b illustrates the measured photocurrent I_{pc} for each point of the $(V_\mu, F)^T$ diagram. The signal peaks in the p-doping

region, as evident from comparing the I_{pc} map with the DR map in Figure A.4a. Interestingly, only hole-mediated charge transfer can be visualized in this type of measurement. However, the origin of this phenomenon was not investigated within the scope of this work. Within the p-doping regime, the photocurrent does not exhibit homogeneity; instead, it features a notable dip across a line of the $(V_\mu, F)^T$ diagram, marked by the black arrow in Figure A.4b. This dip could be interpreted as the formation of an incompressible Mott insulating state at an integer hole filling per moiré unit cell, which hinders charge flow due to on-site Coulomb repulsion, as observed in transport measurements for other TMD heterobilayer systems in the hole doping regime [20, 28, 215].

In addition, in DR measurements, M_1^+ exhibits signs of correlated magnetism on the hole doping side, akin to the behavior of \tilde{M}_2^- on the electron doping side around $\nu = 1$ electron per moiré unit cell, as evident from the pronounced MCD signature in Figure A.4b. Notably, the polarity of MCD is reversed for M_1^+ above $V_\mu = -20$ V compared to M_1 which reflects the negative MoSe_2 g -factor $g_X = -4$. This observation is characteristic of hole-mediated magnetism in $\text{MoSe}_2/\text{WSe}_2$ [29] and WSe_2/WS_2 heterostructures [28].

Polariton engineering at MoSe₂-graphite interfaces

B

This Chapter is a brief excursion to the exploration of the possibilities of polariton engineering in MoSe₂ monolayers with a graphite interface.

As demonstrated in Section 5.2.2, moiré exciton-polaritons exhibit effects arising from interaction-induced nonlinearities, a phenomenon attributable to the localization of underlying excitons induced by the moiré potential. Beyond moiré confinement, trapping and manipulation of polaritons has been realized in various systems implementing artificial polariton potentials for controlling nonlinear interactions and investigating phenomena like topological phase transitions [216–218]. One possible approach for creating artificial trapping potentials for excitons and polaritons in TMDs involves locally tuning the monolayer bandgap by altering the dielectric environment through different encapsulating materials [219]. In our samples, the region where the contacting few-layer graphite (FLG) partially covers the TMD monolayers presents an opportunity to explore such effects, as illustrated in Fig. B.1a. In the following, we denote the area on device D3 (see Fig. A.1) of MoSe₂ monolayer solely encapsulated by hBN as region I and the area of MoSe₂ monolayer covered with a contact FLG flake as region II.

Fig. B.1a shows the spectral evolution of the fundamental X exciton resonance, when moving the focal spot from region I to region II across the FLG edge. The alteration in dielectric environment due to the FLG contact results in a red-shifted exciton resonance compared to the bare monolayer [219]. Owing to the finite size of the excitation spot, Fig. B.1a exhibits a region at the FLG edge where both exciton species - from region I and II - manifest in the spectral response (indicated by the dashed vertical line in Fig. B.1a). The oscillator strength of either of the two exciton species depends on the fraction of the excitation spot area on the corresponding side of the graphite edge.

Device D3 was fabricated on a Distributed Bragg Reflector (DBR) substrate identical to the one used for device D1 (see Section 4.2), enabling us to examine the response of the sample

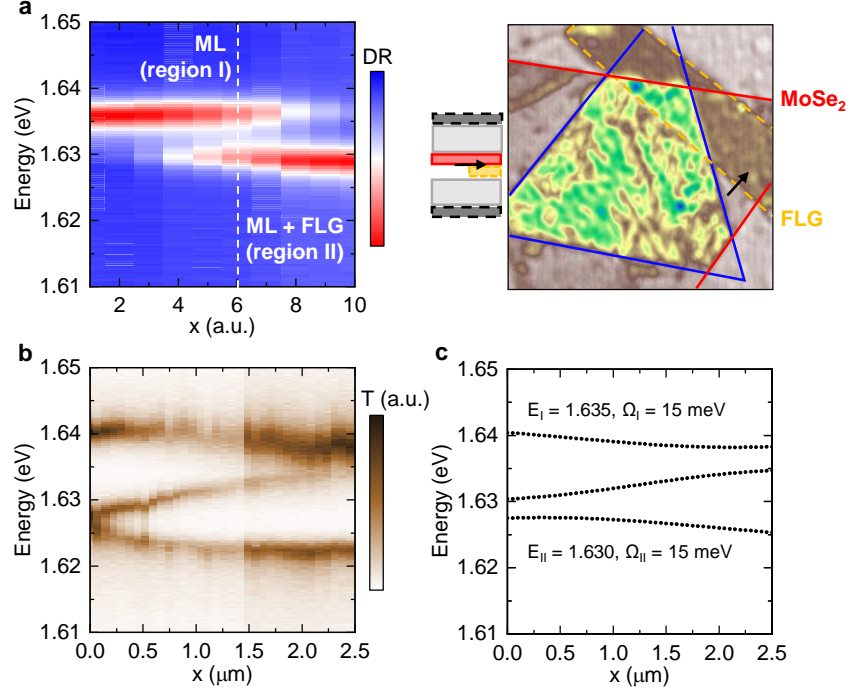


Figure B.1.: **Polariton engineering via position control.** **a**, *Left panel*: DR evolution of a MoSe_2 monolayer X exciton while scanning across an atomically sharp graphite edge on device D3, which partly covers the monolayer. *Right panel*: The black arrow represents the position of this 1D linecut, taken from a larger DR 2D scan (cp. Figure A.1). The dashed black line highlights the position of the graphite edge. **b**, Evolution of the Transmission signal along the same 1D line with the monolayer placed inside the fiber-based microcavity at mode order $q = 5$. The formation of three polariton branches is a hallmark of two excitons strongly coupling to the cavity photons. The spectral separation of the branches changes with the position of the cavity mode relative to the graphite edge. **c**, Simulation of the spectral evolution of the three polariton branches using the model of three coupled oscillators in Eq. (B.1).

area depicted in Fig. B.1a within the fiber-based microcavity with high finesse (see Section 3.3.4 for details on the cavity setup and DBR coating). The evolution of cavity transmission spectra for broadband white light excitation around the X exciton resonance while scanning the cavity mode across the FLG edge is shown in Fig. B.1b. For this measurement, the cavity length was fixed with fundamental mode order $q = 5$ resonating with the MoSe_2 X exciton. The transmission scan is presented in units of micrometers using the calibration of the cavity nanopositioners derived from Fig. 3.20a. In the limits of the scan at $x < 0 \mu\text{m}$ and $x > 2.5 \mu\text{m}$, the transmission signal features the upper and lower polariton branches of the strongly coupled MoSe_2 exciton in region I and II, respectively. In between, where the cavity mode partly covers both regions, we find a middle polariton branch, highlighting the presence of

both polariton species inside the cavity. The system is well described by the Hamiltonian of three coupled oscillators:

$$H = \begin{pmatrix} E_I & \hbar g_{I-II} & \hbar g_I \\ \hbar g_{I-II} & E_{II} & \hbar g_{II} \\ \hbar g_I & \hbar g_{II} & E_c \end{pmatrix}, \quad (\text{B.1})$$

where E_I (E_{II}) denote the X exciton energies in regions I (II), E_c represents the energy of the cavity mode, and g_I (g_{II}) denote the respective exciton-photon coupling strengths. The interaction between excitons in regions I and II is set to zero in this case ($g_{I-II} = 0$). We assume that the coupling constants $g_I(x \ll 0) = g_{II}(x \gg 2.5) = g$ are equal in the limits where the Gaussian cavity mode covers region I or II only. In between, the two coupling constants depend on the fraction of cavity mode area covering regions I and II, respectively. Using the Gaussian error function:

$$\text{erf}(x) = \frac{2}{\sqrt{\pi}} \int_0^x \exp(-t^2) dt, \quad (\text{B.2})$$

we describe them as:

$$g_I = \frac{g}{2} \left(1 - \text{erf}\left(\frac{x - x_0}{2\sigma}\right) \right) \quad (\text{B.3})$$

$$g_{II} = \frac{g}{2} \left(1 + \text{erf}\left(\frac{x - x_0}{2\sigma}\right) \right), \quad (\text{B.4})$$

where x_0 is the position of the graphite edge and σ is the beam waist of the cavity mode. By diagonalizing the Hamiltonian in Equation (B.1) using Equations (B.4), we obtain the eigenvalues of the system as a function of x , depicted in Figure B.1c for $E_I = 1.635$ and $E_{II} = 1.630$, with Rabi Splittings $\Omega_I = \Omega_{II} = 2g = 15$ meV, and a cavity mode waist of $\sigma = 1.3 \mu\text{m}$ (cp. Figure 3.19b). The model effectively captures the experimentally observed dispersion illustrated in Figure B.1b. By altering the position of the graphite edge relative to the center of the cavity mode, it becomes possible to manipulate the polariton system in a controlled manner by locally varying the coupling strength corresponding to different exciton species, as previously demonstrated in a different system [220].

The complexity of the system can be further enhanced by applying a finite doping potential V_μ . When $V_\mu = 0$ V, the dispersion of the transmission signal at the graphite edge $x_0 \approx 1.5 \mu\text{m}$ as a function of the cavity length is depicted in the left panel of Figure B.2. Here, the three polariton branches emerge around the exciton resonances E_I and E_{II} , indicated by the horizontal dashed lines. As V_μ increases, we anticipate the formation of attractive A^- and repulsive R^- polaron resonances due to the interaction of the electron Fermi sea with the excitons [66], which can couple to the cavity to form polaron-polaritons. At $V_\mu = 2$ V (middle panel of Figure B.2), we observe E_I to be blue-shifted with a reduced Rabi splitting Ω_1 , consistent with the formation of the repulsive polaron-polariton. Simultaneously, the

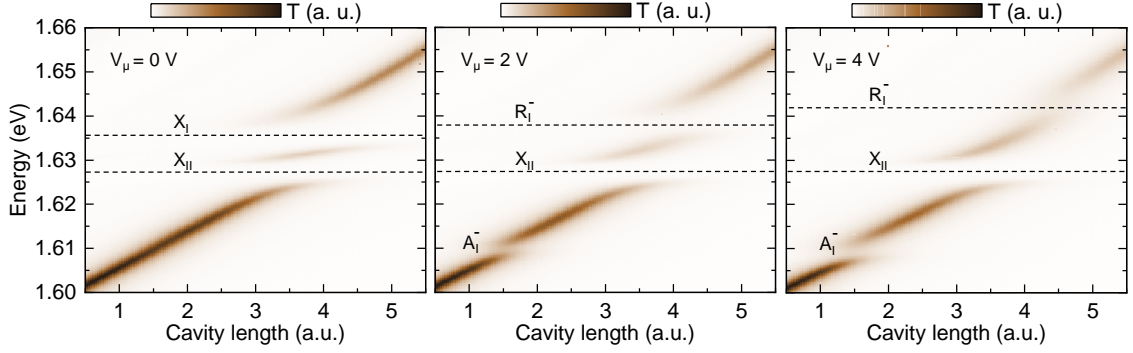


Figure B.2.: **Polariton engineering via charge control.** MoSe₂ polariton dispersion as function of the cavity length for $V_\mu = 0$ V (left panel) $V_\mu = 2$ V (middle panel) and $V_\mu = 4$ V (right panel). The cavity mode ($q = 5$) is centered at the graphite edge where both polariton species, in region I and II, exhibit identical Rabi splitting.

corresponding attractive polaron appears with a red-shift of ~ 30 meV, evidenced by the appearance of two new polariton branches at around 1.61 eV. Interestingly, E_{II} and Ω_{II} remain unchanged compared to $V_\mu = 0$ V. Charged excitons in region II are efficiently transferred to the graphene layer on a picosecond timescale, leading to an effective neutralization of this area [123]. This trend persists with further increases in V_μ , as depicted in the right panel of Figure B.2, where the upper polariton branch further blue-shifts and Ω_I quenches, while the attractive polaron-polariton becomes more pronounced and E_{II}/Ω_{II} remain constant.

Our system provides a platform to mix and manipulate polaritons corresponding to different exciton species inside a 0D cavity via position and charge control. This concept could be employed in more sophisticated sample geometries, confining excitons in region I or II by introducing artificial potential landscapes, for example, via graphene patterning [221, 222], to engineer polariton interactions.

Bibliography

- [1] R. P. Feynman, “The Feynman lectures on physics,” **1963**, *1*, 46.
- [2] L. Pauling, “The nature of the chemical bond. Application of results obtained from the quantum mechanics and from a theory of paramagnetic susceptibility to the structure of molecules,” *Journal of the American Chemical Society* **1931**, *53*, 1367–1400.
- [3] K. S. Novoselov, A. K. Geim, S. V. Morozov, et al., “Electric field effect in atomically thin carbon films,” *Science* **2004**, *306*, 666–669.
- [4] K. S. Novoselov, A. K. Geim, S. V. Morozov, et al., “Two-dimensional gas of massless Dirac fermions in graphene,” *Nature* **2005**, *438*, 197–200.
- [5] Y. Zhang, Y.-W. Tan, H. L. Stormer, et al., “Experimental observation of the quantum Hall effect and Berry’s phase in graphene,” *Nature* **2005**, *438*, 201–204.
- [6] K. S. Novoselov, Z.-f. Jiang, Y.-s. Zhang, et al., “Room-temperature quantum Hall effect in graphene,” *Science* **2007**, *315*, 1379–1379.
- [7] K. I. Bolotin, K. Sikes, Z. Jiang, et al., “Ultrahigh electron mobility in suspended graphene,” *Solid State Commun.* **2008**, *146*, 351–355.
- [8] G. Wang, A. Chernikov, M. M. Glazov, et al., “Colloquium: Excitons in atomically thin transition metal dichalcogenides,” *Rev. Mod. Phys.* **2018**, *90*, 021001.
- [9] E. Y. Andrei, D. K. Efetov, P. Jarillo-Herrero, et al., “The marvels of moiré materials,” *Nat. Rev. Mat.* **2021**, *6*, 201–206.
- [10] K. F. Mak, J. Shan, “Semiconductor moiré materials,” *Nat. Nanotechnol.* **2022**, *17*, 686–695.
- [11] R. Bistritzer, A. H. MacDonald, “Moiré bands in twisted double-layer graphene,” *Proc. Natl. Acad. Sci. U.S.A.* **2011**, *108*, 12233–12237.
- [12] Y. Cao, V. Fatemi, A. Demir, et al., “Correlated insulator behaviour at half-filling in magic-angle graphene superlattices,” *Nature* **2018**, *556*, 80–84.
- [13] F. Wu, T. Lovorn, A. H. MacDonald, “Topological Exciton Bands in Moiré Heterojunctions,” *Phys. Rev. Lett.* **2017**, *118*, 147401.

- [14] Y. Wang, Z. Wang, W. Yao, et al., “Interlayer coupling in commensurate and incommensurate bilayer structures of transition-metal dichalcogenides,” *Phys. Rev. B* **2017**, 95, 115429.
- [15] D. A. Ruiz-Tijerina, V. I. Fal’ko, “Interlayer hybridization and moiré superlattice minibands for electrons and excitons in heterobilayers of transition-metal dichalcogenides,” *Phys. Rev. B* **2019**, 99, 125424.
- [16] C. Jin, E. C. Regan, A. Yan, et al., “Observation of moiré excitons in WSe₂/WS₂ heterostructure superlattices,” *Nature* **2019**, 567, 76–80.
- [17] E. M. Alexeev, D. A. Ruiz-Tijerina, M. Danovich, et al., “Resonantly hybridized excitons in moiré superlattices in van der Waals heterostructures,” *Nature* **2019**, 567, 81–86.
- [18] N. P. Wilson, W. Yao, J. Shan, et al., “Excitons and emergent quantum phenomena in stacked 2D semiconductors,” *Nature* **2021**, 599, 383–392.
- [19] D. Huang, J. Choi, C.-K. Shih, et al., “Excitons in semiconductor moiré superlattices,” *Nat. Nanotechnol.* **2022**, 17, 227–238.
- [20] E. C. Regan, D. Wang, C. Jin, et al., “Mott and generalized Wigner crystal states in WSe₂/WS₂ moiré superlattices,” *Nature* **2020**, 579, 359–363.
- [21] Y. Zhou, J. Sung, E. Brutschea, et al., “Bilayer Wigner crystals in a transition metal dichalcogenide heterostructure,” *Nature* **2021**, 595, 48–52.
- [22] Y. Shimazaki, I. Schwartz, K. Watanabe, et al., “Strongly correlated electrons and hybrid excitons in a moiré heterostructure,” *Nature* **2020**, 580, 472–477.
- [23] L. Wang, E.-M. Shih, A. Ghiotto, et al., “Correlated electronic phases in twisted bilayer transition metal dichalcogenides,” *Nat. Mater.* **2020**, 19, 861–866.
- [24] X. Huang, T. Wang, S. Miao, et al., “Correlated insulating states at fractional fillings of the WS₂/WSe₂ moiré lattice,” *Nat. Phys.* **2021**, 17, 715–719.
- [25] A. Ghiotto, E.-M. Shih, G. S. S. G. Pereira, et al., “Quantum criticality in twisted transition metal dichalcogenides,” *Nature* **2021**, 597, 345–349.
- [26] Y. Xu, S. Liu, D. A. Rhodes, et al., “Correlated insulating states at fractional fillings of moiré superlattices,” *Nature* **2020**, 587, 214–218.
- [27] T. Li, S. Jiang, L. Li, et al., “Continuous Mott transition in semiconductor moiré superlattices,” *Nature* **2021**, 597, 350–354.
- [28] Y. Tang, L. Li, T. Li, et al., “Simulation of Hubbard model physics in WSe₂/WS₂ moiré superlattices,” *Nature* **2020**, 579, 353–358.

-
- [29] A. J. Campbell, M. Brotons-Gisbert, H. Baek, et al., “Exciton-polarons in the presence of strongly correlated electronic states in a MoSe₂/WSe₂ moiré superlattice,” *npj 2D Mater. Appl.* **2022**, *6*, 1–8.
- [30] W. Li, X. Lu, S. Dubey, et al., “Dipolar interactions between localized interlayer excitons in van der Waals heterostructures,” *Nat. Mater.* **2020**, *19*, 624–629.
- [31] X. Sun, Y. Zhu, H. Qin, et al., “Enhanced interactions of interlayer excitons in free-standing heterobilayers,” *Nature* **2022**, *610*, 478–484.
- [32] J. Hopfield, “Theory of the contribution of excitons to the complex dielectric constant of crystals,” *Phys. Rev.* **1958**, *112*, 1555.
- [33] J. Kasprzak, M. Richard, S. Kundermann, et al., “Bose–Einstein condensation of exciton polaritons,” *Nature* **2006**, *443*, 409–14.
- [34] I. Carusotto, C. Ciuti, “Quantum fluids of light,” *Rev. Mod. Phys.* **2013**, *85*, 299.
- [35] D. E. Chang, V. Vuletić, M. D. Lukin, “Quantum nonlinear optics—photon by photon,” *Nat. Photon.* **2014**, *8*, 685–694.
- [36] Y. Tang, J. Gu, S. Liu, et al., “Dielectric catastrophe at the Wigner-Mott transition in a moiré superlattice,” *Nat. Commun.* **2022**, *13*, 4271.
- [37] L. Ciorciaro, T. Smoleński, I. Morera, et al., “Kinetic magnetism in triangular moiré materials,” *Nature* **2023**, *623*, 509–513.
- [38] L. Zhang, F. Wu, S. Hou, et al., “Van der Waals heterostructure polaritons with moiré-induced nonlinearity,” *Nature* **2021**, *591*, 61–65.
- [39] A. K. Geim, I. V. Grigorieva, “Van der Waals heterostructures,” *Nature* **2013**, *499*, 419–425.
- [40] K. F. Mak, C. Lee, J. Hone, et al., “Atomically thin MoS₂: a new direct-gap semiconductor,” *Phys. Rev. Lett.* **2010**, *105*, 136805.
- [41] A. Splendiani, L. Sun, Y. Zhang, et al., “Emerging photoluminescence in monolayer MoS₂,” *Nano Lett.* **2010**, *10*, 1271–1275.
- [42] T. Mueller, E. Malic, “Exciton physics and device application of two-dimensional transition metal dichalcogenide semiconductors,” *npj 2D Mater. Appl.* **2018**, *2*, 29.
- [43] J. Lindlau, PhD Thesis, Ludwig-Maximilians-Universität München, **2019**.
- [44] Z. Y. Zhu, Y. C. Cheng, U. Schwingenschlögl, “Giant spin-orbit-induced spin splitting in two-dimensional transition-metal dichalcogenide semiconductors,” *Phys. Rev. B* **2011**, *84*, 153402.
- [45] T. Cheiwchanchamnangij, W. R. Lambrecht, “Quasiparticle band structure calculation of monolayer, bilayer, and bulk MoS₂,” *Phys. Rev. B* **2012**, *85*, 205302.

- [46] W. Yao, D. Xiao, Q. Niu, "Valley-dependent optoelectronics from inversion symmetry breaking," *Phy. Rev. B* **2008**, 77, 235406.
- [47] D. Xiao, G.-B. Liu, W. Feng, et al., "Coupled spin and valley physics in monolayers of MoS₂ and other group-VI dichalcogenides," *Phys. Rev. Lett.* **2012**, 108, 196802.
- [48] T. Cao, G. Wang, W. Han, et al., "Valley-selective circular dichroism of monolayer molybdenum disulphide," *Nat. Commun.* **2012**, 3.
- [49] A. Kormányos, V. Zólyomi, N. D. Drummond, et al., "Monolayer MoS₂: Trigonal warping, the Γ valley, and spin-orbit coupling effects," *Phys. Rev. B* **2013**, 88, 045416.
- [50] K. Kośmider, J. W. González, J. Fernández-Rossier, "Large spin splitting in the conduction band of transition metal dichalcogenide monolayers," *Phys. Rev. B* **2013**, 88, 245436.
- [51] A. Kormányos, G. Burkard, M. Gmitra, et al., "k·p theory for two-dimensional transition metal dichalcogenide semiconductors," *2D Mater.* **2015**, 2, 022001.
- [52] G. Wang, C. Robert, M. M. Glazov, et al., "In-plane propagation of light in transition metal dichalcogenide monolayers: optical selection rules," *Phys. Rev. Lett.* **2017**, 119, 047401.
- [53] X.-X. Zhang, T. Cao, Z. Lu, et al., "Magnetic brightening and control of dark excitons in monolayer WSe₂," *Nat. Nanotechnol.* **2017**, 12, 883–888.
- [54] Y. Zhou, G. Scuri, D. S. Wild, et al., "Probing dark excitons in atomically thin semiconductors via near-field coupling to surface plasmon polaritons," *Nat. Nanotechnol.* **2017**, 12, 856–860.
- [55] C. Kittel, *Introduction to Solid State Physics*, Wiley, **2004**.
- [56] L. V. Keldysh, "Coulomb interaction in thin semiconductor and semimetal films," *JEPT Lett.* **1979**, 29, 658–661.
- [57] A. Chernikov, T. C. Berkelbach, H. M. Hill, et al., "Exciton Binding Energy and Nonhydrogenic Rydberg Series in Monolayer WS₂," *Phys. Rev. Lett.* **2014**, 113, 076802.
- [58] C. F. Klingshirn, *Semiconductor optics*, Springer Science & Business Media, **2012**.
- [59] B. Radisavljevic, A. Radenovic, J. Brivio, et al., "Single-layer MoS₂ transistors," *Nat. Nanotechnol.* **2011**, 6, 147–150.
- [60] K. F. Mak, K. He, C. Lee, et al., "Tightly bound trions in monolayer MoS₂," *Nat. Mater.* **2013**, 12, 207–211.
- [61] J. S. Ross, S. Wu, H. Yu, et al., "Electrical control of neutral and charged excitons in a monolayer semiconductor," *Nat. Commun.* **2013**, 4, 1474.

-
- [62] A. Chernikov, A. M. Van Der Zande, H. M. Hill, et al., “Electrical tuning of exciton binding energies in monolayer WS_2 ,” *Phys. Rev. Lett.* **2015**, *115*, 126802.
- [63] A. Singh, G. Moody, K. Tran, et al., “Trion formation dynamics in monolayer transition metal dichalcogenides,” *Phys. Rev. B* **2016**, *93*, 041401.
- [64] E. Courtade, M. Semina, M. Manca, et al., “Charged excitons in monolayer WSe_2 : Experiment and theory,” *Phys. Rev. B* **2017**, *96*, 085302.
- [65] R. Schmidt, T. Enss, V. Pietilä, et al., “Fermi polarons in two dimensions,” *Phys. Rev. A* **2012**, *85*, 021602.
- [66] M. Sidler, P. Back, O. Cotlet, et al., “Fermi polaron-polaritons in charge-tunable atomically thin semiconductors,” *Nat. Phys.* **2016**, *13*, 255–261.
- [67] P. Back, M. Sidler, O. Cotlet, et al., “Giant Paramagnetism-Induced Valley Polarization of Electrons in Charge-Tunable Monolayer $MoSe_2$,” *Phys. Rev. Lett.* **2017**, *118*, 237404.
- [68] M. M. Glazov, “Optical properties of charged excitons in two-dimensional semiconductors,” *The Journal of Chemical Physics* **2020**, *153*.
- [69] A. Mitioglu, P. Plochocka, Á. Granados del Aguila, et al., “Optical investigation of monolayer and bulk tungsten diselenide (WSe_2) in high magnetic fields,” *Nano Lett.* **2015**, *15*, 4387–4392.
- [70] Y. Li, J. Ludwig, T. Low, et al., “Valley splitting and polarization by the Zeeman effect in monolayer $MoSe_2$,” *Phys. Rev. Lett.* **2014**, *113*, 266804.
- [71] A. Srivastava, M. Sidler, A. V. Allain, et al., “Valley Zeeman effect in elementary optical excitations of monolayer WSe_2 ,” *Nat. Phys.* **2015**, *11*, 141.
- [72] G. Wang, L. Bouet, M. M. Glazov, et al., “Magneto-optics in transition metal diselenide monolayers,” *2D Mater.* **2015**, *2*, 034002.
- [73] D. MacNeill, C. Heikes, K. F. Mak, et al., “Breaking of Valley Degeneracy by Magnetic Field in Monolayer $MoSe_2$,” *Phys. Rev. Lett.* **2015**, *114*, 037401.
- [74] G. Aivazian, Z. Gong, A. M. Jones, et al., “Magnetic Control of Valley Pseudospin in Monolayer WSe_2 ,” *Nat. Phys.* **2015**, *11*, 148.
- [75] J. Förste, N. V. Tepliakov, S. Y. Kruchinin, et al., “Exciton g-factors in monolayer and bilayer WSe_2 from experiment and theory,” *Nat. Commun.* **2020**, *11*, 4539.
- [76] T. Woźniak, P. E. F. Junior, G. Seifert, et al., “Exciton g factors of van der Waals heterostructures from first-principles calculations,” *Phys. Rev. B* **2020**, *101*, 235408.
- [77] A. Arora, M. Drüppel, R. Schmidt, et al., “Interlayer excitons in a bulk van der Waals semiconductor,” *Nat. Commun.* **2017**, *8*, 639.

- [78] J. Horng, T. Stroucken, L. Zhang, et al., “Observation of interlayer excitons in MoSe₂ single crystals,” *Phys.Rev. B* **2018**, 97, 241404.
- [79] Z. Wang, Y.-H. Chiu, K. Honz, et al., “Electrical tuning of interlayer exciton gases in WSe₂ bilayers,” *Nano Lett.* **2018**, 18, 137–143.
- [80] L. A. Jauregui, A. Y. Joe, K. Pistunova, et al., “Electrical control of interlayer exciton dynamics in atomically thin heterostructures,” *Science* **2019**, 366, 870–875.
- [81] Y. Zhang, C. Xiao, D. Ovchinnikov, et al., “Every-other-layer dipolar excitons in a spin-valley locked superlattice,” *Nat. Nanotechnol.* **2023**, 18, 501–506.
- [82] M. Selig, G. Berghäuser, A. Raja, et al., “Excitonic linewidth and coherence lifetime in monolayer transition metal dichalcogenides,” *Nat. Commun.* **2016**, 7.
- [83] C. Robert, D. Lagarde, F. Cadiz, et al., “Exciton radiative lifetime in transition metal dichalcogenide monolayers,” *Phys. Rev. B* **2016**, 93, 205423.
- [84] P. Rivera, J. R. Schaibley, A. M. Jones, et al., “Observation of long-lived interlayer excitons in monolayer MoSe₂/WSe₂ heterostructures,” *Nat. Commun.* **2015**, 6, 6242.
- [85] B. Miller, A. Steinhoff, B. Pano, et al., “Long-lived direct and indirect interlayer excitons in van der Waals heterostructures,” *Nano Lett.* **2017**, 17, 5229–5237.
- [86] T. Deilmann, K. S. Thygesen, “Interlayer excitons with large optical amplitudes in layered van der Waals materials,” *Nano Lett.* **2018**, 18, 2984–2989.
- [87] I. C. Gerber, E. Courtade, S. Shree, et al., “Interlayer excitons in bilayer MoS₂ with strong oscillator strength up to room temperature,” *Phys. Rev. B* **2019**, 99, 035443.
- [88] S. Zhao, X. Huang, R. Gillen, et al., “Hybrid Moiré Excitons and Trions in Twisted MoTe₂-MoSe₂ Heterobilayers,” *Nano Lett.* **2024**.
- [89] Y. Tang, J. Gu, S. Liu, et al., “Tuning layer-hybridized moiré excitons by the quantum-confined Stark effect,” *Nat. Nanotechnol.* **2021**, 16, 1–6.
- [90] C. Fabry, A. Perot, “Théorie et Applications d’une Nouvelle Méthode de Spectroscopie Interférentielle,” *Annales de Chimie et de Physique 7. Série* **1899**, 16.
- [91] A. E. Siegman, *Lasers*, Mill Valley, CA, **1986**.
- [92] A. Imamoglu, D. D. Awschalom, G. Burkard, et al., “Quantum information processing using quantum dot spins and cavity-QED,” *Phys. Rev. Lett.* **1999**, 83, 4204.
- [93] S.-B. Zheng, G.-C. Guo, “Efficient Scheme for Two-Atom Entanglement and Quantum Information Processing in Cavity QED,” *Phys. Rev. Lett.* **2000**, 85, 2392–2395.
- [94] D. E. Chang, V. Vuletić, M. D. Lukin, “Quantum nonlinear optics - Photon by photon,” *Nat. Photon.* **2014**, 8, 685–694.
- [95] B. E. Saleh, M. C. Teich, *Fundamentals of photonics*, Wiley, **2019**.

-
- [96] N. Hodgson, H. Weber, *Laser Resonators and Beam Propagation: Fundamentals, Advanced Concepts, Applications, Vol. 108*, Springer, **2005**.
- [97] N. Ismail, C. C. Kores, D. Geskus, et al., “Fabry-Pérot resonator: spectral line shapes, generic and related Airy distributions, linewidths, finesses, and performance at low or frequency-dependent reflectivity,” *Opt. Express* **2016**, *24*, 16366–16389.
- [98] M. Mader, J. Reichel, T. W. Hänsch, et al., “A scanning cavity microscope,” *Nat. Commun.* **2015**, *6*, 1–7.
- [99] D. Hunger, T. Steinmetz, Y. Colombe, et al., “Fiber Fabry-Pérot cavity with high finesse,” *New J. Phys.* **2010**, *12*, 065038.
- [100] J. Benedikter, T. Hümmer, M. Mader, et al., “Transverse-mode coupling and diffraction loss in tunable Fabry-Pérot microcavities,” *New J. Phys.* **2015**, *17*, 053051.
- [101] J. Benedikter, T. Moosmayer, M. Mader, et al., “Transverse-mode coupling effects in scanning cavity microscopy,” *New J. Phys.* **2019**, *21*, 103029.
- [102] E. M. Purcell, “Proceedings of the American Physical Society,” *Phys. Rev.* **1946**, *69*, 674–674.
- [103] X. Gan, Y. Gao, K. Fai Mak, et al., “Controlling the spontaneous emission rate of monolayer MoS₂ in a photonic crystal nanocavity,” *Appl. Phys. Lett.* **2013**, *103*.
- [104] S. Wu, S. Buckley, A. M. Jones, et al., “Control of two-dimensional excitonic light emission via photonic crystal,” *2D Mater.* **2014**, *1*, 011001.
- [105] S. Wu, S. Buckley, J. R. Schaibley, et al., “Monolayer semiconductor nanocavity lasers with ultralow thresholds,” *Nature* **2015**, *520*, 69–72.
- [106] M. Förg, L. Colombier, R. K. Patel, et al., “Cavity-control of interlayer excitons in van der Waals heterostructures,” *Nat. Commun.* **2019**, *10*, 3697.
- [107] B. Lee, J. Park, G. H. Han, et al., “Fano resonance and spectrally modified photoluminescence enhancement in monolayer MoS₂ integrated with plasmonic nanoantenna array,” *Nano Lett.* **2015**, *15*, 3646–3653.
- [108] C. Schneider, M. Glazov, T. Korn, et al., “Two-dimensional semiconductors in the regime of strong light-matter coupling,” *Nat. Commun.* **2018**, *9*, 2695.
- [109] M. O. Scully, M. S. Zubairy, *Quantum Optics*, Cambridge University Press, **1997**.
- [110] C. Gerry, P. Knight, *Introductory Quantum Optics*, Cambridge University Press, **2004**.
- [111] E. T. Jaynes, F. W. Cummings, “Comparison of quantum and semiclassical radiation theories with application to the beam maser,” *Proceedings of the IEEE* **1963**, *51*, 89–109.

- [112] C. Weisbuch, M. Nishioka, A. Ishikawa, et al., “Observation of the coupled exciton-photon mode splitting in a semiconductor quantum microcavity,” *Phys. Rev. Lett.* **1993**, 69, 3314–3317.
- [113] A. Kavokin, *Microcavities*, OUP Oxford, **2011**.
- [114] I. Bilgin, A. S. Raeliarijaona, M. C. Lucking, et al., “Resonant raman and exciton coupling in high-quality single crystals of atomically thin MoSe₂ Grown by Vapor-Phase Chalcogenization,” *ACS Nano* **2018**, 12, 740–750.
- [115] Z. Li, F. Tabataba-Vakili, S. Zhao, et al., “Lattice Reconstruction in MoSe₂/WSe₂ Heterobilayers Synthesized by Chemical Vapor Deposition,” *Nano Lett.* **2023**, 23, 4160–4166.
- [116] J. C. Kotsakidis, Q. Zhang, A. L. Vazquez de Parga, et al., “Oxidation of Monolayer WS₂ in Ambient Is a Photoinduced Process,” *Nano Lett.* **2019**, 19, 5205–5215.
- [117] R. Tilmann, C. Bartlam, O. Hartwig, et al., “Identification of Ubiquitously Present Polymeric Adlayers on 2D Transition Metal Dichalcogenides,” *ACS Nano* **2023**, 17, 10617–10627.
- [118] A. Rupp, J. Göser, Z. Li, et al., “Imaging lattice reconstruction in homobilayers and heterobilayers of transition metal dichalcogenides,” *2D Mater.* **2023**, 10, 045028.
- [119] A. Rupp, J. Göser, Z. Li, et al., “Energy-Dispersive X-Ray Spectroscopy of Atomically Thin Semiconductors and Heterostructures,” *Phys. Rev. Appl.* **2022**, 18, 064061.
- [120] E. Courtade, B. Han, S. Nakhaie, et al., “Spectrally narrow exciton luminescence from monolayer MoS₂ and MoSe₂ exfoliated onto epitaxially grown hexagonal BN,” *Applied Physics Letters* **2018**, 113.
- [121] H. Fang, B. Han, C. Robert, et al., “Control of the exciton radiative lifetime in van der Waals heterostructures,” *Phys. Rev. Lett.* **2019**, 123, 067401.
- [122] C. Robert, M. Semina, F. Cadiz, et al., “Optical spectroscopy of excited exciton states in MoS₂ monolayers in van der Waals heterostructures,” *Phys. Rev. Mater.* **2018**, 2, 011001.
- [123] E. Lorchat, L. E. P. López, C. Robert, et al., “Filtering the photoluminescence spectra of atomically thin semiconductors with graphene,” *Nat. Nanotechnol.* **2020**, 15, 283–288.
- [124] F. Pizzocchero, L. Gammelgaard, B. S. Jessen, et al., “The hot pick-up technique for batch assembly of van der Waals heterostructures,” *Nat. Commun.* **2016**, 7.
- [125] D. G. Purdie, N. M. Pugno, T. Taniguchi, et al., “Cleaning interfaces in layered materials heterostructures,” *Nat. Commun.* **2018**, 9.
- [126] C. Mohl, Master Thesis, Ludwig-Maximilians-Universität München, **2022**.

-
- [127] A. Arora, A. Mandal, S. Chakrabarti, et al., “Magneto-optical Kerr effect spectroscopy based study of Landé g-factor for holes in GaAs/AlGaAs single quantum wells under low magnetic fields,” *J. Appl. Phys.* **2013**, *113*, 213505.
- [128] S. Zhao, Z. Li, X. Huang, et al., “Excitons in mesoscopically reconstructed moiré heterostructures,” *Nat. Nanotechnol.* **2023**, *18*, 572–579.
- [129] D. Xiao, G.-B. Liu, W. Feng, et al., “Coupled Spin and Valley Physics in Monolayers of MoS₂ and Other Group-VI Dichalcogenides,” *Phys. Rev. Lett.* **2012**, *108*, 196802.
- [130] K. F. Mak, K. He, J. Shan, et al., “Control of valley polarization in monolayer MoS₂ by optical helicity,” *Nat. Nanotechnol.* **2012**, *7*, 494–498.
- [131] H. Zeng, J. Dai, W. Yao, et al., “Valley polarization in MoS₂ monolayers by optical pumping,” *Nat. Nanotechnol.* **2012**, *7*, 490–493.
- [132] G. Sallen, L. Bouet, X. Marie, et al., “Robust Optical Emission Polarization in MoS₂ Monolayers through Selective Valley Excitation,” *Phys. Rev. B* **2012**, *86*, 081301.
- [133] A. Ranjan, N. Raghavan, M. Holwill, et al., “Dielectric Breakdown in Single-Crystal Hexagonal Boron Nitride,” *ACS Applied Electronic Materials* **2021**, *3*, 3547–3554.
- [134] E. M. Alexeev, D. A. Ruiz-Tijerina, M. Danovich, et al., “Resonantly hybridized excitons in moiré superlattices in van der Waals heterostructures,” *Nature* **2019**, *567*, 81–86.
- [135] B. Alén, F. Bickel, K. Karrai, et al., “Stark-shift modulation absorption spectroscopy of single quantum dots,” *Appl. Phys. Lett.* **2003**, *83*, 2235–2237.
- [136] A. Högele, B. Alén, F. Bickel, et al., “Exciton fine structure splitting of single InGaAs self-assembled quantum dots,” *Physica E* **2004**, *21*, 175–179.
- [137] E. Barré, O. Karni, E. Liu, et al., “Optical absorption of interlayer excitons in transition-metal dichalcogenide heterostructures,” *Science* **2022**, *376*, 406–410.
- [138] W. Lu, Y. Fu in *Spectroscopy of Semiconductors: Numerical Analysis Bridging Quantum Mechanics and Experiments*, Springer International Publishing, **2018**, pp. 185–205.
- [139] S. Vadia, PhD Thesis, Ludwig-Maximilians-Universität München, **2021**.
- [140] T. Tomaru, T. Suzuki, T. Haruyama, et al., “Vibration analysis of cryocoolers,” *Cryogenics* **2004**, *44*, 309–317.
- [141] D. Haft, F. Otto, C. Dal Savio, et al., Optical table, US Patent App. 15/518,646, **2017**.
- [142] L. Balents, C. R. Dean, D. K. Efetov, et al., “Superconductivity and strong correlations in moiré flat bands,” *Nat. Phys.* **2020**, *16*, 725–733.
- [143] K. Hermann, “Periodic overlayers and moiré patterns: theoretical studies of geometric properties,” *J. Phys.: Condens. Matter* **2012**, *24*, 314210.

- [144] S. Zhao, Z. Li, X. Huang, et al., “Excitons in mesoscopically reconstructed moiré heterostructures,” *Nat. Nanotechnol.* **2023**, *18*, 572–579.
- [145] A. Kormányos, G. Burkard, M. Gmitra, et al., “k.p theory for two-dimensional transition metal dichalcogenide semiconductors,” *2D Mater.* **2015**, *2*, 022001.
- [146] F. Wu, T. Lovorn, A. H. MacDonald, “Theory of optical absorption by interlayer excitons in transition metal dichalcogenide heterobilayers,” *Phys. Rev. B* **2018**, *97*, 035306.
- [147] F. Wu, T. Lovorn, E. Tutuc, et al., “Hubbard Model Physics in Transition Metal Dichalcogenide Moiré Bands,” *Phys. Rev. Lett.* **2018**, *121*, 026402.
- [148] C. Zhang, C. Gong, Y. Nie, et al., “Systematic study of electronic structure and band alignment of monolayer transition metal dichalcogenides in van der Waals heterostructures,” *2D Mater.* **2016**, *4*, 015026.
- [149] M. Goryca, J. Li, A. V. Stier, et al., “Revealing exciton masses and dielectric properties of monolayer semiconductors with high magnetic fields,” *Nat. Commun.* **2019**, *10*, 1–12.
- [150] A. Popert, PhD thesis, ETH, Zürich, Switzerland, **2022**.
- [151] Q. Tan, A. Rasmita, Z. Zhang, et al., “Layer-dependent correlated phases in WS₂/MoSe₂ moiré superlattice,” *Nat. Mater.* **2023**, *22*, 605–611.
- [152] L. Ma, P. X. Nguyen, Z. Wang, et al., “Strongly correlated excitonic insulator in atomic double layers,” *Nature* **2021**, *598*, 585–589.
- [153] Z. Wang, Y.-H. Chiu, K. Honz, et al., “Electrical Tuning of Interlayer Exciton Gases in WSe₂ Bilayers,” *Nano Lett.* **2018**, *18*, 137–143.
- [154] N. S. Rytova, “The screened potential of a point charge in a thin film,” *Mosc. Univ. Phys. Bull.* **1967**, *3*, 18.
- [155] M. A. Semina, “Excitons and Trions in Bilayer van der Waals Heterostructures,” *Phys. Solid State* **2019**, *61*, 2218–2223.
- [156] X. L. Yang, S. H. Guo, F. T. Chan, et al., “Analytic solution of a two-dimensional hydrogen atom. I. Nonrelativistic theory,” *Phys. Rev. A* **1991**, *43*, 1186–1196.
- [157] M. Goryca, J. Li, A. V. Stier, et al., “Revealing exciton masses and dielectric properties of monolayer semiconductors with high magnetic fields,” *Nat. Commun.* **2019**, *10*, 4172.
- [158] F. Ceballos, M. Z. Bellus, H.-Y. Chiu, et al., “Probing charge transfer excitons in a MoSe₂/WS₂ van der Waals heterostructure,” *Nanoscale* **2015**, *7*, 17523–17528.
- [159] C. Zhang, C. Gong, Y. Nie, et al., “Systematic study of electronic structure and band alignment of monolayer transition metal dichalcogenides in Van der Waals heterostructures,” *2D Mater.* **2016**, *4*, 015026.

-
- [160] Y. Meng, T. Wang, C. Jin, et al., “Electrical switching between exciton dissociation to exciton funneling in MoSe₂/WS₂ heterostructure,” *Nat. Commun.* **2020**, *11*, 2640.
- [161] L. Zhang, Z. Zhang, F. Wu, et al., “Twist-angle dependence of moiré excitons in WS₂/MoSe₂ heterobilayers,” *Nat. Commun.* **2020**, *11*, 5888.
- [162] Y. Li, J. Ludwig, T. Low, et al., “Valley Splitting and Polarization by the Zeeman Effect in Monolayer MoSe₂,” *Phys. Rev. Lett.* **2014**, *113*, 266804.
- [163] P. E. Faria Junior, J. Fabian, “Signatures of Electric Field and Layer Separation Effects on the Spin-Valley Physics of MoSe₂/WSe₂ Heterobilayers: From Energy Bands to Dipolar Excitons,” *Nanomaterials* **2023**, *13*, DOI 10.3390/nano13071187.
- [164] Y. G. Gobato, C. S. de Brito, A. Chaves, et al., “Distinctive g-Factor of Moiré-Confined Excitons in van der Waals Heterostructures,” *Nano Lett.* **2022**, *22*, 8641–8646.
- [165] M. H. Naik, E. C. Regan, Z. Zhang, et al., “Intralayer charge-transfer moiré excitons in van der Waals superlattices,” *Nature* **2022**, *609*, 52–57.
- [166] A. Allain, J. Kang, K. Banerjee, et al., “Electrical contacts to two-dimensional semiconductors,” *Nat. mater.* **2015**, *14*, 1195–1205.
- [167] Y. Xu, C. Cheng, S. Du, et al., “Contacts between Two- and Three-Dimensional Materials: Ohmic, Schottky, and p–n Heterojunctions,” *ACS Nano* **2016**, *10*, PMID: 27132492, 4895–4919.
- [168] D. S. Schulman, A. J. Arnold, S. Das, “Contact engineering for 2D materials and devices,” *Chemical Society Reviews* **2018**, *47*, 3037–3058.
- [169] K. Kang, B. Shen, Y. Qiu, et al., “Evidence of the fractional quantum spin Hall effect in moiré MoTe₂,” *Nature* **2024**, *628*, 522–526.
- [170] A. Imamoglu, Y. Zhang, private communication (June 2023).
- [171] D. Efimkin, A. Macdonald, “Many-Body Theory of Trion Absorption Features in Two-Dimensional Semiconductors,” *Phys. Rev. B* **2017**, *95*, 035417.
- [172] B. Polovnikov, PhD Thesis, Ludwig-Maximilians-Universität München, **2024**.
- [173] M. A. Ruderman, C. Kittel, “Indirect exchange coupling of nuclear magnetic moments by conduction electrons,” *Physical Review* **1954**, *96*, 99.
- [174] P. Coleman, *Introduction to many-body physics*, Cambridge University Press, **2015**.
- [175] G. Muñoz-Matutano, A. Wood, M. Johnsson, et al., “Emergence of quantum correlations from interacting fibre-cavity polaritons,” *Nat. Mater.* **2019**, *18*, 213–218.
- [176] A. Delteil, T. Fink, A. Schade, et al., “Towards polariton blockade of confined exciton–polaritons,” *Nat. Mater.* **2019**, *18*, 219–222.

- [177] C. Anton-Solanas, M. Waldherr, M. Klaas, et al., “Bosonic condensation of exciton–polaritons in an atomically thin crystal,” *Nat. Mater.* **2021**, *20*, 1–7.
- [178] S. Kéna-Cohen, S. Forrest, “Room-temperature polariton lasing in an organic single-crystal microcavity,” *Nat. Photon.* **2010**, *4*, 371–375.
- [179] A. Amo, S. Pigeon, D. Sanvitto, et al., “Polariton Superfluids Reveal Quantum Hydrodynamic Solitons,” *Science* **2011**, *332*, 1167–1170.
- [180] J. Gu, V. Walther, L. Waldecker, et al., “Enhanced nonlinear interaction of polaritons via excitonic Rydberg states in monolayer WSe₂,” *Nat. Commun.* **2021**, *12*, 2269.
- [181] T. P. Lyons, D. J. Gillard, C. Leblanc, et al., “Giant effective Zeeman splitting in a monolayer semiconductor realized by spin-selective strong light–matter coupling,” *Nat. Photon.* **2022**, *16*, 632–636.
- [182] S. Dufferwiel, S. Schwarz, F. Withers, et al., “Exciton–polaritons in van der Waals heterostructures embedded in tunable microcavities,” *Nat. Commun.* **2015**, *6*, 8579.
- [183] X. Liu, T. Galfsky, Z. Sun, et al., “Strong light–matter coupling in two-dimensional atomic crystals,” *Nat. Photon.* **2015**, *9*, 30–34.
- [184] N. Lundt, S. Klembt, E. Cherotchenko, et al., “Room-temperature Tamm-plasmon exciton-polaritons with a WSe₂ monolayer,” *Nat. Commun.* **2016**, *7*, 13328.
- [185] L. C. Flatten, Z. He, D. M. Coles, et al., “Room-temperature exciton-polaritons with two-dimensional WS₂,” *Sci. Rep.* **2016**, *6*, 1–7.
- [186] M.-E. Kleemann, R. Chikkaraddy, E. M. Alexeev, et al., “Strong-coupling of WSe₂ in ultra-compact plasmonic nanocavities at room temperature,” *Nat. Commun.* **2017**, *8*, 1296.
- [187] D. Zheng, S. Zhang, Q. Deng, et al., “Manipulating coherent plasmon–exciton interaction in a single silver nanorod on monolayer WSe₂,” *Nano Lett.* **2017**, *17*, 3809–3814.
- [188] R. Liu, Z.-K. Zhou, Y.-C. Yu, et al., “Strong light-matter interactions in single open plasmonic nanocavities at the quantum optics limit,” *Phys. Rev. Lett.* **2017**, *118*, 237401.
- [189] T. Hu, Y. Wang, L. Wu, et al., “Strong coupling between Tamm plasmon polariton and two dimensional semiconductor excitons,” *Appl. Phys. Lett.* **2017**, *110*, 051101.
- [190] L. Zhang, R. Gogna, W. Burg, et al., “Photonic-crystal exciton-polaritons in monolayer semiconductors,” *Nat. Commun.* **2018**, *9*, 713.
- [191] R. Emmanuele, M. Sich, O. Kyriienko, et al., “Highly nonlinear trion-polaritons in a monolayer semiconductor,” *Nat. Commun.* **2020**, *11*, 3589.
- [192] A. Steinhoff, E. Wietek, M. Florian, et al., Exciton-exciton interactions in van der Waals heterobilayers, **2023**.

-
- [193] D. J. Morrow, X. Ma, “Trapping interlayer excitons in van der Waals heterostructures by potential arrays,” *Phys. Rev. B* **2021**, *104*, 195302.
- [194] E. C. Regan, D. Wang, E. Y. Paik, et al., “Emerging exciton physics in transition metal dichalcogenide heterobilayers,” *Nat. Rev. Mater.* **2022**, *7*, 778–795.
- [195] G. Moody, C. Kavir Dass, K. Hao, et al., “Intrinsic homogeneous linewidth and broadening mechanisms of excitons in monolayer transition metal dichalcogenides,” *Nat. Commun.* **2015**, *6*.
- [196] V. Savona, C. Piermarocchi, A. Quattropani, et al., “Microscopic theory of motional narrowing of microcavity polaritons in a disordered potential,” *Phys. Rev. Lett.* **1997**, *78*, 4470.
- [197] C. Ell, J. Prineas, T. Nelson Jr, et al., “Influence of structural disorder and light coupling on the excitonic response of semiconductor microcavities,” *Phys. Rev. Lett.* **1998**, *80*, 4795.
- [198] M. Wurdack, E. Estrecho, S. Todd, et al., “Motional narrowing, ballistic transport, and trapping of room-temperature exciton polaritons in an atomically-thin semiconductor,” *Nat. Commun.* **2021**, *12*, 5366.
- [199] J.-C. Drawer, V. N. Mitryakhin, H. Shan, et al., “Monolayer-Based Single-Photon Source in a Liquid-Helium-Free Open Cavity Featuring 65 % Brightness and Quantum Coherence,” *Nano Lett.* **2023**, *23*, 8683–8689.
- [200] M. Koperski, M. R. Molas, A. Arora, et al., “Orbital, spin and valley contributions to Zeeman splitting of excitonic resonances in MoSe₂, WSe₂ and WS₂ Monolayers,” *2D Mater.* **2019**, *6*, 015001.
- [201] A. Weston, Y. Zou, V. Enaldiev, et al., “Atomic reconstruction in twisted bilayers of transition metal dichalcogenides,” *Nat. Nanotechnol.* **2020**, *15*, 592–597.
- [202] S. Susarla, L. M. Sassi, A. Zobelli, et al., “Mapping modified electronic levels in the moiré patterns in MoS₂/WSe₂ using low-loss EELS,” *Nano Lett.* **2021**, *21*, 4071–4077.
- [203] S. Susarla, M. H. Naik, D. D. Blach, et al., “Hyperspectral imaging of exciton confinement within a moiré unit cell with a subnanometer electron probe,” *Science* **2022**, *378*, 1235–1239.
- [204] A. Popert, Y. Shimazaki, M. Kroner, et al., “Optical sensing of fractional quantum Hall effect in graphene,” *Nano Lett.* **2022**, *22*, 7363–7369.
- [205] B. Datta, M. Khatoniar, P. Deshmukh, et al., “Highly nonlinear dipolar exciton-polaritons in bilayer MoS₂,” *Nat. Commun.* **2022**, *13*, 6341.

- [206] C. Louca, A. Genco, S. Chiavazzo, et al., “Interspecies exciton interactions lead to enhanced nonlinearity of dipolar excitons and polaritons in MoS₂ homobilayers,” *Nat. Commun.* **2023**, *14*, 3818.
- [207] J. Hong, Z. Hu, M. Probert, et al., “Exploring atomic defects in molybdenum disulfide monolayers,” *Nat. Commun.* **2015**, *6*, 6293.
- [208] H. Liu, J. Lu, K. Ho, et al., “Fluorescence concentric triangles: a case of chemical heterogeneity in WS₂ atomic monolayer,” *Nano Lett.* **2016**, *16*, 5559–5567.
- [209] A. Neumann, J. Lindlau, M. Nutz, et al., “Signatures of defect-localized charged excitons in the photoluminescence of monolayer molybdenum disulfide,” *Phys. Rev. Mater.* **2018**, *2*, 124003.
- [210] F. G. Aras, A. Yilmaz, H. G. Tasdelen, et al., “A review on recent advances of chemical vapor deposition technique for monolayer transition metal dichalcogenides (MX₂: Mo, W; S, Se, Te),” *Materials Science in Semiconductor Processing* **2022**, *148*, 106829.
- [211] J.-H. Ahn, W. M. Parkin, C. H. Naylor, et al., “Ambient effects on electrical characteristics of CVD-grown monolayer MoS₂ field-effect transistors,” *Sci. Rep.* **2017**, *7*, 4075.
- [212] X. Wang, J. Dan, Z. Hu, et al., “Defect heterogeneity in monolayer WS₂ unveiled by work function variance,” *Chem. Mater.* **2019**, *31*, 7970–7978.
- [213] Y. Sata, R. Moriya, S. Morikawa, et al., “Electric field modulation of Schottky barrier height in graphene/MoSe₂ van der Waals heterointerface,” *Appl. Phys. Lett.* **2015**, *107*.
- [214] Y. Zheng, J. Gao, C. Han, et al., “Ohmic contact engineering for two-dimensional materials,” *Cell Reports Physical Science* **2021**, *2*.
- [215] Z. Lian, Y. Meng, L. Ma, et al., “Valley-polarized excitonic Mott insulator in WS₂/WSe₂ moiré superlattice,” *Nat. Phys.* **2024**, *20*, 34–39.
- [216] P. St-Jean, V. Goblot, E. Galopin, et al., “Lasing in topological edge states of a one-dimensional lattice,” *Nat. Photon.* **2017**, *11*, 651–656.
- [217] R. Su, S. Ghosh, T. C. Liew, et al., “Optical switching of topological phase in a perovskite polariton lattice,” *Science Adv.* **2021**, *7*, eabf8049.
- [218] Y. Luo, Q. Guo, X. Deng, et al., “Manipulating nonlinear exciton polaritons in an atomically-thin semiconductor with artificial potential landscapes,” *Light: Science & Applications* **2023**, *12*, 220.
- [219] A. Raja, A. Chaves, J. Yu, et al., “Coulomb engineering of the bandgap and excitons in two-dimensional materials,” *Nat. Commun.* **2017**, *8*, 15251.

- [220] C. Rupprecht, M. Klaas, H. Knopf, et al., “Demonstration of a polariton step potential by local variation of light-matter coupling in a van-der-Waals heterostructure,” *Opt. Express* **2020**, 28, 18649–18657.
- [221] T. Wei, L. Bao, F. Hauke, et al., “Recent advances in graphene patterning,” *ChemPlusChem* **2020**, 85, 1655–1668.
- [222] T. Wei, F. Hauke, A. Hirsch, “Evolution of graphene patterning: from dimension regulation to molecular engineering,” *Adv. Mater.* **2021**, 33, 2104060.

List of publications

- [P1] L. Husel*, J. Trapp*, J. Scherzer, X. Wu, P. Wang, J. Fortner, M. Nutz, T. Hümmer, B. Polovnikov, M. Förg, et al., “Cavity-enhanced photon indistinguishability at room temperature and telecom wavelengths,” *Nat. Commun.* **2024**, *15*, 3989.
- [P2] B. Polovnikov*, J. Scherzer*, S. Misra*, X. Huang, C. Mohl, Z. Li, J. Göser, J. Förste, I. Bilgin, K. Watanabe, T. Taniguchi, A. Högele, A. S. Baimuratov, “Field-Induced Hybridization of Moiré Excitons in MoSe₂/WS₂ Heterobilayers,” *Phys. Rev. Lett.* **2024**, *132*, 076902.
- [P3] B. Polovnikov*, J. Scherzer*, S. Misra*, H. Schlömer, J. Trapp, X. Huang, C. Mohl, Z. Li, J. Göser, J. Förste, I. Bilgin, K. Watanabe, T. Taniguchi, A. Bohrdt, F. Grusdt, A. S. Baimuratov, A. Högele, “Implementation of the bilayer Hubbard model in a moiré heterostructure,” *arXiv* **2024**, 2404.05494.
- [P4] J. Scherzer*, L. Lackner*, B. Han, B. Polovnikov, L. Husel, J. Göser, Z. Li, J.-C. Drawer, M. Esmann, C. Bennenhei, F. Eilenberger, K. Watanabe, T. Taniguchi, A. S. Baimuratov, C. Schneider, A. Högele, “Correlated magnetism of moiré exciton-polaritons on a triangular electron-spin lattice,” *arXiv* **2024**, 2405.12698.
- [P5] S. Vadia*, J. Scherzer*, K. Watanabe, T. Taniguchi, A. Högele, “Magneto-Optical Chirality in a Coherently Coupled Exciton–Plasmon System,” *Nano Lett.* **2023**, *23*, 614–618.
- [P6] B. Polovnikov*, J. Scherzer*, S. Misra*, X. Huang, C. Mohl, Z. Li, J. Göser, J. Förste, I. Bilgin, K. Watanabe, T. Taniguchi, A. S. Baimuratov, A. Högele, “Coulomb-correlated states of moiré excitons and charges in a semiconductor moiré lattice,” *arXiv* **2022**, 2208.04056.
- [P7] M. Förg, A. S. Baimuratov, S. Y. Kruchinin, I. A. Vovk, J. Scherzer, J. Förste, V. Funk, K. Watanabe, T. Taniguchi, A. Högele, “Moiré excitons in MoSe₂/WSe₂ heterobilayers and heterotrilayers,” *Nat. Commun.* **2021**, *12*, 1656.
- [P8] S. Vadia, J. Scherzer, H. Thierschmann, C. Schäfermeier, C. Dal Savio, T. Taniguchi, K. Watanabe, D. Hunger, K. Karraï, A. Högele, “Open-Cavity in Closed-Cycle Cryostat as a Quantum Optics Platform,” *PRX Quantum* **2021**, *2*, 040318.

* equal contribution

List of Symbols and Abbreviations

| | |
|-------------------|--------------------------------------|
| 2D | Two-dimensional |
| AFM | Atomic force microscopy |
| CCD | Charge-coupled device |
| CHCl ₃ | Chloroform |
| CVD | Chemical vapor deposition |
| CW | Continuous wave |
| DBR | Distributed Bragg reflector |
| DFT | Density functional theory |
| DOS | Density of states |
| DR | Differential reflectance |
| EDX | Energy dispersive X-ray spectroscopy |
| FLG | Few layer graphene |
| FSR | Free spectral range |
| FT | Fourier transform |
| HBL | Heterobilayer |
| hBN | Hexagonal boron nitride |
| MoSe ₂ | Molybdenum diselenide |
| NA | Numerical aperture |
| PC | Polycarbonate |
| PDMS | Polydimethylsiloxane |
| PL | Photoluminescence |

LIST OF SYMBOLS AND ABBREVIATIONS

| | |
|------------------|---------------------------------|
| rms | Root mean square |
| SEM | Scanning electron microscope |
| Si | Silicon |
| SiO ₂ | Silicon dioxide |
| TM | Transfer matrix |
| TMD | Transition metal dichalcogenide |
| WS ₂ | Tungsten disulfide |

Acknowledgments

I would like to express my gratitude to everyone who has supported me on the journey of my PhD. First of all, my sincere thanks go to Alex Högele. Thank you, Alex, for giving me the opportunity to do research under your guidance, for placing your trust in me from the very beginning, and for allowing me to work independently on my projects, while always making time for discussions and support, even when the pipeline was bursting again.

I am very thankful for the supportive and collaborative atmosphere within our group and for the exceptional colleagues who have made my work possible. Thanks to the experienced PhD students Michael Förg and Manuel Nutz, your wealth of knowledge and experience was a great help in the beginning of my PhD. Thank you, Samarth Vadia, for letting me join your cavity project and making it very easy for me to get my PhD started. Many thanks to Borislav Polovnikov, Subhradeep Misra and Anvar Baimuratov for working together on the MoSe₂/WS₂ project. I think the results we achieved together speak for themselves and are a great example for the power of teamwork. Thank you, Lukas Husel, for your openness to all kinds of questions, our joint work on the cavity and our memorable conference trip to Colombia. Thanks to Jonas Göser, Zhijie Li and Ismail Bilgin for bringing the CVD growth to the next level. None of our projects could have been realized without your work and I would probably still be stuck in the cleanroom exfoliating monolayers. Thank you, Jonathan Förste, for creating the "blackbox", your IT support and teaching me some latte art; Victor Funk, for our fun little GUI project and the invaluable espresso supply; Farsane Tabataba-Vakili, for pushing our group activities and gaming nights in rough pandemic times; and Shen Zhao, for your support with the lab course development. I am glad that I was able to pass on my projects and my experience to the next generation: Special thanks to Julian Trapp, Anna Rupp, Tim Wedl, Lukas Krelle and Christian Mohl, for your support and the fun times we spent together in the lab, the cleanroom and outside the university. I was always looking forward to working together with all of you and enjoying our coffee and Mensa breaks and other activities.

Special thanks also to all the colleagues from the former Kotthaus chair – Philipp Altpeter, for your expertise and constant assistance in the cleanroom; Christian Obermayer and Anton Heindl, for your helpfulness with various technical issues; Stefan Manus, for keeping some motivation to answer even basic electronics questions; and Bert Lorenz and Dayse Ferreira e Silva, for your administrative support.

I would also like to express my gratitude to all our external collaborators: Thanks to Khaled

Karraï, Holger Thierschmann and Clemens Schäfermeier from attocube systems AG for the successful collaboration on the cavity project. Thank you, Henning Schlömer, Fabian and Annabelle Bohrdt, for your theoretical contributions and insights on correlated many-body theory for our MoSe₂/WS₂ project. My appreciation also goes to Christian Schneider and his group in Oldenburg, who allowed us to investigate our sample in their magneto-cavity setup. Thank you, Lukas Lackner, for your commitment during the nightly measurements and the warm welcome in Oldenburg.

Lastly, my deepest gratitude goes to my friends, my family and Janna for always being there for me, for your support and reminding me from time to time that there are more important things in life than working on my PhD ;)